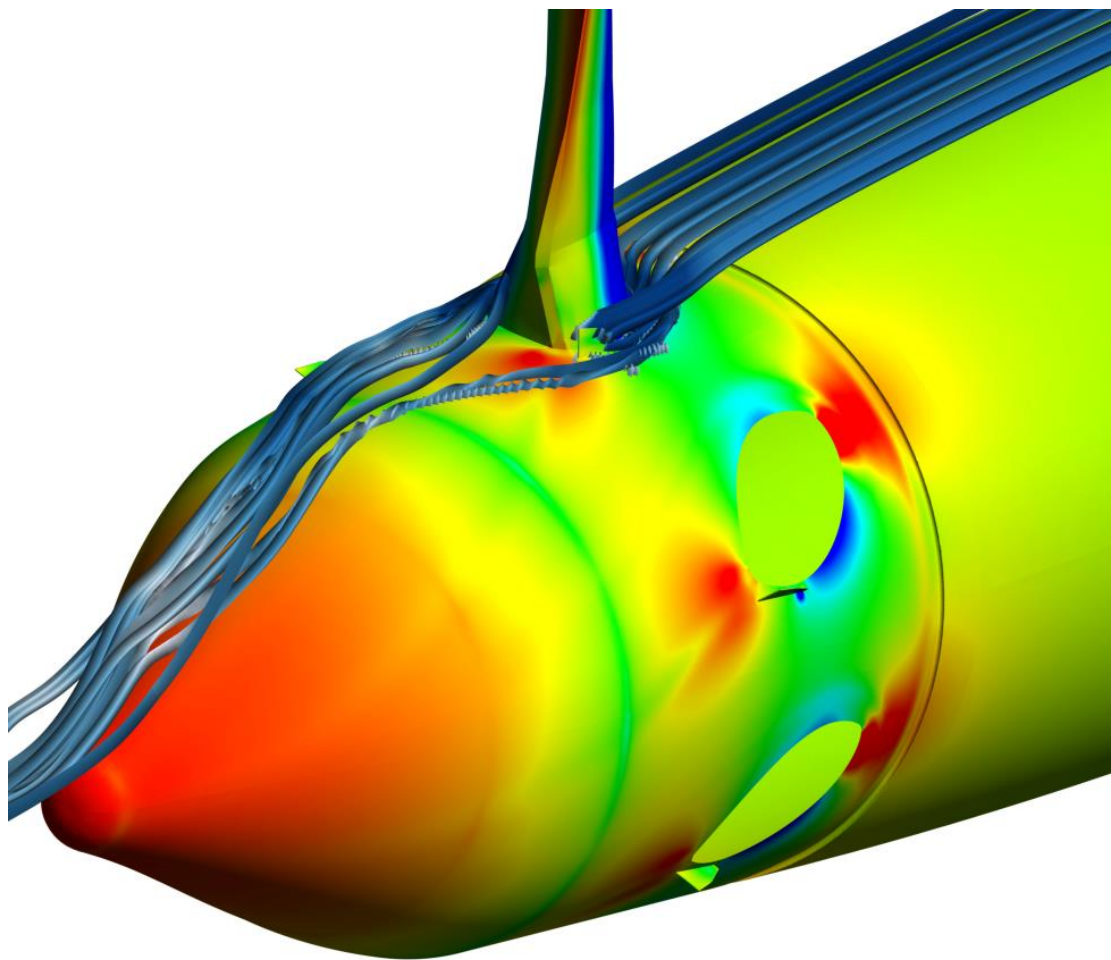


Master of Science Thesis
A. Mota Mera

Aerodynamic design for a pusher propeller spinner



Aerodynamic design for a pusher propeller spinner

By

A. Mota Mera

in partial fulfilment of the requirements for the degree of

Master of Science
in Aerospace Engineering

at the Delft University of Technology,
to be defended publicly on April 2, 2020 at 13:00.

Supervisors: Prof. dr. ir. L.L.M. Veldhuis
Ir. T.C.A. Stokkermans

Thesis committee: Dr. ir. T. Sinnige
ir. W.A. Timmer



Contents

Acknowledgements.....	iii
Nomenclature.....	v
1 Introduction	1
1.1 State of the art of spinner designs for efficiency improvement.....	2
1.2 Research objective	5
1.3 Thesis outline	5
2 Propeller simulation setup	7
2.1 Geometry and CFD setup	7
2.1.1 Turbulence model	9
2.2 Mesh Independence study and grid selection.....	10
2.2.1 GCI mesh independence study.....	11
2.2.2 Refinement of the reference mesh	15
2.3 Conclusions of mesh independence test.....	20
3 Influence of the spinner design on the propeller performance	22
3.1 First spinner geometrical variations	22
3.2 Effect of spinner length reduction on the propeller performance	24
3.2.1 Effect on thrust and propeller drag	24
3.2.2 Effect on separation	28
3.2.3 Swirl formation at blade root and spinner.....	33
3.2.4 Effect of blade exposure on the performance of short spinners.....	43
3.3 Effect of spinner length increment on the propeller performance	48
4 Blade-off spinner assessment	59
4.1 The boat tail effect	59
4.2 Blade-off spinner design.....	62
4.3 Blade-off flow separation assessment.....	65
5 Spinner re-design	71
5.1 Low drag axisymmetric body effect on propeller efficiency.....	71
5.2 Nacelle-Spinner tangency as a propeller efficiency enhancer	75
5.2.1 Flow separation among tangent spinners.	77
5.2.2 Vortex formation and blade root loading	80
6 Passive boundary layer separation control	87
6.1 Baffle concept as a flow interaction tool.....	87
6.1.1 Effect of the baffle concept on the original design.....	87
6.1.2 Effect of the baffle concept on efficient spinner designs.	93
6.2 Spinner grooves and their effect on the propeller performance	103
7 Conclusions and recommendations	111
Appendix	117
Bibliography	121

Acknowledgements

I always liked to describe an engineer as someone that creates a routine out of difficult tasks and makes the impossible look like probable. I hope that one day I can give the world something as significant as what engineering has given to me and I consider this thesis one of first steps in that pursue. I would like to thank the people that I have found during this journey and that helped to make this possible, starting with my supervisors. First of all, thanks to the Professor Leo Veldhuis whose knowledge, expertise and passion had inspired me to complete this stage of my student life. Furthermore I would like to pay special attention to thank Tom Stokkermans for all his support, patience, and hours of time dedicated to help this thesis project, without him, this would not have been possible.

Being a student in a different country is a challenge in many ways, culturally, professionally and personally; however, this experience gave me one of the best gifts that any person could ever had: Friends. I thank to all that made my life here better in every sense. Thank to my fellow colleagues of the room 1.07 for all the Nerdy talks we had no matter how unproductive (Pablo, Íñigo, Sylvain, k etc.) and to all my colleagues from Aerospace that I crossed paths with. I would like to also thank to the friends I made both in Delft and in Rotterdam because without you guys I would have been bored in no time (Daniel Victor, Valentina, Juliana, Marina, Memo, Andrés, etc). In a similar way, thank you Thomas and Alex for being the best roommates that I could have had.

Finally, I would also like to thank to the people that formed part of my personal life in a more direct way. First, thanks to my girlfriend Genesis because she became a very important part of me and because she provided the stability and the support that I needed. Last but not least I thank to my family that has been there for me all the time and to whom I dedicate a few words in Spanish.

Gracias a mi familia, porque siempre han estado ahí en los momentos más difíciles. Gracias papá porque siempre has creído en mí y porque me has servido de inspiración para llegar a ser quien soy y hacer lo que hago buscando la excelencia. Gracia mamá por preocuparte desde siempre por mi aunque te dijera que estaba bien y gracias por las largas llamadas que me hacían sentir como si estuviera en casa. Mis recetas de cocina fueron un éxito en Europa y eso te lo debo a ti. Gracias a los dos por hacer el esfuerzo de mantenerme en la búsqueda de mis sueños a costa de su trabajo duro, espero pagarlo pronto pero con bajos intereses por favor. Gracias a mi hermana Pamela por ser una confidente y un soporte mental clave en mi estadía fuera del país. Te agradezco Pam por las risas que nunca dejamos de compartir a pesar de la distancia y porque tu valentía y hambre por afrontar los nuevos retos me dieron el coraje necesario para ver las cosas de una manera positiva, los amo mucho familia.

Nomenclature

a	Non-dimensional length of the cavity minor axis	
C	Constant	
$C_d = \frac{D}{q}$	Drag coefficient for 1 m ² reference	
$C_p = \frac{p}{q}$	Pressure coefficient	
$C_f = \frac{\tau}{q}$	Skin friction coefficient	
D	Drag	[N]
D	Maximum thickness of Nacelle	[m]
δ_{RE}	Estimation error from Richardson extrapolation	
e_r	Relative error among iterations	
ε	Variable difference between a coarse grid and a finer one	
$F_{ex} = T - D$	Net axial force, Excess Thrust	[N]
F_x	Axial component of force	[N]
F_y	Radial component of force	[N]
F_z	Tangential component of force	[N]
F_s	Security factor for the grid convergence index methodology	
FR_{body}	Nacelle-spinner fineness ratio	
$FR_{spinner}$	Spinner fineness ratio	
f, f_{exst}	Variable value for a given grid size; Zero grid spacing value	
h	Representative grid element size; Non-dimensional Cavity depth	
I_n	n th iteration number	
$J = U/2nR$	Propeller advance ratio	
k	Turbulent kinetic energy	[m ² /s ²]
n	Rotational speed	[rad/s]
n	Rotational speed for advance ratio	[rev/s]
ng	Number of grids	
η_p	Propeller propulsive efficiency	
η	Relative propeller efficiency in terms of the control variable (Original design)	

p	Order of convergence	
p	static pressure	[Pa]
Q	Propeller Torque	[Nm]
Q	Q criterion	[1/s ²]
$q = \frac{1}{2}\rho U_{\infty}^2$	Free stream dynamic pressure	[Pa]
R	Propeller radius	[m]
R_c	Convergence ratio	
r	Radial position relative to the propeller radius	
ρ	Flow density at free stream	[kg/m ³]
s	Distance from the boat tailed section to the groove major axis	
T	Propeller thrust	[N]
t	Normalized extension of the groove from the major axis	
τ	Local wall shear stress	[Pa]
U	Velocity magnitude	[m/s]
U_x	Axial component of velocity	[m/s]
U_y	Radial component of velocity	[m/s]
U_z	Tangential component of velocity	[m/s]
U_s	Standard deviation	
V_{∞}, U_{∞}	Inlet velocity, Freestream velocity	[m/s]
ω	Specific rate of dissipation	[1/s]
y^+	Dimensionless wall distance	

1 Introduction

In the transport industry the use of energy has reached very high efficiency values, which makes more difficult to continue improving propulsion methods that have been used for decades. One of this methods is the propeller. This can be observed either on maritime or in aerospace current designs. Independently of the specific requirements that every condition demands, there are two main groups in which the propeller can be designed: Tracker propeller or Pusher propeller. This research plan is focused on the latter one and one of its specific disadvantages.

A strict technical definition of a pusher propeller would be the one found in scientific literature that describes it as the propeller in which the driving shaft is in compression; however, the inherent problem that is commonly associated with a pusher propeller is the interaction with the wake of any of the bodies that are located upstream of the rotor [1]. In most of the cases, the pusher propeller is located either behind the wing or behind the fuselage, making it in principle more prone to interact with the wake in a more significant way than its tracker counterpart. The propeller used as baseline for this thesis is mounted on a nacelle-spinner configuration in which the fore-body or nacelle will be represented as a static region while the spinner will be rotating together with the blades. Even when the rotor might be predicted to ingest less turbulent boundary layer (Depending on the turbulence modelling) developed over the nacelle, the spinner that is located behind the rotor would inevitably encounter highly turbulent wake of the lowest part of the blade. The wake to blade interaction triggers different problems, such as undesired aeroacoustics [2] or energy loss due to swirl motions induced by the rotation of the propeller which inevitably ends up in a reduction of the propeller efficiency.

The interaction between the rotor and the upstream flow is especially different in the pusher propeller configuration because of the presence of a nacelle or a forebody. This particular difference influences the way in which the blade root is loaded and thus the interaction of the flow and the spinner downstream ahead. In a more specific way, the idea of the spinner modification is more related to the increment of the propeller efficiency by two means: Boundary layer separation delay and the reduction of swirls induced drag [3]. Given that the larger flow speeds are obviously observed at the tip of the blade, it can be expected that the tip vortices are larger than the ones encountered at the blade root [4]. This is one of the reasons, in the author's opinion, of why most of the available research has been dedicated to the study of the tip vortex rather than to the hub one. This research will be performed under cruise conditions, meaning that both rotational speed and flight speed will remain constant. Since the rotor diameter is not changing either, the efficiency term can be expressed as the ratio of Excess Thrust (F_{ex}) over Torque (Q) for comparative purposes taking into account that a constant advance ratio would be assessed during the research.

$$F_{ex} = T_{Blade} - D_{nacelle+spinner}$$
$$\eta_p = \frac{\text{work done}}{\text{shaft power}} = \frac{F_{ex} U_{\infty}}{2\pi n Q} = C \frac{F_{ex}}{Q}$$

As the spinner geometry is changed, the excess thrust and the Torque change as well. If the efficiency term (η_p) is larger than the one of the control variable (Original design) then it could mean two things: That the increment of Excess thrust is larger than the increment of Torque or that the decrement in Excess thrust is lower than the decrement in Torque. Even when in both cases the efficiency would have been improved, values of torque that are lower than the one of the original design would not be considered as improved designs.

1.1 State of the art of spinner designs for efficiency improvement

One of the problems that would be addressed along the present thesis is related to the vortices system that has been observed close to the hub, particularly due to the low pressure regions induced by certain swirl formations. In a more concrete way, the research aims for the reduction of the drag caused by the so-called hub vortex. This is considered as a detrimental feature mostly in marine pusher propeller designs. The hub vortex inevitably ends up increasing the propeller drag, thus reducing the efficiency [3]. Even when the vortex drag in pusher propellers is a topic that has been addressed by several authors, the ones dedicated to the maritime sector are the ones that have focused on the particular effects of the spinner design as a potential solution [5], even suggesting the placement of performance enhancing methods directly on the spinner section [6]. One of the reasons is the significantly lower aspect ratios and the lower rotor radius that marine propellers normally exhibit compared to the ones for aerial applications. This difference would evidently increase the chances for the formation of a hub vortex, especially due to the closer interaction of the trailing vortices. Another reason is the presence of cavitation due to the reduction of pressure induced by strong vortices/swirls. In the cases where the hub vortex was successfully reduced, pusher propeller of very large cargo ships showed improvements up to 2% in efficiency [7].

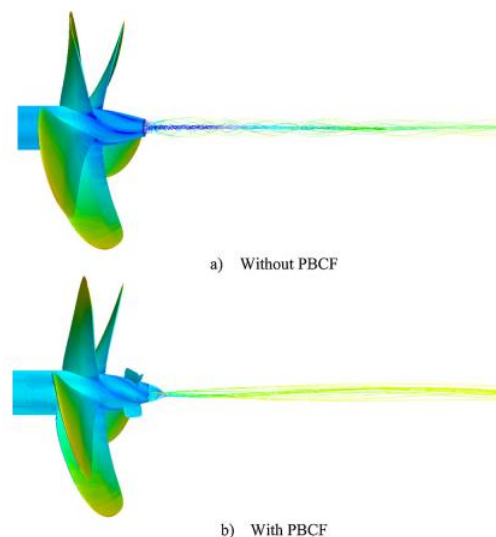


Figure 1.1: Hub vortex reduction with propeller boss cap fins [6].

In figure 1.1 the low pressure region that was observed in a cargo ship pusher propeller was decreased by the means of propeller boss cap fins placed in the spinner [6]. The fins were reported to be the responsible for the 2% increment of the propeller efficiency. The use of methods that can potentially be applied on the spinner in order to interact with the vortex formation would require further understanding on how exactly would the spinner shape affect the propeller drag in a different fluid such as air; nevertheless, the effect of the spinner design has been studied before in marine podded propellers. One of these studies was carried out by M. Islam [5], where the hub taper angle was modified for a pusher and a puller configuration. Some of the conclusions derived from the experiment suggested that the propeller efficiency increased for a hub taper angle (Fig. 1.2) of 15° more than it did for the 20° case, both referring to a pusher configuration. However, it was observed that the 20° tapered hub increased the torque more than the one of 15° at the same time that both cases presented practically no variations on the thrust coefficient [5]. Following the schematic representation of the Figure 1.2, it can be interpreted that the hub with a less steep slope favored the efficiency improvement of the pusher propeller.

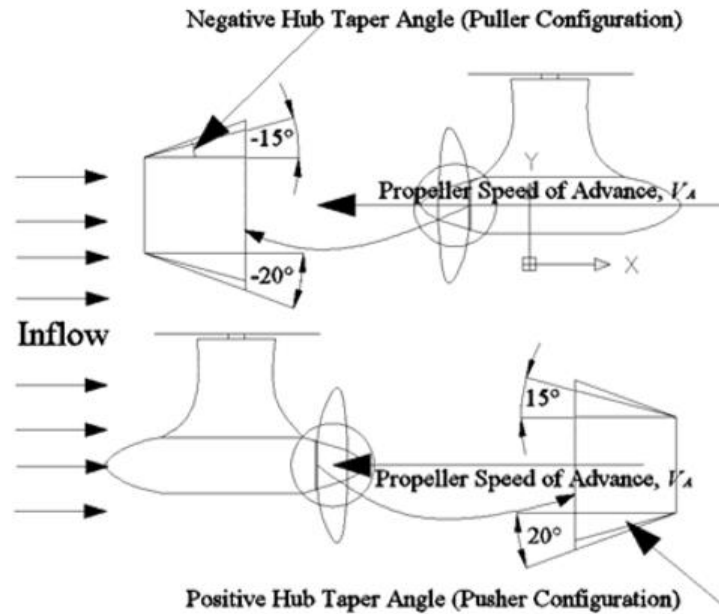


Figure 1.2: Hub taper angle of 15° and 20° in a marine podded propeller [5].

A tendency of having narrower hubs/spinners in pusher configurations has been repeatedly found to be beneficial. According to the results obtained by Shamsi [9], a pusher propeller with a moderate hub curvature, especially at the end, showed that the flow separation observed around the spinner was significantly delayed in comparison with a sharpened edge hub end. The more moderate pressure gradient induced by the curvature of the hub prevented the flow from a sudden deceleration allowing a better pressure recovery due to the relatively larger velocities. On the other hand, a steep curvature such as the one encountered on a cylinder induced rapid separation that increases the overall drag.

While the maritime industry has been well aware of the potential benefits of reducing the propeller hub vortex, the aerospace industry has paid most of the attention to the tractor propellers where the detrimental effects of the hub vortex are not a recurrent issue. In fact, due to the current struggle that is being faced by the transport industry related to the reduction and eventual replacement of the fossil fuels, the electrical engines seemed to be commonly combined with pusher propellers, especially in small aircraft or UAV's where the propeller has shown that it can delay the flow separation on the bodies acting upstream the rotor [10]. This also seemed to be the cases of the later versions of certain UAV produced by a worldwide manufacturer such as General atomics where not only electrical engines seemed to be preferred but also pusher propeller configurations. However, the lack of a low drag aftbody or spinner such as the one of Figure 1.3, seemed to be taken into account for the latest designs. In the experiment carried out by Hall [11], it has been pointed out the particularly large vorticity observed at the rotor hub of the US Army UAV RQ-7B. Despite being a relatively recent design (1991), the hub vortex seemed to be of very little importance for the UAV's design efficiency back then. Nevertheless, later versions of the same manufacturer such as the RQ-11 Raven (2001) or MQ-1C Grey Eagle (2009) changed the spinner design into a design that resembled a low-drag aft body (Fig. 1.4).

Figure 1.3 depicts another example of the aftbody design that was preferred for a mini-UAV test performed in the university of Sidney in Australia [12], where the flow separation was expected to be decreased due to the aftbody design.

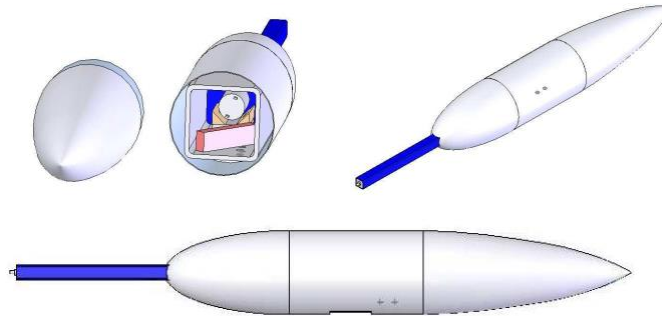


Figure 1.3: Test rig aerodynamically design so the flow did not encounter a turn larger than 11° [12].



Figure 1.4: RQ-7B (Left) and MQ-1C Grey Eagle (Right).

The importance of the spinner design seemed to be emphasized on the latest designs at the point that regional aircraft manufacturers such as Eviation, Joby Aviation and Piaggio seemed to come up with similar designs for their pusher propeller spinners respectively. The similitude might very well be related to the improvement of the pusher propeller performance since certain manufacturing companies such as Piaggio seem to be aware of the complex aerodynamics of the vortex-spinner interactions [13].

In summary, the spinner design of the pusher propeller configurations has not been overlooked; however, the author has found that a large part of the research available has been made for maritime purposes in the sense of hub vortex explicit reduction. On the other hand, aerial industry has focused more on the implementation of low drag bodies in both tractor and pusher propellers. And even when the detrimental effects of the hub vortex have been observed in literature, most attention has been placed on the interference effects mainly due to the most common use of tractor propellers rather than pusher ones, at the point of being considered negligible effects [14]. Micro aerial vehicles and UAV's, together with low capacity regional aircraft were found to concentrate an important part of the research made on pusher propeller spinner design. The designs that are currently in use did offer a starting point from which the original design can be modified.

Based on the existing data it can be said that better aerodynamic spinner designs that might eventually reduce the drag associated with the hub vortex, could represent a valuable tool for future pusher propeller designs. The information provided by this research is expected to be use in order to generate a better understanding of the Blade root/Spinner interaction and its influence in the propeller efficiency.

1.2 Research objective

The objective of the research is to provide a spinner aerodynamic design that can potentially increase the efficiency of a pusher propeller specifically for cruise conditions. The following goals describe in a broader way the steps followed to accomplish the objective.

1. Obtain initial information about the propeller design used as control variable in order to give an idea of the current benefits, flaws and potential improvements through a reliable CFD simulation.
2. Establish a relation between the spinner geometrical changes such as length and diameter and the variation of the performance variables through a series of CFD simulations.
3. Prepare a set of blade-off experiments (Spinner designs) focused on the flow separation delay that low drag bodies tend to show in order to offer an idea of the pressure recovery of the nacelle-spinner configuration alone.
4. Compare the efficiency changes of the blade-off designs with the ones of the blade-on conditions. Re-design the spinner based on the results obtained in points 2 and 3. Select the most efficient design of the extensive series of simulations (At the moment of the selection, a deep understanding of the cause-effect of the aerodynamics of that particular propeller is expected).
5. Assess the effect of Baffles and Spinner Grooves (cavities) as passive boundary layer control method in order to improve the propeller efficiency.
6. Establish a relation between the selected passive method applied to the new spinner and the variation of the performance variables through a series of CFD simulations. Based on the results obtained, prepare a set of experiments than combine an X spinner design + X passive performance enhancing method in order to select the most efficient design.

1.3 Thesis outline

The thesis is composed of four research stages from chapter 2 to the chapter 6 and culminates with a final 7th chapter dedicated to the summary and discussion of the results. The chapter 2 describes the given geometry that is used a control variable during the entire research; at the same time that it establishes the CFD setup followed for all the simulations. CFD elements necessary for the simulations such as the boundary conditions and turbulence models are discussed with an especial emphasis in the mesh independence study that was carried out following both the classic and the least squares grid convergence index (GCI) methodology. Chapter 3 provides an initial guess to the performance variations caused by simple length modifications where variables such as drag, nearby pressure coefficients, vortex visualization and propulsive efficiency are compared among each other as performance indicators. Chapter 3 ends up providing enough information to form a realistic idea of the performance improvement that might be achieved by changing the spinner design. Chapter 4 approaches the aerodynamic design of the spinner as a whole axisymmetric body that included the nacelle and that was tested under blade-off conditions. Given that the pressure recovery observed in the spinner showed to be particularly important for the drag reduction and thus for the performance improvement, the design assessment carried out in chapter 4 led to the use of large fineness ratio spinners that encountered the largest values of pressure recovery.

In chapter 5, an extensive series of simulations are discussed in order to provide a spinner design that can potentially induce a significant improvement in efficiency. The discussion starts with the comparison of the results obtained in chapter 4 (Blade-off) and the Blade-on more realistic approach, followed by a spinner re-design that points out the benefits gained by a smoother geometrical transition such as tangency between the static part (Nacelle) and the rotational one (Spinner). Lastly in the chapter 6, two passive boundary layer control mechanisms are presented as a means of performance enhancement. The first of the mechanisms was the use of baffles as flow deflectors, mainly focused on the flow separation delay observed at the blade root suction side. The second one was the use of transversal spinner cavities or grooves, that based their effectiveness in the reduction of no slip condition of the incoming boundary layer of the spinner thanks to the “trapped vortex” generated inside the cavity. The conclusions derived from the research are presented in chapter 7 together with recommendations for future pusher propeller spinner designs.

2 Propeller simulation setup

The thesis research that is being shown in the next chapters was performed under the assumption that no experimental data was available to validate the outcome of the simulations. This is why special importance was placed on the CFD setup. The selection of the setup and boundary conditions was based on the idea of capturing the aerodynamic interaction at the hub (Blade root and spinner) with no significant dependency on the size of the grid at the same time that relatively low computational power was used. The selection of CFD parameters such as the control volume characterization, boundary conditions for CFD simulation, the solver or the grid size will be described in the next chapter in order to establish the basis for a reliable simulation of the propeller that was given as the original design. In later chapters two out of the three components of the original configuration will be kept original (Nacelle and Blade) while the spinner design will be modified. This is why it is important to have a clear idea of the performance of the original design. In pursuance of the verification of the original simulation results, a mesh independence test was performed in order to select the grid size used for the entire research.

2.1 Geometry and CFD setup

The rotor was a six-bladed pusher propeller model with a diameter of roughly 2m. Both, nacelle and spinner were axisymmetric bodies of revolution which facilitated the posterior re-design using 2D sketches in CAD software. The rotor had a positive rotational sign in downstream direction.

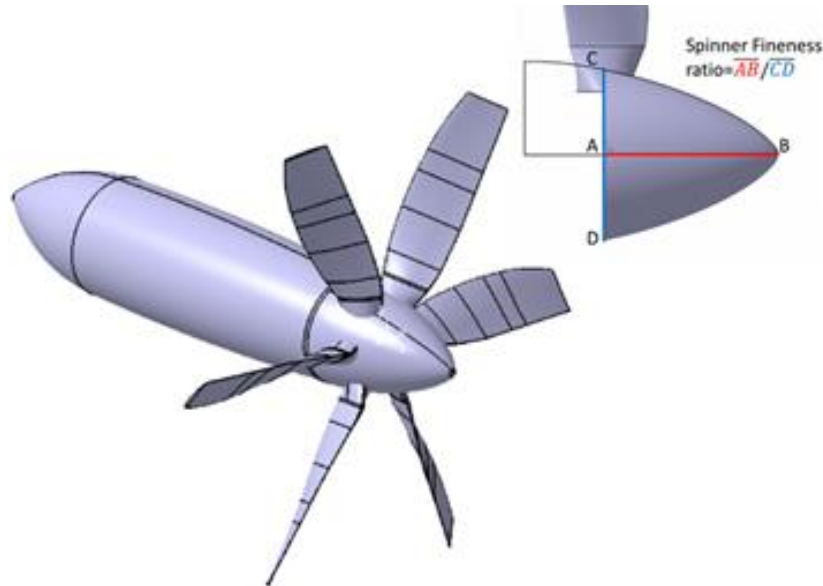


Figure 2.1: Spinner fineness ratio definition.

The coordinate system established for the research had its origin at the intersection of the rotational axis of the propeller and the blade root airfoil center.

The entire axisymmetric body (Nacelle + Spinner) fineness ratio (FR_{body}) was 4.7, where the FR_{body} was defined as the body length over the maximum thickness. Due to the spinner re-design, a local fineness ratio was defined for the spinner alone (Fig.2.1). The spinner fineness ratio ($FR_{spinner}$) was defined as the

spinner length divided by the diameter both measured from and at the blade root center ($0 x/R$) and had a value of 1.02 for the original design.

The CFD domain was defined according to the original model but also for the future geometrical changes of the new designs. Although steady state simulations were performed throughout the thesis, one comparison was made with a transient simulation. This brought the necessity of dividing the domain in 4 parts: The enclosure, the nacelle, the wake and the rotational parts. With the last one being the sub-domain where transient methods such as sliding mesh could be selected. Even for steady state propeller simulation methods such as moving reference frame (MRF) where the fluid is the one that moves around a static rotor, a sub-domain that contains the moving parts can be helpful in order to perform the simulations post-processing in a simpler manner.

The largest section or enclosure was the one holding the previous 3 sub-domains within it and it was used to apply boundary conditions that impose freestream and periodicity conditions since only one blade was used for the simulations (Fig. 2.2).

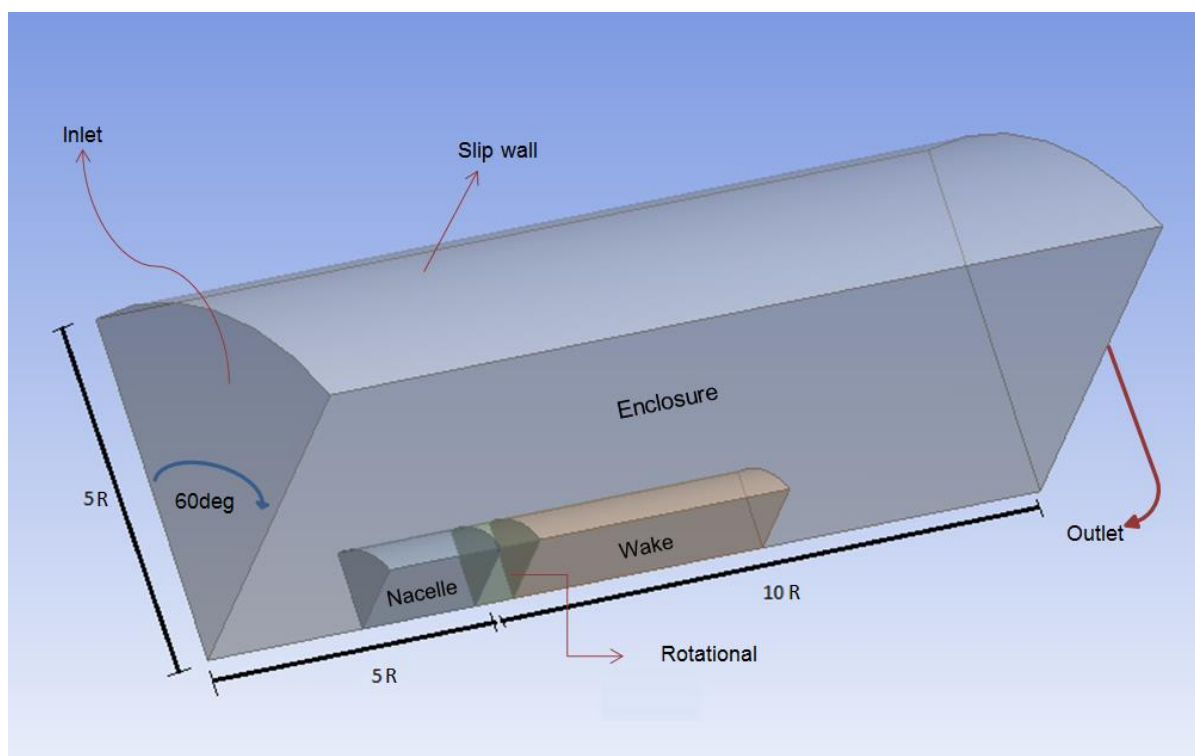


Figure 2.2: Control volume, sub-domains and boundaries.

The control volume extended 10 blade radius (R) downstream the origin point, $5R$ upstream and $5R$ in radial direction, similar to the setup used in other propeller simulations [15]. The Nacelle, Rotational and Wake regions concentrated most of the mesh elements although the mesh was especially refined in the rotational zone.

The solver used in this research was ANSYS fluent. This solver has shown good agreement with the experimental results of previous simulations of propellers [16] and particularly when solving the RANS equations [17]. An important part of the simulation setup was saving time and computational power without compromising the results of the simulations performed with a coarse grid. The tests were performed as a steady state type of simulations, not only because of the relative lower computational time compared to the transient methods but also because only cruise conditions were assessed during the spinner design.

As mentioned before the steady state method used was MRF or frozen rotor. This method has been used before with acceptable result agreement between propeller simulations carried out with sliding mesh (Transient) and MRF (Steady) methods [18]. In summary the simulations were performed with MRF, Pressure-Based couple solver, pseudo-transient method, Fluent multigrid Initialization (FMG) and upwind second order accuracy for all the equations as suggested by the commonly used solver settings [19]. The figure 2.3 depicts the rotational sub-domain that hosted the blade and spinner tested for cruise conditions (Table 2.1).

Table 2.1: Cruise conditions for CFD simulation

Inlet velocity (V_{∞})	113.17 m/s
Advance ratio (J)	1.724

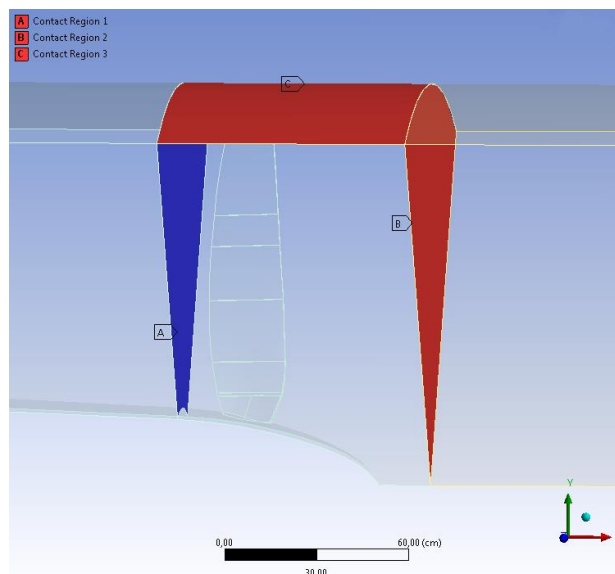


Figure 2.3: Contact/Interface regions between the Two parts of the control volume.

2.1.1 Turbulence model

The k- ω SST turbulence model was used for the simulations carried out in the thesis. This approach modeled the turbulence with two equations, one equation for turbulent kinetic energy (TKE) and the one for turbulence dissipation rate. This model has been largely used to perform MRF simulations [20] and some of those previous propeller simulations have tended to use turbulence models that require the solution of the viscous sublayer; however, this would be related to an inherent increment in the computational power needed mostly due to the large number of elements encountered close to the wall [21]. The moderate refinement on the walls would tend to solve the boundary layer using the logarithmic region approach instead of a near wall approach mostly because of the larger values of y^+ . It is expected that the main difference would be observed at the regions where flow separation occurs or in regions with relatively large turbulent values such as TKE. Taking into account that one of the goals regarding the spinner design is the flow separation delay, the difference between both types of wall treatment should not represent a significant difference compared to simulations with low Reynolds flows [22].

The version of solver used in the thesis used blended wall functions for the turbulence model k- ω SST that gave priority to a cell solving solution (Near wall approach) or a logarithmic region one (Wall functions) depending on the value of y^+ . This avoided the necessity of a large resolution mesh close to the wall. Since a fully turbulent approach was preferred over a transitional flow option, the automatic

wall functions will be used if the wall's adjacent cell centroid lies within the logarithmic-law layer at a $y^+ < 30$ [22]. As shown in Figure 2.4, the maximum Y^+ value of one of the coarsest grids lied within 32, being this the highest value encountered only at the tip of the blade. On the other hand, y^+ values below 1 were encountered on the region close to the end of the spinner where the flow was very likely to encounter separation.

In order to keep track of the convergence of the simulation, the drag of different parts of the propeller was used as monitor. However, the oscillations of monitors such as drag has been observed before in simulations with presence of flow separation and SST $\kappa\text{-}\omega$ turbulence models [23] together with the lack of accuracy of RANS equations to predict turbulent stresses in the detached shear layer emanating from the separation [24]. In other words, even when the simulation has converged at low residuals levels ($1e\text{-}7$) and the values of certain variables seemed to be stable, this might not be the case for the regions of the propeller where flow separation was occurring. This is why in order to obtain a final value of drag after the simulation converged, the average of the last 100 iterations was taken. An average of the last iterations would be expected to decrease the chances of getting a drag value that was outside of the converged error band, especially at regions such as the spinner where the flow separation produced larger oscillations for the monitor values of the converged solution.

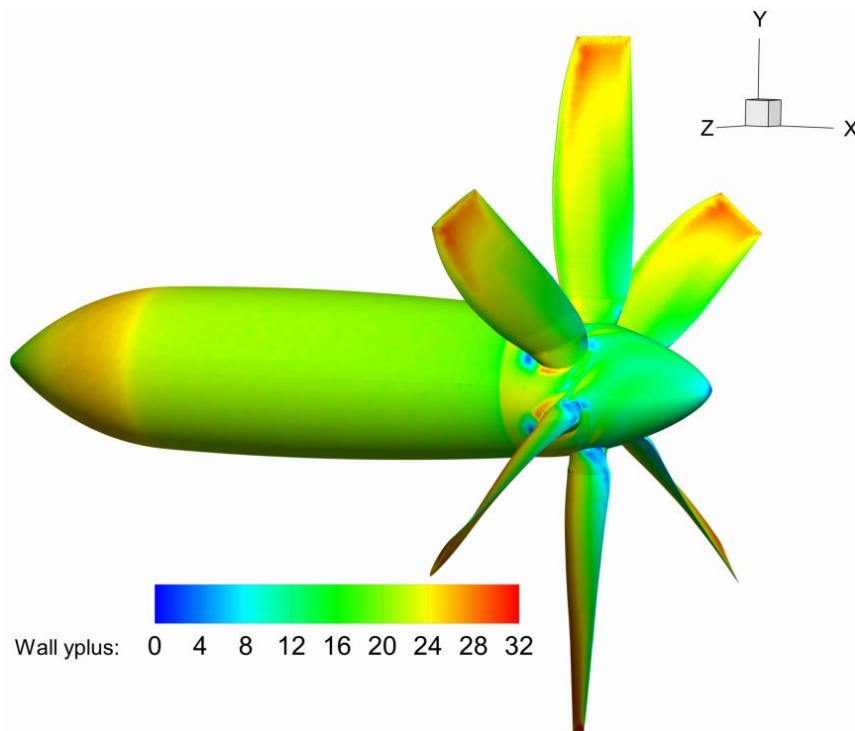


Figure 2.4: Values of y^+ on the baseline propeller configuration with the coarsest grid. X axis values are positive in downstream direction.

2.2 Mesh Independence study and grid selection

The meshing environment of ANSYS Fluent was used in order to generate the grid for the propeller simulations. It is important to emphasize that due to the different spinner geometries that were tested, light meshes were preferred. The objective was then to ensure that the mesh selected was predicting a simulation outcome that had very low dependency on the grid sizing. Two different inflation layer values were given to the geometry, one for the blade and other for the spinner and nacelle, in order to keep similar y^+ values. The first layer thickness method was used in compliance with the y^+ of around 17 with maximum values of 32 in the nacelle and spinner.

The results of the simulations that were performed depended of course on the domain discretization imposed by the mesh size. These mesh elements sizes are presented in table 2.2 and 2.3 and corresponded to a grid of 11.48 million elements that was refined at the spinner region. Despite the relatively small size of the grid elements next to the walls and at the inflation layers, it was necessary to assess the influence of the mesh sizing on the simulation results. This was done by the means of a mesh independence study. In order to produce different grid sizes, all the elements shown in tables 2.1 and 2.2 were scaled using a factor of 1.3 with the exception of the number of inflation layers, the growth rate and the first layer thickness in order to maintain a similar y^+ along all the walls. It is important to mention that the region around the spinner was refined prior to the grid scaling.

Table 2.2: Element sizes for the mesh used as reference. (Values shown as a fraction of the propeller radius)

Wall sizing (2D)	Element size
Pressure and suction sides	$4.57 \times 10^{-3} R$
Trailing edge	$4.57 \times 10^{-4} R$
Nacelle and hub	$9.32 \times 10^{-3} R$
Leading edge	$5.50 \times 10^{-4} R$
Body sizing (3D)	Element size
Wake and Rotational sub-domains	$1.86 \times 10^{-2} R$
Nacelle sub-domain	$2.28 \times 10^{-2} R$
Enclosure sub-domain	$1.10 \times 10^{-1} R$
Vortex region (Blade root)	$4.57 \times 10^{-3} R$

Table 2.3: Reference mesh characteristics in ANSYS meshing

Mesh parameter	Value/Option selected
Sizing preference	Proximity and curvature
Relevance center	Fine
Transition	Slow
Smoothing	High
Span angle center	Fine
Minimum element size	$1.06 \times 10^{-4} R$
Proximity minimum size	$2.54 \times 10^{-4} R$
Maximum face size	$1.02 \times 10^{-1} R$
Nodes	2 852 983
Elements	11 486 668
Nacelle inflation First layer thickness	23 layers, 1.2 growth rate $1.27 \times 10^{-4} R$
Blade inflation First layer thickness	18 layers, 1.2 growth rate $8.47 \times 10^{-5} R$

2.2.1 GCI mesh independence study

As referred in literature [25] & [26], 1.3 was a common factor for scaling the mesh element size in order to produce a coarser or finer mesh and perform a mesh independence study using the grid convergent index methodology (GCI). The method relied on the Richardson extrapolation and the objective of the mesh independence study was to assess whether or not a given mesh is close to the theoretical zero

grid spacing value. A common way to perform the mesh dependence study is the classic GCI approach that is based on the comparison of 3 grids of different sizes (Coarse, Medium and Fine) in which an apparent order of convergence can be determined and thus a theoretical zero grid spacing value can be extrapolated. The table 2.4 shows 5 meshes that resulted from scaling the element size of the reference mesh (11.4 million elements). Two coarser grids were obtained as well as two finer ones.

Table 2.4 Mesh sizes for the independence study

Mesh designation	Number of elements (Millions)
Coarsest (5)	4.1
Coarse (4)	6.6
Reference (3)	11.4
Fine (2)	21.9
Finest (1)	43.2

Given that there were more than three grids available for the classic GCI calculation, the apparent order of convergence was calculated using the combinations of three grids out of the five available ones. But also using a least squares approach of the CGI methodology [27].

The excess thrust of the entire propeller (Nacelle + Spinner + Blade) was used as a reference for the assessment of the mesh size dependency. Given that different spinner shapes were going to be tested and there were regions of flow separation, the mesh independence test was carried out using local drag measurements in the blade root, the nacelle and the spinner. It is important to emphasize that in order to obtain the drag values that were compared, the simulations were run between 4.5 and 6 thousand iterations with velocity residuals below 1E-7 and relatively stable values of propeller excess thrust that were relatively stable since the first 2.5 thousand iterations.

The GCI methodology bases the assessment under the assumption that the error estimation between a given value obtained by a certain grid size and the theoretical zero grid spacing value can be predicted using a Richardson extrapolation (Eq. 2.1). The error estimation would then be calculated based on the apparent order of convergence which was then multiplied by a safety factor of typically 1.25 [25] [28].

(2.1)

$$GCI = F_s(\delta_{RE})$$

(2.2)

$$\delta_{RE} = f_i - f_{exact} = \alpha h_i^p$$

Where F_s is the safety factor and δ_{RE} is the estimation error obtained from the Richardson extrapolation (Eq. 2.2). The estimation error is defined as the difference of the local scalar quantity of any given grid (f_i) and the exact solution (f_{exact}). In equation 2.2 α is a constant and h represents the mesh discretization understood as the average element size. The difference between the classic fit and a least squares one is of course the number of grids used to calculate the apparent order of convergence p . For the classic method the apparent order of convergence is calculated as shown in equation 2.3 and 2.4.

(2.3)

$$p = \frac{\log \left| \left(\frac{f_3 - f_2}{f_2 - f_1} \right) \right| + q(p)}{\log r_{21}}$$

$$(2.4) \quad q(p) = \log \left(\frac{r^p_{21} - s}{r^p_{32} - s} \right)$$

In the GCI calculation r represents the refinement ratio and the smaller subscripts are assigned to the finest grids. On the other side, the least squares fit requires minimizing the equation 2.5 in order to find the values of f_{exact} , α , and p

$$(2.5) \quad s(f_{exact}, \alpha, p) = \sqrt{\sum_{i=1}^{ng} (f_i - (f_{exact} + \alpha h_i^p))^2}$$

$$(2.6) \quad U_s = \sqrt{\frac{\sum_{i=1}^{ng} (f_i - (f_{exact} + \alpha h_i^p))^2}{ng - 3}}$$

Where ng is the number of available grids. As it can be inferred from equation 2.6, the larger the number of the grids tested, the lower the uncertainty (U_s) of the fit. Both the classic method and the least squares version might present different convergence conditions that can be evaluated either using the ratio of convergence (Classic fit) or the apparent order of convergence p (Least squares fit) [27].

1. $p > 0$ for f Monotonic Convergence
2. $p < 0$ for f Monotonic Divergence
3. $p^* < 0$ for f^* Oscillatory Divergence
- Otherwise Oscillatory convergence

Where p^* was obtained with equation 2.5 by substituting f_i for $f_i^* = |f_{i+1} - f_i|$. Although the classic GCI method was carried out using a combination of 5 available grids, the apparent orders of convergence were either indicating divergence or monotonic convergence with values of p that were considerably larger than the theoretical order of the model (Second) in most of the cases. The different orders of convergence were result of the combination of the grids. This indicated the presence of scattered data. The mesh independence study was then performed using the least squares version of the GCI methodology.

For this type of GCI the error estimation based on the Richardson extrapolation can be used only when there is a monotonic convergence [27]. The grid convergence index is then defined in equation 2.7.

$$(2.7) \quad GCI = 1.25(\delta_{RE}) + U_s$$

Eq. 2.7 is used when p lies between 1 and 2; however, when $p < 1$ then δ_{RE} becomes over conservative and the points evaluated seem to be far away from the exact solution. On the other hand when p is larger than the theoretical order of the model then the apparent order of convergence was set to two [27]. In this case equation 2.5 has to be minimized only for two variables f_{exact} and α .

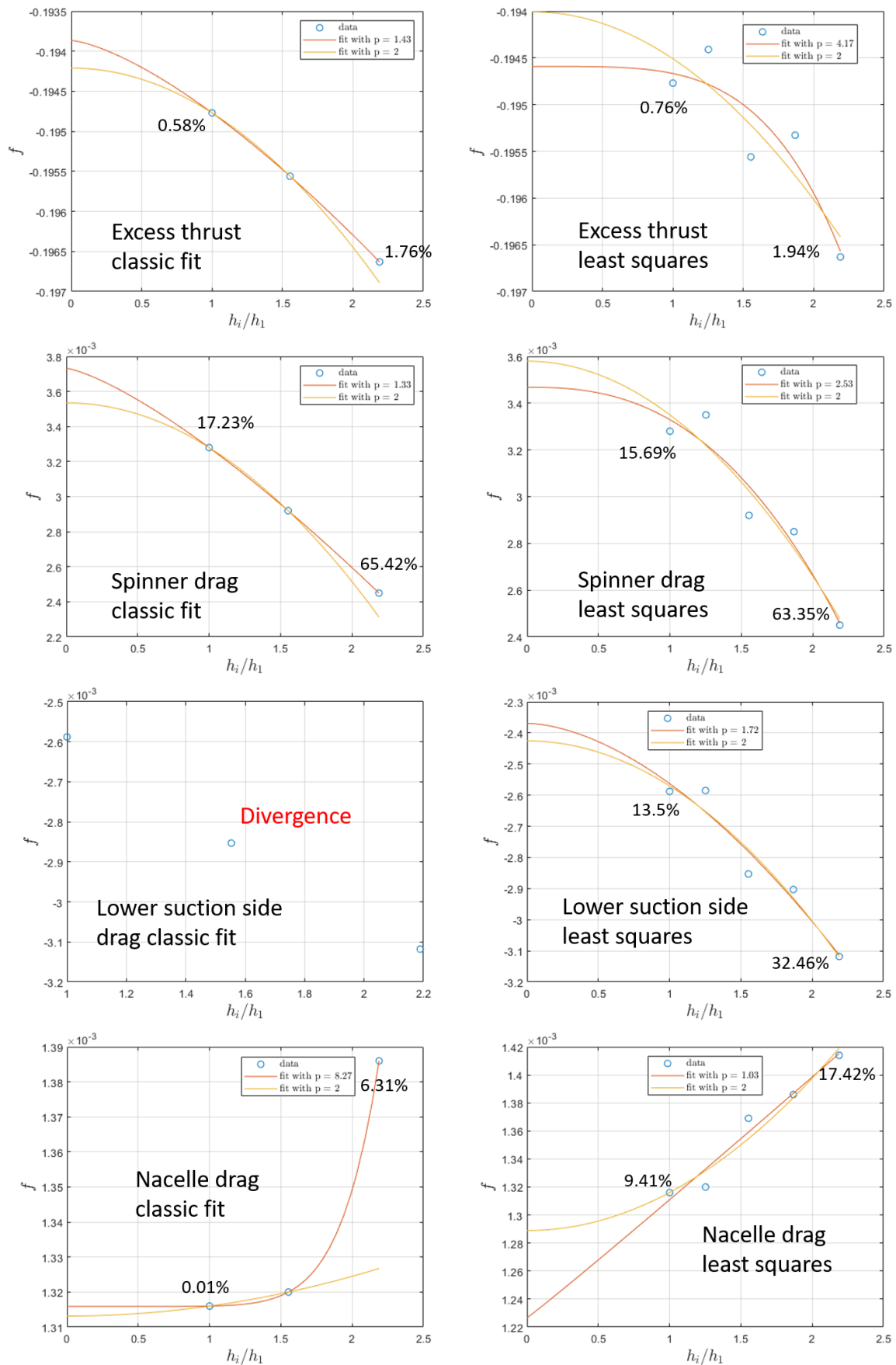


Figure 2.5: GCI values for classic and least squares fits of propeller excess thrust and local drag values. The GCI values are shown for the finest and the coarsest grids. (Force coefficients were calculated for free stream dynamic pressure and 1 m² surface reference).

In Figure 2.5 the first two comparisons made between the classic and the least squares methodologies showed agreement among each other for the overall excess thrust and the spinner drag. However, the later comparisons that assessed the drag values of the blade root suction side and the nacelle showed larger discrepancies between the classic and the least squares fit. All the cases showed convergence except for the one of the lower suction side and all the least square fits presented monotonic convergence.

It was evident that the excess thrust presented lower GCI values than the ones showed by any other drag variable assessed in the mesh independence study. GCI values of 1.94 for the coarsest mesh indicated that the net axial force (Thrust – Drag) did not change significantly when compared to the theoretical zero grid spacing value. On the other hand, part of the total amount of excess thrust was the spinner drag that exhibited significantly larger GCI values for the coarsest mesh (63.35%).

The propeller excess thrust was at least two orders of magnitude larger than the spinner drag force with spinner drag values that represented around 1.5% of the propeller excess thrust. Regardless the low influence of the spinner contribution to the overall axial force of the propeller mostly produced by the blade, the calculated drag showed large dependency on the grid size (Figure 2.5). This would lead to think the finest grid would be more suitable in order to perform more reliable simulations for the new spinner designs. However, other way to approach the large dependency on the grid size for the spinner was to apply a refinement around the spinner region. This would be expected to resolve the simulation with less dependency on the size or in other words, the spinner drag would be closer to the theoretical zero grid spacing value calculated with the GCI.

The local refinement would allow to use a coarser mesh than the finest one of 43 million elements and obviously reduce the computer power needed. Taking into consideration that both the excess thrust that was mostly produced by the blade (97%) and the nacelle drag showed values that were closer to the zero grid spacing one, only the spinner region was refined. Nevertheless, it was necessary to identify the part of the blade where the flow separation that was occurring at the spinner might have affected the blade loading and thus the mesh size dependency. In order to obtain more information about the influence that the blade root has on the overall drag, the blade was referred as a two sections blade, the lower region localized below 0.25 r/R and the upper part which comprised the rest of the blade.

As it can be observed in the Figure 2.6 and 2.7, the grid refinement seemed to affect mostly the blade root but also the blade tip in a lesser extent. The blade root was the only region of the blade that produced drag instead of thrust and it was especially predicted by the finer grids. The two coarsest grids seemed to be over-predicting the blade root thrust while the 11.4 million, 21.9 elements and 43 million element grids showed similar blade loading predictions. These observations led to the conclusion that the reference mesh (11.4 million) might present spinner drag values that were closer to the theoretical zero grid spacing value after a local refinement around the spinner region and the blade root one.

2.2.2 Refinement of the reference mesh

The 11.4 million grid was refined using the spherical refinement zone previously located at the blade root trailing edge. Through the extension of the sphere radius, the number of elements inside the local refinement was increased as shown in Figure 2.9. The new refinement decreased the size of the elements behind the spinner for later assessment of longer designs. Given that the refinement was extended inside the rotational region, the total number of elements of the grid was increased; however, the length of the domain where the wake was calculated was reduced since it was considered unnecessary long (Fig. 2.8).

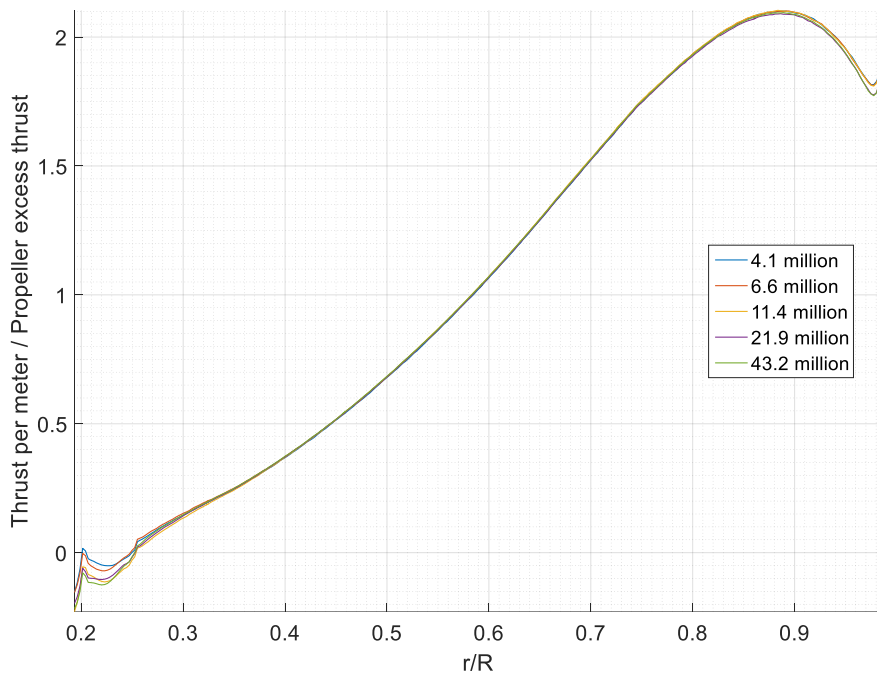


Figure 2.6: Propeller blade thrust encountered on the five grid sizes simulations.

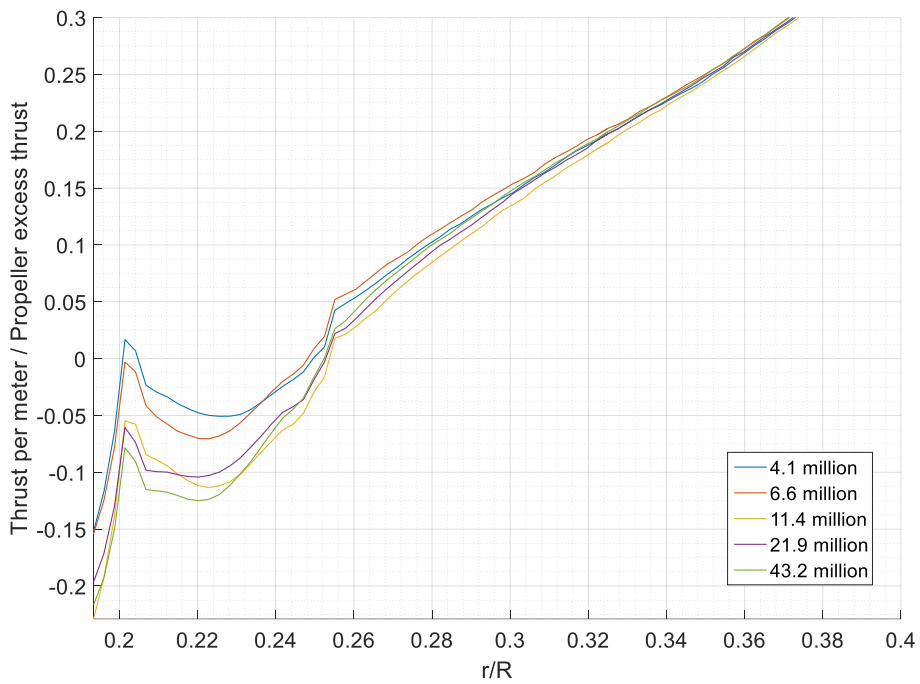


Figure 2.7: Blade root thrust distribution encountered on the five grid sizes.

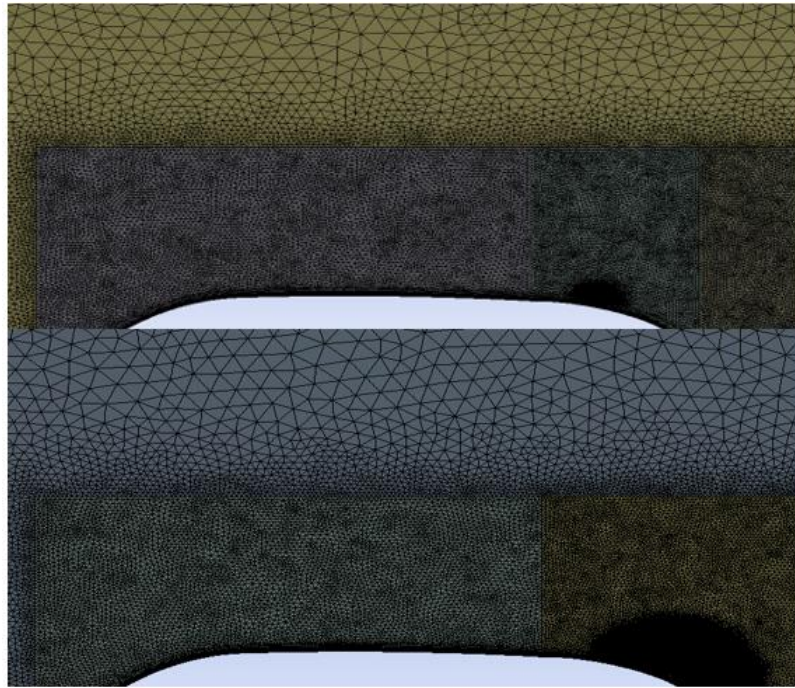


Figure 2.8: 11.4 million elements reference mesh (Up) and 13.1 million elements Original refined mesh (Down).

The new refinement was expected to show a spinner drag value that was closer to the theoretical zero grid spacing value but also to capture more flow information due to the larger number of resolved cells. Even when this refined mesh, hereinafter called Original Refined, had a 64% shortened wake-sub domain, it predicted similar results especially close to the blade root.

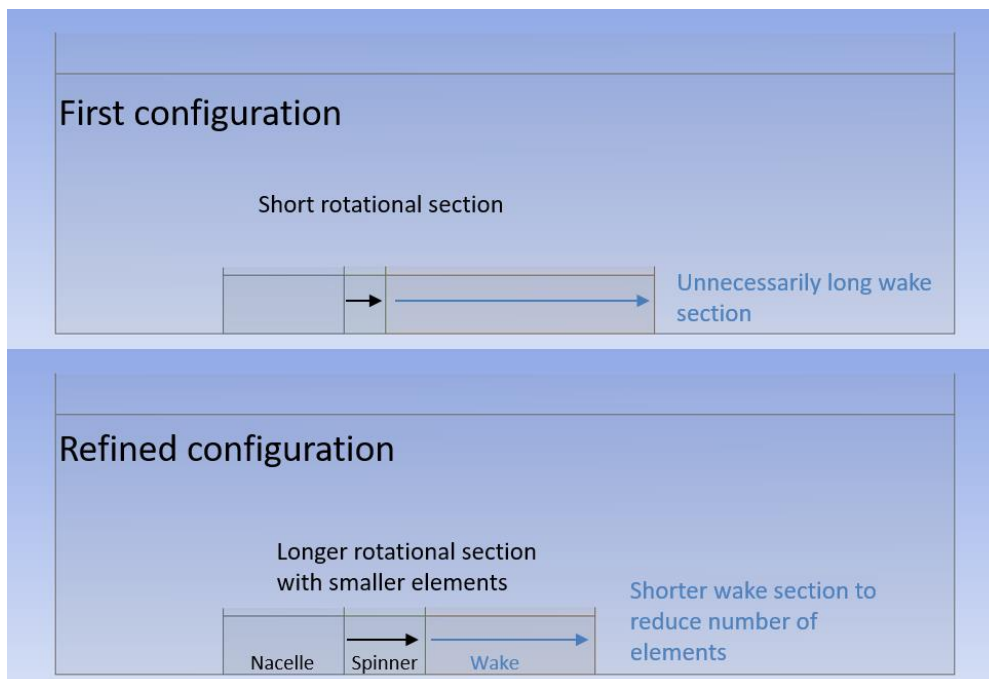


Figure 2.9: Mesh independence study domain layout (Up) and refined mesh domain layout (Down).

The rotational zone had the smallest grid element size so its extension increased the total number of elements despite the reduction of the wake sub-domain. Table 2.6 shows the estimated GCI of every component of the propeller for the different mesh sizes. In addition to that, the Original refined GCI

was also computed using the same safety factor and the same uncertainty used for the reference mesh of 11.4 million elements together with the theoretical zero space grid calculated for the apparent order of convergence indicated in table 2.5. The GCI of the Original refined mesh showed in Table 2.5 was calculated using the same exact value obtained by the least squares fit, a safety factor of 1.25 and the same uncertainty of the reference mesh (11.4 million). The Original refined mesh showed values that were closer to the calculated exact value than the 11.4 million for all the locations, especially at the spinner where the prediction was similar to the one made by the finest grids.

Table 2.5: Relative error with respect to the values for zero spacing grid including the original-refined mesh.

Mesh size (Millions of elements)	Excess thrust GCI with P=2	Spinner Cd GCI with P=2	Lower suction Cd GCI with P=1.72	Nacelle Cd GCI P=1.08
4.1	1.94%	63.35%	32.46%	17.42%
6.6	1.12%	36.92%	25.60%	15.24%
11.4	1.27%	33.00%	23.86%	13.88%
21.9	0.53%	12.75%	13.37%	9.76%
43.2	0.76%	15.69%	13.50%	9.41%
Original refined 13.1	1.13%	16.84%	21.83%	13.50%

The solution provided by the refined mesh was used as reference for all the solutions shown in the thesis. This is why, some flow variables were assessed in order to provide an idea of the performance of the original configuration of the propeller. Assuming that the spinner of any pusher propeller configuration is generally immersed in the propeller wake, the pressure field of the wake was likely to affect directly the spinner drag. In order to compare the flow characteristics encountered in the original spinner design, four YZ planes parallel to the propeller rotor disk were defined. The planes were located at 0.46, 0.55, 0.63 and 0.72 R respectively from the origin (Figure 2.10). The values of pressure coefficients were assessed and circumferentially averaged so they could be shown as function of the propeller radius.

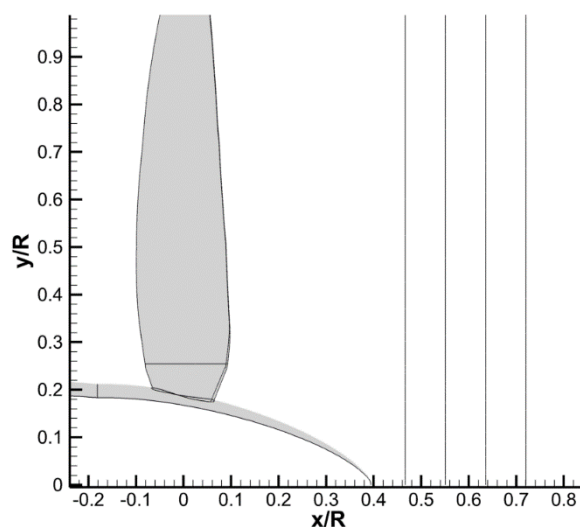


Figure 2.10: Propeller wake testing planes.

The pressure distribution behind the propeller rotor seemed to be more similar among the 6 grids when it was tested further downstream and showed larger differences when tested closer to the blade origin (Figure 2.11). The radial section that was depicted in Figure 2.11 remained below 0.4 r/R where the pressure drag was mostly related to the spinner flow separation and the interaction with the low pressure zones produced by vortical structures. The pressure distribution observed for the Original refined mesh seemed to have similar results to the ones of the finest grids, especially below the 0.1 r/R in fact, the more distant the plane is, the greater the resemblance among the Original refined and the finest grid pressure distribution of Figure 2.11. The resemblance in the pressure coefficients of the lowest radial locations was an indication of the presence of the so called hub vortex. Nevertheless, the prediction shifts away for the closest planes, especially at radial positions where the pressure field is mostly determined by the flow separation.

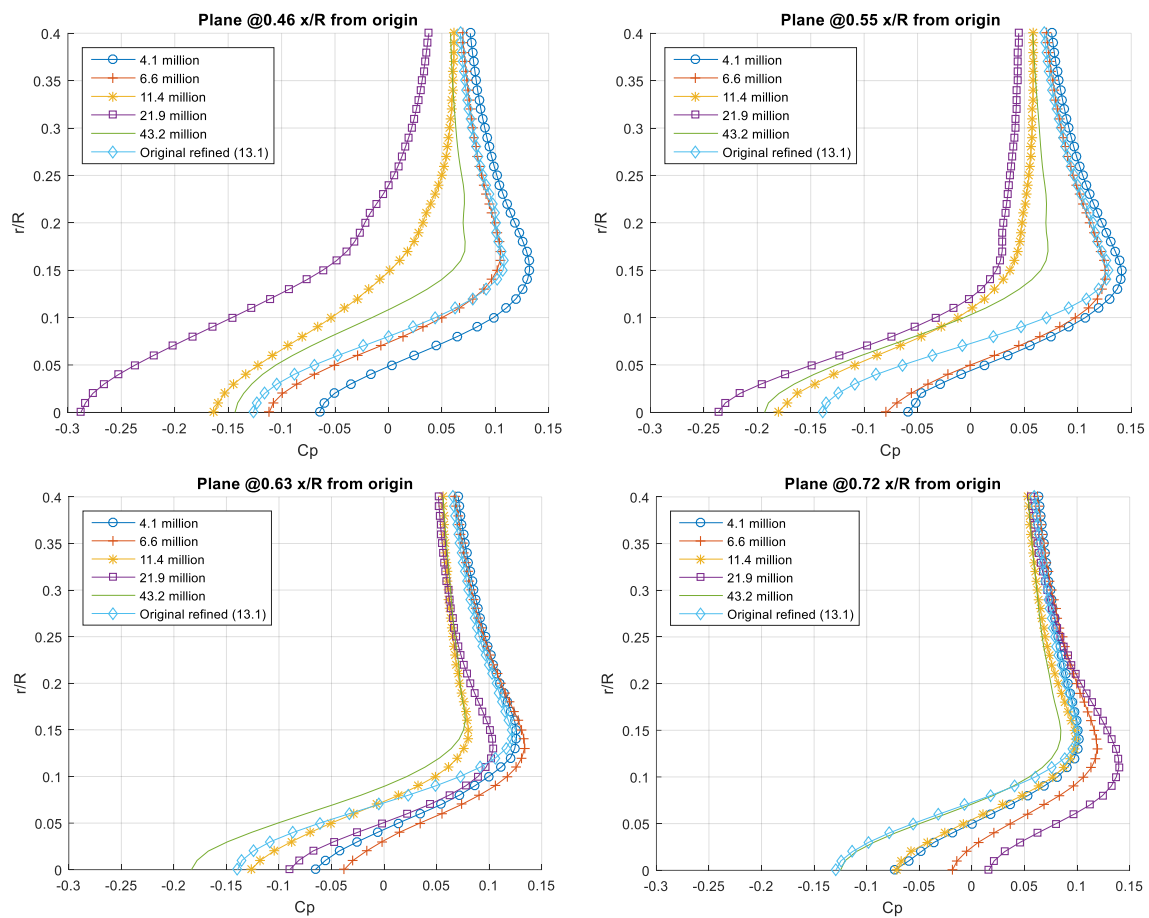


Figure 2.11: Circumferentially averaged pressure distribution for five grid sizes and for the refined mesh.

Given that the magnitude of the pressure coefficients was circumferentially averaged, the values shown at higher radial positions were averaged over longer circumferences. This did not represent a comparison problem for the Cp; however, it would be a problem for the depiction of the vortical structures. In order to look at the strength and position of localized flow characteristics such as vorticity, different radial positions and thus different circumference radius would mislead the results indicating, for example, that the tip vortex would be significantly weaker than the hub one. The Figure 2.12 depicts the maximum values Q criteria as a vortex method of visualization encountered at the testing planes. In a similar way as the pressure field, the Original refined grid predicted similar values of Q criteria than those obtained with the finest grid, especially at the last testing plane located further downstream. It was evident that the strongest swirl was encountered at the closest testing plane at a radial position around 0.2 r/R similar to the position of the blade root trailing edge.

Both the finest grid and the Original refined one showed stronger Q criterion peak values at the hub when compared to the other grids. The similar behavior of the Original refined grid and the finest one can also be observed when comparing the radial-averaged pressure values especially at the distant testing planes. Contrary to the fine grids, the coarsest grids did not predict swirl structures with the same strength neither at the blade root nor at the spinner end. The Q values of the refined mesh presented in Figure 2.12 are very similar to the ones of the finest mesh. This suggests that it is especially related to the blade root refinement. Speaking about the Q values encountered at the sample plane that was located closer to the blade root, both the Original refined grid and the finest grid exhibited the largest values. On the other hand, the coarsest grids seemed to under predict the swirl formation at that particular refined mesh, the blade root swirl seems to be stronger than the one at the spinner end, especially at the closest plane. This might be noticed on the pressure distribution location.

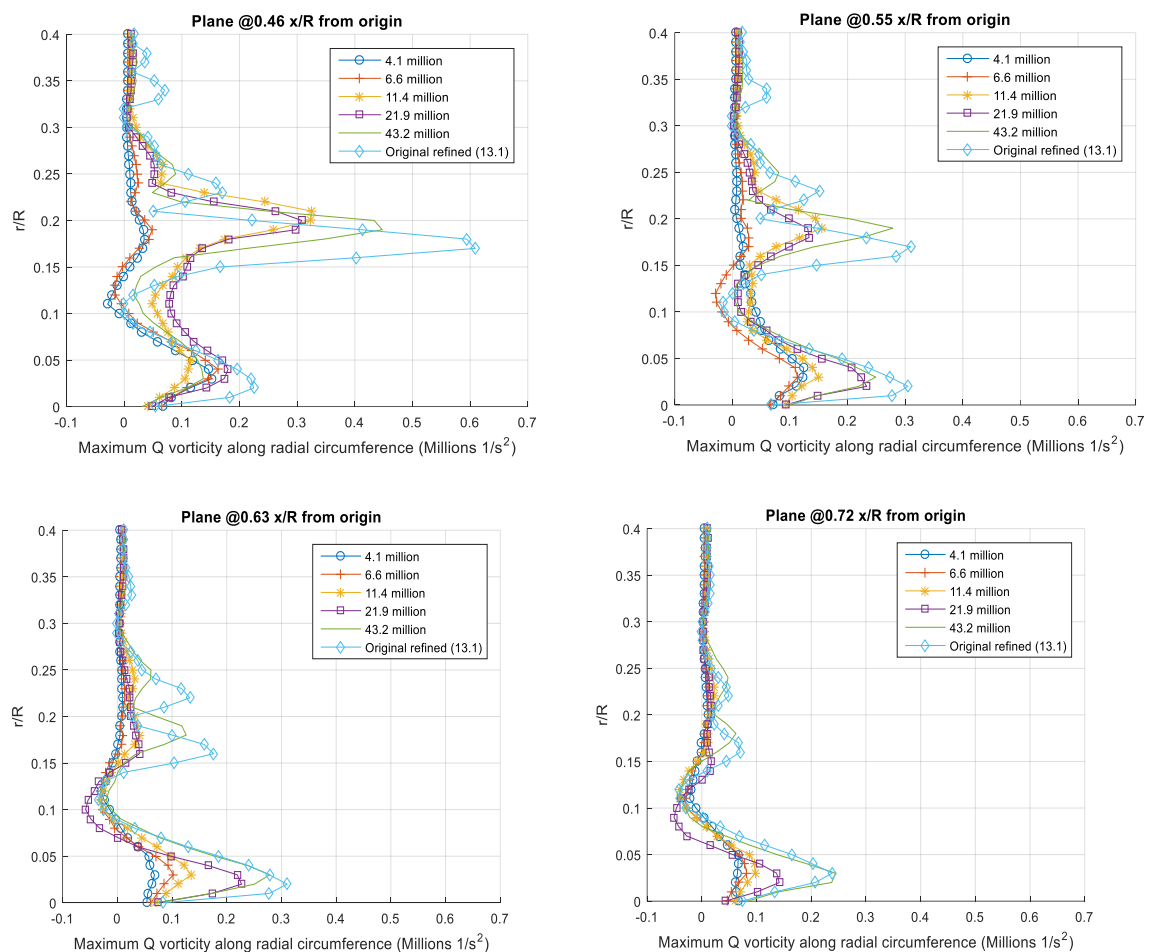


Figure 2.12: Maximum Q vorticity encountered at every radial position for five grid sizes and for the refined mesh.

2.3 Conclusions of mesh independence test

A mesh independence study was carried out using both the classic and the least squares version of GCI in combination with 5 grid sizes that were scaled 1.3 times in the element size. Given that the classic fit that required only 3 grids predicted super convergent orders or even divergence, only the results of the least square approach were used in order to avoid scatter data. The excess thrust (Drag-Thrust) values of the entire propeller together with the nacelle and spinner drag were compared to the zero grid spacing values found with the least squares version of GCI. The coarsest grid presented a GCI value of 1.94% while the two finest (21.9 and 43.2) showed 0.53% and 0.76% respectively. Finally, the Original

refined mesh chosen to be used in the following simulations showed a GCI value of 1.13% for the overall excess thrust.

The Original refined mesh with 13.1 million elements decreased the GCI value measured for the spinner drag from 33% to 16.84% compared to the zero grid spacing value calculated using the least squares fit of the 5 initial grids.

The Original refined mesh not only reduced the overall relative error of the predicted drag, but showed similar values between its pressure field behind the propeller and the ones obtained with a mesh that had 1.69 times smaller element length with more than 3 times the total number of elements. The similitudes in the flow solution was more evident further away from the rotor than closer to it, meaning that the rotor hub refinement influenced the wake characterization even when the elements of the wake region were no longer refined.

The largest Q values were encountered at the three highly refined grids and also at the Original refined and similar to what was observed at the pressure field; the values of the Q criterion observed at the finest mesh were very similar to the ones observed using the Original refined grid at around 0.7 propeller radius downstream ahead.

Overall, the Original refined mesh showed similar results than the ones obtained with the finest grid of 43.2 million elements. The simulations were performed using the TU Delft aerospace cluster mostly by nodes of 128 GB RAM where the time to solve an Original refined simulation was about 34% of the time used for the 43.2 million elements grid for equal number of iterations. Due to the similarity in results and the savings on computational time, the Original refined mesh simulation was used for the rest of the simulations performed throughout the thesis.

Independently of how coarse was the spinner region of the mesh, the time of convergence of the spinner drag coefficient was longer than the one observed at the nacelle for every mesh tested. The last 100 iterations average got closer to a constant value when the drag was assessed at the nacelle unlike the more fluctuating values observed at the spinner. Separation was likely the cause of such oscillating yet convergent behavior at the spinner (Fig. 2.13).

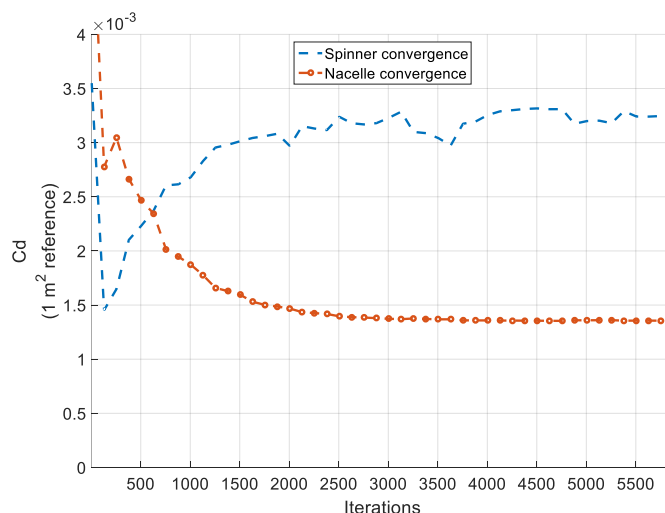


Figure 2.13: Convergence history of spinner and nacelle drag for the Original refined mesh (13.1 million).

3 Influence of the spinner design on the propeller performance

The different propeller excess thrust (F_{ex}) achieved by the spinner re-design was the result of multiple processes that changed the velocity field, the pressure field, the vortex formation and other variables that depended on geometrical changes. In order to have a better understanding of how some of these processes affected each other, a more complete assessment was performed. In the next chapter, it was intended to establish a correlation between the general effect of changes in spinner geometry and their contribution to the propeller performance due to quantitative values obtained directly by the simulations but also a more qualitative approach given by the CFD post processing and comparison between the original design and the new changes in the spinner.

This chapter starts with a preliminary assessment of the simulation taken as reference where the original design was tested. Special attention was placed on the streamlines that were observed on the original design configuration of the propeller. The following part of the chapter comprises the effects that a shorter spinner design had on the propeller excess thrust, flow separation and vortex/swirl formation. As it can be expected, the boundary layer on a shorter spinner design in a pusher propeller will encounter steeper adverse pressure gradients if the diameter is kept constant. This is why this chapter included a comparison among different spinner diameters with constant length in order to assess the effect of the blade exposure in the propeller performance.

Finally, the last section discussed the longer spinner designs and their effect on the propeller performance just as done for the shorter spinner geometries but in a more direct way.

The first changes made on the original spinner geometry provided a first look to both the magnitude and the sensitivity of the variation of the performance variables. Either because of flow separation delay, changes in pressure coefficients, blade loading or the formation of vortices, flow field variables undoubtedly provided a broader picture that helped to establish an initial relation between the spinner geometry and the overall propeller performance, possibly applicable to other pusher propeller configurations. The geometrical modifications followed three main guideline patterns:

- Length reduction, independently of the blade exposure
- Blade exposure variation at a fixed length
- Length extension, independently of the blade exposure

3.1 First spinner geometrical variations

As seen before, the original design showed separation at the spinner section. This seemed to be one of the causes of the poor pressure distribution that could potentially be improved (Figure 3.1). Nevertheless, the spinner drag represented only 1.66% of the entire propeller excess thrust, meaning that the thrust gain would represent a relatively small amount of similar order of magnitude. It is

important to mention that unless indicated otherwise, the post processing analysis was mostly taking into account the rotational frame of reference of the spinner and the rotor, especially for the velocity streamlines depiction.

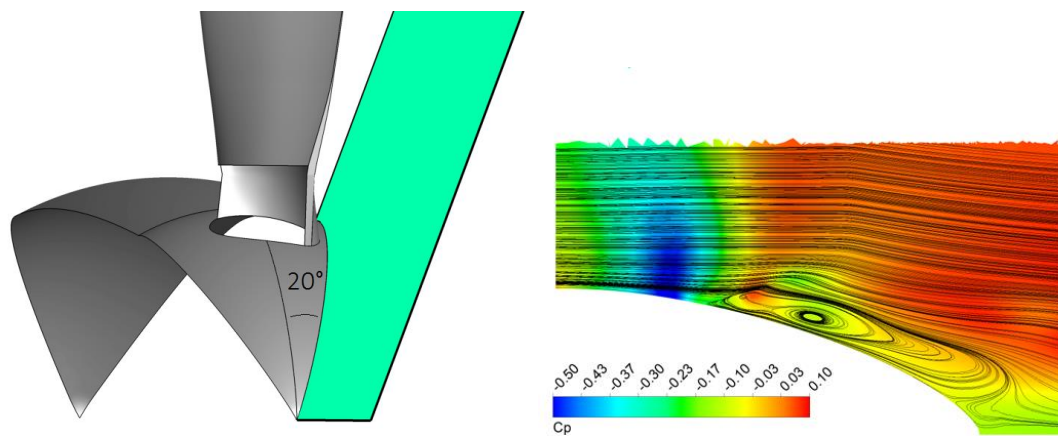


Figure 3.1: Original design spinner separation visualized at 20° tilted plane.

The separation shown on the spinner baseline design started at around the blade root trailing edge. The separation can be observed in Figure 3.1 either by looking to the reverse flow shown by the streamlines or by looking at one of the turbulence indicators such as the turbulent kinetic energy (TKE) [29]. The TKE increased after the blade root which suggested that the root loading was influencing the spinner flow separation especially because of the suction side separation (Figure 2.11). So the root loading has to be taken into account in order to induce a more favorable pressure gradient on the spinner flow.

Besides the evident flow separation, a low pressure zone was also encountered at the spinner end. The low pressure region seemed to confirmed the presence of the swirl that has been found before in several pusher propeller configurations and described as a hub vortex. [11] [30]

The pressure drag seemed to be the main factor affecting the total spinner drag in the original design due to the high flow separation on the spinner. That is why the magnitude and location of the low pressure zones of the spinner needed to be identified as reference points for comparison. In the viscous forces contour shown in Fig. 3.2, the viscous forces encountered after the blade root were close to zero or even negative as part of flow reversal. On the other hand, there were larger viscous forces on the pressure side due to the relatively delayed flow separation (Fig. 2.11).

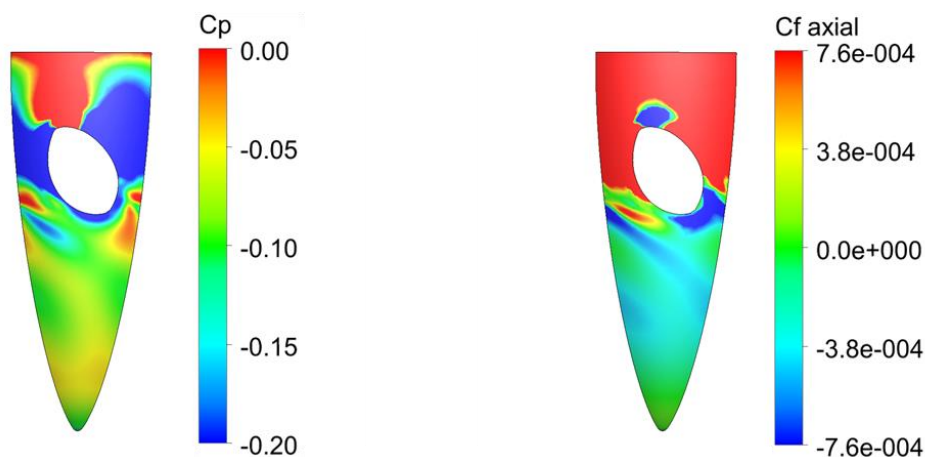


Figure 3.2: Top view of original spinner pressure distribution (Left) & spinner axial viscous forces (Right).

The relation between the blade root loading and the spinner flow separation was discussed in further chapters as one of the main reasons for the spinner drag reduction and thus for the pusher propeller increment in efficiency. The other important part of the analysis was focused on the changes detected in the pressure field around the spinner where the location and magnitude depended mostly on how was the flow expanding. In the contours showed in Figure 3.2 particularly looking at the trailing edge it was possible to see positive values of C_p in a very similar location where there were negative axial shear stresses due to the reversed flow that was coming from the pressure side.

3.2 Effect of spinner length reduction on the propeller performance

All the new designs of spinners were axisymmetric bodies, so the changes in geometry were made by parametrizing a 2D profile of the original design (Figure 3.3). The goal of the first designs was assessing the effect of a shorter spinner design, so the independent variable among the parameters of the profile was the length. Neither the height nor the gradient of curvature was set to a specific value; nonetheless, given that at the hub the blade had to be connected to the shaft certain limits were defined in order not to expose the cylindrical part of the blade root.

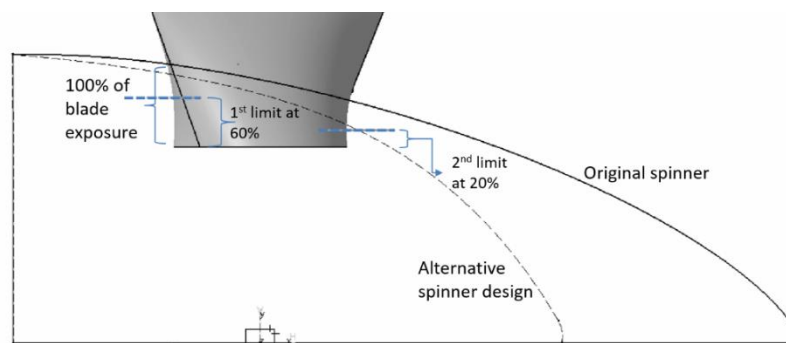


Figure 3.3: 2D projection of the original design of the spinner.

In order to carry on the simulations of shorter spinner designs and any other spinner modifications, the spinner diameter was limited to host the blade root at least 60% of the amount of blade root hosted by the original design as shown in Figure 3.3. The limit was set considering that if less than 60% of the blade root is hosted (Measured in radial direction) the airfoil of the lowest r/R position would eventually become a circle. Common pusher propeller installations [31] suggested that the blades with cylindrical roots not only did not expose their lowest positions, but they even implemented blending surfaces in order to connect the root to the spinner. Hence, increasing the wet surface at the lowest radial positions would most likely end up with a decrement the propeller efficiency since there wouldn't be distinction among pressure and suction side.

3.2.1 Effect on thrust and propeller drag

A gradual shortening from 5% to 35% of the original length was tested (Figure 3.4). Figure 3.5 depicts the propeller excess thrust of the shorter spinner designs. Seven designs shorter than the original were tested under the same cruise conditions using the same CFD setup and the same Original refined grid. As it can be seen from the graph, the greater excess thrust was observed at around 15% of the spinner length reduction. The thrust increment never exceeded 0.5% when compared to the original propeller thrust; however, when the comparison was made among the spinner drag then a larger difference was observed. The overall propeller excess thrust (Thrust-Drag) was a convenient way to measure the general impact that the spinner had on the propeller performance; however, the assessment of the individual contributions of the spinner, nacelle and blade root was also necessary in order to improve the overall propeller efficiency (Figure 3.6).

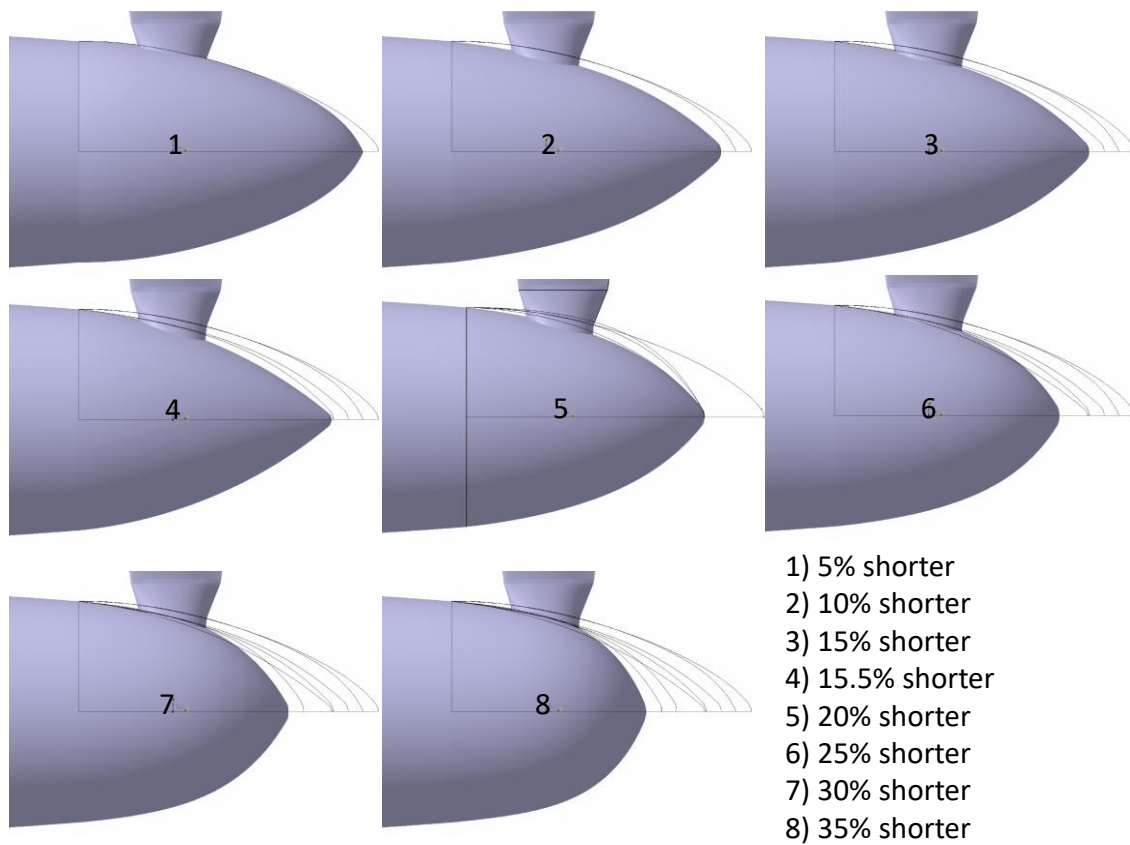


Figure 3.4: Shorter spinner group.

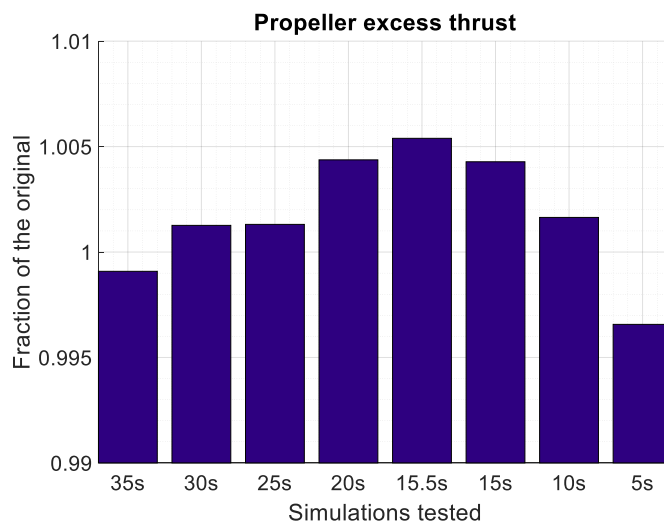


Figure 3.5: Propeller excess thrust variation among shorter spinners.

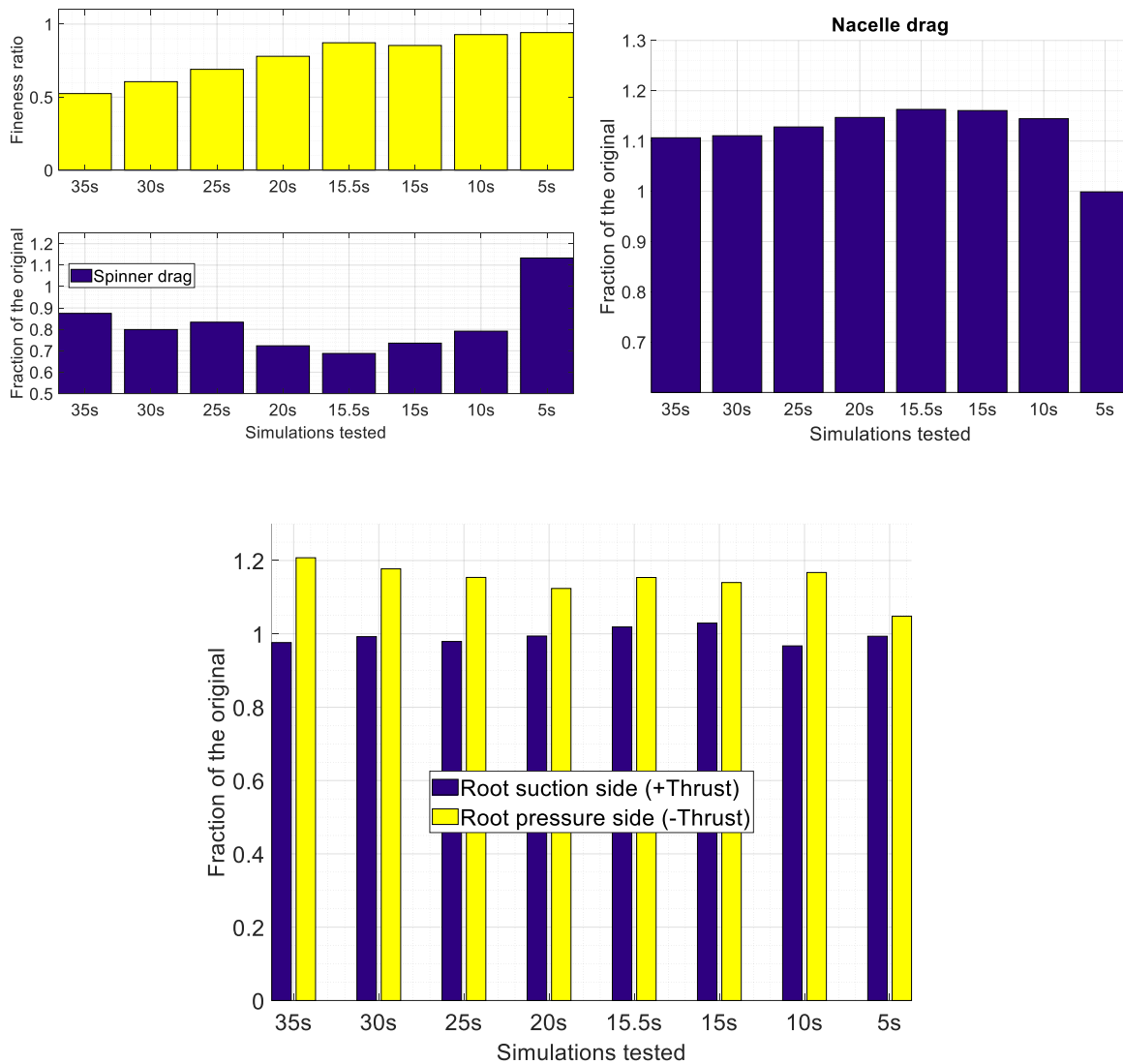


Figure 3.6: Spinner shortening effect on spinner, nacelle and blade root drag.

In most of the cases (7 out of 8) the shorter spinners reduced the spinner drag. At the same time the shorter spinner length had the effect of increasing the excess thrust in 5 out of 8 cases so, it can be said that the length reduction had an overall positive influence in the propeller performance although the magnitude was relatively small. Most of the spinner designs that induced a lower excess thrust also presented larger spinner drag; however, the shortest design showed lower values of excess thrust independently of the spinner drag reduction. The reason is that the blade root produced the largest negative component of thrust of all the cases due to the largest blade exposure where the flow was mostly separated in the suction side and the suction was actually produced in the pressure side. This is why the negative thrust that was produced in the pressure side seemed to be increased as the spinner length was reduced.

In order to have a better understanding of the individual contribution of Nacelle, Spinner and Blade root they can be compared to the excess thrust reported for the whole propeller of the original design.

Table 3.1: Fraction of the excess thrust per component of the propeller (Original design)

Propeller component	Individual fraction (%)
Summation of absolute axial forces	100%
Spinner (Drag)	1.56%
Nacelle (Drag)	0.65%
Blade root (Negative thrust)	0.69%
Rest of the blade (Thrust)	97.1%

The part of the blade comprised beyond $0.3R$, was the only part of the propeller that generated positive thrust, meaning that the spinner, the blade root and the nacelle induced axial forces that acted in opposite direction. Table 3.1 depicted the induced negative thrust forces as a percentage of the propeller excess thrust where the spinner drag represented the largest contribution with 1.66%. The second largest component of negative thrust was found at the blade root that represented 0.73% of the excess thrust, 0.04% more than the nacelle. The negative C_p values found in the pressure side of the blade root represented the largest contributor to the reversed thrust encountered on the blade root.

Six out of the eight shorter spinner designs induced larger values of propeller excess thrust when compared to the original one. This indicated that even when all the shorter cases presented flow separation, the initial spinner design had a larger drag not only because of the separation but also because of a strong interaction with the hub vortex.

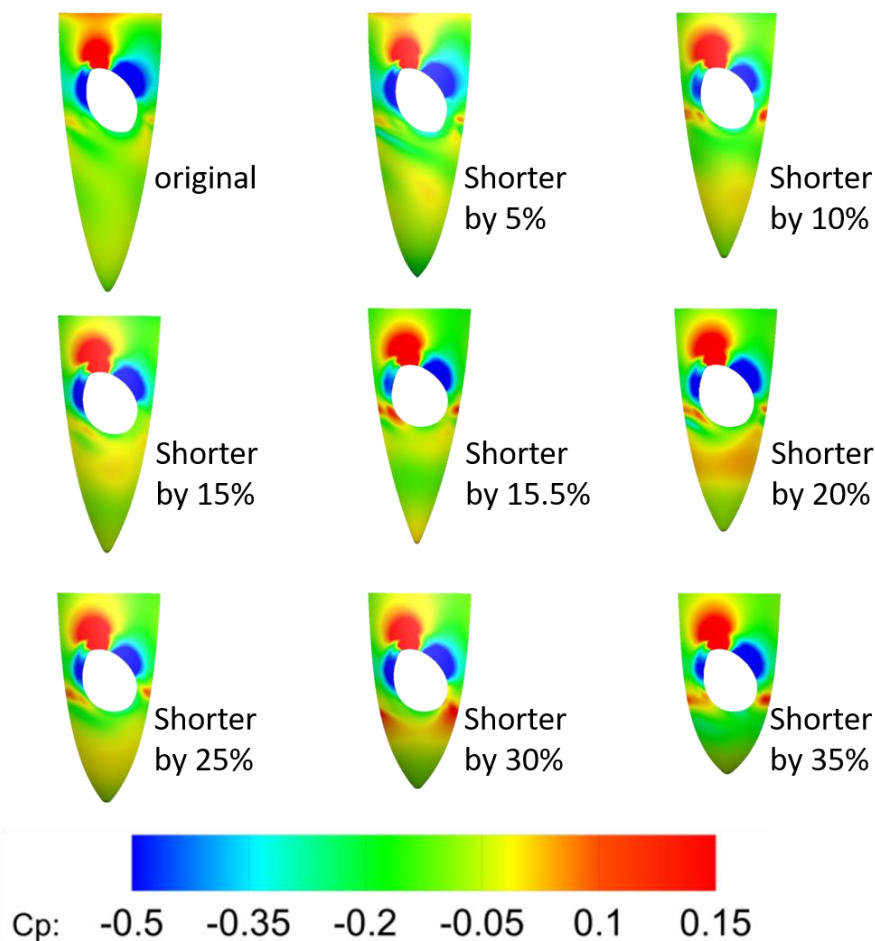


Figure 3.7: Top view of C_p contours on shorter spinners.

As it can be appreciated from the Figure 3.7 a low pressure zone was generated on both suction (Right edge) and pressure side (Left edge) of the spinner wall but also towards the end of the spinner. The effect of a strong root vortex can also be observed on the original spinner design and on the 5% shorter as a low pressure trace that extends from left to right just after the trailing edge. On the original design it is also possible to see that the low pressure contour that crosses the spinner from left-up to right-down comes from the previous blade. This also indicated that the low pressure trace observed downstream comes from two blades before.

Other variables that influenced the spinner pressure recovery was the blade exposure as a result of spinner diameter variation. The blade loading played a very important role since its design seemed to be enhancing the vortex formation. This affected both the attached flow and the overall pressure distribution on the spinner. As the spinner became shorter, the height in radial direction got decreased in order to maintain a similar adverse pressure gradient by reducing the slope of the spinner. For this particular propeller configuration, it had to be taken into account that as the spinner diameter was reduced, then the lowest airfoil of the blade root started to be more similar to a cylinder than to an aerodynamically designed airfoil.

Among the short spinner group, only the 5% shorter had the same blade exposure as the original design while the 10%, 15%, 20%, 25%, 30% and 35% shorter spinner design keep a similar blade exposure that was larger than the original design. On the other hand, the spinner that is 15.5% shorter than the original had the greatest blade exposure of all (See Figure 3.4). In theory, for similar spinner diameters but shorter lengths the pressure coefficients should be increased along the spinner for as long as the flow remained attached where positive pressure coefficients would be observed due to the greater expansion of the attached flow. When looking at the shortest spinner (35% shorter than the original) that has the steeper curvature and thus the greatest adverse pressure gradient, the boundary layer separates and most of the flow is detached, which explains the absence of the larger positive C_p values on the spinner (Figure 3.7).

3.2.2 Effect on separation

As the length was shortened the flow separated in a different way along the spinner thus changing the pressure distribution. Earlier flow separation produced by steeper adverse pressure gradients would explain why is that the pressure drag represented a more dominant effect when compared to the viscous drag (Table 3.2).

Table 3.2 shows the pressure and viscous components of the drag of shorter spinners as part of their total drag respectively.

Table 3.2: Pressure and viscous drag contributions for shorter spinners

Spinner length	Spinner pressure drag	Spinner viscous drag
5% shorter	97.1%	2.9%
10% shorter	96.6%	3.4%
15% shorter	96.3%	3.7%
15.5% shorter	97.0%	3.0%
20% shorter	96.7%	3.3%
25% shorter	95.8%	4.2%
30% shorter	95.4%	4.6%
35% shorter	97.5%	2.5%

Flow separation was clear in all the designs including the original one where recirculation was observed for the entire group. Given that the flow separated in all cases close to the trailing edge of the blade root, it was evident that separation was largely induced by the blade root and not only because of the adverse pressure gradient imposed by the spinner curvature. The streamlines showed an initial hint for detachment towards the end of the suction side where the velocity field was clearly disturbed. The change in direction of the streamlines was followed by a concentrated recirculation region indicating that most of the flow was separated from the spinner wall. Outside of the recirculation region formed along the spinner, the flow that came from the blade root pressure side interacted with the one coming from the suction side, forming the main vortical structure or blade root vortex mostly due to rotational flow that was induced by opposite radial components of velocity like observed in the blade tip vortices (Fig 3.8). The main root vortex exhibited a positive rotational sign in axial direction (Downstream positive) and in some of the cases the rotational flow observed at the root vortex was found downstream ahead with similar magnitude towards the slipstream direction.

The shear stresses shown on the 15.5% shorter spinner (Fig. 3.8) indicated that the flow separation for this design started in the portion of the spinner that was close to the blade root suction side. The recirculation was indicated by the direction of the shear stress vectors due to the negative axial component. The transverse flow coming from the blade root pressure side encountered flow with significantly larger axial velocity components outside from the recirculation region. This indicated that to favor the boundary layer detachment. A “separation” vortical structure was observed as a result of the crossflow generated in the blade root. This vortical structure extended in a more pronounced negative tangential direction when compared to the main blade root vortex, which emphasized the effect of the greater negative tangential velocity component of the flow that was coming from the recirculation region. Both the magnitude of the vortex structures and their effect on performance are discussed in further sections.

The detached flow originated the swirl that interacted with the boundary layer coming from the nacelle. The spinner drag related to the vortex structures is discussed in further sections; however, the relation of the main root vortex with the low pressure region formed at the end of the spinner was evident, especially when looking at the pressure contours.

The vortex-induced spinner drag was observed to be especially strong on the Original design but also at other cases such as 5%, 10% and 25% shorter spinners. The low pressure region generated at the end of the spinner represented the largest spinner drag contribution for cases such as the 5% shorter spinner despite its relatively low presence of reverse flow on the spinner wall.

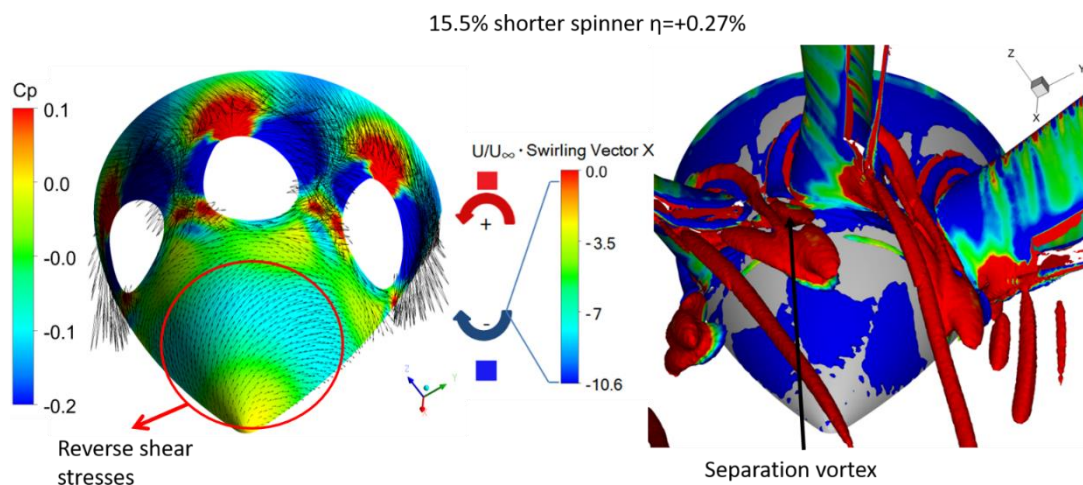


Figure 3.8 Shear stress vectors and Vortex structures visualization on 15.5% shorter spinner. (Q criterion isosurface of $470\,000\text{ s}^{-1}$, X axis are positive in downstream direction)

The regions of reversed flow that were present among the short spinners (Blue contours of Figure 3.9a) varied in magnitude and location. This changed the way the flow expanded on the spinner and hence it modified the pressure drag of every design. Pressure recovery showed to be improved as the flow separation was delayed, so it can be inferred that the spinner designs with early flow separation would very likely induce a poorer performance.

The separation observed in (Fig. 3.9 a) was occurring mainly in two different ways. The first one was the one showing a large recirculation region that extended along most of the spinner wall like the one observed at the 15%, 15.5% and 30% shorter spinners. There was separation in the three of them without any hint of reattachment; nevertheless, since the recirculation region was formed in a more flattened shape instead of growing from the spinner wall in the 15% and 15.5 % cases, the main flow still encountered a larger expansion as observed in certain two dimensional diffusers [32]. The increment of pressure coefficient values especially towards the spinner end meant larger normal outward components of force in direction of thrust which helped to decrease spinner drag. This is why the 15% and the 15.5% shorter spinners showed the best pressure recovery of the entire short group as well as the lowest spinner drag.

A relatively greater spinner drag was observed for the original design and for the 5% shorter spinner in contrast to the one of the 15% or 15.5% shorter spinners. As mentioned before the difference relied mostly on how differently the flow separated in the spinner but also on whether or not there were strong negative pressure coefficients induced by the hub vortex at the end of the spinner. The second type of separation observed on most of the spinners and especially on the original one, was characterized by the thin and elongated recirculation region that didn't reach the end of the spinner. Instead, the end of the spinner encountered reattached flow that induced positive axial shear stresses on the spinner wall in similar direction to the one of the propeller slipstream. Even when the spinners that encountered this type of separation seemed to show relatively large positive pressure coefficients mostly around the midsection of the spinner, the overall spinner drag was not reduced as much as for other designs. A large portion of the flow in the vicinities of the spinner end had a relatively low momentum, suggesting that the hub vortex formed at the end of the spinner resulted from the interaction of the negative tangential velocity of the separated flow and the main flow.

When looking to the flow field of the 15.5% shorter spinner, the pressure contours were very similar to the one observed at 15% shorter meaning that even when the two designs had different blade exposure due to difference in diameters (See Figure 3.4), the similarities in length were predominant on the pressure field; however, the greatest reduction in drag was observed in the spinner with the lowest diameter. The lower diameter of the 15.5% shorter spinner seemed to reduce the drag because of the greater space that the main flow had to expand; however, other reason was the relatively larger flow velocities encountered close to the spinner in comparison with the rest of the tests. By looking to the axial velocity contours of Figure 3.9, it was possible to see that the 15.5% shorter spinner had the largest negative components nearby the spinner and also the lowest pressure coefficient within the recirculation region (Fig. 3.9b); nevertheless, the spinner drag was lower than the one of the original design emphasizing the importance of the pressure recovery towards the end of the spinner independently of the separated flow.

In order to continue assessing the separation effect on the spinner drag it was necessary to take into account that the blade root influenced the spinner flow separation in a different way on the pressure side than it did in the suction side. In Table 3.2 the viscous forces produced by the axial shear stresses showed to be almost negligible in terms of its direct propeller axial force contribution (Excess thrust). Nonetheless, despite their small contribution, the contours of viscous forces worked as an indicative of where the separation started.

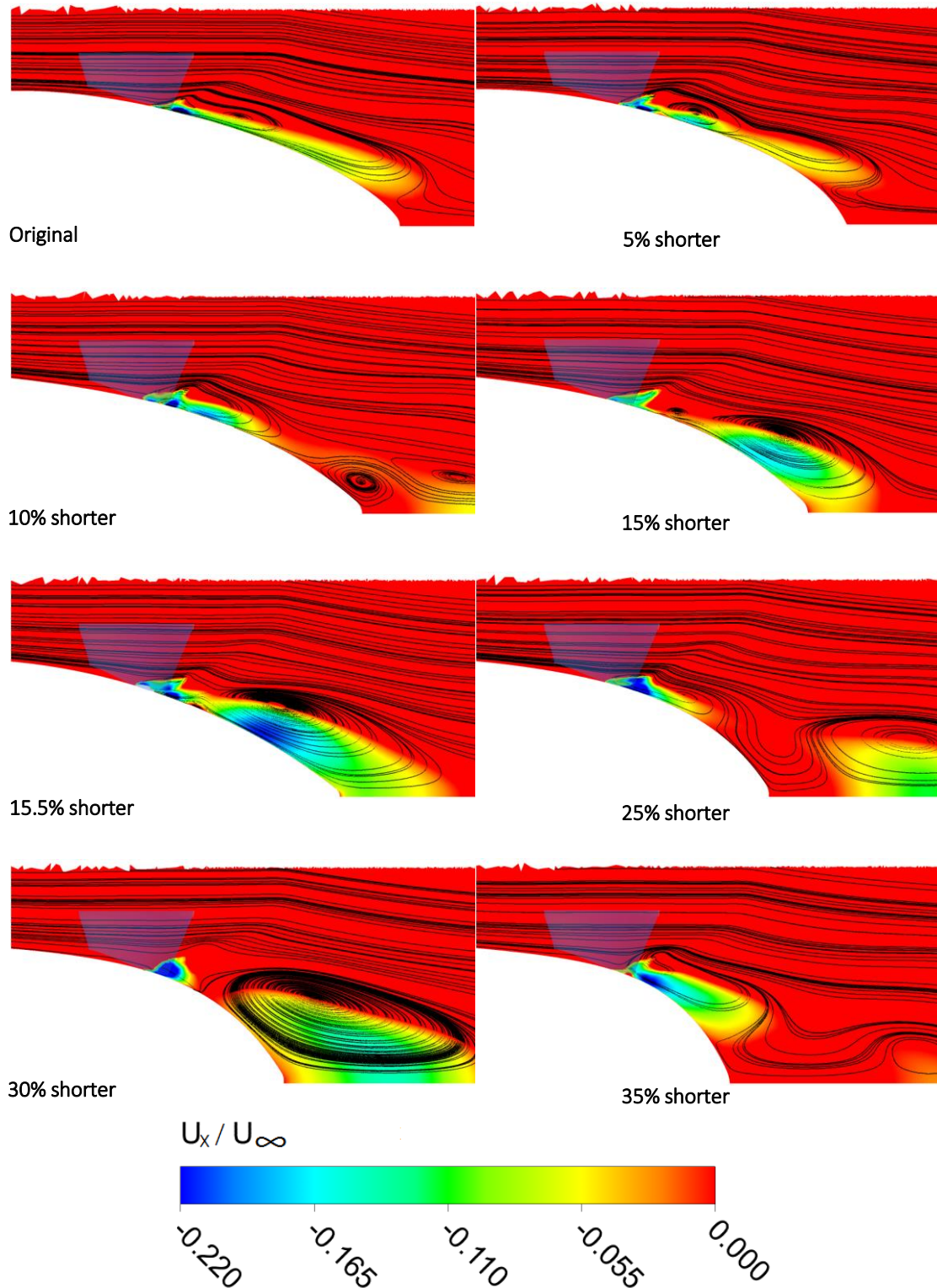


Figure 3.9: a) Separation streamlines on shorter spinners and negative axial velocity contours at 20° tilted plane. (See. Figure 3.1)

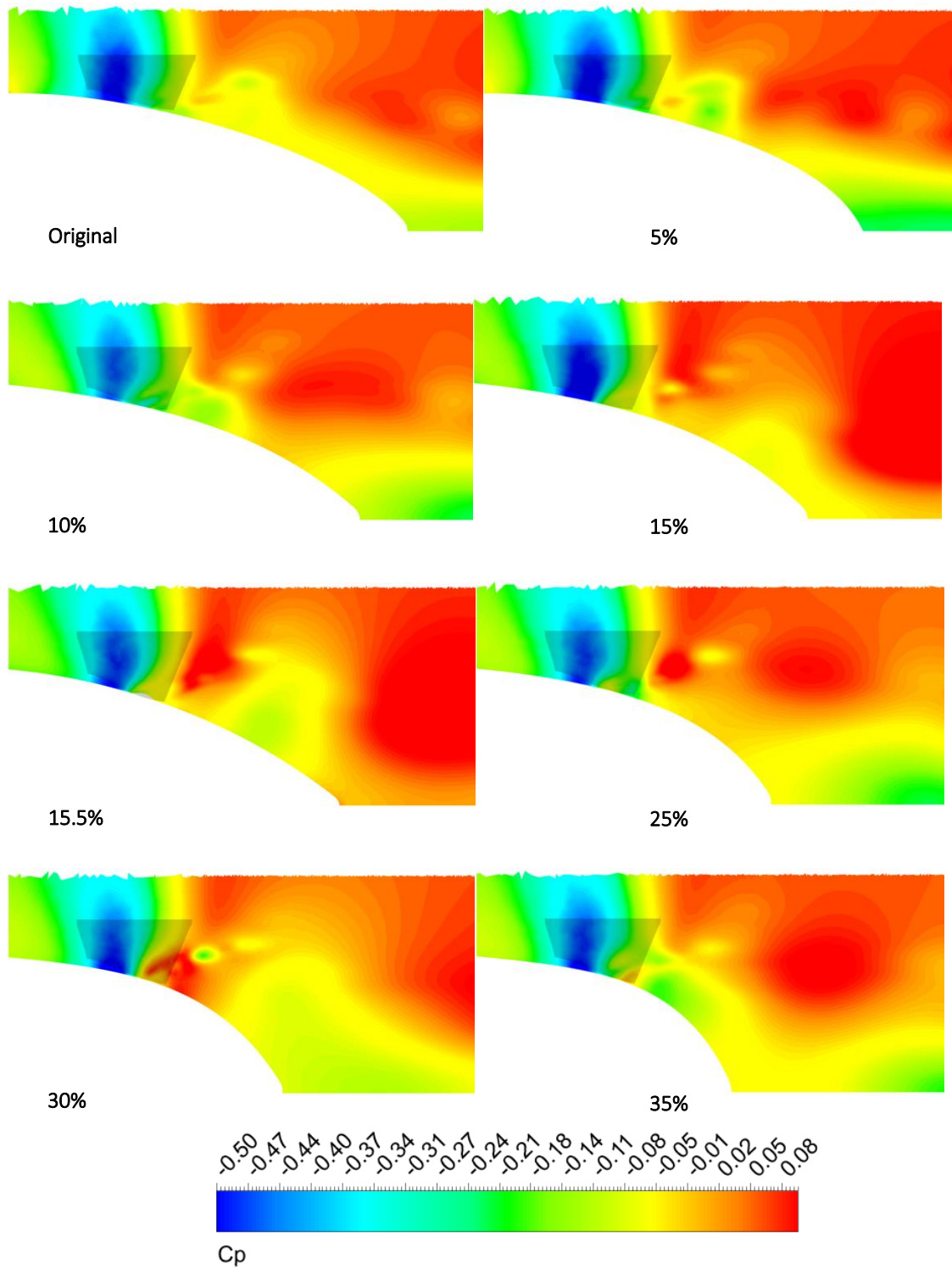


Figure 3.9: b) C_p contours on shorter spinners at 20° tilted plane. (See. Figure 3.1)

By looking at the Figure 3.10 it was clear that the two zones with the highest negative shear stresses were at the stagnation point of the blade root and also at the rear part of the suction side of the blade root. This spotted the presence of reverse flow due to separation, enhancing the blade loading on the pressure side (Producing suction). Given the predominant influence of the pressure in the total spinner drag, the flow separation was obviously not wanted; however, even when shorter designs did not delay the flow separation in any way, the spinner drag was still decreased largely because shorter spinners kept their rear part further way from the low pressure zone generated by the hub vortex.

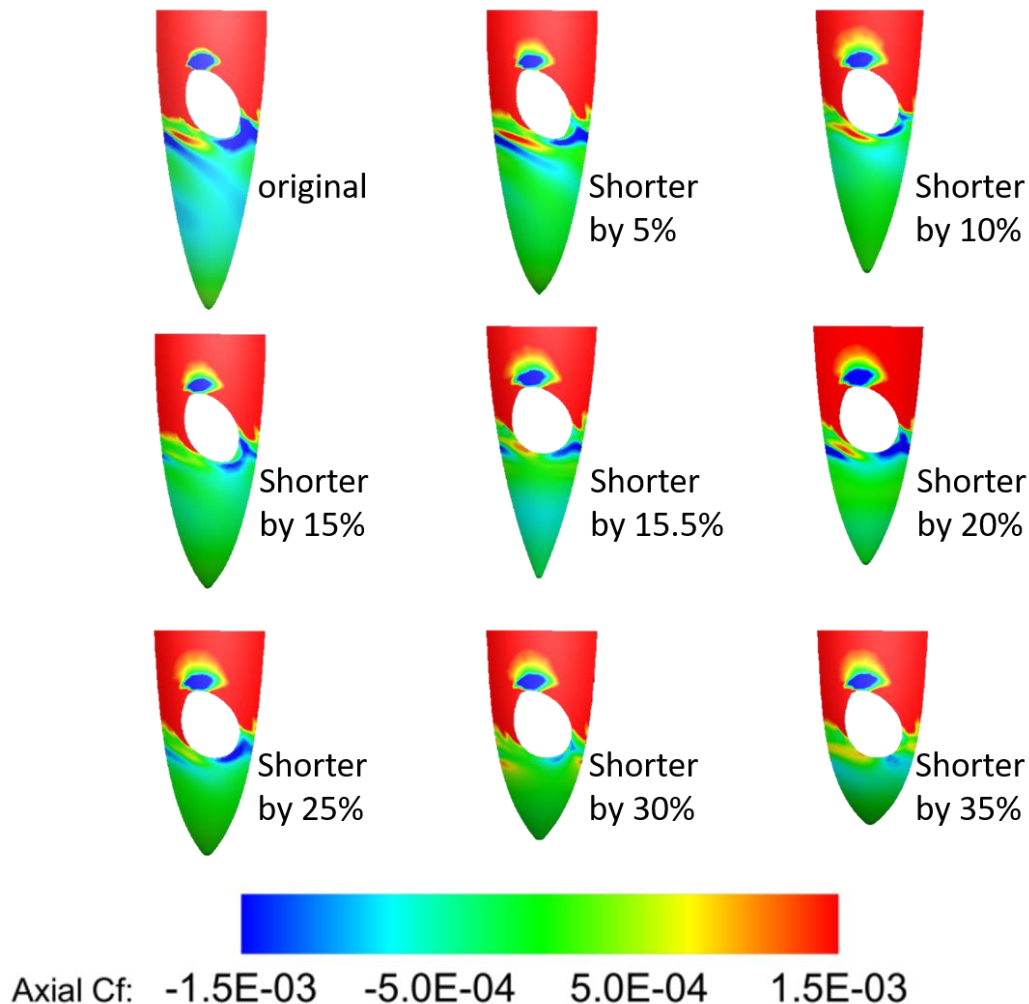


Figure 3.10: Top view of axial friction coefficient contours on shorter spinners.

3.2.3 Swirl formation at blade root and spinner

The vortex structures formed at the blade root have shown to be a very important element that formed part of the flow separation by both triggering it and being originated by it. In other words, the flow separation observed at the blade root seemed to induce the formation of the separation vortex which at the same time produced earlier flow separation along the entire spinner. Its assessment might become complex due to the vortex breakdown happening at the blade root and thus at the hub vortex of the propeller [3]. As mentioned before, the pressure distribution offered an insight about certain flow-vortex interaction as well as the separation streamlines so a clear observation of the vortex system acting on the blade root and at the hub (Spinner rear end) was necessary. There were several methods for vortex visualization and in general any swirl structure visualization used in literature. Q criterion has shown to be one of the most common methods to visualize vortex structures [33] [34]. The Q criterion

method defines the vortex as the connected region where the second invariant of the velocity gradient is positive. The characteristic equation of the velocity gradient is given by:

$$(3.1) \quad \lambda^3 + P\lambda^2 + Q\lambda + R = 0$$

Then using the decomposition into symmetric and anti-symmetric parts of the velocity gradient tensor, the invariant Q can also be expressed as:

$$(3.2) \quad Q = \frac{1}{2} [\|\Omega\|^2 - \|S\|^2]$$

Where $\|\Omega\|$ and $\|S\|$ are the Euclidean norms of the anti-symmetric and the symmetric parts of the velocity gradient respectively. According to the definition shown in equation 3.2, the Q criterion describes a vortex as the region where the rotating values are dominant over the straining ones. Vorticity understood as the curl of velocity has been used as well in order to visualize vortex structures but its relative inability to distinguish among swirling and shearing motions might not produce a visualization as defined as the Q criterion, especially failing close to the walls [35]. This is why other options were tested such as Lambda2 or Swirl strength methods as possible alternatives to Q criterion. The first one bases its vortex definition on the velocity gradient decomposition into symmetric and anti-symmetric parts just as the Q criterion does; nevertheless, it focuses on the eigenvalues of $S^2 + \Omega^2$, requiring at least two of them to be negative and it adds a pressure minima requirement to consider the vortex existence.

The swirl strength method, on the other hand, relies on the imaginary parts of the complex eigenvalues of the velocity gradient tensor. The local swirl strength of the vortex is then quantified by the positive complex imaginary part of the eigenvalue.

The four methods described above are the ones that the author has found to be the most used for current vortex visualization. The low pressure zone that some of the methods require due to its inherent vortex description seem to be a useful tool for the characterization of some of the vortex structures because the low pressure that acts on the spinner walls is directly affecting the propeller drag; nonetheless, small swirls that do not necessarily represent a strong low pressure region are important due to their interaction with the boundary layer and thus the flow separation of the spinner.

Figure 3.11 shows the blade root vortex system acting on the original design of the spinner at around the same level of vorticity in their own scales. It was clear that Q-Criterion, Lambda2-Criterion and the Swirl Strength-Criterion had a similar definition of the vorticity field and that all of them showed the main vortex bodies with clarity. That is not the case for Vorticity-Criterion that although it depicted the four main vortex structures, there was a marked absence of clarity. Vorticity method did not depict the weaker swirls formed at the trailing edge and the suction side of the blade root. In addition, the hub vortex at the end of the spinner was missing only with the Vorticity method for the same relative level of depiction. At this point the terminology "Hub vortex" has been used in the thesis in the same way that has been used in literature that described the vortex-like structure that was mainly observed in marine propellers [6] [7]. However, the structure seemed to be formed by the interaction of the flow with both the blade root loading and the spinner early/delayed flow separation.

The clearest identification of main vorticity structures and small swirl formation was given by the Q-Criterion and the Swirl-Strength. Taking into account that Q-Criterion seemed to be the most common vortex definition used in literature and in CFD post-processing software, the vortex-related assessment was performed using Q-Criterion method.

The vortical structures identified at the root were different from the ones seen at the blade tip mostly because of the opposite sign of rotation. The blade tip vortex had a negative sign of rotation in downstream direction (X axis; Fig. 3.8), while the vortices coming from the blade root presented positive rotation signs with exception of the vortex formed at the end of the spinner. The different sign was a good indication that the structure identified as hub vortex was most likely a swirl that was formed by the interaction of the particular blade loading. Given that the blade loading will be obviously modified at the root with every spinner design, a clear depiction of the vortical structures was preferred, especially because in this particular blade design the blade root encountered flow separation on the root suction. This characteristic of the blade would likely decrease the kinetic energy of the boundary layer while increasing the vortex merging from blade to blade [3].

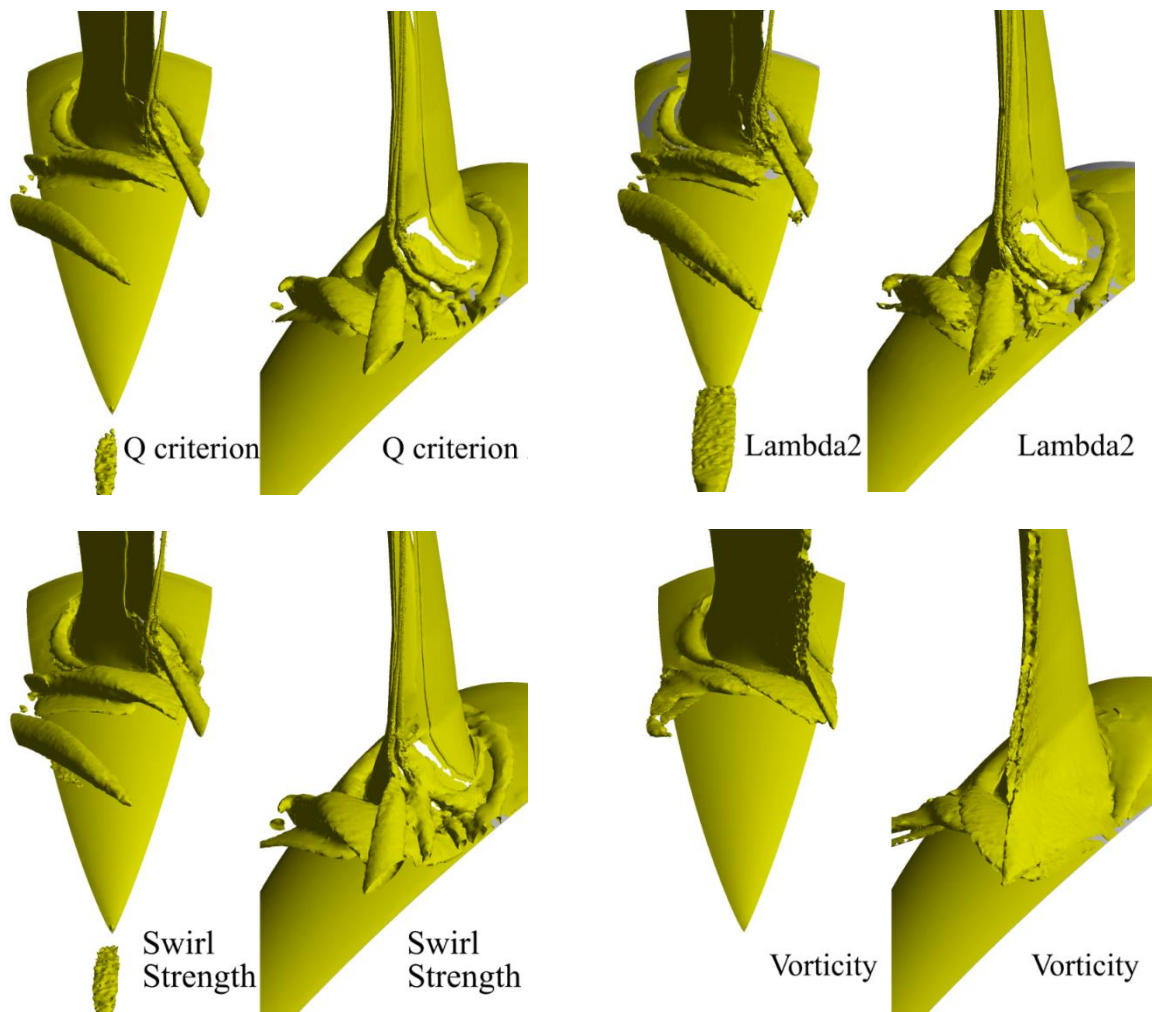


Figure 3.11: Original Blade root/hub vortex visualization with different methods (Isosurface shown at the same level on their own normalized scale; i.e. $Q=470,000 \text{ s}^{-2}$ and $Vorticity=3060 \text{ s}^{-1}$).

In order to assess the influence of the vortex induced drag and any change in the spinner geometry, an efficiency term was introduced using the efficiency definition of chapter 1.

(3.3)

$$\eta_p = C \frac{F_{ex}}{Q}$$

(3.4)

$$\eta = \frac{\eta_{p;new\ design}}{\eta_{p;Original}} = \text{Relative propeller efficiency}$$

Where F_{ex} is the excess thrust of the propeller and Q is the torque of the propeller. As mentioned before, the research was made for cruise conditions and a fixed advanced ratio so the flight speed and the rotational speed were considered as a constant term that was neglected for comparison purposes, being the ratio of excess thrust over torque the one that has been compared throughout the research as a relative term with respect to the original propeller efficiency.

The Figure 3.12 depicts the main vortical structures encountered on the original design of the spinner after the propeller simulation. The Q-criterion makes possible to observe four main structures: Horseshoe vortices, the blade root vortex, the separation vortex and the hub vortex.

The horseshoe vortices (HSV) were located near the suction and pressure side of the blade root. These structures were shown to be repeatedly in the same position regardless the spinner case that was tested. Despite being vortices with large Q criterion values, neither of them represented a major contribution to the spinner drag. It was possible to see that the HSV of the pressure side dissipated in the same frame of the picture. This meant that there was no trace of it coming from the previous blade. On the other hand, the HSV from the suction side not only reached the next blade frame but also merged with the early phase of the separation vortex that suggested a possible contribution to the flow separation on the spinner. HSV showed to be very concentrated regions of stable vortices that were observed independently of the flow separation occurring at the spinner.

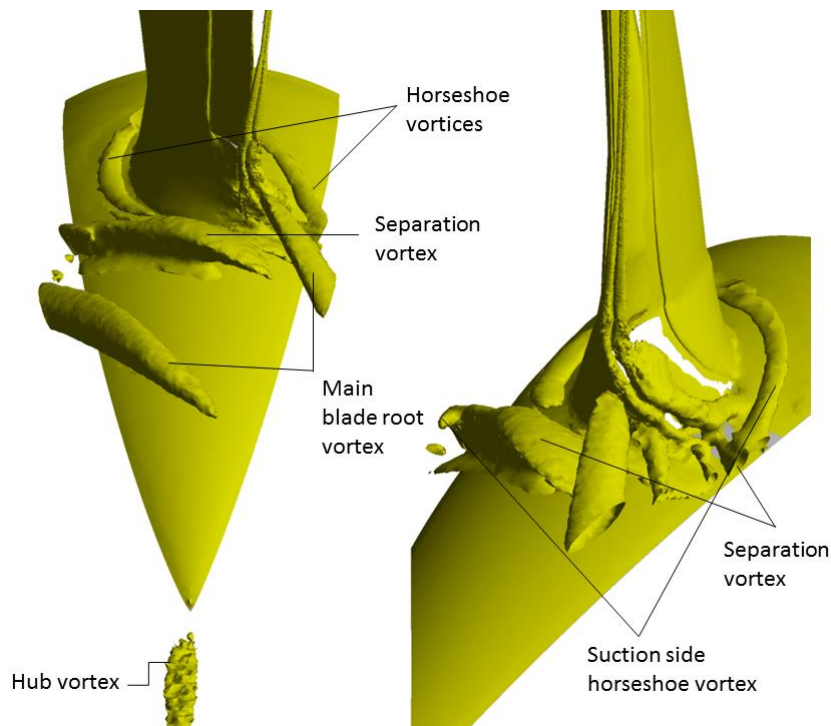


**Figure 3.12: Main vortical structures on original spinner (Tip vortex is not taken into account).
(Q-criterion Isosurface of $470\ 000\ s^{-2}$)**

The “separation vortex” is the vortical structure formed by the interaction of the disrupted boundary layer on the suction side. The effect of the vortex can be appreciated in Figure 3.9b as a concentrated low pressure region that was encountered before and after the trailing edge. Its formation was mostly

due to the crossflow produced by the negative components of radial and axial velocities of the flow that came from the root pressure side and reached the rear separated region of the root suction side, constantly indicating the separation point. The main flow remained close to the spinner wall where the flow recirculating in the spinner induced the crossflow that ended up originating the vortical structure. Due to the swirl magnitude, the separation vortex in the original design was shown to be present in the next periodical wedge, most likely interacting with the next blade. Among the short spinner cases, the spinner flow separation started at the same place where this vortex was formed.

The main blade root vortex was one of the strongest among the structures acting at low radial position, only compared to the separation vortex. Both swirls carried along low pressure regions that inevitably end up increasing the spinner drag especially when they are closer to the spinner wall. The main blade root vortex was clearly observed among all the simulations made with shorter spinners, contrary to the separation one.

The hub vortex or also called “forced vortex” by some authors [8], was the structure that was depicted with a relatively large Q criteria values at the end of the spinner. It was produced by the downwash induced by the each of the blade roots. This downwash was mainly produced by the negative pressure coefficients of the pressure side which explains the opposite sign in comparison with the main root vortex. The hub vortex presented a lower magnitude but in most of the cases it induced a lower pressure zone. Although the root vortex or the separation vortex induced larger negative pressure coefficients zones, the influence of the hub vortex was greater since it acted where the wall had its largest outer normal component in axial direction such as the case of the 5% shorter spinner design where the spinner drag was significantly increased (See Fig. 3.6). As observed in the Figure 3.13, the vortices encountered at low radial positions of the shorter spinners were depicted in relation with their sign of rotation with respect to the axial direction. Based on this, the hub vortex showed a constant negative sign of rotation regardless its position or its magnitude.

In order to assess the differences of the vortical structures among the shorter spinner group, the maximum values of Q-criteria were extracted from a plane parallel to the rotor disk at 0.15 and 0.55 propeller radiuses from the defined origin. For reference purposes, the maximum Q-criteria values encountered at the hub represented around half of the magnitude of the blade tip vortical structures.

Both Figure 3.14 and 3.15 depicted the maximum values of Q-criterion measured close to the blade root and after the spinner respectively. The location of the planes was kept constant for all the designs tested among the short group. As a mean of comparison a 50% shorter spinner with the exact same diameter distribution was added.

Contrary to what was observed for pressure coefficients or flow velocities, the Q values shown were not averaged circumferentially. Instead, the maximum values were depicted, allowing a more direct assessment of the vortical structures strength independently of the radial position that the measurement was taken at. In addition, if only the strongest vortical structures are been shown then the sample becomes clearer since it leaves out the weaker regions of the rotational flow.

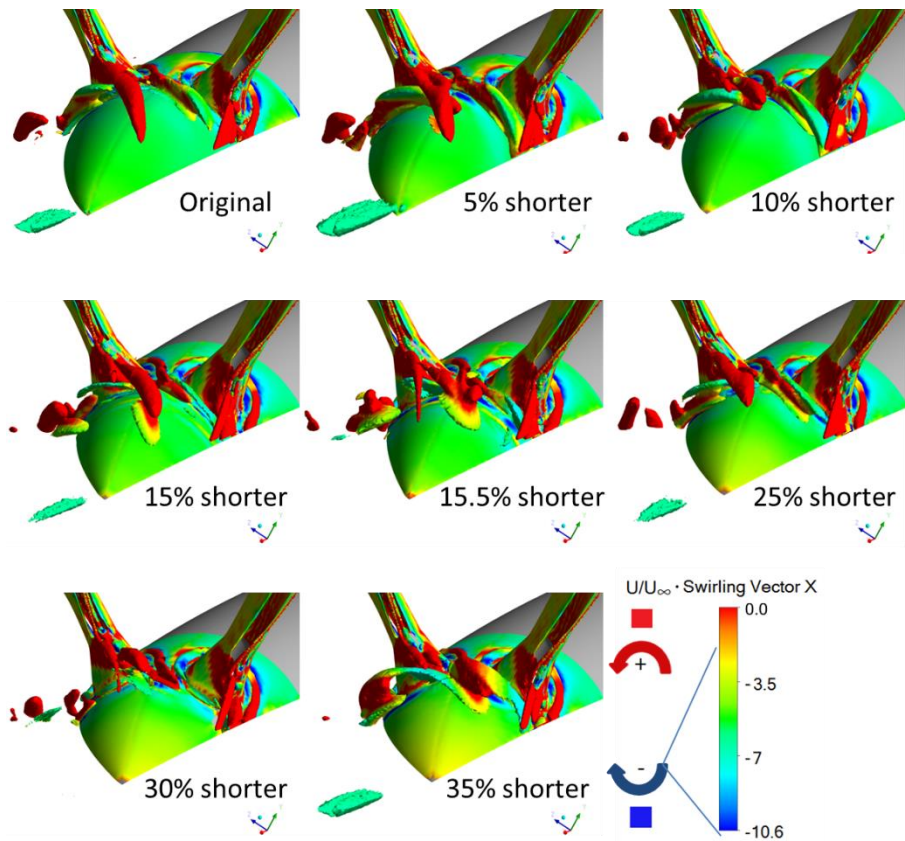


Figure 3.13: Vortex structures of short group (Q -criterion Isosurface of $470\,000\text{ s}^{-2}$). Vortical structures in red presented a positive sign of rotation respect to the X direction.

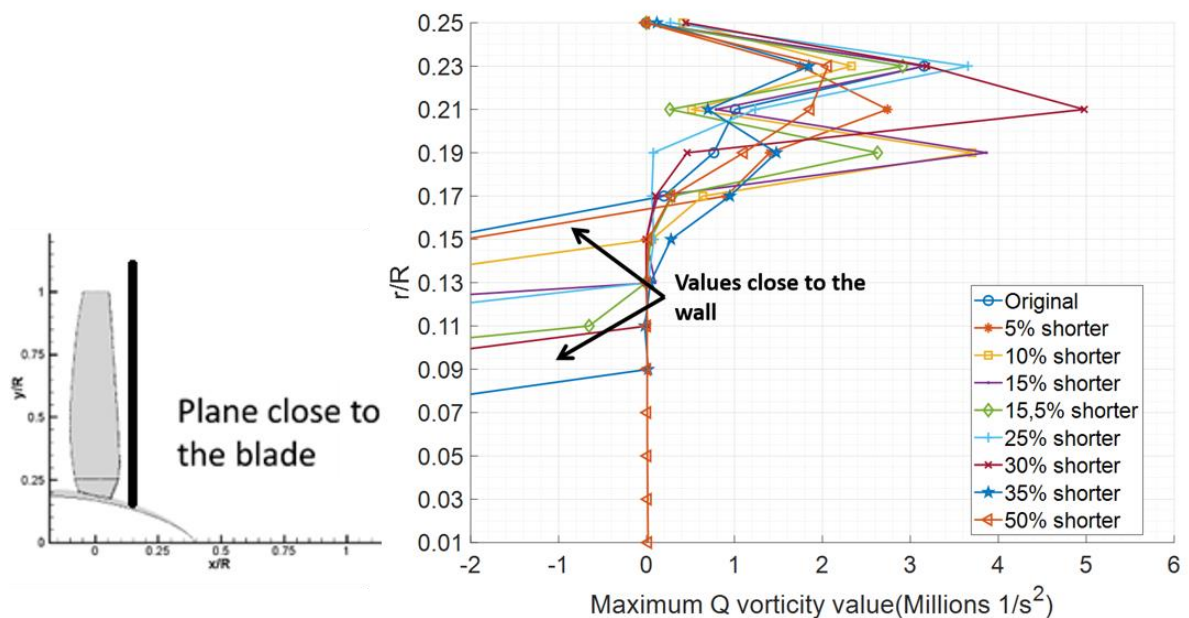


Figure 3.14: Maximum Q criterion values for short spinners close to the blade at 0.15 propeller radius from origin. Relative propeller efficiency is shown in the legend.

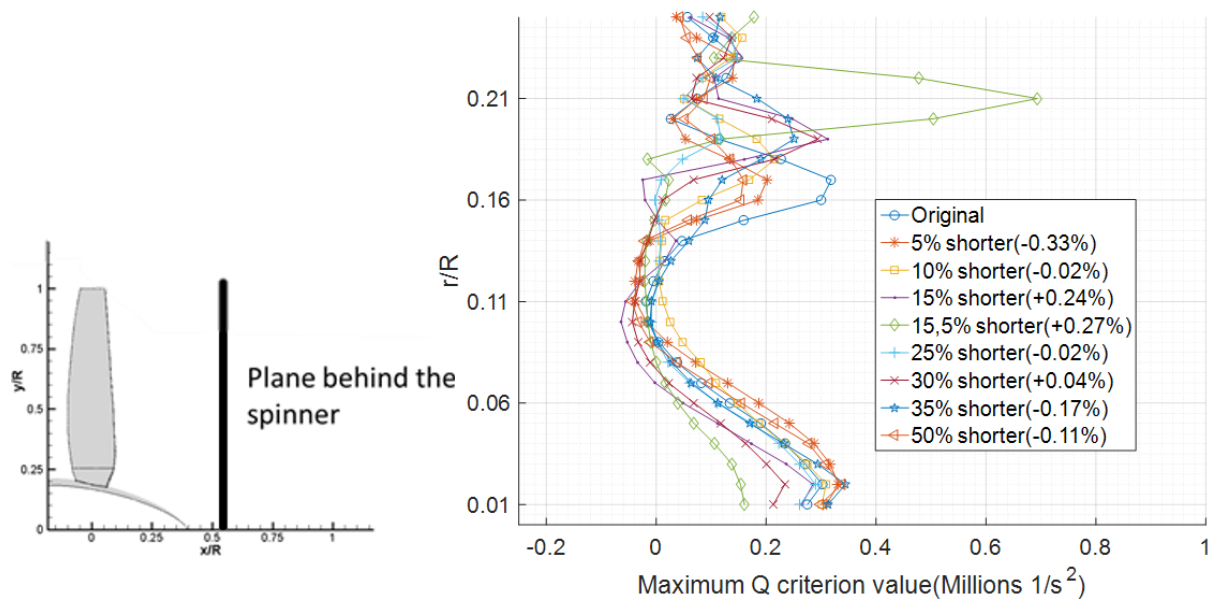


Figure 3.15: Maximum Q criterion values for short spinners at 0.55 propeller radius from the origin. Relative propeller efficiency is shown in the legend.

By looking at the pressure coefficient contours it becomes evident that the spinner end was significantly affected by a low pressure region. According to values of Q-criterion (Figure 3.14), the magnitude of the structures at the early formation of the vortex system (Close to the blade) was considerably larger than the ones encountered at the end of the spinner further downstream. The main blade root vortex was found to be the vortical structure at low radial positions with the largest Q criterion magnitude that sometimes became two swirls instead of one.

Most of the peaks of vorticity shown in the graphs of Figure 3.14 represented the first and the second part of the root vortex but in some cases the separation vortex presented a large Q-criterion value as well. According to the magnitude peaks it was possible to establish a correlation that connects the vortical structures of the lower part of the rotor with the formation of the hub vortex and thus its detrimental impact on the spinner drag.

The maximum Q values read from the plane located at 0.15 R (0.18 m) were split in two observable groups. In most of the cases the peaks belonged to the upper and the lower part of the main root vortex but in the 5% shorter, the 35% shorter and the 50% shorter spinners, the peaks closer to the spinner wall represented the separation vortex. The Q criterion peaks reported in the graphs of Figure 3.15 stopped abruptly at the radial position that coincided with the spinner wall, so proximity reference between the spinner wall and the nearest peak was read in r/R counts.

Table 3.3 depicts the vortical structures formed at the blade root with the lowest radial positions, showing the largest spinner drag and hub vortex Q criterion values that exceeded 0.3 million. The 15.5% shorter spinner case showed the lowest spinner drag and the lowest Q criterion value for the hub vortex. While the spinner drag increased in most of the cases when the hub vortex was stronger, the influence on the spinner drag seemed to depend on whether or not the hub vortex was close enough to the spinner wall. The pressure coefficients depicted in Figure 3.16 showed larger Cp values for the 15.5% shorter spinner, the 30% shorter spinner and the 15% shorter spinner, even when the last one had a relatively strong hub vortex. Given that the hub vortex was formed only at very low radial positions of the 15% shorter spinner, its influence was limited to the very last part of the spinner which

prevented it from affecting the spinner pressure drag as much as it did for other designs such as the 5% shorter.

Table 3.3: Effect of proximity among the blade root vortex and the hub vortex (Measured at 0.55 R plane).

Shorter spinner length (%)	Radial position of the largest Q criterion value of any blade root vortex between 0.1 and 0.25 r/R.	Hub vortex strength (Q criterion in millions of s^{-2})	Spinner drag relative to the original design
Original	0.17 R	0.30	1
5	0.17 R	0.33	1.13
10	0.18 R	0.30	0.79
15	0.19 R	0.28	0.74
15.5	0.21 R	0.15	0.69
25	0.19 R	0.29	0.83
30	0.19 R	0.23	0.80
35	0.19 R	0.35	0.87
50	0.17 R	0.34	1.05

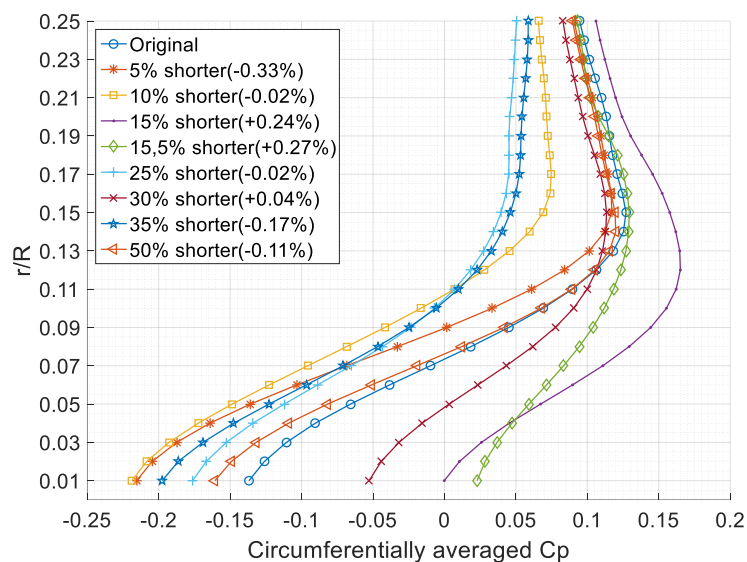


Figure 3.16: Pressure coefficients at 0.55 R downstream from origin (Plane after the spinner end). Relative propeller efficiency is shown in the legend.

It is important to recall that even when the 5% shorter spinner design exhibited a strong hub vortex, the only geometrical difference compared with the original spinner was at the tip and not at the diameter distribution; nevertheless, the stronger hub vortex in combination with the flow separation ended up decreasing the relative propeller efficiency significantly. The poorer performance induced by the 5% shorter spinner was observed to be the result of the flow separation produced by the steeped curvature of the shorter length even when it induced an increment in C_p due to the flow expansion after the point of separation. The larger adverse pressure gradient encountered only at the spinner end seemed to induce earlier separation on the suction side as well.

As the loading of the pressure side increased, the magnitude of the transverse jet flow coming from the pressure side did as well. This not only strengthened the separation vortex but also enlarged the separation bubble size causing flow acceleration at first and then flow deceleration due to its expansion. As mentioned before, the flow deceleration induced a positive C_p after the recirculation created by the separation vortex which could have been initially inferred as beneficial; however, the increased

negative tangential component of the velocity field, together with the larger pressure coefficients contributed to the formation of the strong hub vortex observed at the 5% spinner length reduction.

Figure 3.17 shows the axial component of the force produced by pressure and viscous effects which was expressed as a fraction of the propeller excess thrust (F_{ex}). Larger values are observed in the 5% shorter spinner even when the only change in design was at the spinner end.

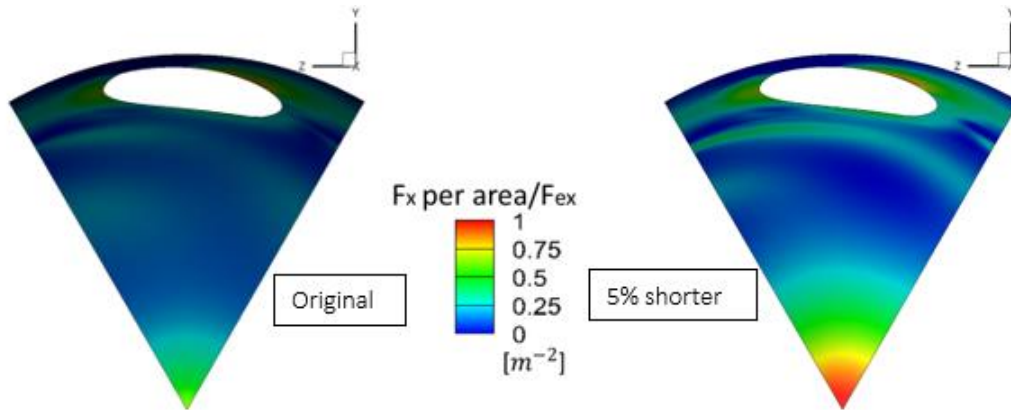


Figure 3.17: Hub vortex effect at the spinner end.

The low C_p induced by the separation vortex of the 5% shorter spinner was clearly observed in the Figure 3.17; however, spinner drag related produced by the flow separation was significantly lower when compared to the one induced by the hub vortex one.

While the original spinner's drag represented 1.66% of the excess thrust, the 5% shorter spinner produced a drag force as large as 1.89% of the excess thrust. It was clear that the increment of the spinner drag was the main factor that caused the poorer performance; nevertheless, it is important to know how relevant the contribution of the last part of the spinner was. Taking into account that only the last portion of the spinner was affected by the hub vortex, the drag force produced by the spinner area between the 90% and the 100% of the spinner length was found to be 5.2% of the total spinner drag while in the 5% shorter spinner 9.5% of the spinner drag was produced.

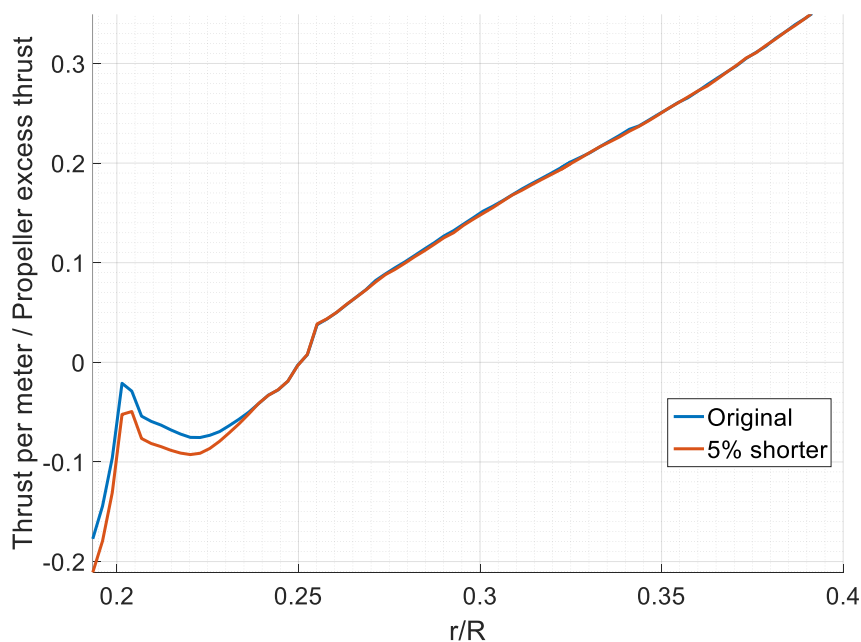


Figure 3.18: Blade root loading comparison.

Figure 3.18 depicts the blade loading with the 5% shorter spinner. Even when the blade exposure was kept constant for both designs, the blade root region below 0.25 R encountered larger values of negative thrust. The reduction of thrust was the result of the increased negative C_p observed in the pressure side of the blade root. As the spinner got reduced in length, the blade root produced larger amounts of negative thrust that were observed only at the blade root.

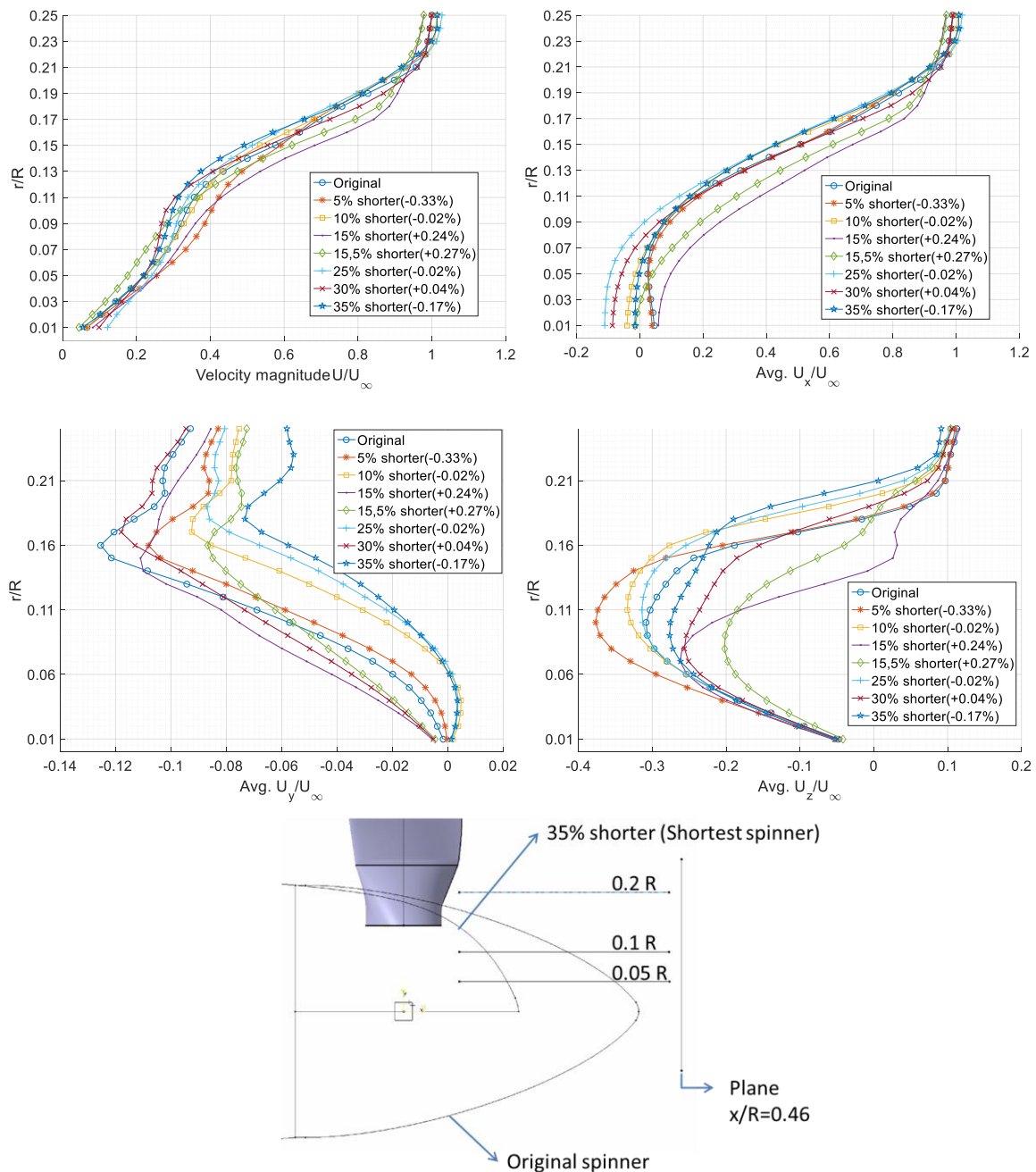


Figure 3.19: Circumferentially averaged velocity magnitude and velocity components of shorter spinners (Relative propeller efficiency increments are indicated in their respective labels). Values displayed in the graphs were averaged at a plane located at 0.46 R.

Contrary to the 5% shorter spinner, the 15.5% shorter one showed the largest performance improvements among the shorter spinners group, despite the negative thrust encountered at the blade root. The relative propeller efficiency was increased due to a more significant reduction in the spinner

drag that could also be observed at the recirculation region of the 15.5% shorter. As the flow separated in this spinner design, the negative axial velocities showed some of the largest values inside the recirculation region at the same time that the recirculation region was extended in axial direction. Figure 3.19 depicts the circumferentially averaged velocity magnitude among the shorter spinners as well as its components and it can be appreciated that for both, 15% and 15.5% shorter spinners, the magnitude of the velocity was relatively larger compared to the rest of the cases. Below 0.15 r/R , the velocity magnitude started to decrease relatively faster and around the radial position of 0.08 r/R , the velocity magnitude of the 15.5% shorter spinner became the lowest among the group. The velocity magnitude reduction obeys an evident flow deceleration that increased the C_p towards the end of the spinner regardless the longer recirculation region.

On the other hand, the velocity magnitude of the 5% shorter spinner increased at low radial positions with the difference that the component of velocity that was enlarged was not the axial but the tangential one. Figure 3.19 shows the large negative tangential velocity observed for the 5% shorter spinner. This ended up forming a hub vortex with a very large Q criterion value. In other words, the blade positive downwash was only produced at radial locations higher than the blade root, hence the negative rotational sign of the hub vortex.

The different ways in which flow separation occurred among the spinners, affected directly the flow expansion and thus the pressure coefficient distribution. So, it can be inferred that the spinner geometrical design affected mostly the spinner pressure drag; however, the hub vortex formation was mostly affected by the direction of the outflow at the blade root section.

3.2.4 Effect of blade exposure on the performance of short spinners

Figure 3.20 showed that in terms of the propeller excess thrust (Thrust - Drag), most of the designed geometries that were tested showed an improvement when compared to the original design. Due to the larger flow expansion induced by a “Flattened” recirculation region instead of a thick in combination with a relatively weak hub vortex, the propeller exhibited larger excess thrust for the 15.5% shorter spinner; nevertheless, even when the propeller thrust increased 0.6% for a 15.5% shorter spinner, the greater blade exposure increased the blade root torque.

Given that the torque variations not only depended on the spinner flow separation but more directly on the blade exposure, the efficiency term defined before was used when referring to the performance of the propeller.

When the efficiency term is taken into account, the gain in excess thrust that the propeller had was not as meaningful as it seemed at first. As mentioned before, the variations in the blade root exposure changed the blade root loading which at the same time changed both, the magnitude of the force that acted in axial direction and the torque. One of the problems that have been addressed throughout the research was that the significant changes caused by the spinner represented a very small order of magnitude when compared to the values for the entire propeller, which is why the variations in blade loading were mainly assessed at the blade root where they were proportionally more significant.

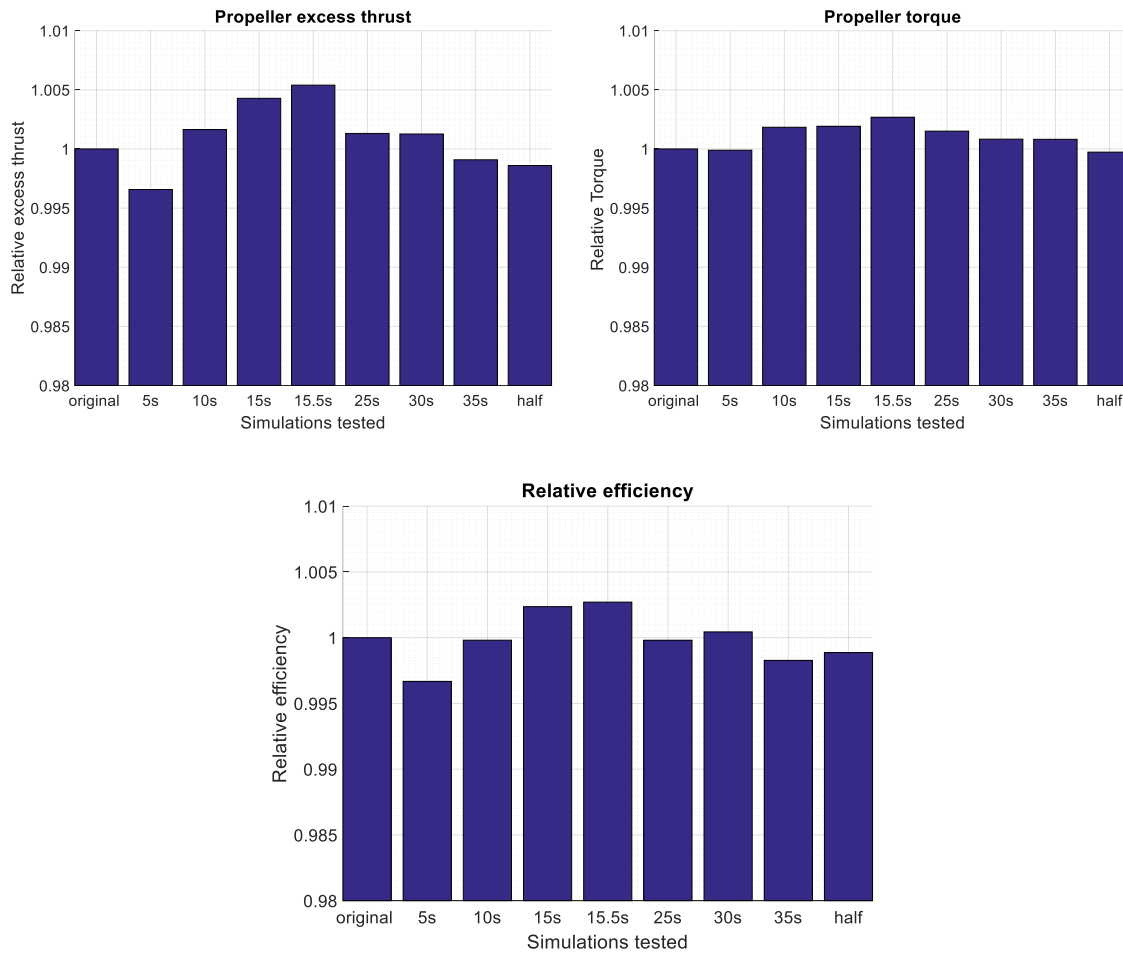


Figure 3.20: Relative propeller efficiency of shorter spinners relative to the original design.

Despite that the excess thrust and the torque have been computed for the entire propeller configuration (Including nacelle and spinner) with acceptable convergence criteria, the performance comparisons relied on the average of the results over the last iterations in order to decrease the small fluctuations in the resolved flow, especially inside regions of clear separation.

The flow separation occurring on the spinner changed the blade loading mainly below $0.25 r/R$, so it can be said that the main variations of torque occurred at the blade root. The torque induced by the spinner alone was observed to be around one order of magnitude lower than the one produced by the blade root. This was expected since it is a body of revolution. The 5% shorter and the 50% shorter spinner suffered no changes in blade exposure compared to the original; however, both spinners changed the length and curvature. Both original and 5% shorter designs exhibited similar values of torque, while the 50% shorter had around 0.1% lower torque.

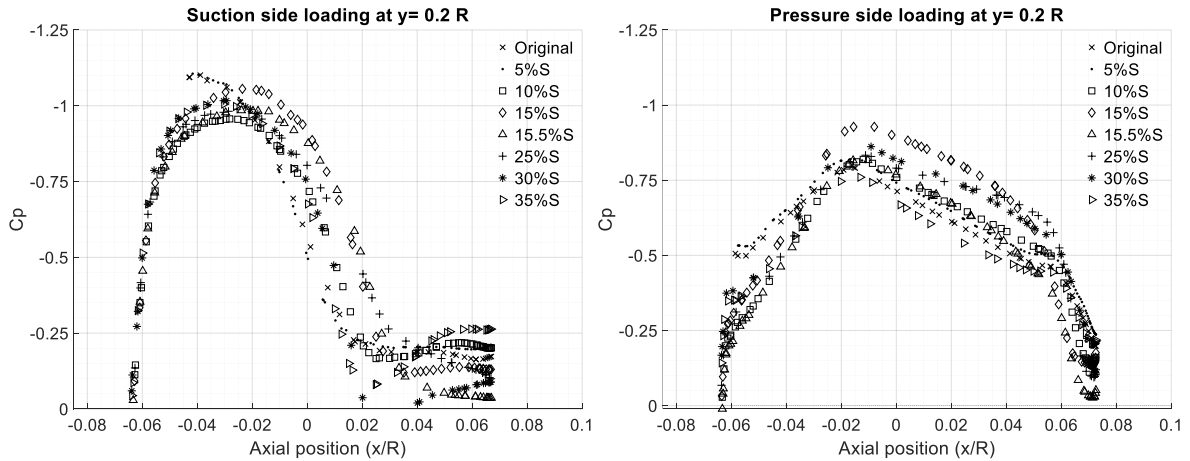


Figure 3.21: Pressure distribution of the blade root of shorter spinners.

As observed in Figure 3.21, at around $0 x/R$ the blade root suction side showed more negative pressure coefficients when the propeller was simulated with shorter spinners, especially for the 15% and 15.5%. The lower C_p values were maintained further downstream up to $0.02 x/R$ due to the flow separation delay occurring on the rear part of the suction side.

The pressure side of the blade root showed negative pressure coefficients as shown in Figure 3.21. Even when the flow seemed to be separated at a relatively same axial location for all the cases, the suction side loading was clearly larger for the 15%, 25% and 30% shorter spinners. Nevertheless, the 15.5% shorter one did not induce a pressure side loading as large as the one observed for similar spinner lengths due to its larger blade exposure. Given that both 15% and 15.5% shorter spinners showed the largest increment on the suction side loading, not only the thrust but also the torque was increased, especially when the flow separation was delayed; however, the largest increment in efficiency was induced by the 15.5% shorter mostly due to the lower pressure side loading. In order to isolate the effect that the blade exposure had on the torque, on blade loading and on the spinner performance, a series of constant length cases were simulated.

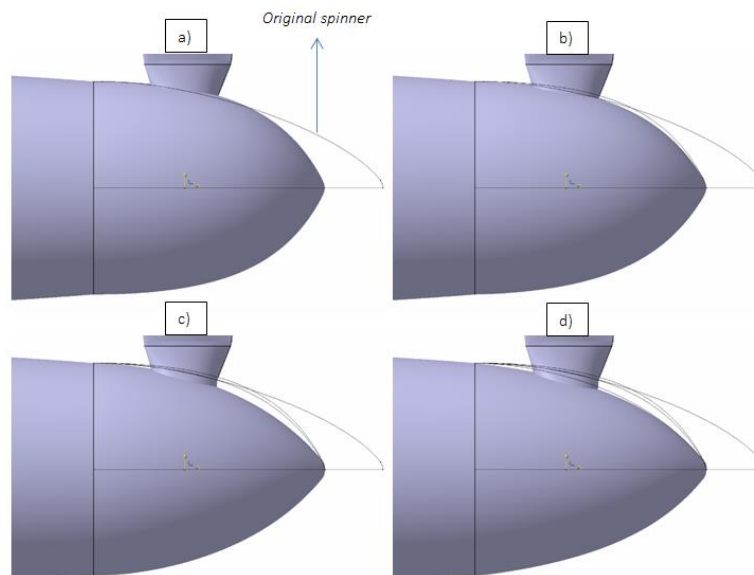


Figure 3.22: Blade exposure test with spinners 20% shorter than the original.

a) Less blade exposure than the original (FR=0.7); b) Same blade exposure than the original (FR=0.72); c) Larger blade exposure than the original (FR=0.75); d) Narrowest spinner with the largest blade exposure (FR=0.78).

The increment in blade exposure at a fixed length decreased the curvature steepness (Fig. 3.22), so the variations that occurred in the propeller performance were no longer related to the spinner length but only to the variation of its own curvature and the blade exposure. The boundary layer clearly encountered less adverse pressure gradients at a higher blade exposure; however, the hub vortex was formed at similar axial positions regardless the point of flow separation.

It is important to recall that the blade root was defined as the part of the blade where the spinner re-designs had most of their influence (Below $0.25 r/R$). As the spinner designs exposed longer portions of the blade root, the negative thrust component was increased in a larger percentage compared to the thrust component of the blade root (Fig. 3.23). This increment indicated that as the blade exposure increased, the blade design tended to favor the pressure blade loading rather than the suction one.

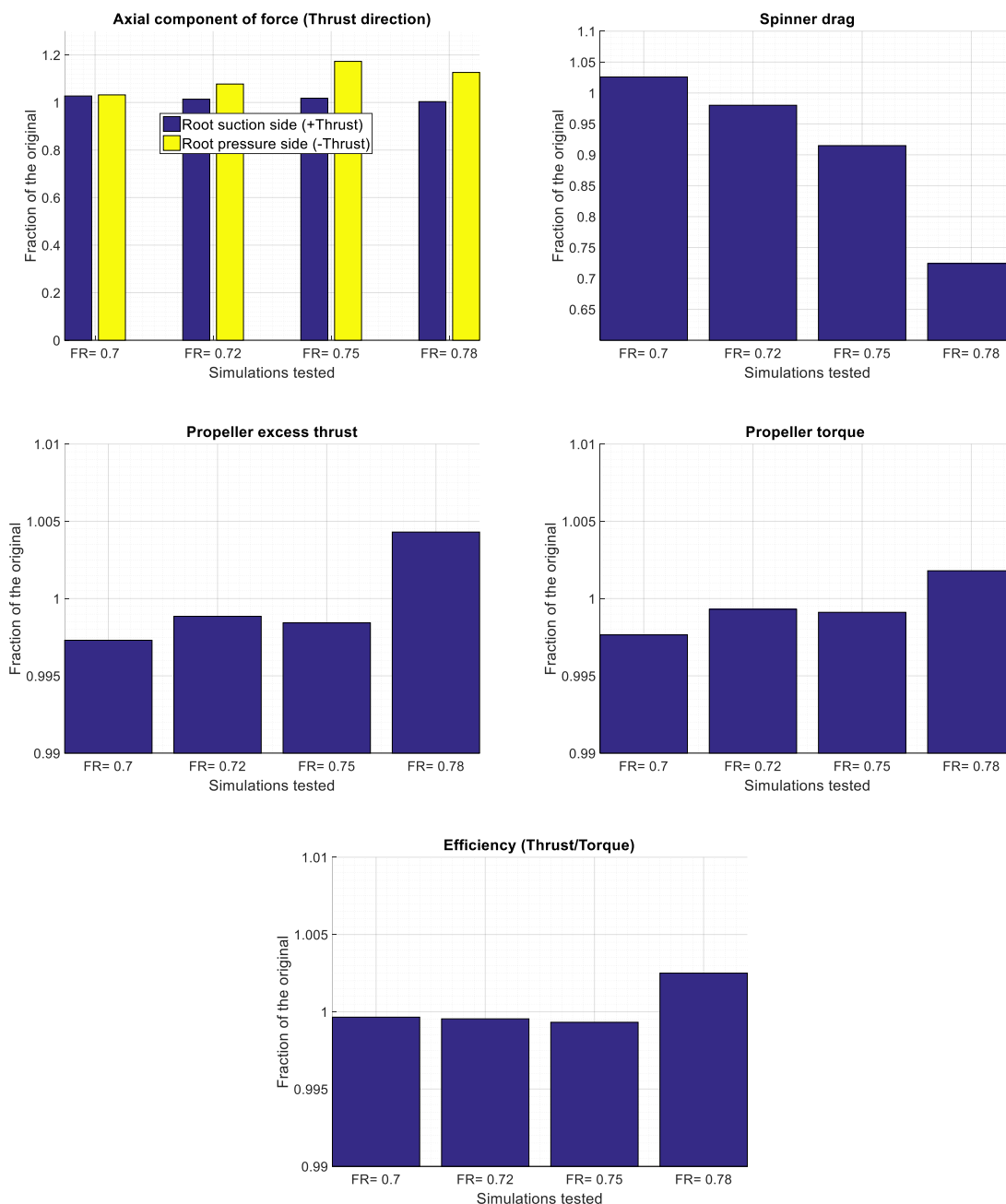


Figure 3.23: Blade exposure variation effect on performance at a constant length 20% shorter than the original.

It is necessary to take into account that the magnitude of the increment in the propeller performance that was achieved by modifying only the spinner and not the blade was expected to be relatively small. This meant that the efficiency improvements would most likely be achieved by both the spinner re-design and the blade loading modification. Especially due to the similar order of magnitude of their respective efficiency variations.

The change in torque among the different designs depended mostly on the blade root loading, since the spinner contribution was two orders of magnitude smaller than the one of the blade root. On the other side, the changes in propeller net axial force were mostly related to the separation/vortex effects acting on the spinner. The torque values for the entire propeller shown in Figure 3.23 did not present significant variations on the overall value; nonetheless, Figure 3.25 depicts the torque variations observed at the root loading, where the difference in loading became more evident.

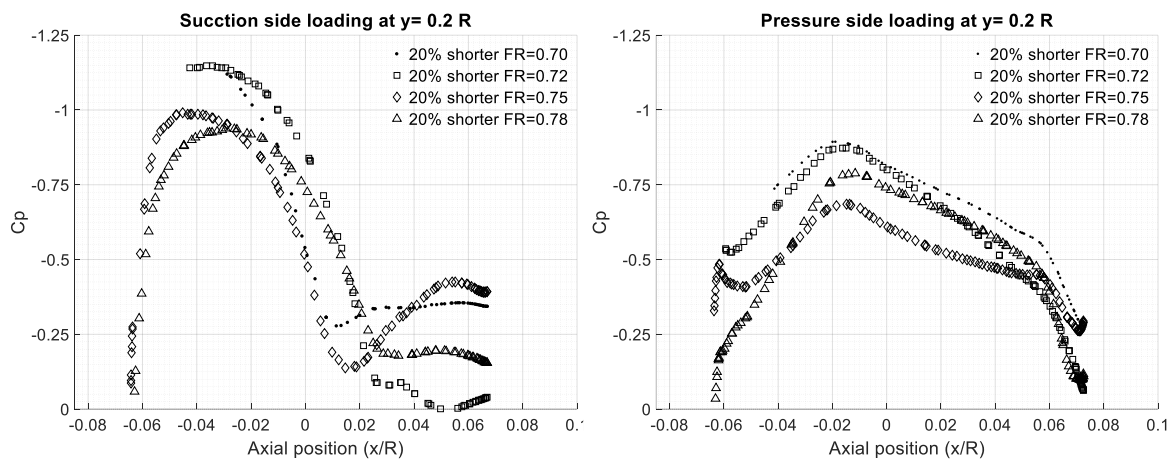


Figure 3.24: Blade root ($y=0.2 R$) pressure distribution for the 20% shorter spinners at different blade exposures.

As it can be observed in Figure 3.24, the spinner fineness ratio was increased and the blade root was more exposed. This more positive values of C_p on the pressure side most likely due to the lower velocity magnitude caused by the larger flow expansion. The spinners with the largest fineness ratios induced a less abrupt flow separation in the suction side of $0.2R$, causing the decrement of the pressure coefficients towards the trailing edge. In a similar way, the pressure side encountered larger pressure coefficients when the blade exposure was increased due to finer spinner designs. It is important to notice that the suction side of the blade root was clearly more affected in terms of flow separation when compared to the pressure side of the blade root.

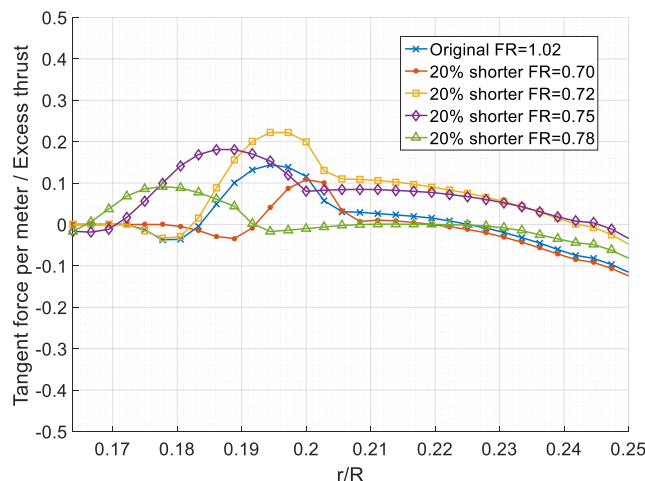


Figure 3.25: Effect of blade root exposure on tangential force distribution.

As the blade was more exposed, the 20% shorter spinner designs showed blade root resultant forces with positive axial components (Positive in downstream direction). This meant that those components acted against the propeller thrust; however, after looking to the tangential force produced at the blade root of the four spinner designs with different blade exposure, it was possible to see that all of them presented a tendency to reduce the torque due to the positive tangential force of the blade root (Negative pressure coefficients in the pressure side). In figure 3.25 the tangential force at the blade root was compared among the four tested spinner designs. Each of the tests showed a peak of maximum positive torque (In direction of rotation); however, the distance in radial direction at which the maximum value was observed was different. This distance seemed to have the largest influence in the blade root torque, even more than the magnitude of the maximum value. The spinner with the least blade exposure ($FR=0.70$) exhibited its maximum peak of positive tangential force at around $0.2 R$, while the one with the largest blade exposure ($Fr=0.78$) exhibited the maximum peak of positive tangential force at around $0.18 R$. The shorter lever arm observed in the cases with more blade exposure seemed to prevent them from reducing the torque in a more significant way.

Independently of the disadvantage of having higher torques with larger blade exposures, the largest increment in excess thrust was found with spinners of relatively smaller diameter or larger fineness ratios. So in order to improve the relative propeller efficiency while modifying the spinner, the torque was kept as low as possible or at a moderate increment justified by a significant reduction of the spinner drag.

3.3 Effect of spinner length increment on the propeller performance

In principle longer spinners with larger fineness ratios (FR_{spinner}) would mean that the curvature steepness could be decreased and the flow separation would be delayed. A second test made on a group of longer spinner designs was performed in order to assess their impact on the propeller performance. After assessing the effect that shorter spinners had on the propeller performance it became evident that the improvement on efficiency was driven by two main factors: The increment of propeller excess thrust and the decrement of torque, as long as the first one remained at least the same as the one for the original design.

The longer designs were expected to decrease the spinner drag due to the relaxation of the adverse pressure gradient that should induce a delay in flow separation. Contrary to short designs, the longer ones could maintain similar adverse pressure gradients as the length was increased at a very low blade exposure variation. This would mean that the blade exposure would influence the relative propeller efficiency less than in the short designs.

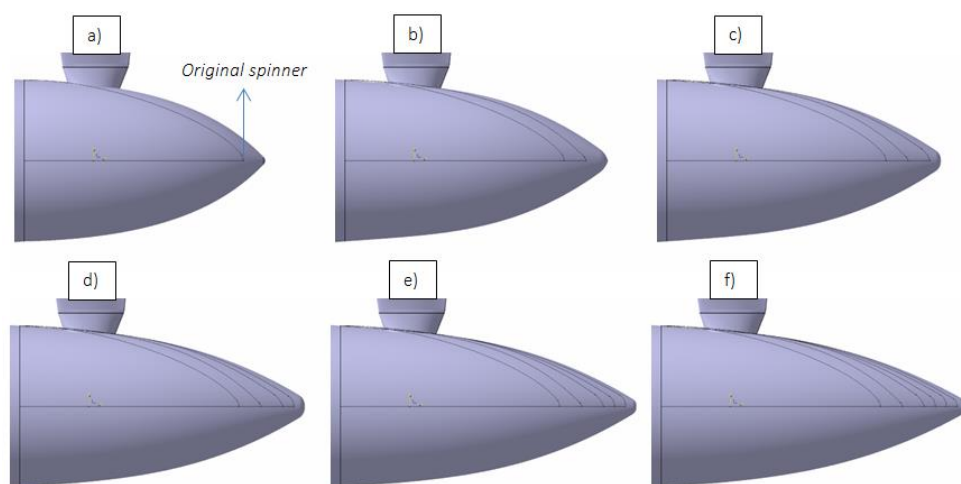


Figure 3.26: Testing group longer spinner design.

a) 10% longer; b) 20% longer; c) 25% longer; d) 30% longer; e) 35% longer; f) 40% longer

As it can be seen from Figure 3.26, the group of long spinners maintained a similar blade exposure in order to decrease the effect of blade root loading variation due to exposure. In this way, the blade loading variations would be originated mostly by the difference in spinner geometry and not by the blade exposure. Given that both, blade exposure and flow separation were expected to exhibit similar values as the spinner length was increased, the hub vortex strength was expected to present similar Q criterion values.

The performance of longer spinners is shown in Figure 3.27. The spinner drag was reduced in all the tests; nonetheless, only 5 out of 6 designs increased both the efficiency and the propeller thrust, being the shortest spinner the one with lowest propeller efficiency. Despite the increment in propeller excess thrust, none of the long spinners improved the thrust as much as it was improved among the short spinners group. At first glance and given the reduced the spinner drag of longer designs, this could have been attributed to the blade root loading; however, large blade exposure increased the blade loading at higher radial positions as well. While this increment was evident, its contribution to the propeller efficiency was negligible, especially because less blade exposure would also induce a lower torque.

In terms of efficiency, the 30% longer spinner showed the best results of the group. It also showed the lowest spinner drag of all the tests (Around 64% of the original) at this point of the research. The streamlines of Figure 3.28 indicated that the separation point was shifted further downstream for all the cases when compared to the shorter spinners group and with the exception of the 10% longer spinner, all cases showed only positive axial velocities downstream ahead the blade root section. Both, streamlines direction and positive axial velocity contours indicated that recirculated flow was not as common as it was with shorter designs. The variations of the propeller torque were negligible since the blade exposure was very similar among the tests. This emphasized the relevance of the spinner drag reduction in order to improve the propeller efficiency.

Table 3.4: Pressure and viscous drag contributions for longer spinners

Spinner length compared to the original	Spinner pressure drag	Spinner viscous drag
Original	96.9%	3.1%
+10%	95.4%	4.6%
+20%	92.9%	7.1%
+25%	92.9%	7.1%
+30%	90.6%	9.4%
+35%	92.8%	7.2%
+40%	93.4%	6.6%

The larger wetted area of the longer spinners, together with delayed flow separation increased the percentage of the spinner viscous drag when compared to the original design (Table 3.4); however, the largest part of the spinner drag was still due to the pressure drag. In cases of relatively large efficiency increments (+0.29%) such as the 30% longer, the pressure drag represented 90% of the spinner drag. On the other hand, the simulations made with longer spinners showed a clearer correlation between spinners with earlier flow separation and their predominant pressure drag compared to the ones that maintained attached flow over most of the spinner wall in which the influence of the viscous drag was as big as 9.4%.

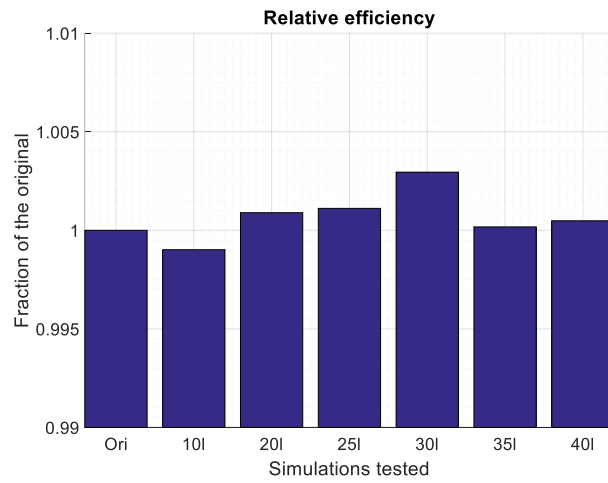
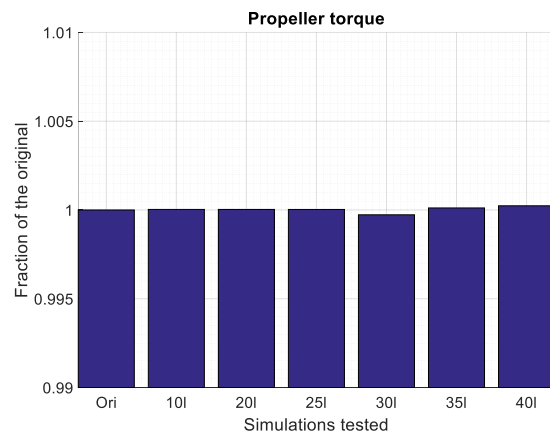
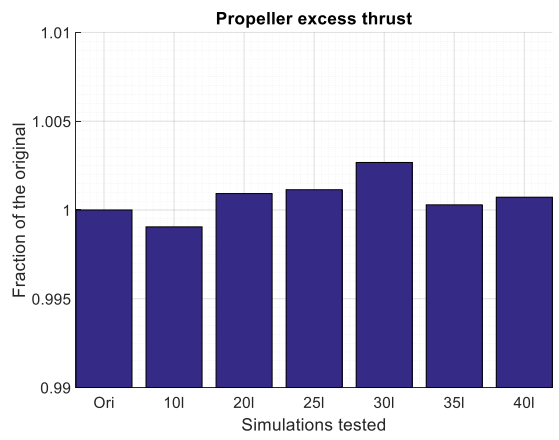
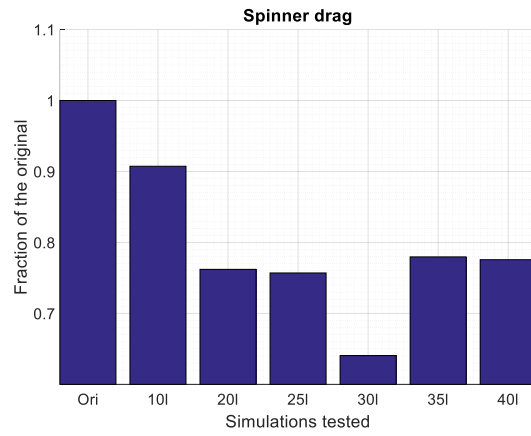
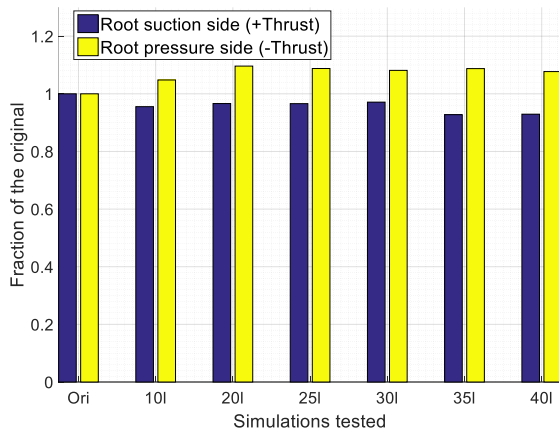


Figure 3.27: Performance graphs of longer spinner group.

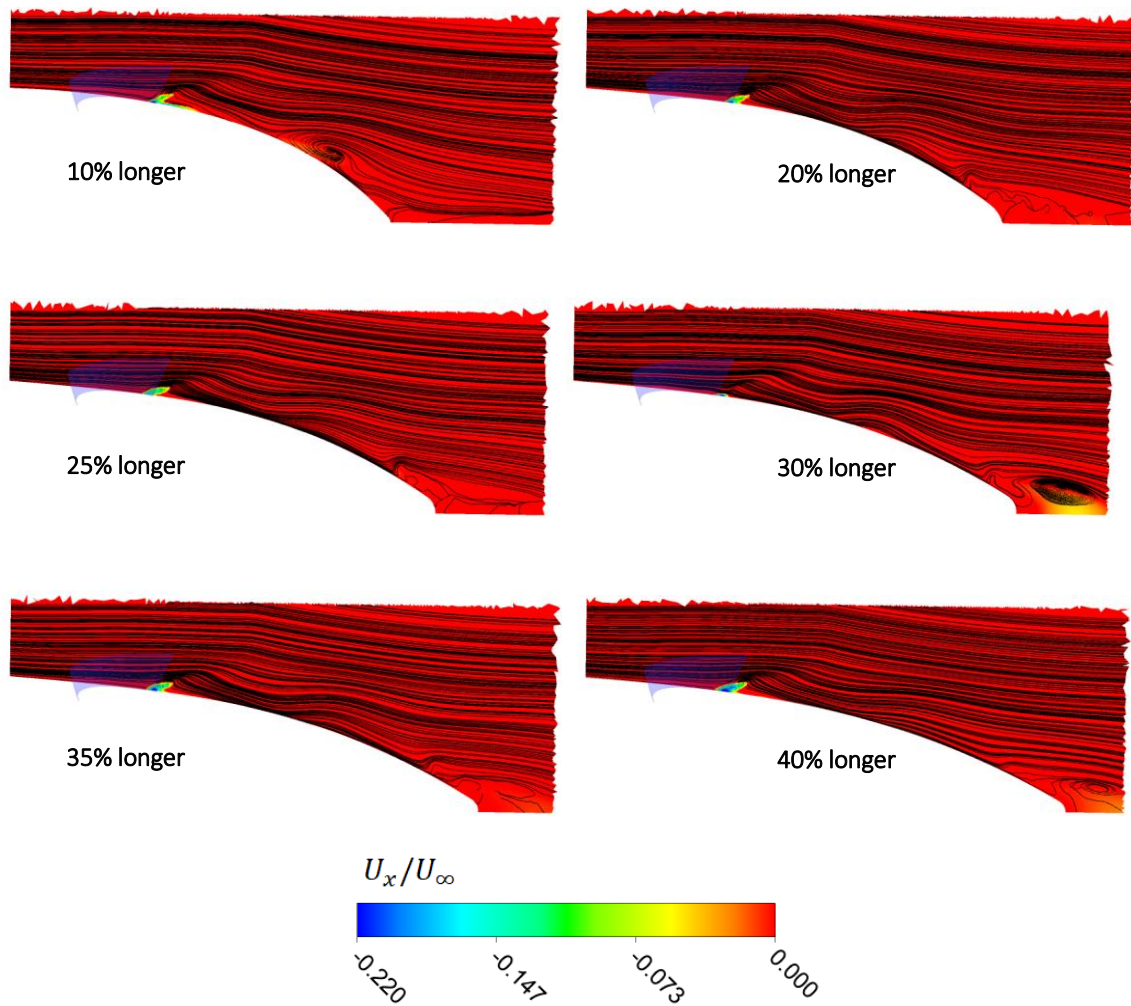


Figure 3.28: Streamlines and negative axial velocity contours among the long spinner group (20° tilted plane of Figure 3.1). Projection of the lower suction side is shown at every picture.

Figure 3.29 portrays the pressure coefficient contours observed at the same testing plane used for short spinners. The plane goes through the spinner portion that lies ahead of the suction side of the blade, where the flow separation has constantly showed to be triggered. Contrary to what was observed for shorter designs, longer ones showed larger positive values of C_p closer to the spinner wall; however, the pressure coefficients decreased in all cases towards the last portion of the geometry at the point of streamlines separation.

Just as the flow separation, the region of low pressure coefficients seemed to start at the same axial location for the 30%, 35% and 40% longer spinners. This suggested that independently of increasing the spinner fineness ratio, spinner designs with the same blade exposure would not result in shifted separation points. In fact, the two longest designs increased the spinner drag mostly because a larger portion of the spinner was inside the region of low pressure coefficients.

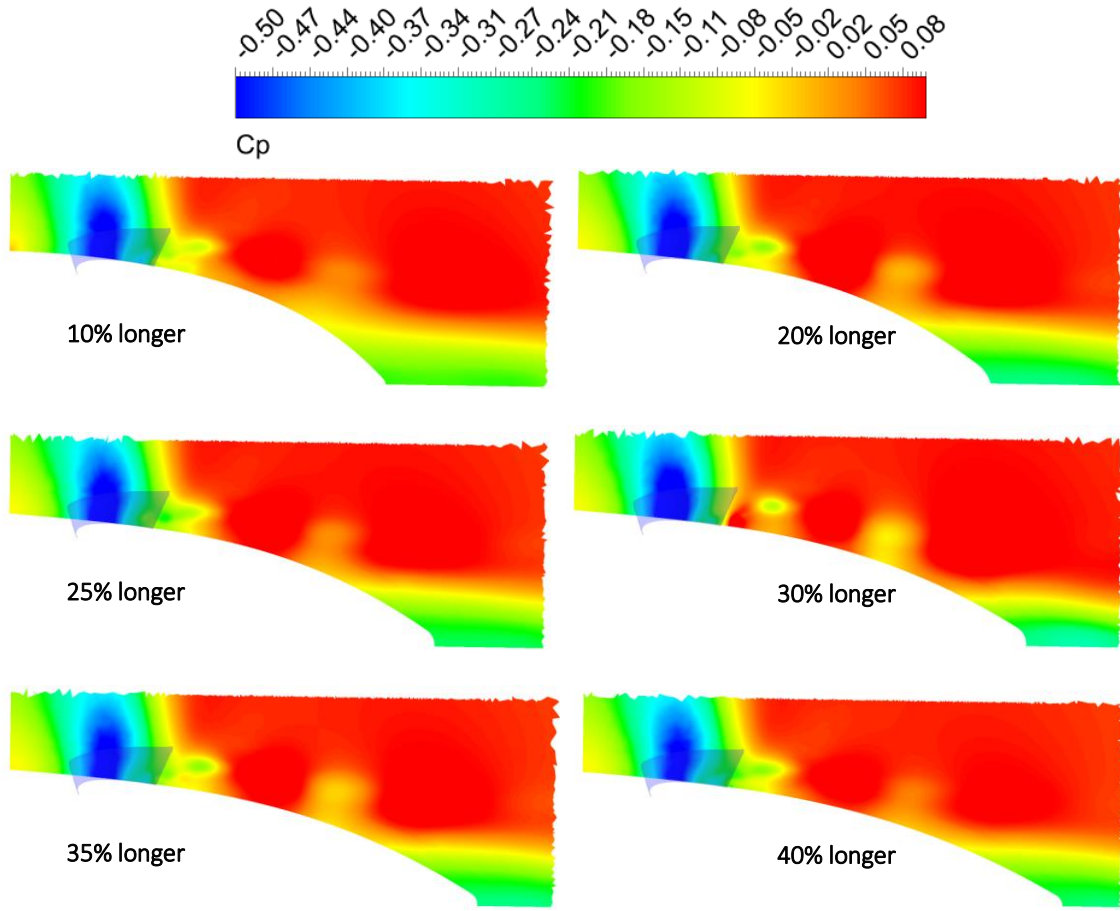


Figure 3.29: C_p contours among the long spinner group (20° tilted plane).
Projection of the lower suction side is shown at every picture.

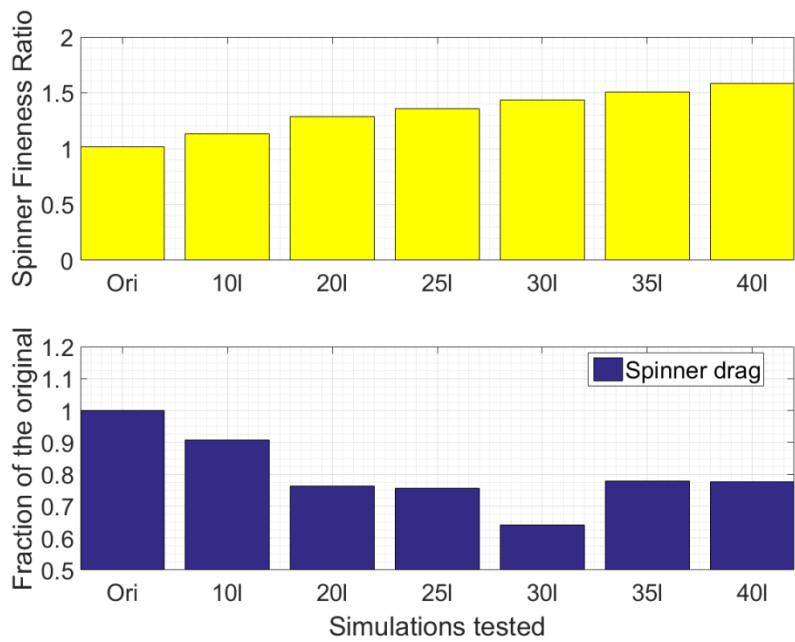


Figure 3.30: Variation of $FR_{\text{spinner}} (L/H)$ compared to the variation of spinner drag for longer spinners.

The blade root suction side kept exhibiting flow separation regardless the delay in flow separation. It can be said that although the negative tangential component of the outflow velocity was not as large as it was for shorter designs, the velocity field still showed negative tangential velocities at low radial positions, which helped to the hub swirl formation.

As mentioned before, the blade exposure was kept very similar among the tests. This allowed to establish a correlation between the spinner drag and its fineness ratio (L/H). Where L was the maximum length of the spinner measured from the center of the blade root profile (Stacking axis) to the spinner end and H was the spinner diameter also measured at the center of the blade root profile. Figure 3.30 shows the fineness ratio of longer spinners and their spinner drag variations. It was possible to see a decreasing trend in the spinner drag as the FR_{spinner} got increased; nonetheless, once the flow separation was delayed, the gain in performance depended mostly on the spinner pressure recovery improvement.

The vortical structures depicted as a Q criterion isosurface of $470\,000\text{ s}^{-2}$ (Figure 3.31) showed an evident reduction of the hub vortex in comparison with the original and shorter spinner designs. In fact, for the level of Q criterion shown in the picture, the only recognizable hub vortex structure was encountered on the 30% longer spinner.

It was important to recognize the vortex system after the blade root because the identification of the vortical structures formed close to the spinner offered a hint about the propeller performance related to the particular spinner design. In a similar manner it has been shown that the hub vortex induced a detrimental effect for the performance in most of the cases tested so far; however, other vortical structures such as the separation vortex have served as indication of how and where was the separation initiated.

This was the case of the separation vortex in the 30% longer spinner that contrary to the strong hub vortex encountered on this simulation, it showed the weakest separation vortex structure. None of the other long cases showed less strength or extension for the separation vortex than the 30% longer one; so judging by the Q criterion isosurface inspection, the relative absence of a separation vortex at the blade root could indicate a potentially better propeller performance in terms of attainable pressure recovery. In general, longer spinners were expected to decrease the influence of the hub vortex on the spinner pressure recovery, mostly because the hub vortex formation showed to be enhanced by the larger tangential direction of the blade root outflow that was mostly produced when large amount of flow was separated.

The strongest separation vortex among the long spinners test, was observed at both 10% and 40% longer cases. Although the first one decreased the original propeller efficiency, the longest case did not show a significant improvement in efficiency either.

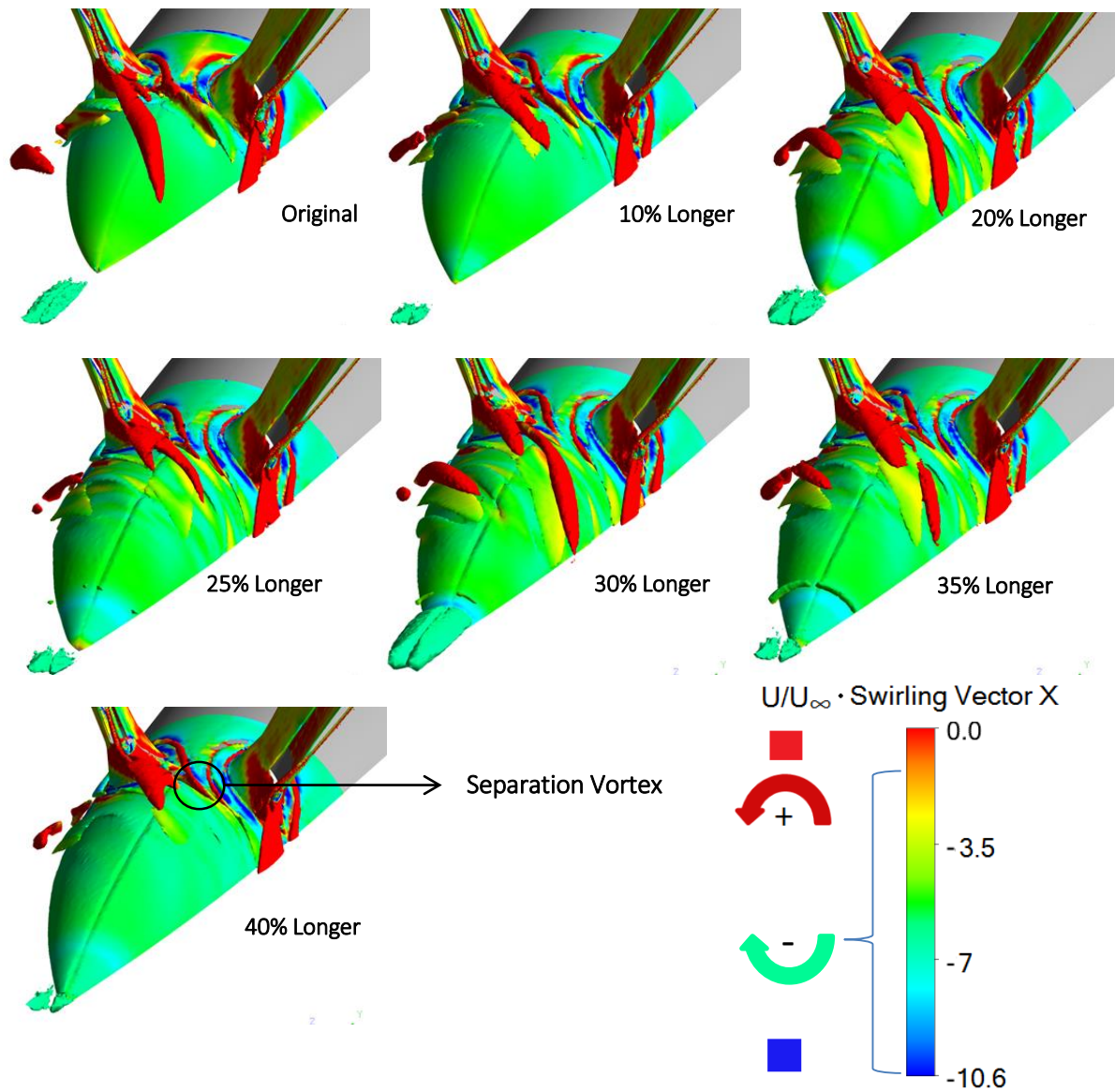


Figure 3.31: Vortex structures of longer spinners (Positive rotational sign in axial direction shown in red; Q-criterion Isosurface of $470\,000\text{ s}^{-2}$).

As it can be observed at the Figure 3.32, the location and strength were very similar among the vortices. Regarding the magnitude, the differences among the structures at a same radial location hardly exceeded $0.1\text{ million s}^{-2}$; however, at lower radial positions, the 30% longer spinner did show a much larger difference between maximum Q criterion values.

The peaks observed at the Figure 3.32 between $0.21\text{-}0.23\text{ r/R}$ and between $0.19\text{-}0.15\text{ r/R}$ belonged to root vortices that were induced by the difference in radial velocity directions from the suction and the pressure side. The grouped peaks with the highest radial position corresponded to the previous blade passage while the second highest radial group of peaks corresponded to the blade of 2 passages before.

When looking to the pressure distribution encountered at the spinner wall of the longer designs (Fig. 3.33), it can be noticed that positive values of C_p were rarely encountered among the spinners. In fact, the original spinner geometry did not show positive values at all, similar to the pressure distribution on shorter spinners. Positive values of C_p were mostly encountered around 0.25 propeller radius downstream the origin where most of the tests showed attached flow.

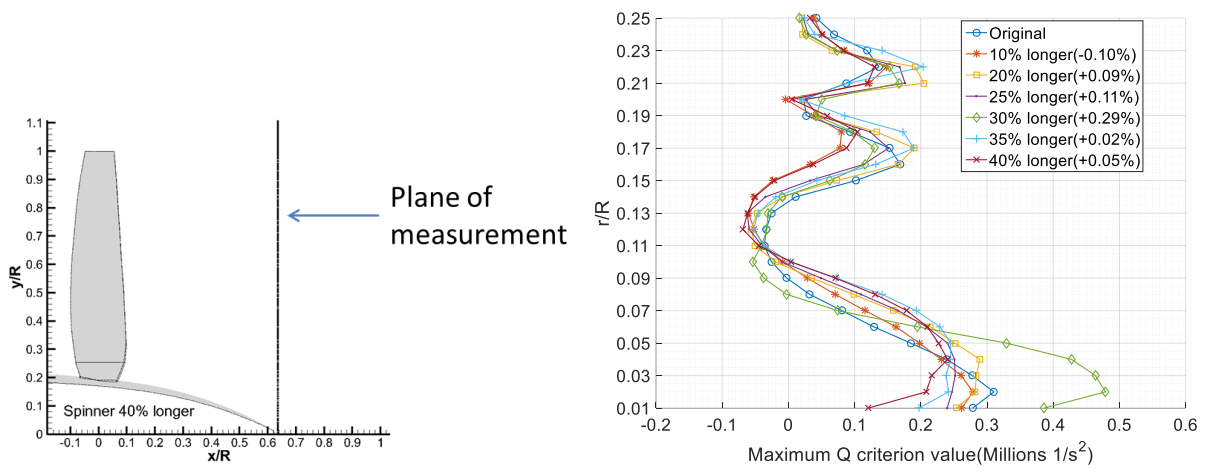


Figure 3.32: Maximum values of Q criterion observed for longer spinner designs at low radial positions at 0.64 x/R plane. Relative propeller efficiency is shown in the legend.

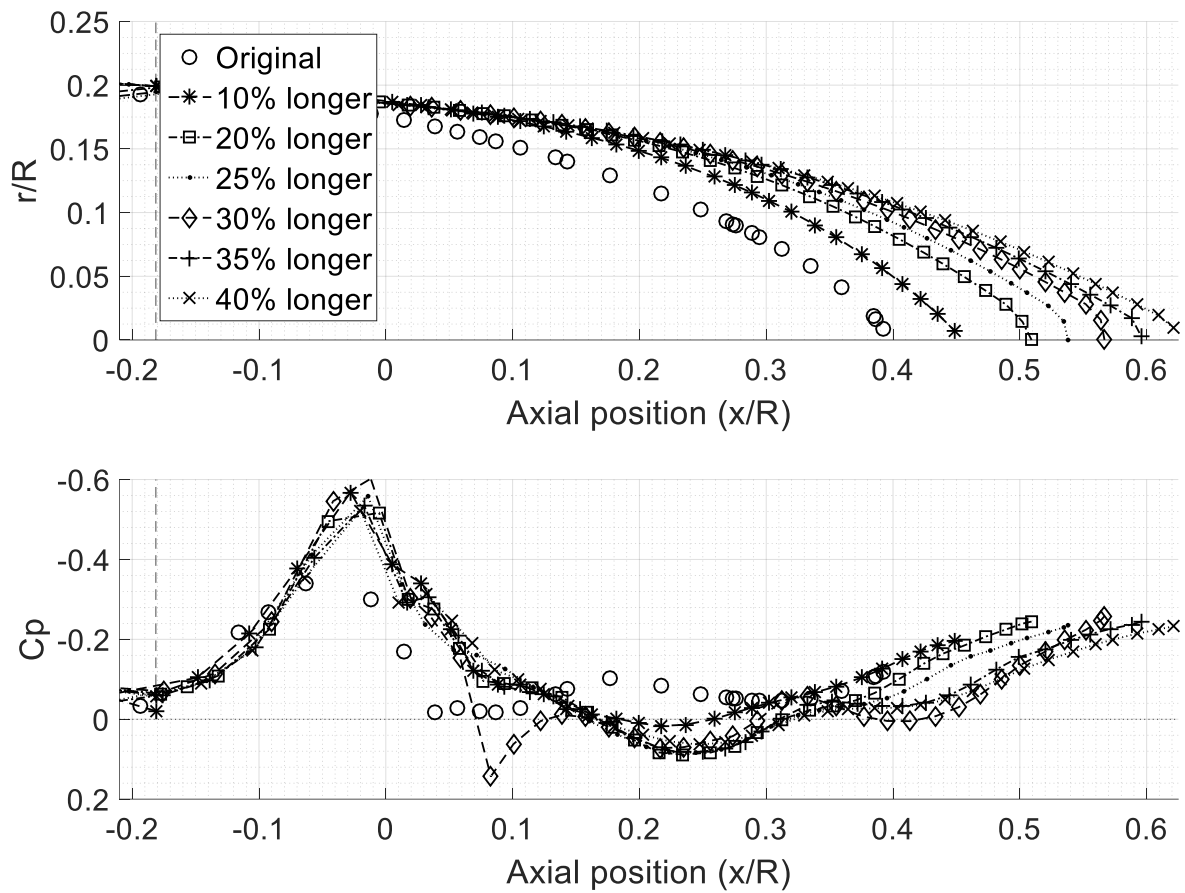


Figure 3.33: Pressure coefficients on longer spinners along the intersection of a 20° tilted longitudinal plane.

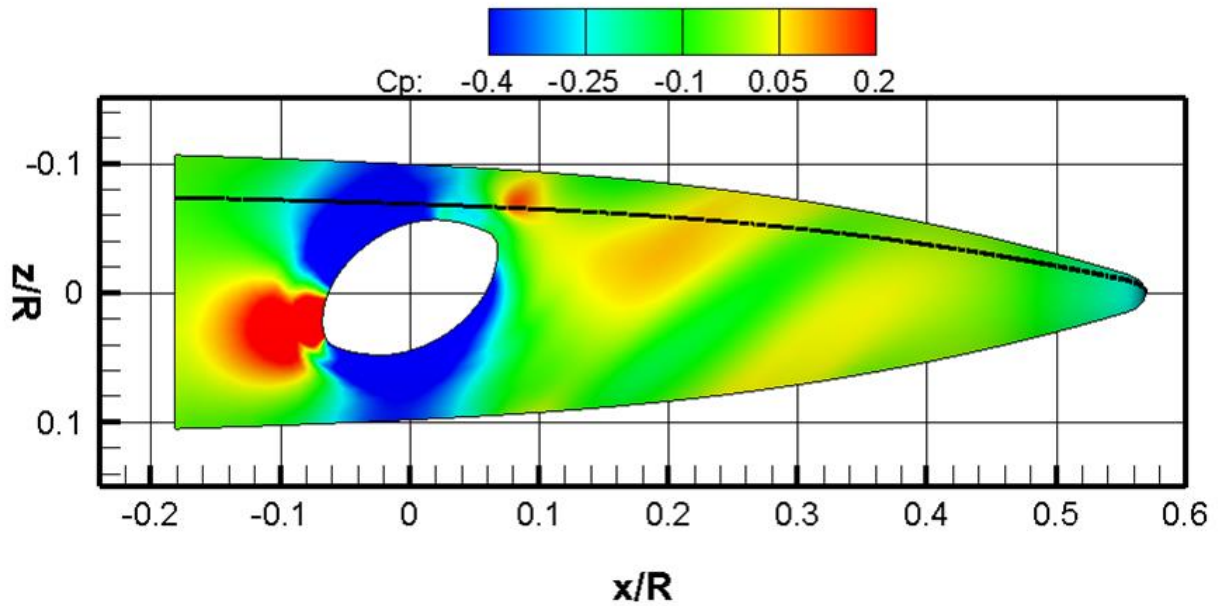


Figure 3.34: C_p contours on 30% longer spinner and 20° tilted sampling line.

Figure 3.34 depicts the C_p distribution of the 30% longer spinner and the line on which the sample of Figure 3.33 was taken. As the sampling line crosses both regions of attached and separated flow, the pressure distribution of Figure 3.33 varies accordingly. From left to right, the large negative values of C_p were mostly induced by the suction side of the blade root followed by an increment of static pressure due to the merging of both suction and pressure side flows. As the flow that is coming from the suction side separates, the one coming from the pressure side remains attached and expands immediately after it leaves the trailing edge (Fig. 3.35). Downstream ahead, the pressure coefficient alternates along the testing line between positive and negative pressure coefficients that belonged to the attached flow form pressure side and to the separated one from the suction part respectively.

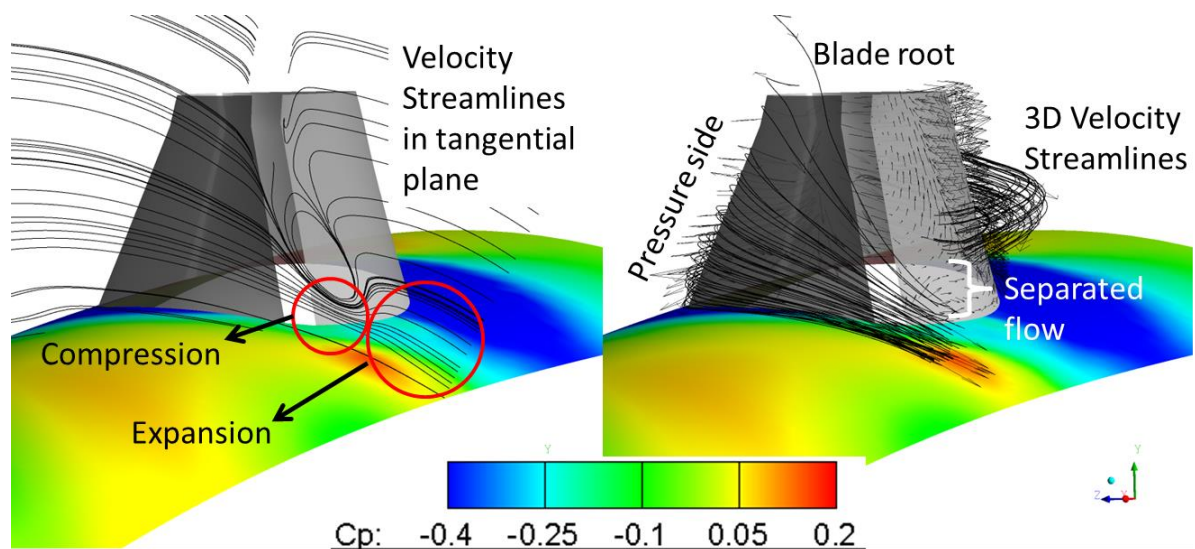


Figure 3.35: Velocity streamlines expansion close to the trailing edge on the 30% longer spinner.

Finally, at the end of the spinner, no traces of attached flow were found among the long spinners. However, around $0.42 x/R$ the 3 longest spinners (30%, 35% and 40% longer) did show larger pressure coefficients very likely related to the expansion of attached flow.

It is necessary to emphasize that the direction of the attached flow that eventually expanded was greatly determined by the blade root outflow angle. In other words, the downwash induced by the blade (Tangential velocity in the same direction of the rotation) depended on the particular blade loading at each of its radial positions. In the case of the root (Below $0.3 R$), the downwash was no longer inducing a positive tangential velocity but the opposite for both shorter and longer tests.

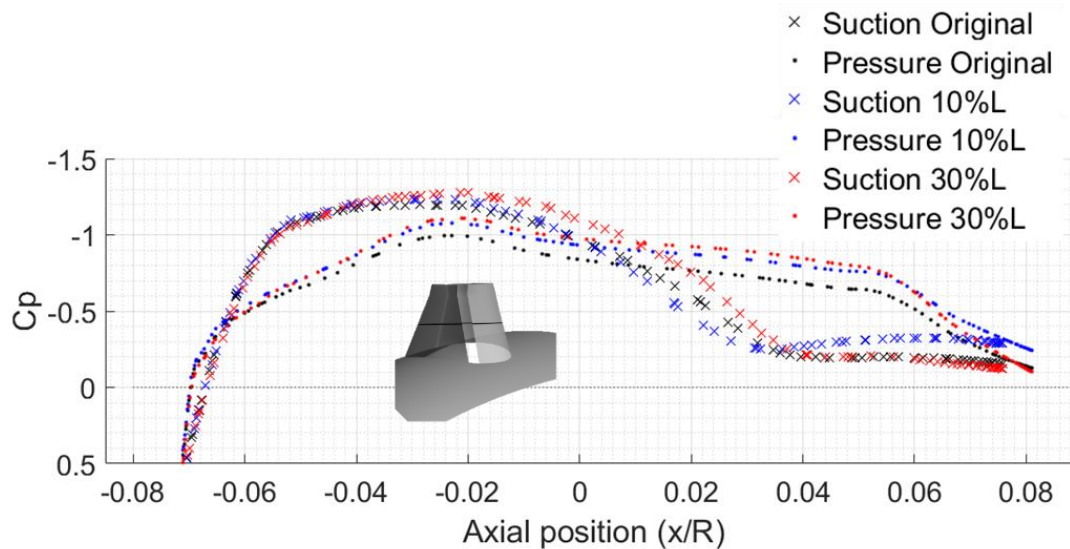


Figure 3.36: Pressure distribution of the blade root at 0.22 R (Original, 10% and 30% longer spinners shown).

By looking to the Figure 3.36 it is easily noticed that the pressure side loading at that particular radial position of the blade root was inverted. In fact, due to the apparent flow separation on the suction side, the three tests sustained lower C_p values on the pressure than in the suction side, especially towards the trailing edge. The relatively early flow separation observed on the suction side of the 10% longer spinner together with a lower C_p at the end of the pressure side contributes to the decrement in efficiency due to the reduction of blade root thrust. However, the axial component of the resultant force is the one that affects the entire propeller excess thrust.

The thrust contribution of the blade root at $0.22 R$ is shown in Figure 3.37. The thrust distribution showed similar values in the suction side, while the pressure side exhibited some differences among the spinners shown especially towards the trailing edge. Figure 3.38 shows the trailing edge at $0.22 R$ for the simulation that had a 30% longer spinner. The shear stress vectors in combination with the thrust distribution of Figure 3.37 indicated that either because of the expansion of the attached flow ($0.22 R$) or because of flow separation ($0.20 R$), the 30% longer spinner decreased the amount of negative thrust produced near the trailing edge in comparison to the 10% longer spinner, thus explaining the increment in the relative propeller efficiency when the simulation was made with a 30% longer spinner.

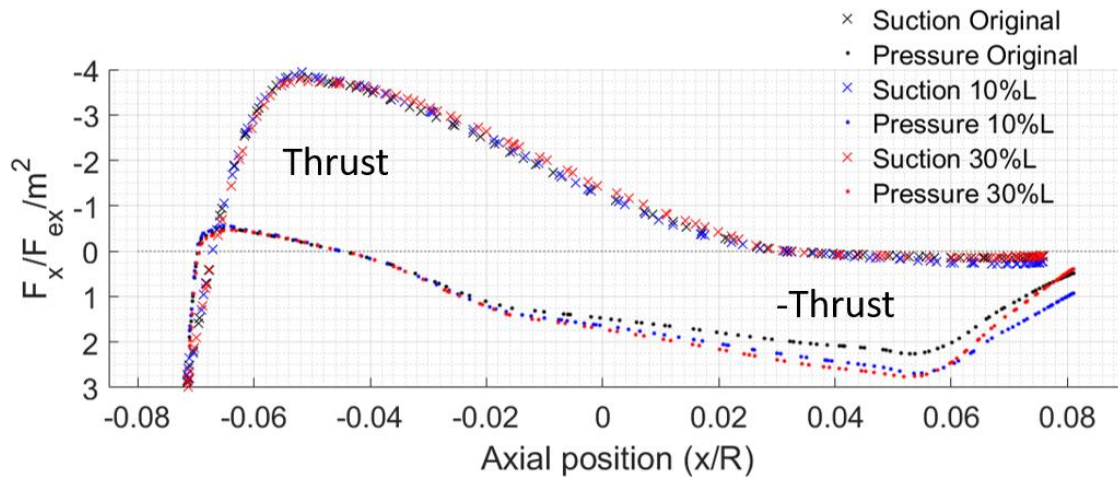


Figure 3.37: Thrust distribution of the blade root at 0.22 R for Original spinner, 10% longer spinner and 30% longer spinner.

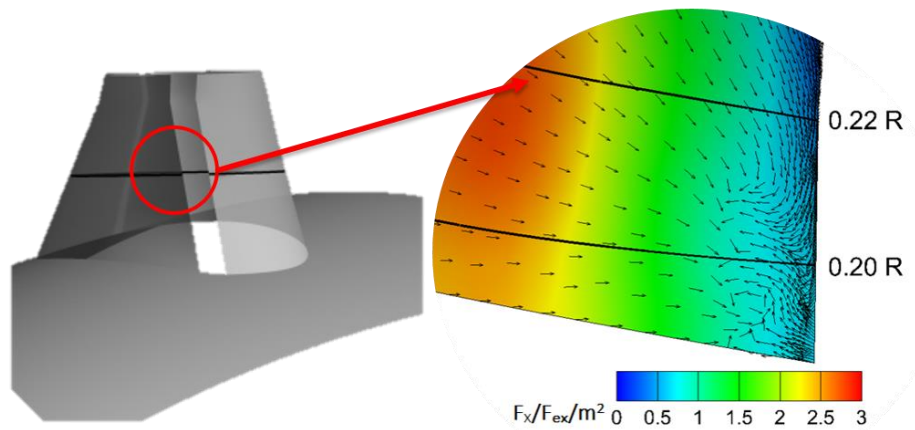


Figure 3.38: Shear stresses near the blade root trailing edge of pressure side for the 30% longer spinner.

The length modifications made on the spinner geometries indicated that the relative propeller efficiency was improved. Although the efficiency gain remained relatively small (+ 0.29% for the 30% longer), the propeller performance showed to be sensitive enough to very simple changes in the spinner geometry. The reduction of the hub vortex seemed to be a common factor in order to induce a gain in performance; however, the flow separation delay that was observed with longer spinners, not only decreased the magnitude of the hub vortex but also decreased the total drag of the spinner mostly due to larger pressure coefficients around the spinner (Larger pressure recovery).

Under the assumption that the flow separation could be delayed on the spinner, it was necessary to provide an idea of how was the actual shape of the spinner affecting the pressure recovery in order to continue decreasing the spinner total drag. Despite that the blade loading seemed to be a very important variable to take into account in order to improve the relative propeller efficiency though a different spinner design, the spinner axisymmetric shape was assessed for blade-off conditions that allowed to assess the effect of the spinner shape when the effect of the rotor was not taken into account.

4 Blade-off spinner assessment

The influence that the spinner design had on the propeller excess thrust had been assessed using 3D RANS CFD simulations and although the blade loading was one of the factors that determined the performance of the propeller, flow separation has shown to be the greatest contributor to the relative propeller efficiency variations. At the same time the 3D propeller simulations have shown that the boundary layer separation interacted with the vortical structures formation changing the components of both pressure and viscous drag. In general, it has been observed that spinners with higher fineness ratio (FR_{spinner}) delayed flow separation which resulted in better pressure recovery and thus less pressure drag. So, in order to expand the assessment of the nacelle-spinner configuration and its relation with the boundary layer separation, a series of 2D RANS CFD simulations for an axisymmetric flow reference frame were carried out due to the simplicity of the axisymmetric nacelle-spinner modelling. The blade effect was ignored in order to isolate the axisymmetric body contribution from the rotor one so a low drag spinner design could potentially be tested later as a mean to improve the propeller efficiency.

4.1 The boat tail effect

The blade-off effect was simulated in both 3D and 2D configurations, showing a strong agreement on the pressure distribution along the nacelle-spinner, except for the rear section where the pressure distribution shows discrepancy at the region that exhibited flow separation (Figure 4.1).

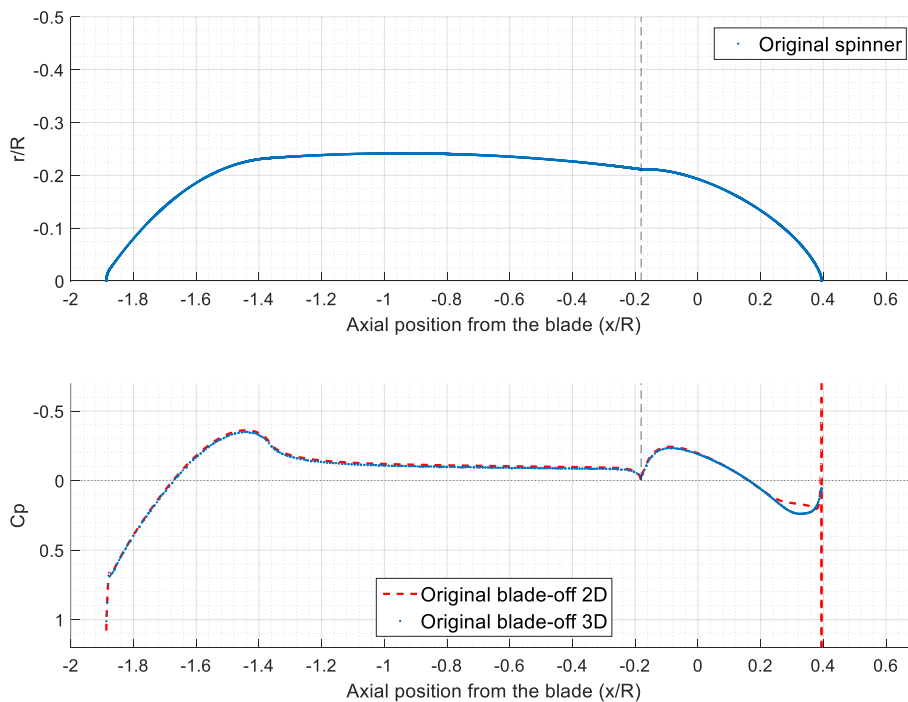


Figure 4.1: Original spinner pressure distribution among 3D and 2D simulations without the blade effect.

The inflation, the turbulence model and the minimum element size of the mesh was kept the same on the 2D and 3D simulations; nevertheless, the agreement decreased at the highly separated region. Even when there was a small discrepancy among the 2D and the 3D results the study was carried out taking into account that any drag improvement would most likely be achieved by delaying separation before and not after the blade.

The axisymmetric body drag has been studied before in numerous cases and for different flow conditions so the separation can be avoided and thus the drag can be minimized for a certain design regime. One of the main resources used in order to decrease the drag is the boat tail shape that typically increases the pressure at the end of the axisymmetric body especially when the boundary layer remains attached until the edge of the body. As shown by Reubush [36], the Reynolds number (Based on length) of the axisymmetric body had not significant effect on the pressure distribution of the boat tail section even when it was varied from 6.9 to 43.2 million; in fact, the typical pressure distribution of a boat tailed body looked very similar to the one encountered on the original nacelle-spinner configuration of the propeller used for this research. The pressure coefficients on the original blade-off configuration decreased at the fore section and then it keeps an almost constant negative value throughout the nacelle until it decreases again when the spinner section is reached just like the pressure distribution when it reaches the edge of the boat tail section [36]. As encountered on the original configuration and best efficiency spinners found so far, the last part of the pressure distribution has shown to have positive pressure coefficients which counterbalance the enlarged negative ones that a boat tail shape produces right after the flow encounters the spinner/boat tail section.

As shown before, avoiding separation improved the pressure recovery because of the larger positive pressure coefficients; nevertheless, even when the spinner redesign did not modify the magnitude of the pressure distribution in a significant way, the thrust could still be improved if the pressure recovery reaches its maximum value over a highly steep portion of the spinner where the axial force component is larger.

The optimal shape for minimum drag of a revolution body has been found in several studies. An optimized revolution body has most of the time a large portion of natural laminar boundary layer (NLF) [11]. This moved the transition point downstream ahead which facilitated the flow expansion on the aft-body decreasing the drag. Since the 2D spinner study carried out in this thesis was restricted to make changes only on the spinner section and only for cruise conditions, the tendency of the optimized axisymmetric bodies of having narrow ends was constantly observed. Reynolds number is one of the most influential parameters on the optimal drag shape of an axisymmetric body [37]. Several authors concur on a defined trend for the optimal drag shape at around the same range of Reynolds number but also coincide on certain aspects of the pressure distribution encountered on those optimized bodies [38] [37] [39]. The pressure distribution of many drag optimized axisymmetric bodies for similar fineness ratio (FR_{body}) and similar Reynolds number depicted a small favorable pressure gradient along most of the body because the maximum thickness is located at around 0.75% of the length. The minimum C_p was mostly located a bit after the leading edge in order to decrease the initial diameter so the turbulent skin friction could act over a smaller wetted area, thus reducing the viscous drag [37].

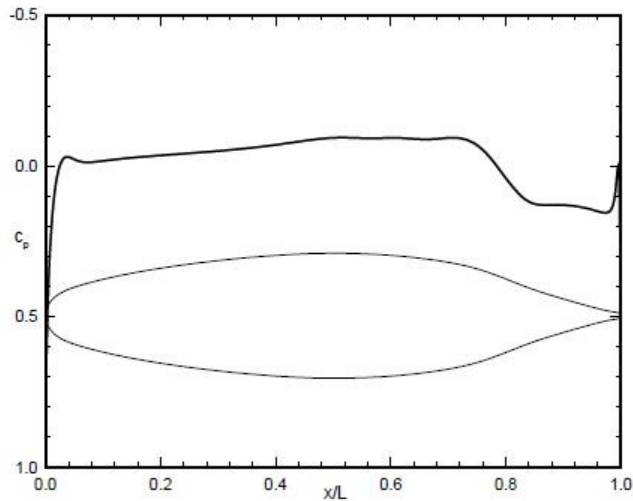


Figure 4.2: Optimized pressure distribution for an axisymmetric body at $Re_v = [1e6... 3.16e6]$ and fineness ratio $FR_{body} \approx 4.5$ [37].

Figure 4.2 depicts an optimized pressure distribution for a similar axisymmetric body under similar conditions as the ones of the original nacelle-spinner configuration $FR_{body} = 4.7$ and a volumetric Reynolds number of 2.7 million. If the body shape of the Figure 4.2 is compared to the one of the original nacelle-spinner configuration it is noted that the maximum thickness is not located around 0.75% of the body length as shown by Dodbele [38], Lutz [37] or Parsons [39] but at around 50% of the body, additionally thickness of the forebody is similar to the one of the maximum thickness for the original case, meaning that the strongest favorable pressure gradient was not encountered at 75% or 50% of the body length but more upstream at around 20%. The difference can be noticed on the pressure distribution of the original configuration where the minimum C_p is found at the beginning and not at the region where the body starts to decrease its thickness in order to induce a moderate adverse pressure gradient over most of the length. In a similar way as the optimal configuration, the original pressure distribution presented a second peak of negative C_p downstream ahead where the thickness started to decrease; nevertheless, the negative peak was not as strong as the one encountered upstream contrary to the results obtained for the optimized bodies.

Figure 4.3 depicts the pressure distribution of the original nacelle-spinner configuration with and without the effect of the rotor. The pressure distribution did not change greatly along the nacelle although the pressure seems to be slightly lower most likely due to the induced acceleration of the rotor disk. The main change of the pressure distribution is located after the blade, at the spinner section. The C_p value at around $-0.1 x/R$ is similar to the strength of the minimum C_p due to the low pressure region created by the root suction side. Right after the negative pressure peak the pressure increases and keeps a more constant value that remained negative most likely indicating flow separation.

When the blade effect was taking into account, the earlier flow separation avoided a better pressure recovery, so no positive values of C_p were observed as suggested by their corresponding blade-off configurations; however, due to the simplicity of the 2D simulations for axisymmetric bodies with no blade effect, several simulations were carried out following the similar shapes found on optimized bodies. A blade-off design with a relatively low drag can be used as a potential baseline in order to redesign a low drag spinner that takes into account the effect of the rotor.

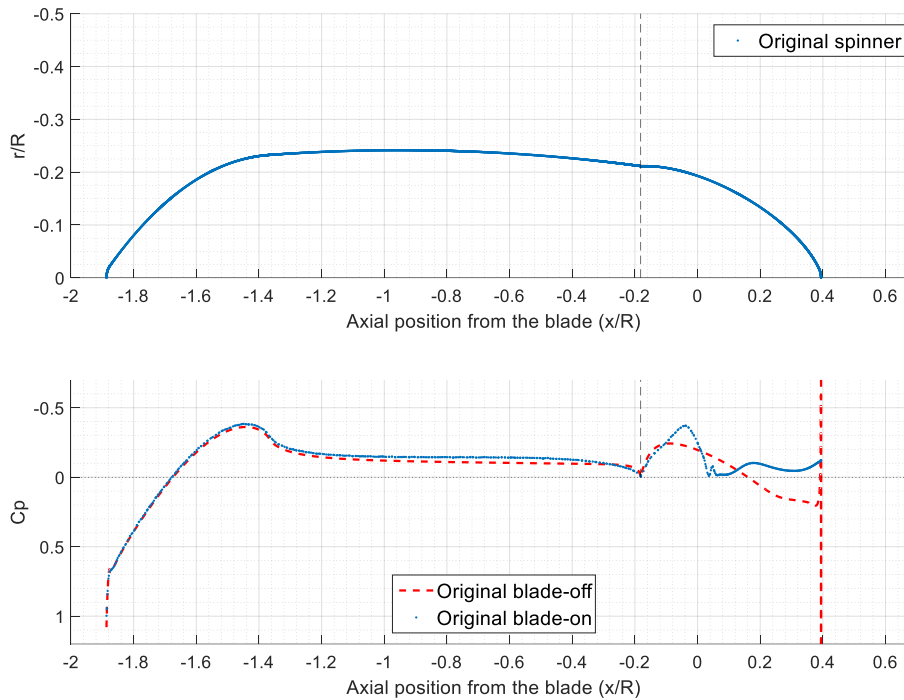


Figure 4.3: Blade-on and blade-off pressure distribution for original spinner. (The blade-on pressure distribution has been sampled at 20° from the blade opposite to the direction of rotation)

4.2 Blade-off spinner design

As seen before, the axisymmetric bodies that were optimized for minimum drag for similar Reynolds number regimes, showed a relatively flat pressure distribution unlike the original design. So the first three changes on the spinner geometry were related to the reduction of the initial spinner diameter so a flatter pressure distribution could be achieved. The spinner geometries were connected to the nacelle by a convex section that eventually became concave downstream ahead.

Figure 4.4 shows three design cases with larger spinner diameters than the original one. Nevertheless, a small diameter reduction has been made at each one of the tests (Denoted by the letter *b*) in order to observe the influence that the maximum spinner thickness had on the spinner drag. Even with a small diameter reduction made before the inflection point, the spinner drag of the *b* tests decreased according to the blade-off simulations results. The first variation (t1b) had a slightly larger diameter after the inflection point while second and third, t2b and t3b respectively, had shorter diameters after the inflection point, close to the spinner end. All three variations have a spinner length that is 35% larger than the one of the original design.

The viscous component of the spinner drag did not seem to change as much as the pressure component. Even when both presented the same order of magnitude, the pressure component varied considerably more after the diameter reduction. This might suggest that there is no separation acting on the axisymmetric body. The blade-off effect was tested on other spinner designs as well. Figure 4.5 portrays the entire group of the spinners tested. The spinner geometrical modifications were mainly focused on the increment or decrement of the convex or concave depth as well as length modification aiming for a spinner drag reduction. Every design was modified in order to reduce its predecessor drag in a trial and error approach.

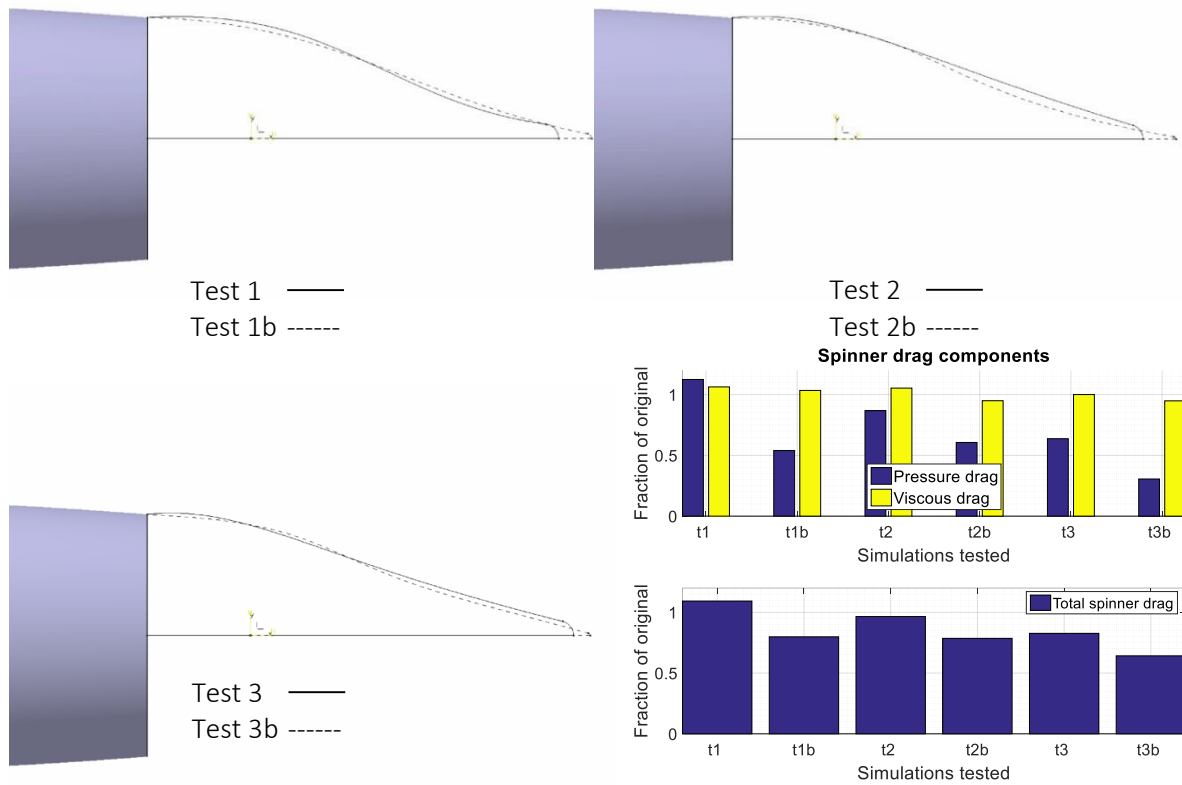


Figure 4.4: Sketches of the modifications of Test 1, Test 2 and Test 3 with their Blade-off spinner drag components.

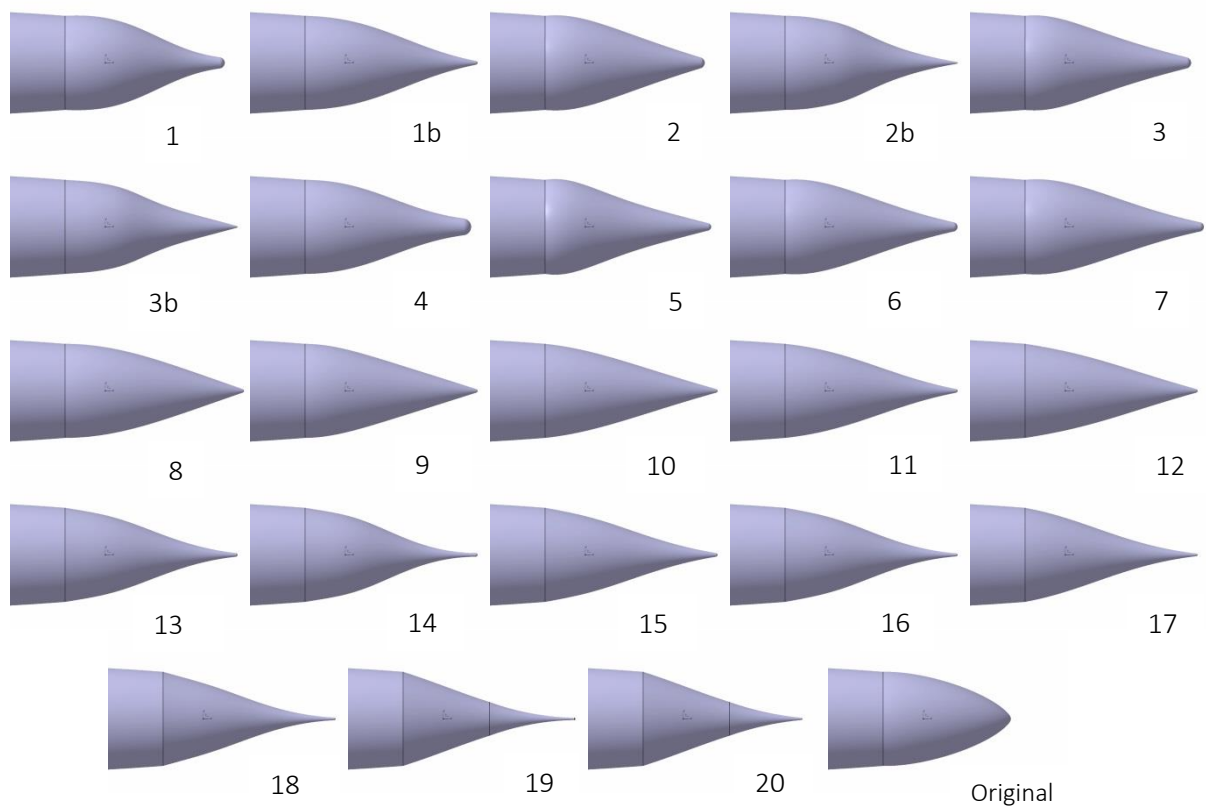


Figure 4.5: Blade-off tested spinner designs layout.

Figure 4.7 shows the drag variations at every nacelle-spinner configuration which decreased in a more noticeable way after the test 9. The blade-off spinner drag reduction was particularly noticeable when the maximum diameter of the spinner was equal or lower than the one at the start of the spinner or in other words, when the spinner did not induce an adverse pressure gradient in the transition from nacelle to spinner.

Some of the designs that were similar to the ones shown on the second half of Figure 4.5 have been used not only in pusher propeller configurations of relatively new Electrical Regional Aircraft companies such as Eviation and Joby Aviation, but also in the Business Jets and UAV's markets by companies like Piaggio Aero [13]; in fact, the second half of spinners showed a similar shape to the one of one of the Piaggio spinner design (Fig. 4.6). A similar spinner fineness ratio was also observed among the spinner designed by Piaggio and the test 2 and 3 with values of 1.4, 1.37 and 1.45 respectively.

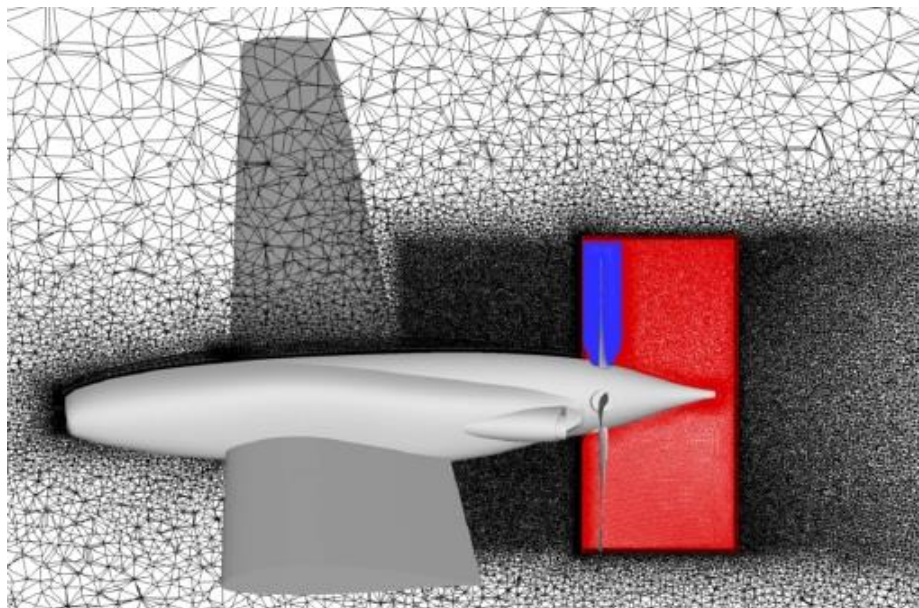


Figure 4.6: Piaggio pusher propeller spinner; Lateral view of the mesh used by Yin & Stuermer [13].

Figure 4.7 shows the axisymmetric body drag with different spinners, including the blade-off results of the 30% longer spinner that previously improved the relative propeller efficiency by 0.29%. The viscous drag obtained for the test group represented on average 80% of the drag of the entire body (Nacelle + Spinner). The 30% longer spinner showed the largest viscous drag while test 19 and 20 presented the lowest one; nonetheless, pressure exhibited larger changes like the one observed at test 10, where the pressure drag accounted for only 50% of the original axisymmetric body one.

The last tests showed the lowest drag of the blade-off simulations accounting for a maximum total drag reduction of around 22% of the original axisymmetric body (Nacelle + Spinner).

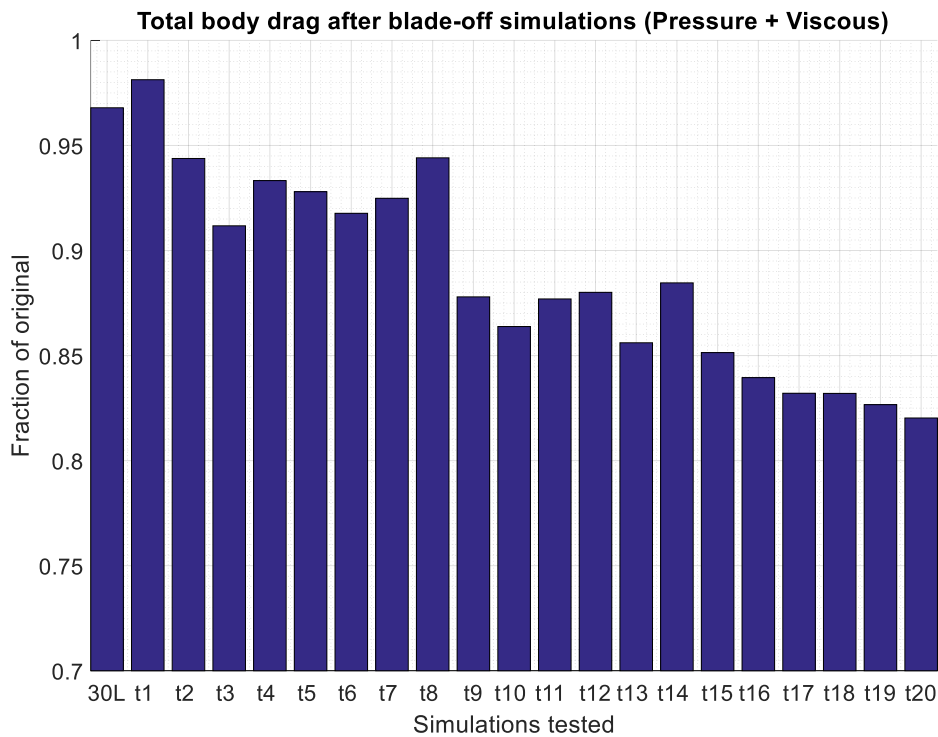
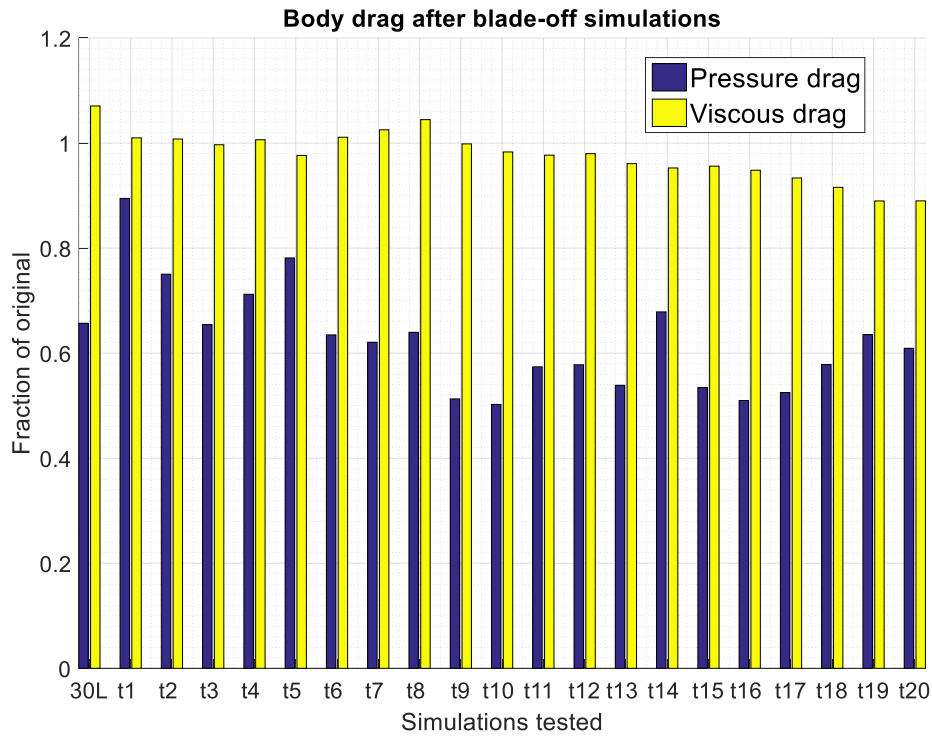


Figure 4.7: Total drag of the Blade-off axisymmetric bodies with different spinner designs.

4.3 Blade-off flow separation assessment

As the spinner thickness was decreased, the axisymmetric body drag was reduced. In a similar way as for blade-on cases, the largest drag reduction came from the spinner pressure component that not only got decreased, but it changed its sign acting as thrust instead of drag from test 10 onwards (Fig. 4.8).

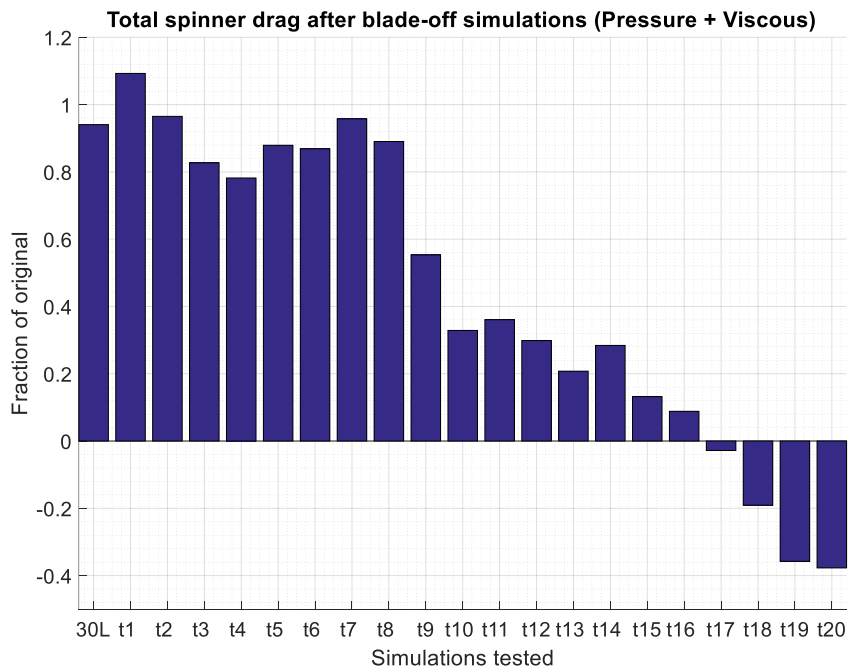
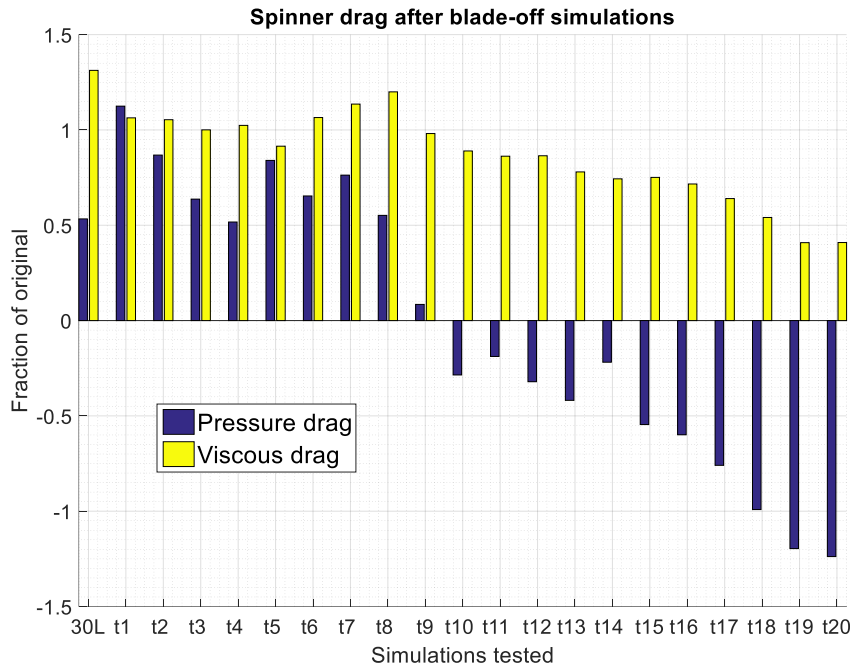


Figure 4.8: Total drag of the Blade-off spinners group.

Even when the pressure drag of the spinner changed its sign since test 10, the total drag of the spinner remained positive up to the test 17 where the negative axial force due to pressure became larger than the viscous positive one. On the other hand, the viscous drag changed in a less severe way. Figure 4.8 shows that viscous drag got especially reduced after test 9. The viscous drag reduction was clearly related to the lower velocities of flow expansion and not to flow separation because of the pressure recovery was improved.

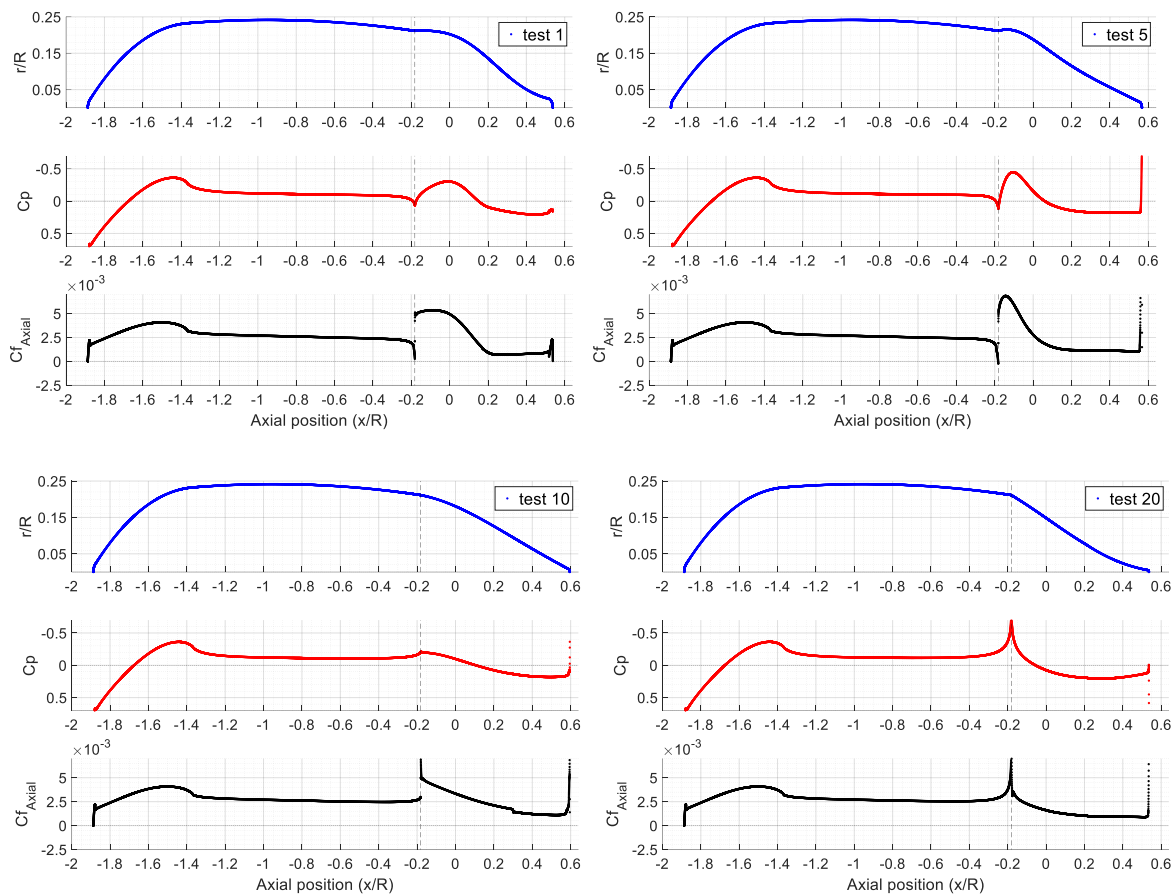


Figure 4.9: Pressure and shear stress distributions of tests 1, 5, 10 and 20.

Test 1 and 5 showed large negative pressure coefficients due to the larger diameter observed at around $-0.1 x/R$ (Fig. 4.9); nonetheless, the velocity contours of Figure 4.10 showed that only test 1 presented negative values of axial velocities along the spinner wall. The spinner maximum diameter of test 1 clearly larger than the one at the nacelle-spinner transition. This caused the flow to encounter a steeper adverse pressure gradient at the moment that flow expanded further downstream. As a result, lower axial velocities were encountered and possibly earlier flow separation, indicated by the sudden drop of shear stresses on the spinner with eventual reverse flow after $0.2 x/R$ (Fig. 4.9 and 4.10).

On the other hand the pressure distribution of the narrowest spinners showed a large negative pressure coefficient right at the beginning of the spinner; however, the suction peak on the pressure distribution was formed by the localized acceleration of the flow outside the boundary layer due to the convex curvature of the streamlines, similar to the effect seen on boat tailed bodies [40], [41]. This was accentuated by the relatively low radius of curvature of the rear edge of the nacelle that has been observed before on similar boat tailed bodies [42]. Despite that the negative C_p spiking value of test 20 was even larger than any other case, the pressure distribution showed positive values of C_p more upstream than any of the other cases. This explains the significant spinner drag reduction as a result of the pressure recovery due to the deceleration of the flow and that sustained negative C_p values such as the ones observed for the test 1 increased the total drag of the nacelle-spinner configuration even when there were no clear signs of flow separation.

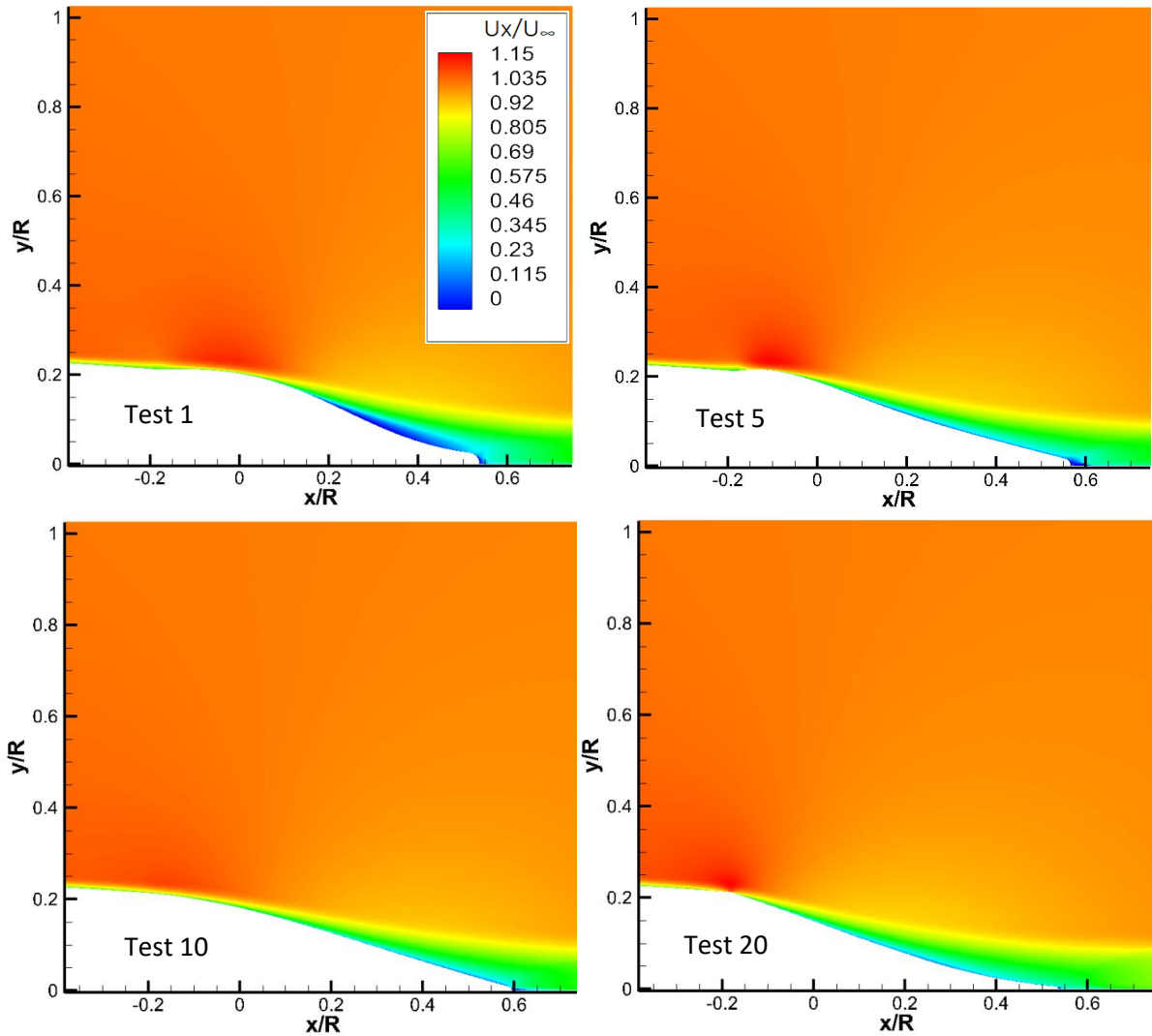


Figure 4.10: Axial velocity contours on spinner section.

Out of the 20 designs only the last 4 presented negative pressure drag that acted as thrust on the spinner. Although the test 20 induced the lowest total drag on the entire axisymmetric body, the lowest pressure drag was found at test 10 (Fig. 4.7). This is because the pressure drag of the nacelle was decreased in test 10 mostly due to its flatter pressure distribution. The maximum thickness of the body is located at the nacelle, relatively far from the spinner compared to the optimized bodies found in literature, so the gradual diameter reduction of the nacelle induces a convex curvature that causes the boundary layer to get thicker because of the adverse pressure gradient but more important, that transforms the suction created at the nacelle-spinner transition ($-0.2 x/R$) into direct nacelle pressure drag. This leads to an increment in nacelle drag every time that the spinner drag is decreased (Fig. 4.11) even when the overall axisymmetric body drag was still reduced.

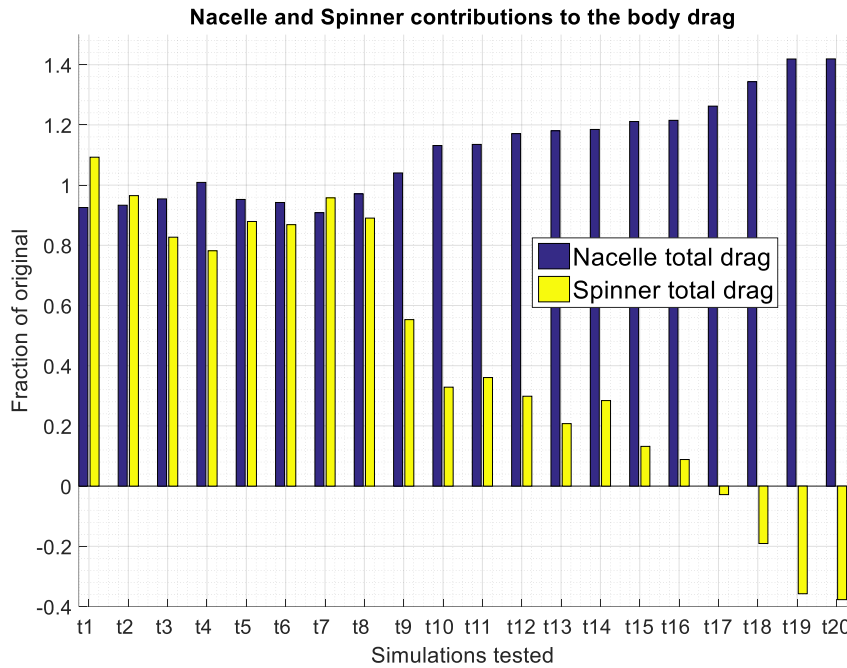


Figure 4.11: Nacelle and Spinner contributions for the blade-off axisymmetric body drag.

In order to know the effect of the low drag axisymmetric body on the propeller performance, the last spinner design with the reduction of 18% of the nacelle-spinner drag should be assessed in blade-on conditions. However, design that induced the largest reduction in total drag (Test 20) would have required the blade to be moved from the original position because it would have exposed the entire blade root. In order to carry on with the blade-on simulation, the test 16 was selected instead because it induced a drag reduction of 16% while keeping a blade exposure that fell into the defined boundaries (Fig. 4.12). It is important to recall that both the blade and the nacelle design parameters were kept constant.

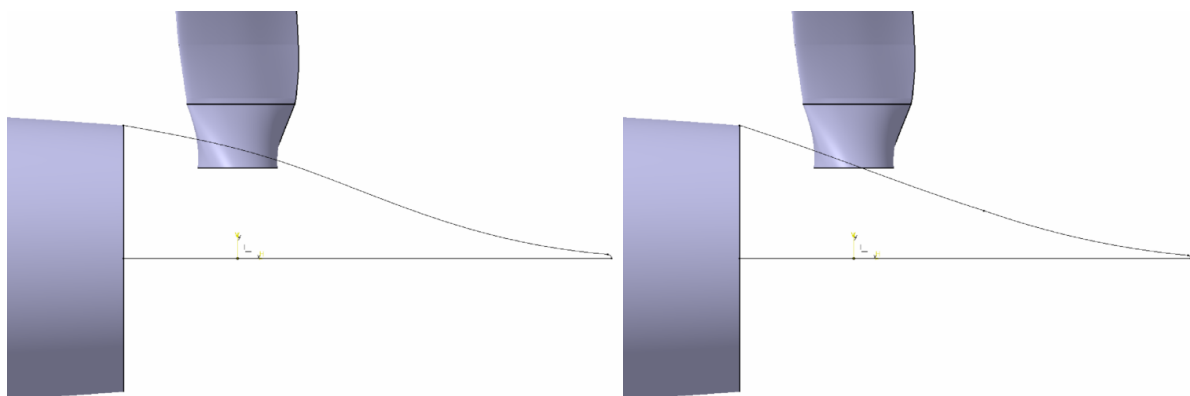


Figure 4.12: Spinner sketch of blade exposure for test 16 (Left) and test 20(Right).

The pressure distribution for test 16 was similar to the one observed at the test 20 in the sense that both presented a large suction peak before the flow started to expand (Fig. 4.10 & Fig 4.13). However, in order to perform a 3D simulation that takes into account the effect of the blade, test 16 was selected. The spinner design that corresponded to the test 16, exhibited positive values of C_p close to the spinner with no evidence of early separation. These characteristics will be evaluated in the next chapter with blade-on 3D simulations just as the simulations performed on shorter and longer spinners.

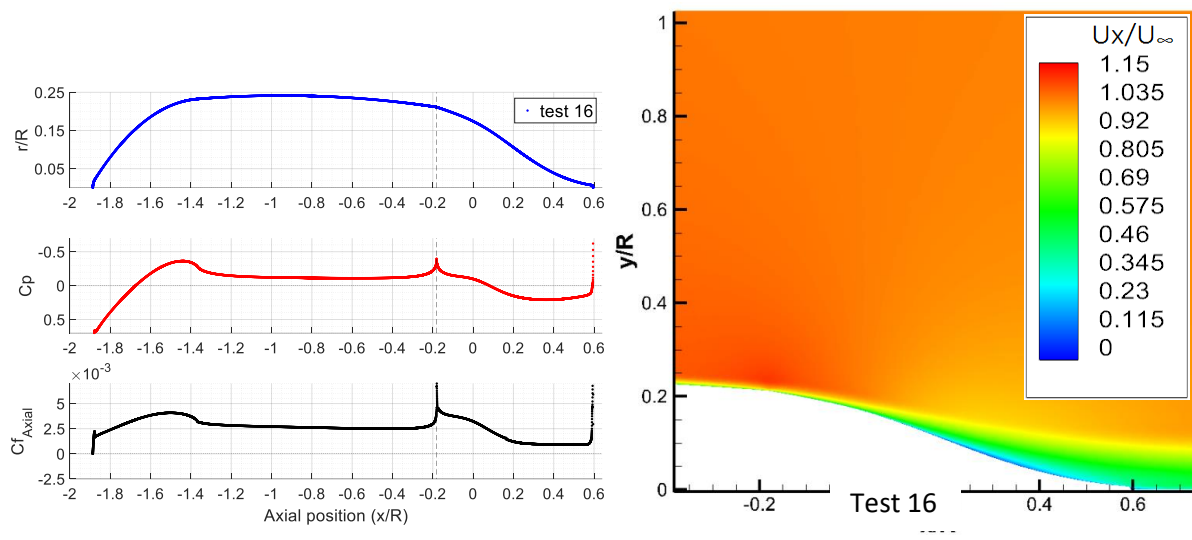


Figure 4.13: Blade-off test 16 pressure distribution and spinner axial velocity contours.

5 Spinner re-design

In order to enhance the efficiency of the propeller through a new spinner design, the following considerations have to be made. The influence of a low drag axisymmetric body is expected to be reflected in the overall propeller performance. Spinner modifications in length and height had direct impact on the blade root loading and thus on the torque and thrust of the rotor. The maximum performance improvement was achieved by spinner designs that delayed flow separation on the spinner, mostly related to designs with high fineness ratios.

5.1 Low drag axisymmetric body effect on propeller efficiency

In general, the nacelle-spinner body drag was reduced by narrow spinner designs with high aspect ratios that kept their maximum diameter at the nacelle-spinner transition and below an imaginary nacelle extension line. It was determined throughout a blade-off series of simulations that the 16th spinner design that reduced the original nacelle-spinner body about 16% would be a starting point for a redesign; nevertheless, the axisymmetric drag represents less than 2.5% of propeller excess thrust (F_{ex}) for the original configuration. The same CFD setup for shorter and longer spinners was used in order to carry on the blade-on simulations. The mesh parameters and the turbulence model were kept the same so the results could be compared. The low drag body effect was immediately observed since the relative propeller efficiency improved 0.56% from the original design which turned out to be the maximum increment out of all the spinner designs.

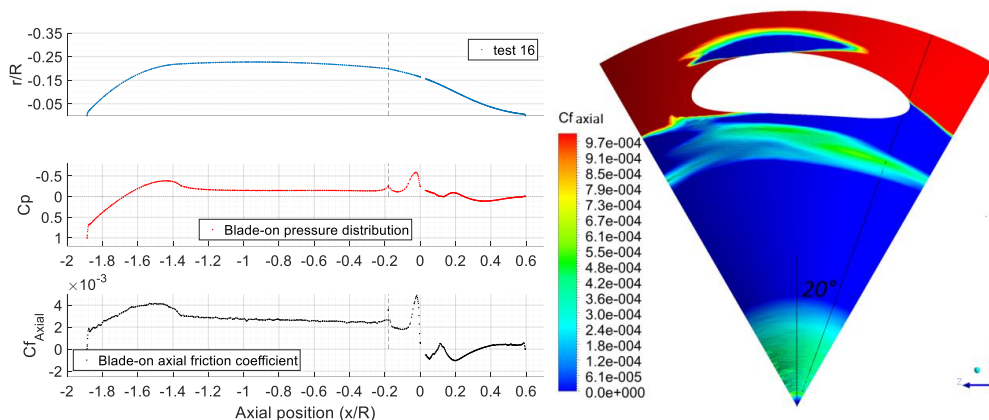


Figure 5.1: Blade-on pressure distribution and axial friction coefficients for test 16 spinner. (Sample taken at 20° of spinner; only positive contours of axial friction coefficients are shown)

The pressure distribution of the test 16 (Fig 5.1) was only similar to its corresponding blade-off one along the nacelle section. After the dotted line which indicates the nacelle-spinner transition, the Cp distribution dropped at around -0.2 x/R in a similar way as without the blade effect; nevertheless, a stronger pressure coefficient drop could be observed right before 0 x/R that corresponded to the low pressure region induced by the blade root suction side. Unlike the blade-off simulation, the rotor produced a sudden drop of the axial shear stresses indicating separation at around 0 x/R. This axial location corresponds to the formation of the separation vortex shown in other spinner designs before. Although there was early flow separation on the suction side of the test 16, there was still favorable pressure recovery further downstream indicating flow reattachment. The Cp distribution observed along test 16 reached its maximum value when the axial shear stresses began to increase at the spinner

end (Fig. 5.1). This increment of axial friction coefficient indicated that most of the flow reattached was coming from the root pressure side of previous blades (Fig. 5.2). Similar to the way that flow separation started on shorter spinners, the highly loaded pressure side of the blade root changed the outflow angle at the trailing edge contributing to the flow separation even when the test 16 seemed to delay flow separation under blade-off conditions.

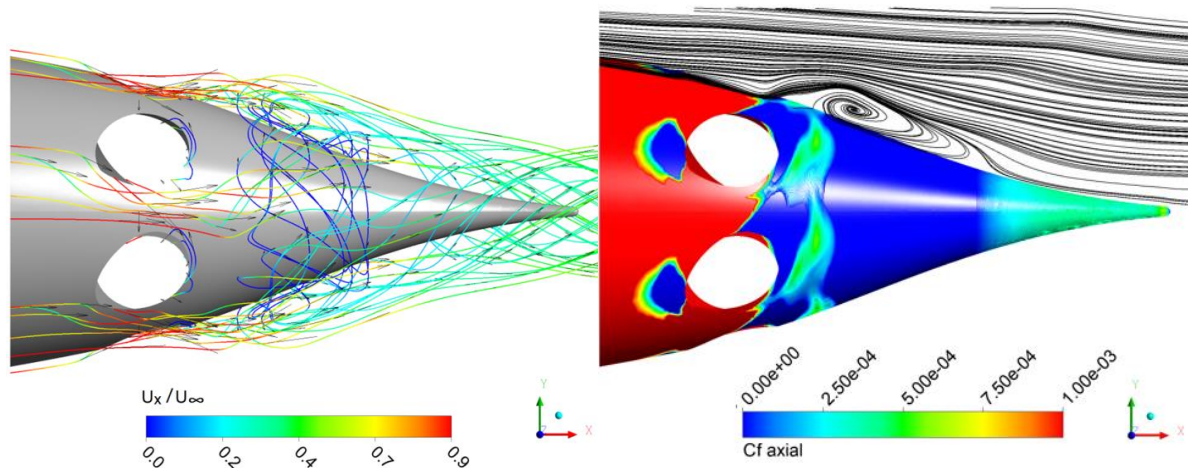


Figure 5.2: Test 16 stationary frame velocity streamlines and axial friction coefficients contours.

Since flow separation was observed on test 16 as well, it could be said that the gain in efficiency and excess thrust depended mostly on the pressure recovery rather than on the flow separation delay. However, the second best efficiency improvement (0.29%) was achieved by the 30% longer spinner that increased the pressure recovery mostly because of the reduction of separation at the same time that kept a similar torque than the one for the original spinner design.

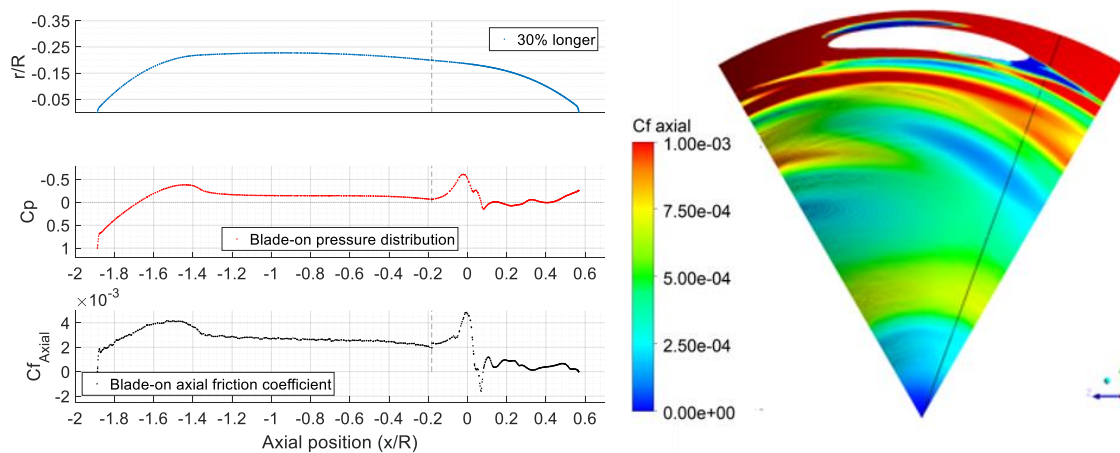


Figure 5.3: Blade-on pressure distribution and axial friction coefficients for 30% longer design. (Sample taken at 20° of spinner; only positive contours of axial friction coefficients are shown)

When the Cp distribution is compared it is possible to see that the one belonging to the 30% longer spinner was not as good as the one for the test 16 in the sense that few portions of the spinner presented positive Cp values. The result was a lower spinner drag for the test 16 despite presenting early flow separation and a defined recirculation bubble.

Table 5.1: Performance comparison among the two most efficient designs

Parameter for comparison	30% longer compared to the original	Test 16 compared to the original
Relative propeller efficiency	100.29%	100.56%
Torque	99.97%	100.36%
Relative Excess thrust (Thrust-Drag)	100.27%	100.93%
Nacelle drag	103.90%	123.58%
Spinner drag	64.05%	48.89%

Table 5.1 presents the main propeller performance indicators for the 2 designs cases with the largest efficiency improvements compared to the original baseline design. In total, the relative propeller efficiency has been improved by test 16 0.56% even when the spinner drag was reduced more than 50%. Despite the spinner drag reduction induced by test 16, the nacelle drag was enlarged by 23.58% as explained below.

Given that the improvements in performance did not exceed 1%, the reduction of nacelle drag and propeller torque had to be considered as important as the spinner drag reduction. The propeller torque has shown a direct dependence on the blade exposure. This means that the spinner should not expose the blade root in order to prevent the torque from increasing, even when the increment of torque is very low. On the other hand, the increased diameter of the spinners with the fewer blade exposures induced strong adverse pressure gradients at the nacelle-spinner transition causing the nacelle drag to increase. The increment of nacelle drag was observed as a detrimental effect; however, in the 30% longer spinner, the increment of nacelle drag was only 3.9% compared to the 23.6% obtained for the test 16.

The cause of the low nacelle drag of the 30% longer spinner design was the absence of a strong suction peak at the nacelle-spinner intersection, contrary to the ones observed for most of the blade-off simulations with large spinner diameters. It can be said that besides the relatively lower spinner drag, the 30% longer spinner improved efficiency mainly due to the reduction of torque and to the reduction of the nacelle drag at an acceptable flow expansion, while the test 16 improved efficiency mainly due to a significantly better flow expansion that decreased the spinner drag considerably. As a result, the flow expansion has been observed to be the most influential parameter in order to improve the efficiency of the pusher propeller when only the spinner is redesigned.

Taking into account these considerations, a potentially better spinner design would be such that the portion of the spinner that is located prior to the blade acts as a tangential extension of the nacelle in order to suppress the suction peak created by any local flow acceleration produced by a curvature different from the one of the last portion of the nacelle. In this way, the blade exposure could be fixed in order to have a constant low value of torque. In addition, the portion of the spinner over which the flow expansion has been observed would maintain certain resemblance with the test 16 or with the Piaggio's convex-concave designs as a means of achieving a proper pressure recovery.

Figure 5.4 depicts the pressure distribution of the first tangential spinner geometry that was designed as an extension of the nacelle and that follows a straight line tangent to the last portion of the nacelle. The inclination respect to a horizontal reference that resulted from a tangent line to the last portion of the nacelle was 4.51°. The pressure distribution seemed to be more constant at the nacelle-spinner transition (Dotted line) until the section where the spinner reduced its diameter in order to induce flow expansion, similar to the pressure distributions encountered in optimized axisymmetric bodies. No suction peak was observed at the nacelle-spinner transition, suggesting a relatively low nacelle drag. The pressure distribution of figure 5.4 showed positive values for the axial friction coefficients

encountered along most of the tangent spinner indicating the presence of attached flow over most of the spinner surface; however, the pressure recovery was not large enough to reduce the spinner drag as much as the test 16. While test 16 reduced the spinner drag to only 49% of the original one, the tangent design exhibited a spinner drag of 59% of the original one.

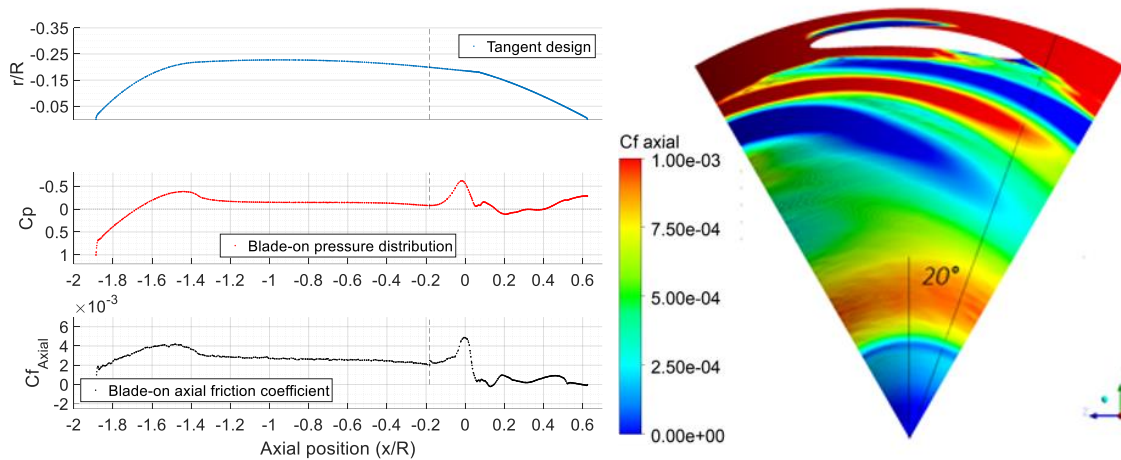


Figure 5.4: Pressure and axial shear stress distribution for the tangent spinner design. (Sample taken at 20° of spinner; only positive contours of axial friction coefficients are shown)

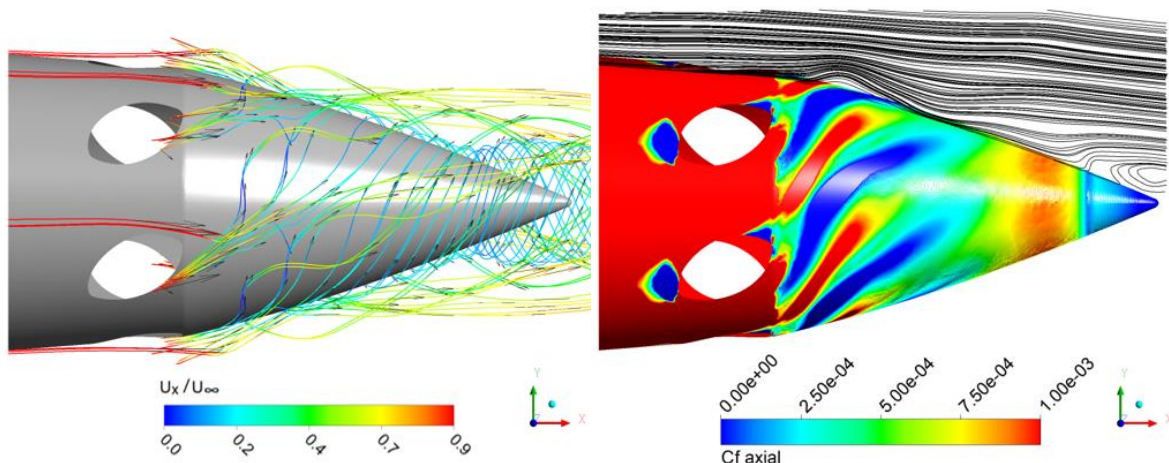


Figure 5.5: Stationary frame velocity streamlines (3D left and 2D right) and axial friction coefficient contours of Tangent design (T1).

The direction of the slipstream corresponding to the part of the flow that was still attached to the spinner was clearly dependent on the blade root loading, not only on the tangent design but also on longer spinners that delayed the flow separation. This dependency can be observed on the contours of axial shear stresses of Figure 5.5 where the red stripes located downstream ahead the blade root indicated the parts of the spinner where the velocity field was formed by both suction and pressure outflows. The positive values of axial shear stresses were mostly induced by the suction side outflow since the direction of the pressure one was mainly tangential. Similar to the test with long spinners, the tangent design maintained attached flow along most of the lower part of the root pressure side. This resulted in the large negative tangential velocity component that not only helped to the formation of the separation vortex but also induced a negative tangential velocity component on the suction side outflow. The induced direction affected directly the pressure recovery mostly because the flow that was still attached traveled a longer distance on the spinner at a relatively lower pressure gradient, especially when compared to the pressure gradient that flow would have encountered along a more axial trajectory. The larger component of axial velocity was reflected in the red elongated contours of axial shear stress of Figure 5.5 and this was the reason why those presented the largest values of C_p .

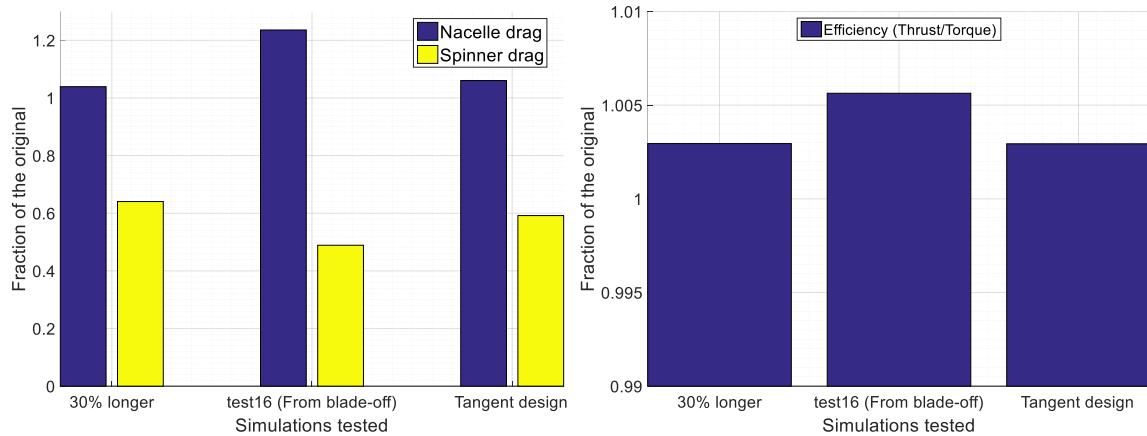


Figure 5.6: Nacelle-Spinner drag contributions and relative propeller efficiency for the tangent spinner design compared to previous spinners.

The tangent spinner design that acted as a nacelle extension reduced the nacelle drag (Fig. 5.6) when compared to the test 16. However, the spinner drag was not as reduced as it was for the test 16 or for the 30% longer spinner. This resulted in a 0.29% relative propeller efficiency improvement, same as the 30% longer spinner. By looking to the efficiency, it seems that the nacelle drag reduction had no effect whatsoever on the propeller performance. Nevertheless, the efficiency of the tangent design might have been affected by the low pressure region of the hub vortex, especially because the spinner had a larger diameter than the one of test 16, meaning that higher velocities were acting closer to the spinner wall increasing the influence of vortical structures. The detrimental effect of the hub vortex was already observed at other tests; nevertheless, it showed that it can be countered with a narrower spinner that enlarge the pressure raise due to flow expansion and at the same time would reduce the vortex formation.

5.2 Nacelle-Spinner tangency as a propeller efficiency enhancer

Even when the tangent spinner design presented the second best efficiency improvement and decreased the nacelle drag, the part of the spinner where the flow expands still needed to be modified so the pressure recovery was increased. A group of spinners that extend the nacelle (Tangent) were tested under the same conditions of the original propeller configuration. The spinners were identified with a capital letter T standing for tangent followed by the number of simulation.

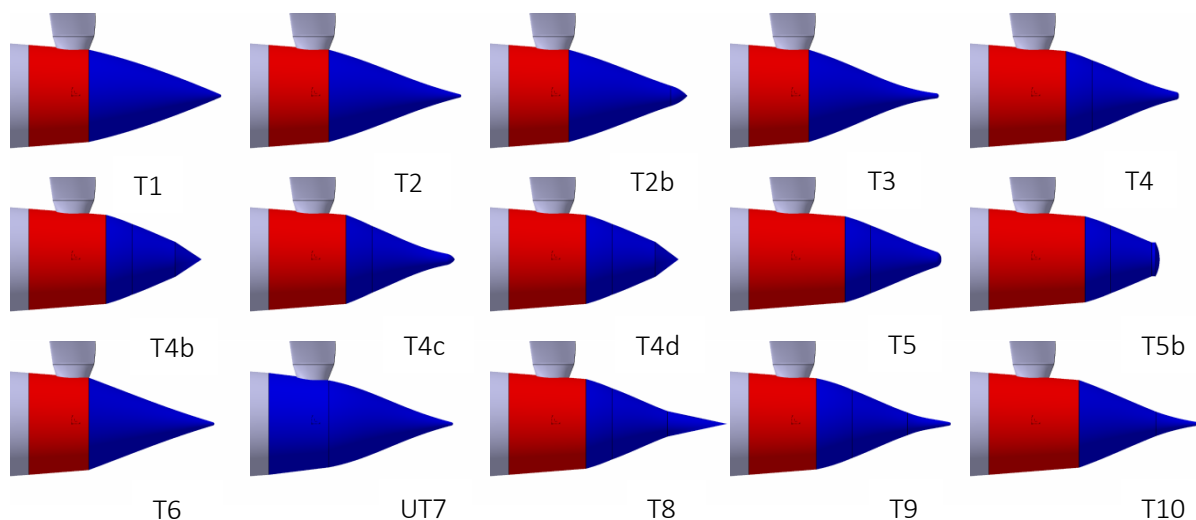


Figure 5.7: Tangent spinner designs (Tangent section of the spinner in red and expansion section in blue)

As it can be seen in Figure 5.7, the expansion part of the spinner was modified in order to find the maximum relative propeller efficiency achieved by the spinners tested. The sub-tests denoted with lowercase letters, are result of mainly tip variations of their base design. This is why they share the same tangent extension among them.

Test T4c changed the curvature but still has the same nacelle extension than the T4 (Fig. 5.8). The spinner part that acted as a nacelle extension was initially extended up to the intersection of the tangent line at 4.51° towards the rotational axis and the end of the trailing edge of the blade root. This first tangent extension (T1) represented 44% of the original spinner length, same as the extension for T2, T3, and T6 spinner designs. On the other hand, T9, T4, T8, T10 and T5 have tangent sections that extend up to 49%, 56%, 56%, 66% and 70% of the original spinner length respectively.

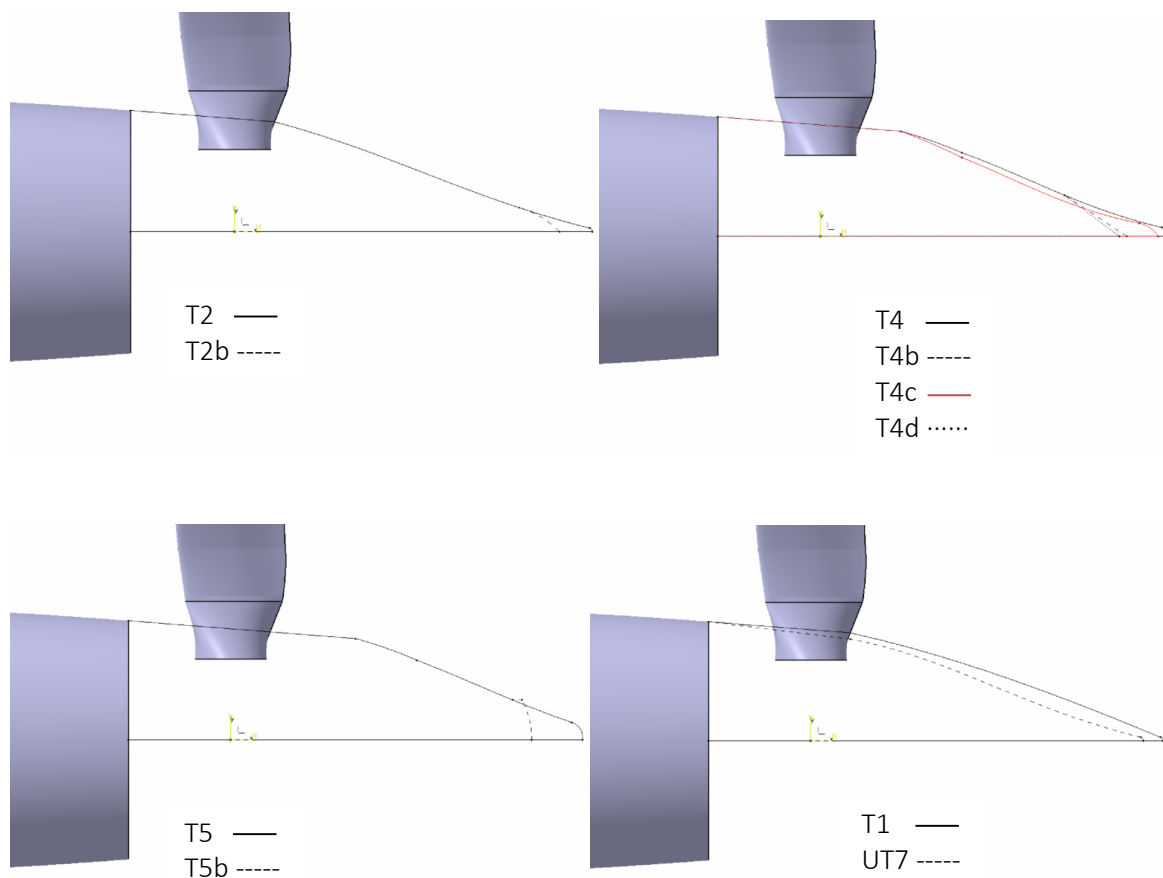


Figure 5.8: Expansion section Sub-variations of tangent spinner group.

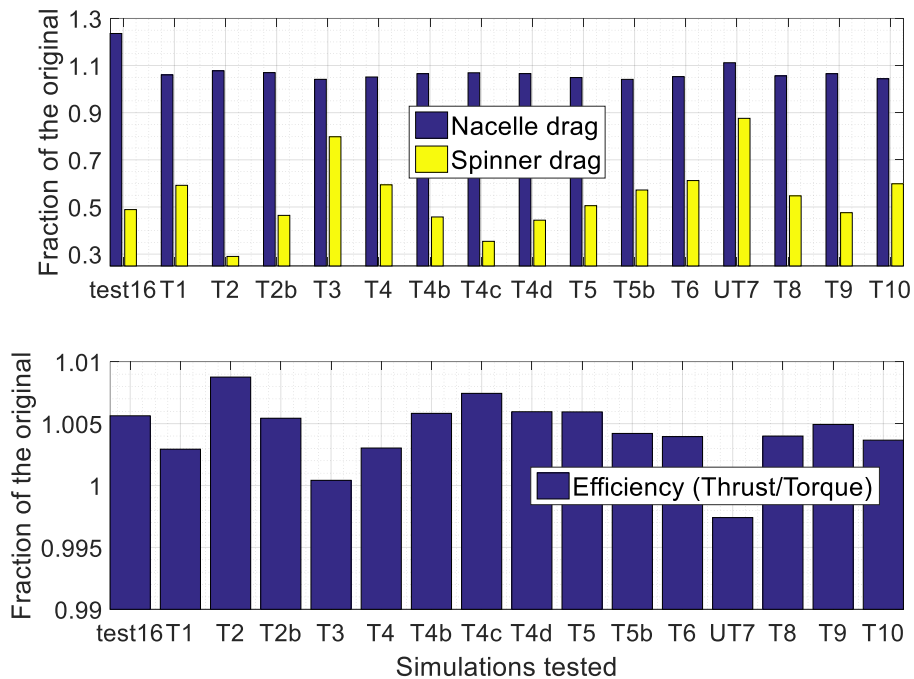


Figure 5.9: Drag and efficiency of tangent spinner design group.

Despite the different diameter distribution at the spinner expansion section, the tangential extension or the spinner length, the tangent experimental group followed an improving trend in efficiency. When the series of tests of the experimental group reached the T6, all the spinners from the group had shown higher efficiency than the original propeller configuration, suggesting that a steeper adverse pressure gradient might increase the pressure without flow separation. This is why the one of the spinner case was designed to have a straight similar to the tangent one but with a larger angle in such a way that the spinner geometry would remain under the tangent line of the nacelle extension (Under tangent design UT7). UT7 resulted in a decrement of the relative propeller efficiency compared to the original design, pointing out the importance of the constant pressure distribution achieved among the tangent group due to the nacelle extension. The effect of the tangent designs was observed at their relatively constant nacelle drag independently of the spinner drag reduction (Fig. 5.9); however, 4 out of the 5 cases with the lowest nacelle drag were the spinners that had longer tangent portions T5, T10 and T4.

The relative propeller efficiency was improved 0.88% using the T2 and 0.74% with the T4c (Fig. 5.9).

5.2.1 Flow separation among tangent spinners.

Since the blade exposure was kept constant, with the exception of UT7, it could be said that the improvements on the propeller performance were related to the significant reduction in spinner drag observed in spinners such as the T2. This case, for example, showed a spinner drag reduction of around 70% compared to the original one.

Figure 5.10 depicts the pressure and axial shear stress distributions for the two spinners that showed the largest improvement in efficiency (T2, T4c) and the two spinners with the worst results (UT7, T3). It was evident that T2 and T4c had larger positive pressure coefficients on the spinner than their counter parts of low efficiency; nevertheless, relatively early flow separation was observed on both designs. T4c showed a maximum C_p value further downstream than the T2 and it did it over a longer distance in axial direction. Similar to what was observed with blade-off tests, the pressure distribution of the T4c was preceded by a pressure drop at the tangent-expansion transition. Both T2 and T4c presented

negative pressure coefficients at the end of the spinner indicating separation and possible presence of a hub vortex.

The axial shear stresses distribution depicted in Figure 5.10 indicated that the design T4c encountered larger values than the other designs compared in the same picture. The reason of the increment was the larger velocities that were produced due to the longer tangent portion of the spinner that postponed the full flow expansion.

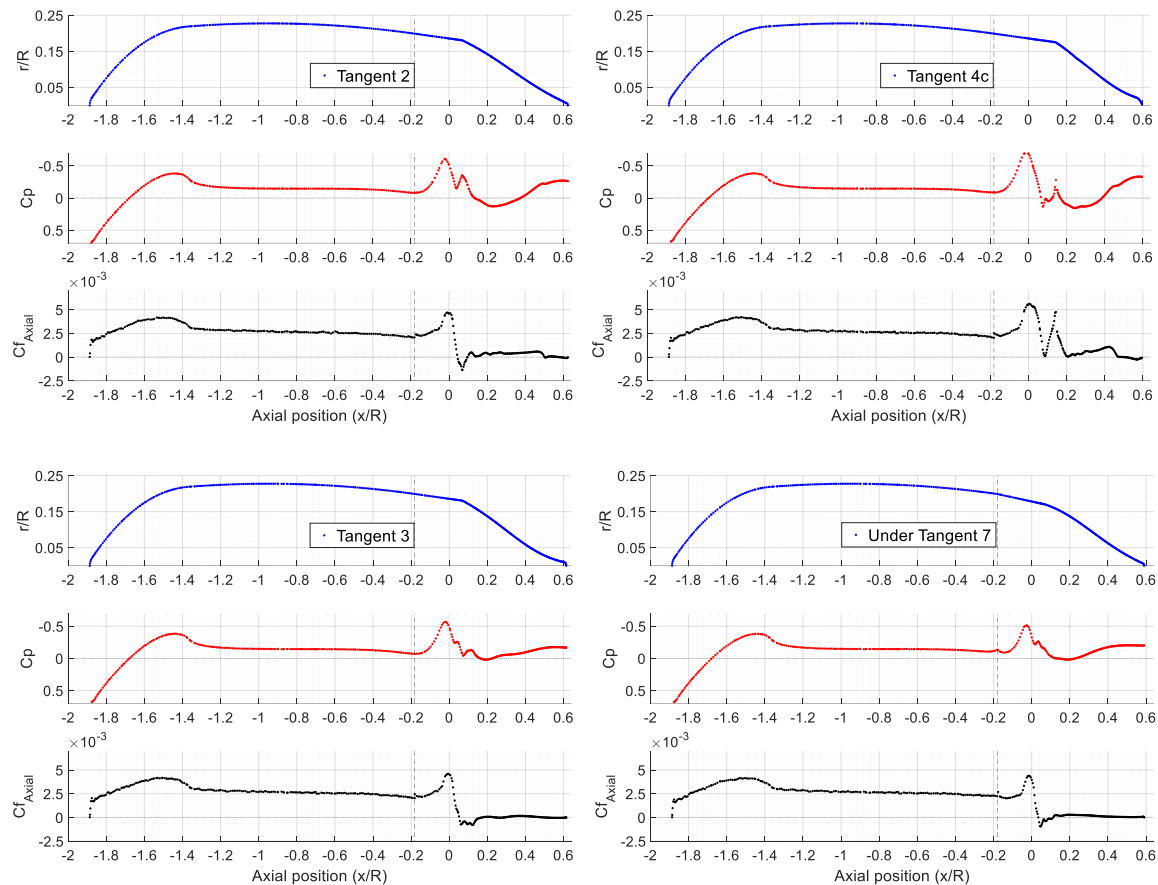


Figure 5.10: Pressure and shear stress distribution of T2 and T4c spinner designs with efficiency gains of +0.88% and +0.74% respectively (Above). Low efficiency designs T3 and UT7 (Down) with efficiency gains of +0.04% and -0.26% respectively. (Sample taken at 20° of spinner)

Figure 5.11 shows the velocity streamlines of the two most efficient spinners compared to the UT7 that induced a reduction in propeller efficiency. The flow that remained attached along the spinner was largely influenced by the tangential velocity component of the outflow from the lower part of the pressure side in the same way that happened for test 16 and the first tangent design (T1). The designs with a greater efficiency also showed larger axial shear stresses, especially prior to the separation point. By looking at the axial friction coefficient contours of T2 and T4c, it is clear that the first one showed a larger area of reversed flow around the blade root, while T4c showed mostly positive values of axial shear stresses around the blade root especially close to the suction side. This suggests that the longer tangent portion of the spinner not only benefitted the nacelle performance but also the blade root loading in the sense that it delayed the flow separation at the lowest radial positions of the blade root suction side.

For the most efficient designs, the flow separation started closer to the spinner end than for less efficient spinners such as the UT7. As the streamlines approached to the separation point it was possible to see the change in direction of the flow close to the spinner wall, where a predominantly

tangential direction was depicted. Once again, the separation occurring at the blade root suction side of UT7 seemed to affect the outflow angle at the lowest radial positions, thus changing the trajectory followed by the streamlines.

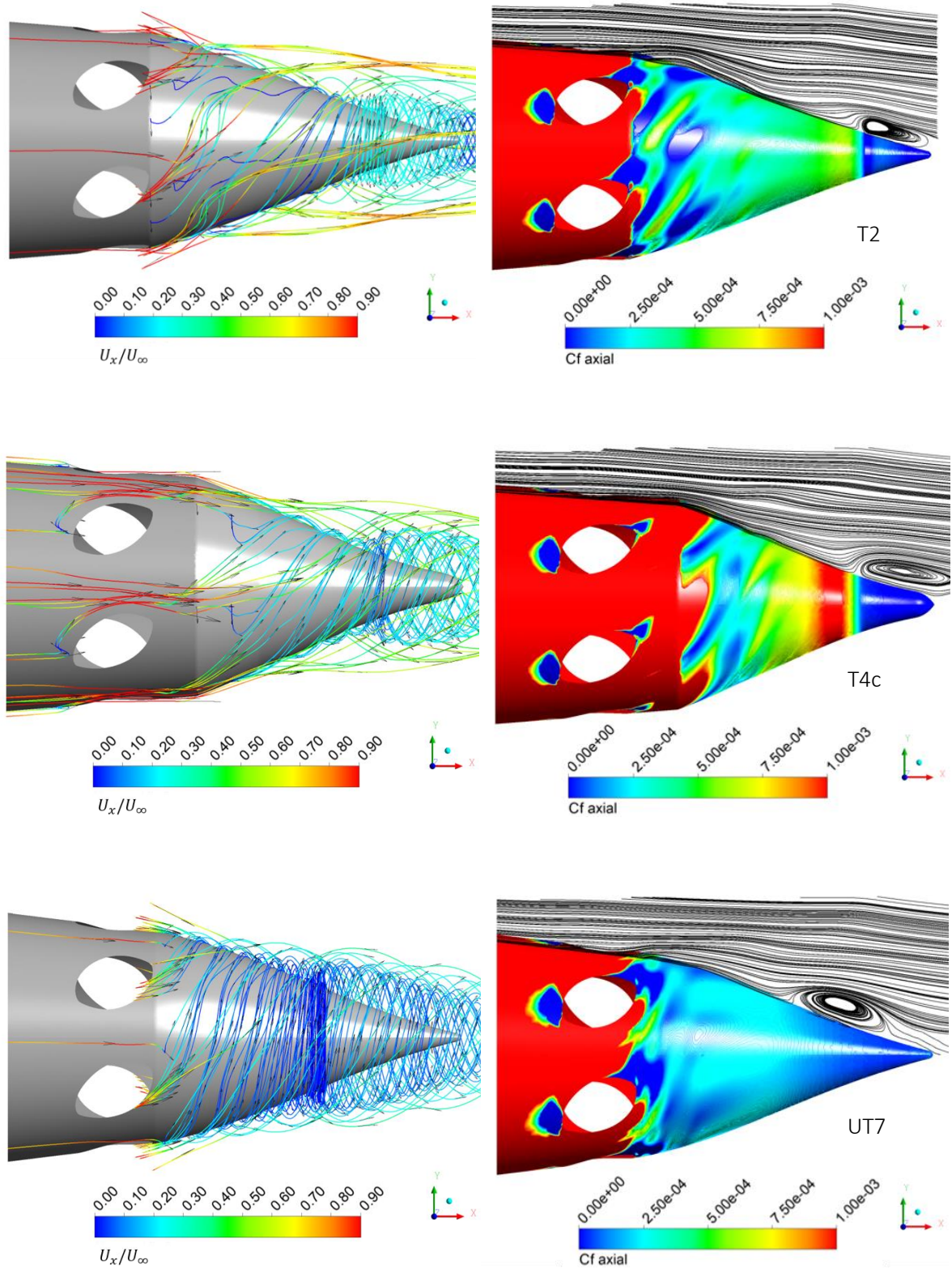


Figure 5.11: Stationary frame velocity streamlines and axial friction coefficient contours for T2, T4c and UT7 spinners (Only positive friction coefficients values are shown).

5.2.2 Vortex formation and blade root loading.

The flow separation delay showed to be the most significant parameter in order to improve the relative propeller efficiency since attached flow over the spinner would inevitably increase the pressure recovery. However, the spinner drag has shown to be also dependent on whether or not is the hub vortex formation strong enough to counter the flow expansion and the positive pressure coefficients at the rear part of the spinner.

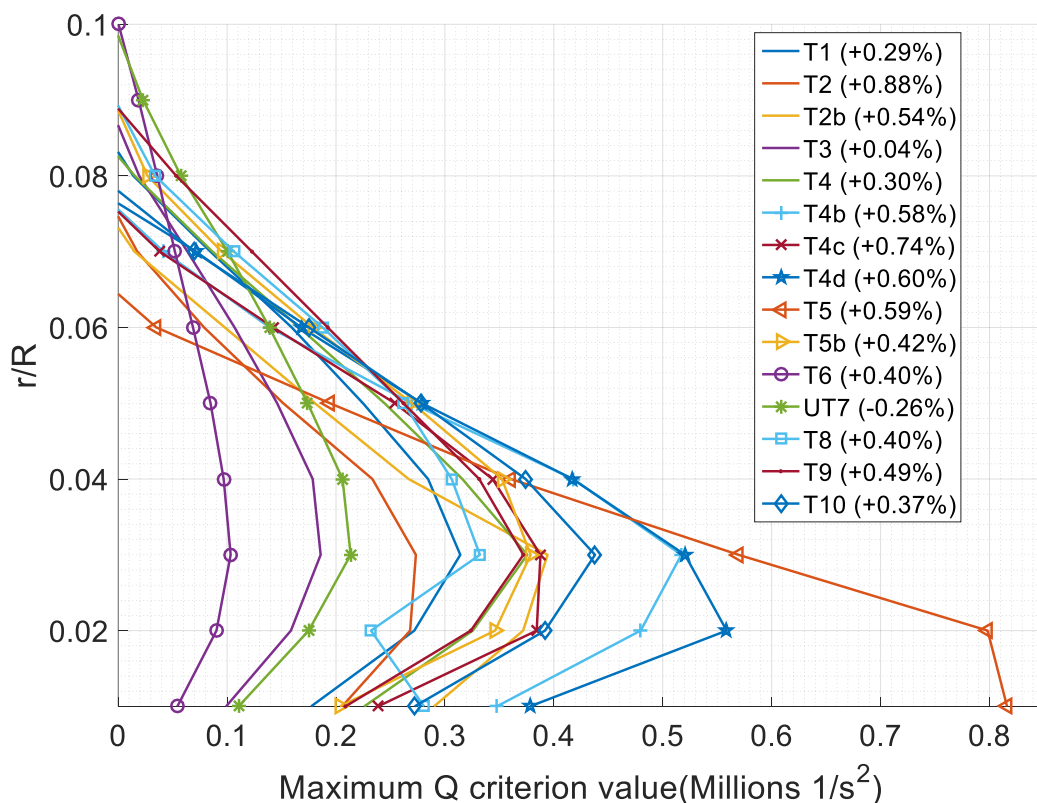


Figure 5.12: Spinner vortex strength for the tangent group tested at a plane located 0.72R downstream ahead. (Corresponding relative propeller efficiency variations are shown in the legend).

The Figure 5.12 shows the maximum values of Q criterion encountered along the circumferences of radius r/R . The testing plane is normal to the axis of rotation and it was located at $0.72 x/R$ from the origin. As observed for the shorter and longer spinners, the hub vortex (Around $0.03 r/R$) had lower magnitudes when a second relatively large peak was observed at higher radial position. Spinner designs that have narrow shapes or that extend the nacelle not further than the blade root such as T6, test 16, T3 and UT7 have all Q values below 0.2 million at the hub vortex radial position. On the other hand, spinners that prolonged further the nacelle extension such as T10, T4b, T4d and especially T5, had Q criterion values that exceeded 0.4 million at the hub vortex radial position ($0.03 r/R$).

Figure 5.13 depicts contours of the axial force acting on the spinners of the tangent group as a fraction of the propeller excess thrust. The areas in red indicate that the axial force component has a drag direction while the blue contours indicated thrust direction.

The pressure recovery indicated by the blue contours of axial forces in direction of thrust was produced mostly by the flow expansion coming from the blade root, especially from the pressure side. The blue contours followed a negative tangent direction that indicated the trajectory of the attached flow. On the other side, the red contours that represented the axial force induced by a region of low pressure

coefficients seemed to be exhibited mostly at the end of the spinner. This indicated the presence of a hub vortex: however, cases such as T6 showed positive axial forces (Drag direction) with similar strength at the beginning of the expansion section of the spinner.

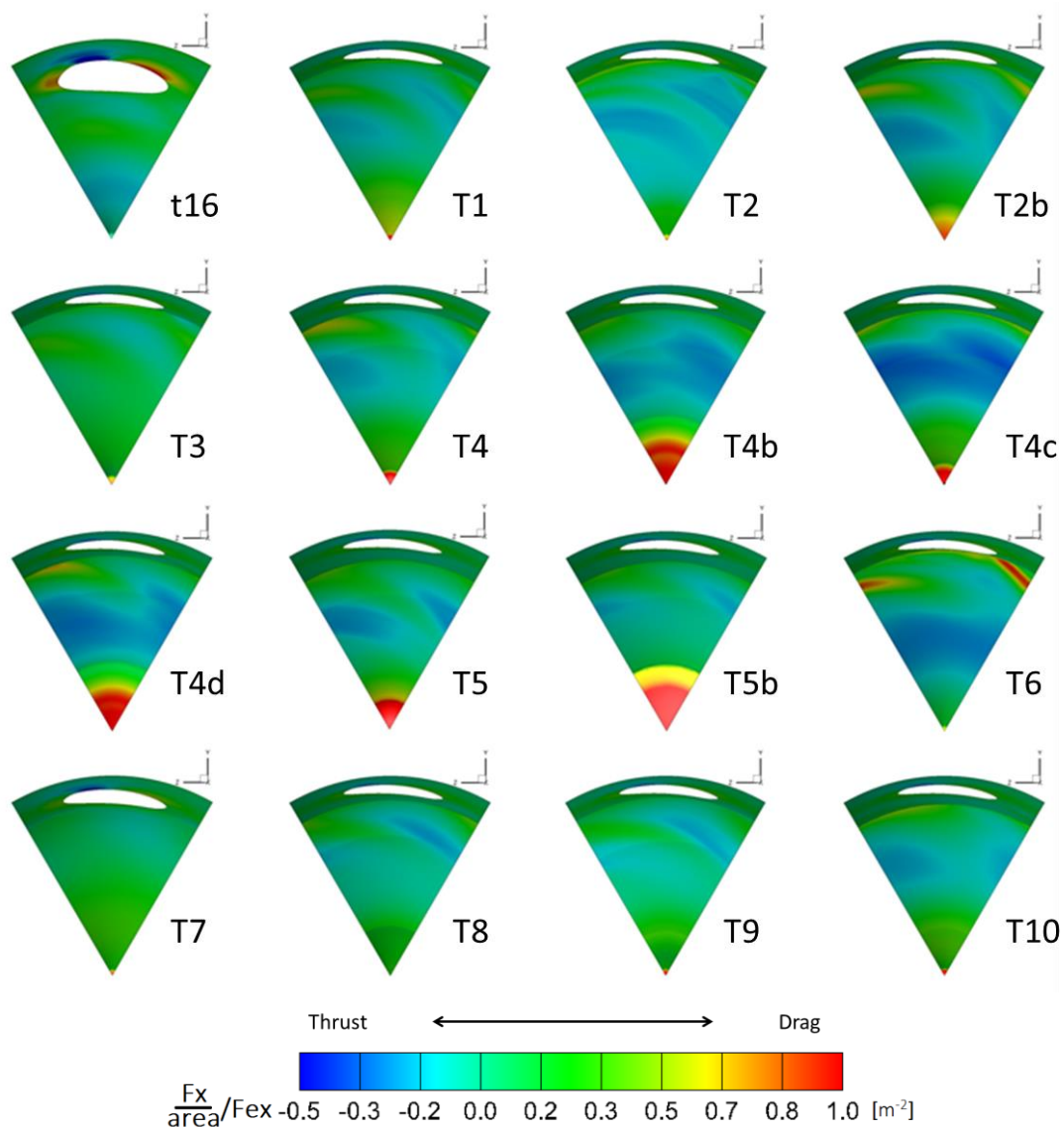


Figure 5.13: Contours of axial component of the force acting on Tangent spinners and test 16. Axial force coefficient calculated for 1 m² area reference.

The contours of axial forces that acted in drag direction observed in T6 were induced by a strong separation vortex. This suggested that early separation occurred at the blade root suction side and that the large negative component of tangential velocity coming from the pressure side was most likely separated as well. The flow separation was reflected in both, the low velocities and the low Q criterion values encountered at low radial positions.

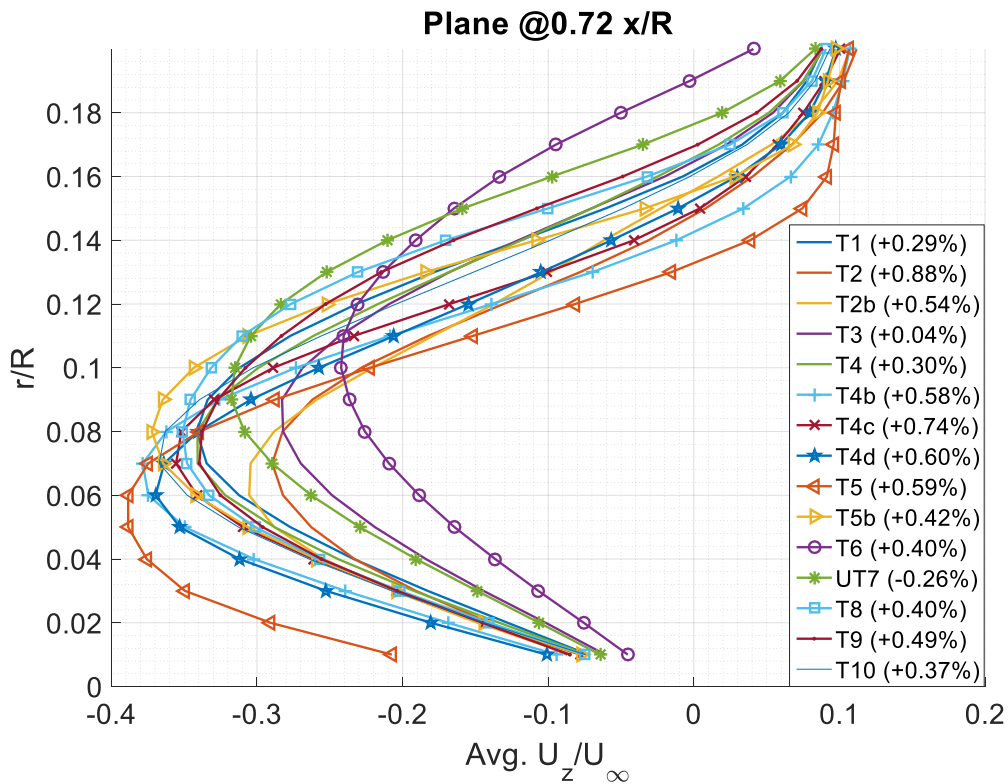
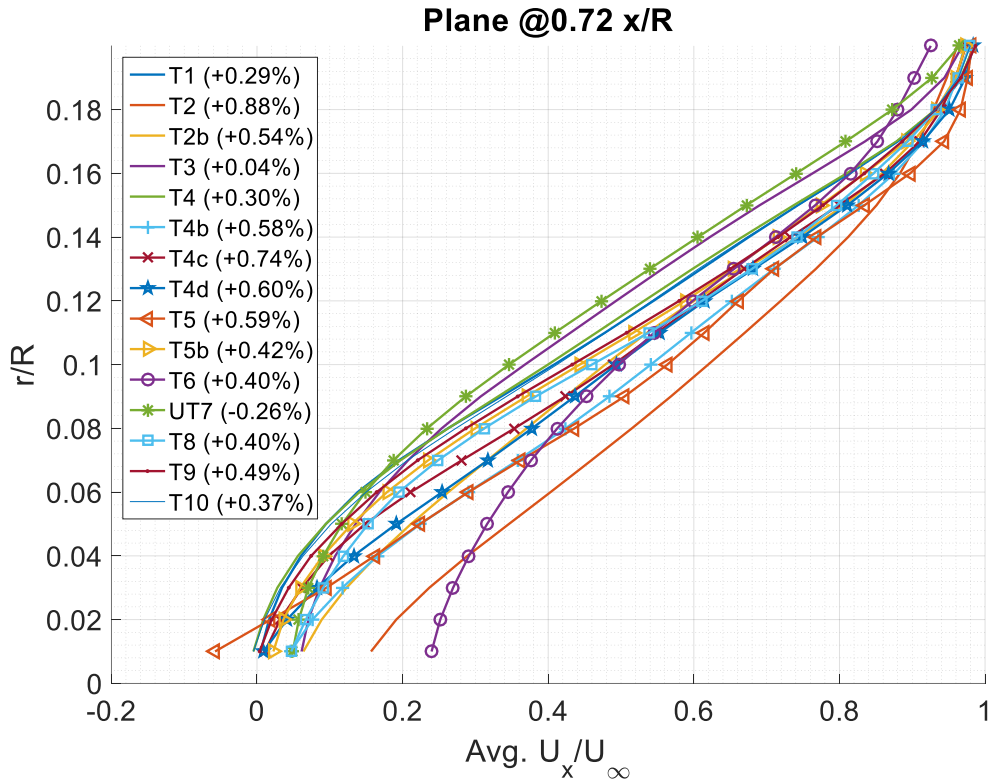


Figure 5.14: Circumferentially averaged axial and tangential velocities for the spinners of the tangent group. Corresponding relative propeller efficiency variations are shown in the legend.

Figure 5.14 depicts the axial and tangential velocities averaged circumferentially at the blade root and spinner zones. By looking to the velocity plots it comes into sight that the spinners that extended the

nacelle further downstream presented the highest velocities for the same radial position and at the same plane of reference. The larger values of velocity were observed in both axial and tangential components, especially in T2, T5, T4b and T4c at radial positions between 0.11-0.16 R. Despite of similarities of the velocity profiles measured close to the spinner, T5, T4b and T4c did not produce the same improvement on propeller efficiency than the T2. Unlike the other spinners with relatively high efficiency, T2 showed practically no evident traces of low pressure (Fig. 5.13).

Table 5.2: Hub vortex strength among tangent spinner group (Sample taken at 0.72 x/R plane)

Spinner design	Hub vortex (Max. Q value) / Original tip vortex (Max. Q value)
Original	22.4%
T1	29.9%
T2	25.7%
T2b	37.4%
T3	16.8%
T4	34.6%
T4b	48.6%
T4c	36.4%
T4d	52.3%
T5	74.8%
T5b	41.1%
T6	9.3%
UT7	20.6%
T8	30.8%
T9	34.6%
T10	41.1%

The tangent group of spinners permitted a gradual flow expansion that delayed the separation due to the less steep adverse pressure gradient. This explains the generalized tendency to improve the propeller performance. If any, flow separation was encountered only at the end of the spinner which allowed encountering greater static pressure over longer portions of the spinner wall. However, independently of the spinner design that was tested, relatively strong vortical structures were observed at the lower radial positions. Table 5.2 shows a comparison among the largest Q criterion values found at the hub vortex region as a percentage of the original tip vortex where the three largest percentages are highlighted in red. From the same table it can be derived that all of the spinner designs that had longer nacelle extensions (Spinner tangential part) exhibited a hub vortex that represented at least 30% of the tip vortex strength. In a similar way, the results depicted in the tangential velocity graph of the Figure 5.14 showed that T4b, T4d and T5 displayed not only the largest negative tangential components of velocity, but also at the lowest radial positions closer to the hub vortex formation.

It can be said that by increasing the tangential part of the spinner, the flow expansion started at a very moderate adverse pressure gradient which helped maintaining part of the flow attached to the spinner. Nonetheless, the separation delay permitted larger velocities induced by the propeller rotor to be closer to the spinner wall since the streamlines were following the spinner curvature in a similar way as for the blade-off tests. For most of the tangent designs that were tested, this was the reason of stronger vortices since the larger velocities found closer to the wall interacted with the low ones encountered in the separated region.

However, the low pressure region observed in the spinner case T5 started before the formation of the hub vortex. In fact, the hub vortex was formed downstream ahead of the spinner since no separation was observed for this design. The low pressure region of T5 was induced by a swirl motion that took place inside the boundary layer. The swirls close to the T5 spinner wall were caused by the difference in tangential velocity components among the upper and lower part of the boundary layer. Eventually these swirls coming from each of the rotor blades merged towards the end of the spinner which caused the low pressure region observed in Figure 5.15 and 5.16.

The relative propeller efficiency was improved by the spinners that induced a sustained flow deceleration with flow separation occurring late in the spinner or not happening at all. Nevertheless, either the hub vortex or the merging of boundary layer vortices carried a local decrement of the pressure coefficients. Given that the detrimental effect of vortical structures was also observed in designs with no evidence of early flow separation, the importance of the tangential component of the blade root outflow velocity was highlighted as an inherent cause of vortex induced drag. In the same way, the adverse effects could also be alleviated by tuning the blade root loading. It is known that large magnitudes of crossflow can be typically observed at surface mounted objects as horseshoe vortices due to the interaction of a laminar boundary layer and a transverse jet [43]. This was the case for the vortical structures found at low radial positions with the different spinner geometries; nevertheless, the hub vortex and the boundary layer ones observed in T5 showed high dependency on the separation vortex, which at the same time depended on the blade root loading, especially on the outflow direction and magnitude of the stream coming from the root pressure side.

A recirculation bubble at the end of the spinner can be observed in Figure 5.15 as a vortical structure in the shape of a ring. The ring shape was also observed on most of the tangent designs that exhibited flow separation. While all of the vortical structures were formed mostly due to the difference in tangential velocity, the ring vortex was formed mainly due to the difference in axial velocities that created the swirling motion (Fig. 5.15). The pressure coefficient contours that are shown in Figure 5.16 were an indication of why the T2 spinner design presented the best of the efficiency improvements. The spinner wall of T2 was surrounded by positive pressure coefficients more than any of the other spinners of the picture; moreover, the streamlines showed that the flow separated only at a very small section at the spinner end.

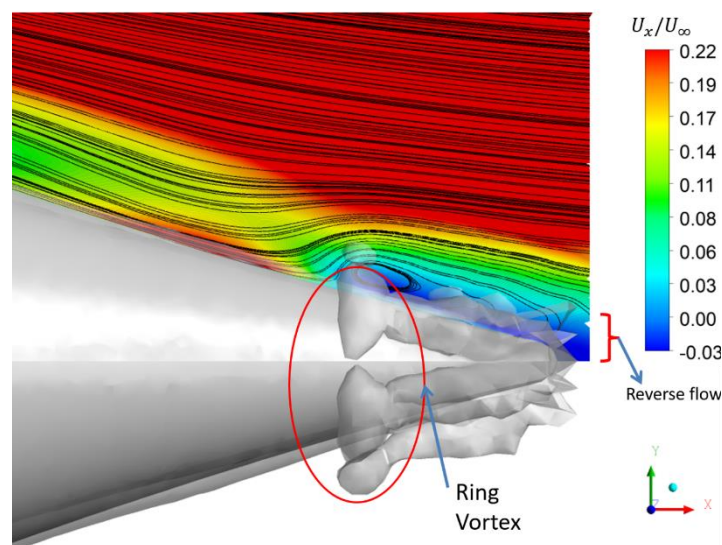


Figure 5.15: 'Ring Vortex' formation at T2 spinner end.

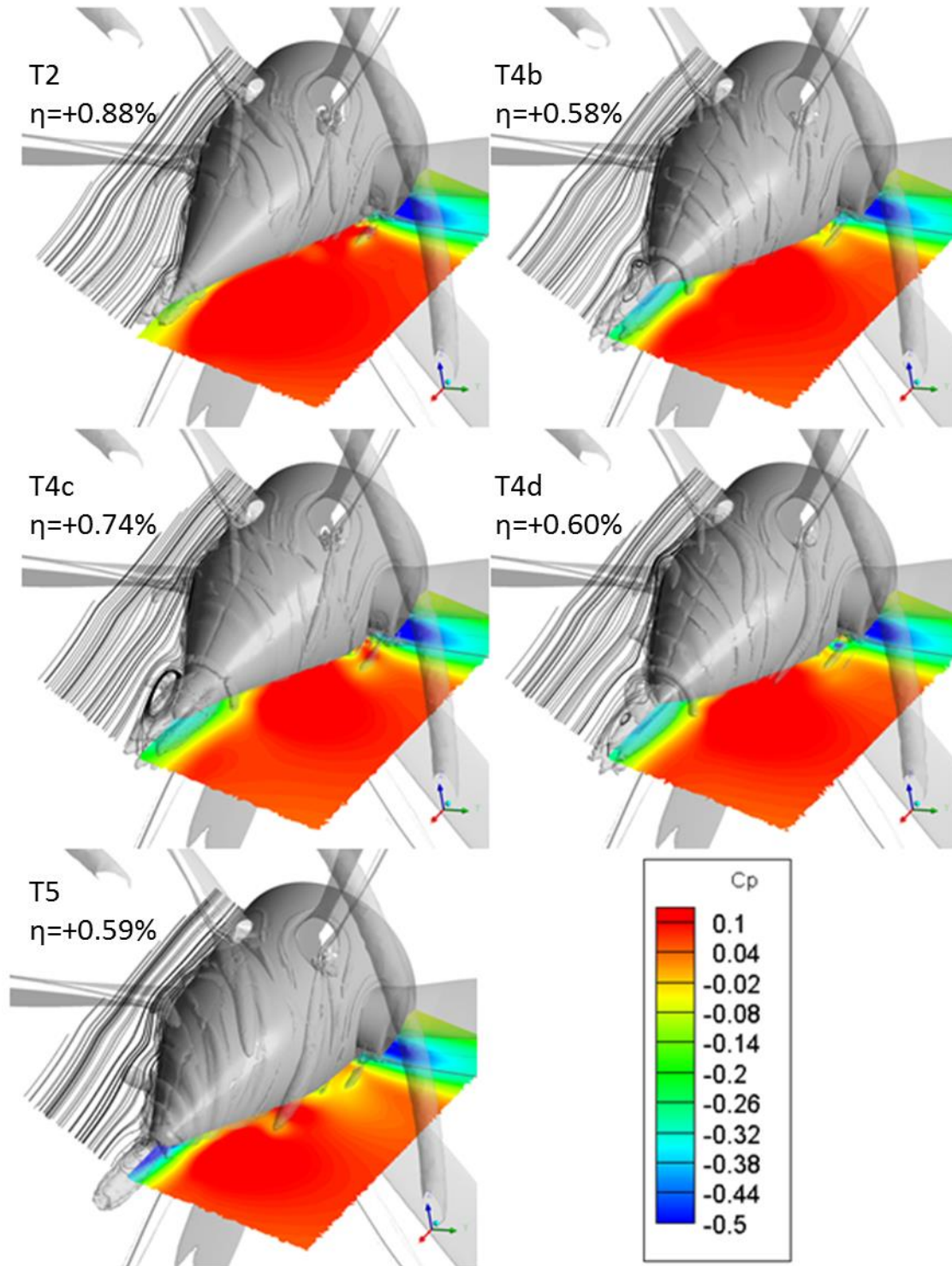


Figure 5.16: Streamlines, pressure coefficients and Q-criterion Isosurface (470000 s^{-2}) on most efficient spinners.

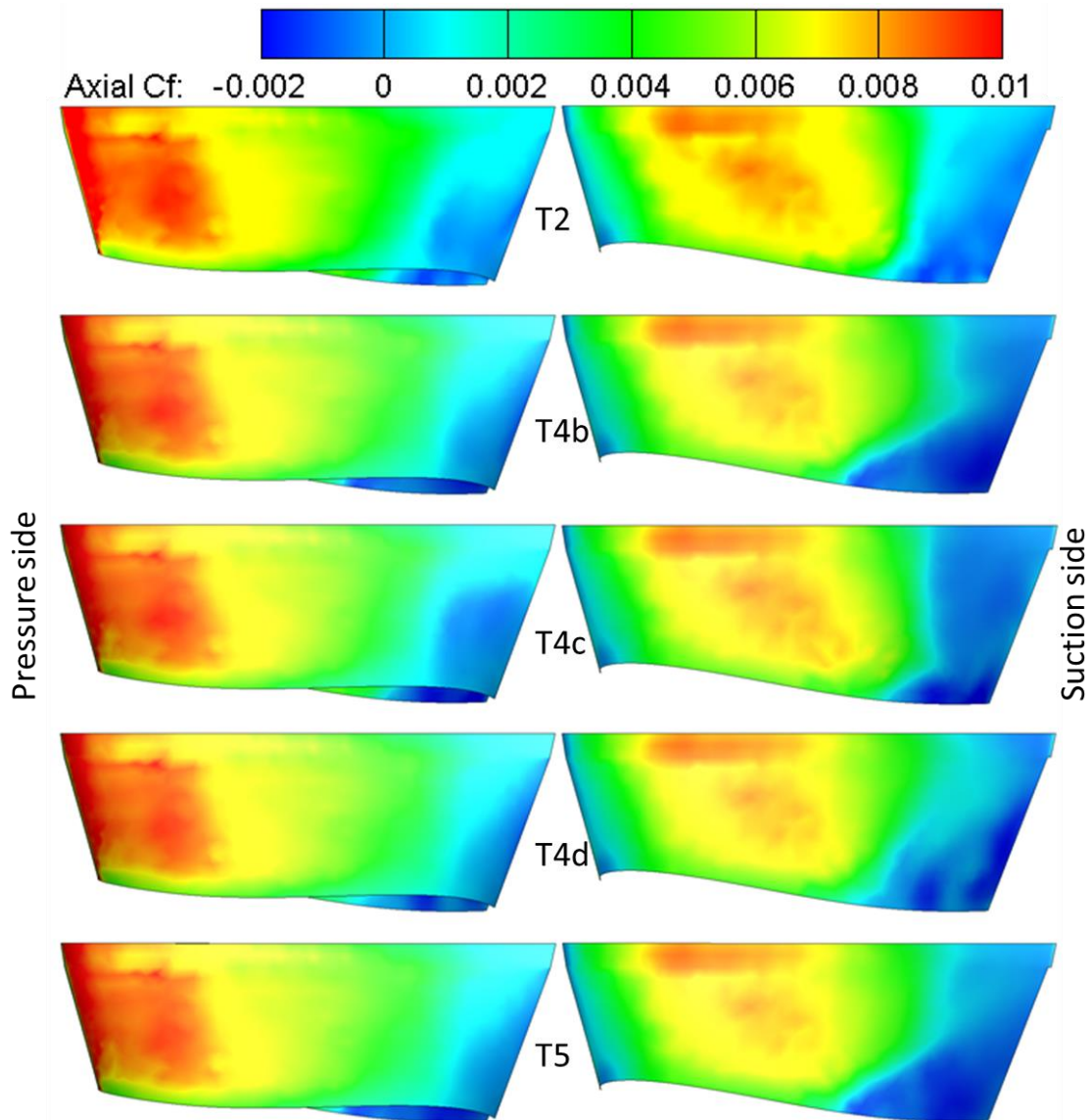


Figure 5.17: Axial friction coefficient contours at the blade root of the tangent most efficient spinner designs.

Figure 5.17 depicts the axial friction coefficient observed at the blade root of the 5 most efficient spinners where T2 and T4c can be distinguished because of their wider blue area on the pressure side, indicating lower axial shear stresses acting close to the trailing edge. This effect was also reflected on the suction side, where the opposite happened and larger axial shear stresses were observed over longer portions of the suction side, especially close to the spinner wall. The largest values of hub vortex Q criterion were observed at the T4b, T4d and T5 models that also showed the earliest flow separation on the blade root suction side. The flow separation not only occurred upstream ahead but also closer to the spinner wall, increasing the chances of interaction between the boundary layer of the blade and the one of the spinner.

The gain in propeller efficiency that was achieved with the modification of the spinner shape was limited to the improvement of the pressure recovery obtained by tuning the slope and curvature of the expansion section of the spinner; however, the direction followed by the flow depended on the root blade loading. This suggested that by modifying the blade root loads, the pressure recovery might be improved and so the propeller efficiency.

6 Passive boundary layer separation control

The efficiency of the pusher propeller studied in this research has been improved by means of a spinner aerodynamic design. Several spinner shapes have been simulated according to the required boundary conditions and they were built from axisymmetric sketches as solids of revolution; however, despite the gains in flow separation delay, it is the author's opinion that the spinner performance could be increased by inducing localized boundary layer control. The objective of the manipulation of the boundary layer would be changing the root blade loading in a way that propeller performance would be improved. Not only the vortex system could be influenced but also the blade thrust, torque and the pressure recovery for a given spinner design. Only passive boundary control methods were reviewed in order to obtain the largest efficiency improvements without the need of added energy.

6.1 Baffle concept as a flow interaction tool

The passive boundary layer control has been used widely as a simple and effective tool in fluid dynamics. One example is shown in the study performed by Liu and Xiong [44], where a physical barrier was used in order to break the core of a typical horse shoe vortex formed on a junction of a wall and an airfoil. Liu and Xiong showed that the wake that a submarine propeller (Pusher) encounters can show a more uniform velocity field if the core of the horse shoe vortex formed at its sail (Dorsal fin) was broken. The expenses of having baffles that dissipate the vortex energy in quicker manner were found to be negligible in terms of added trimming forces. The apparent uniformity of the wake velocity field resulted in lower velocities for the same radial position when compared to the model without the junction baffle. The concept of uniformity in the wake field was especially important for the spinner design of a pusher propeller configuration because the improvements in efficiency depended mostly on the flow expansion after the rotor with relatively low gradient of tangential velocity so the unwanted effects of the vortices can be reduced.

The baffles were rectangular shapes placed inside of the horseshoe vortices. Their height was matched to be the same of the vortex core, while the longitude was set to be around 60% of the height. The intention was breaking the horseshoe vortices at its transition from transverse to longitudinal.

The concept of baffle as a boundary layer control device was tested on the original design of the spinner in first instance, followed by tests made on the spinner designs that presented the largest efficiency so far.

6.1.1 Effect of the baffle concept on the original design.

The first test of the baffle as a passive vortex control tool was made on the original spinner design given for this research. Two baffles were placed on each of the horseshoe vortices observed in the original blade-spinner configuration. The objective, was to induce a more uniform wake just as suggested by Xiong in order to assess its effect on the flow separation and thus on the spinner pressure recovery. The geometrical parameters for the baffle design are depicted in Figure 6.1 as well as the vortical structures formed due to the interaction of the baffles.

The height of the HSV core was around 11mm and 7mm for the suction and pressure vortical structure respectively. This is why the baffle located in the vortex formed on the suction side was designed slightly higher than the one at the pressure side. The height of the baffles was designed so it matched the height of their respective vortex core. The vortices had an axial core length of around 26mm and 19mm for the suction and pressure one respectively. As indicated by Xiong [44], the HSV baffles were located close to the point where the HSV changed from a transverse to longitudinal structure. For this test the height of both baffles was kept constant in axial direction. The vortex core was measured using a Q criterion isosurface of $470\,000\text{ s}^{-2}$. The HSV dimensions did not show significant changes at the measurement point when different values of Q criterion were plotted.

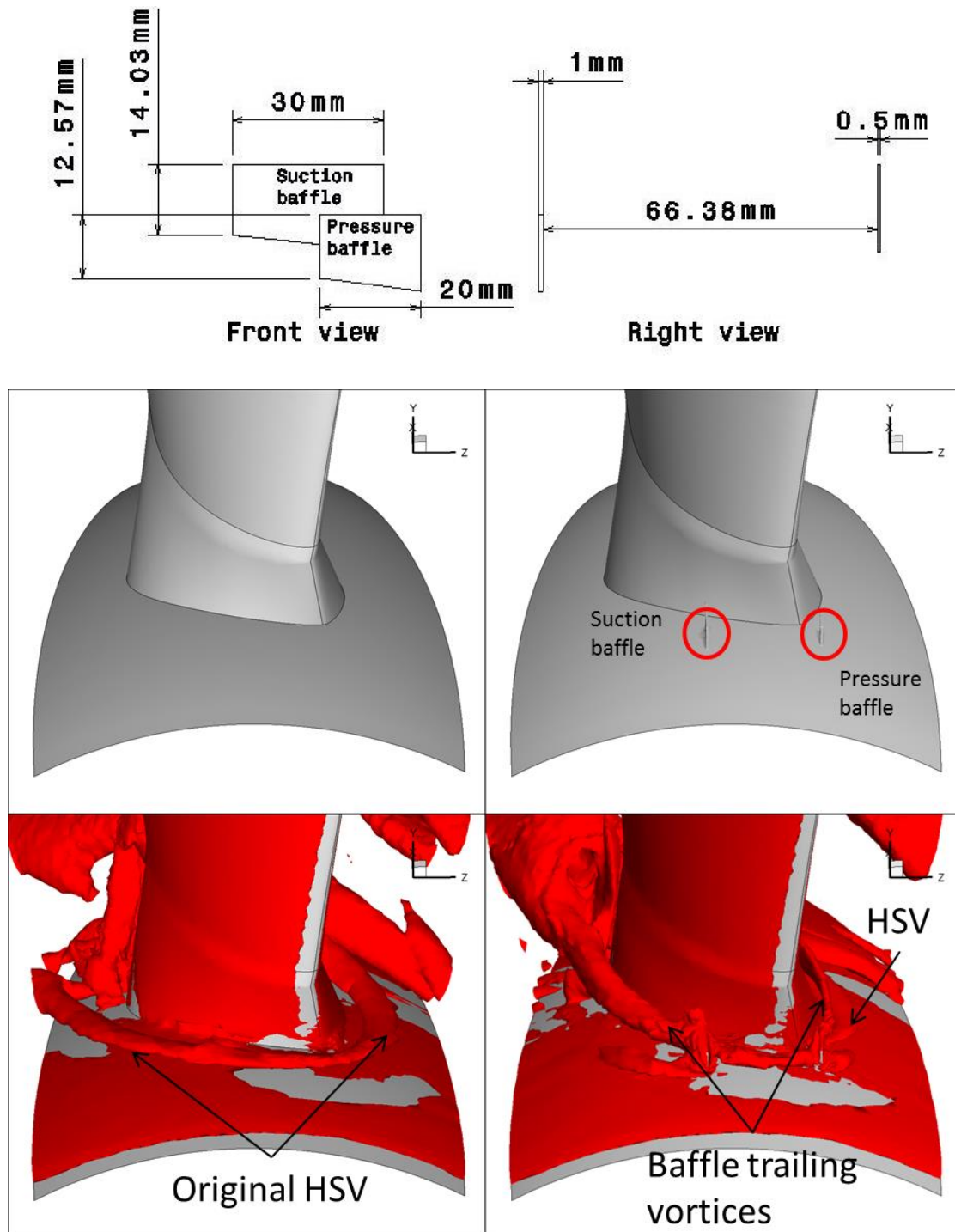


Figure 6.1: Baffles dimensions for HSV and Q criteria Isosurface at $470\,000\text{ s}^{-2}$.

Figure 6.1 depicts the effect of the baffles on the HSV. Two different vortical structures appeared as trailing vortices that come from each of the baffles. In principle, the baffle effect could be inferred as positive since the baffle trailing vortices were formed further from the spinner wall thus preventing the boundary layer from directly interacting to the HSV. However, traces of a HSV were observed in the pressure side due to the presence of transverse flow that went in between of the blade root leading edge and the lower part of the pressure baffle.

Since the pressure side baffle continued showing the formation of the horseshoe vortex, other baffle configurations were tested on the original spinner design. The second test was made using only the baffle that was located at the suction side since it was the one that induced a significant change in the HSV, followed by two more baffle configurations. The first one included a baffle placed in the side of the suction side close to the trailing edge (Trailing baffle) in order to interrupt the separation vortex instead of the HSV. The second configuration combined the HSV of the suction side and the trailing baffle.

As observed in Figure 5.17, the spinner designs that induced the best relative propeller efficiency showed lower axial shear stresses on the pressure side, especially close to the trailing edge due to the earlier flow separation. This led to the design of a baffle whose function was to spoil the boundary layer of the root pressure side. Figure 6.2 shows the design of the spoiler.

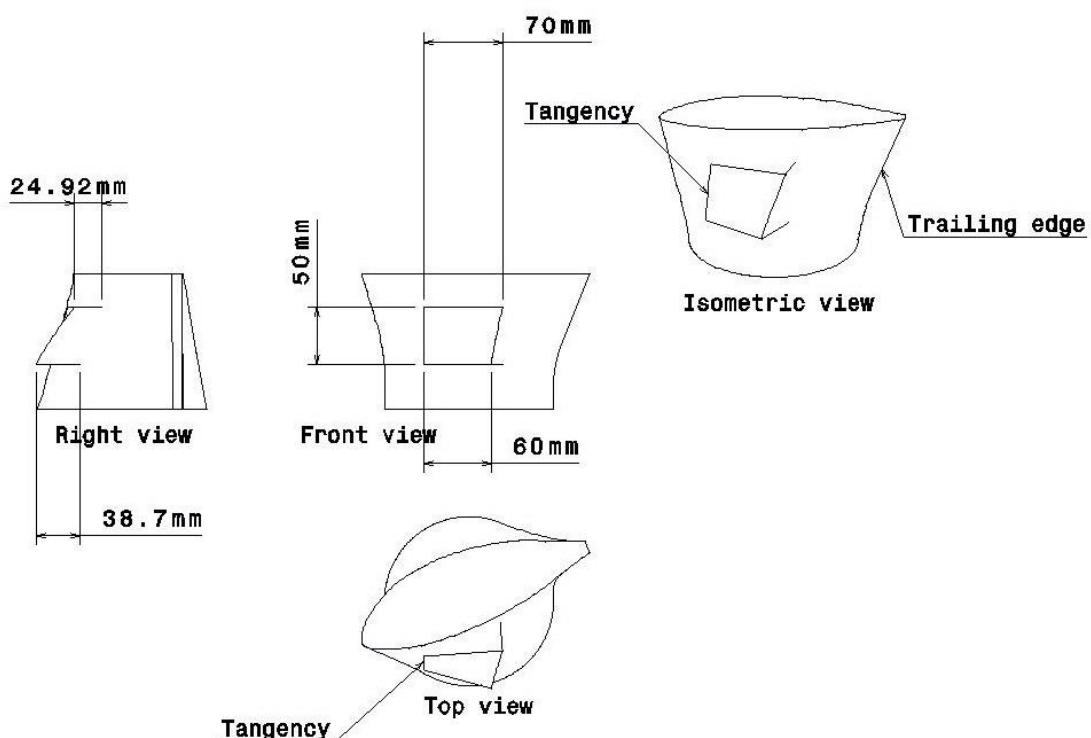


Figure 6.2: Pressure side spoiler sketch and dimensions.

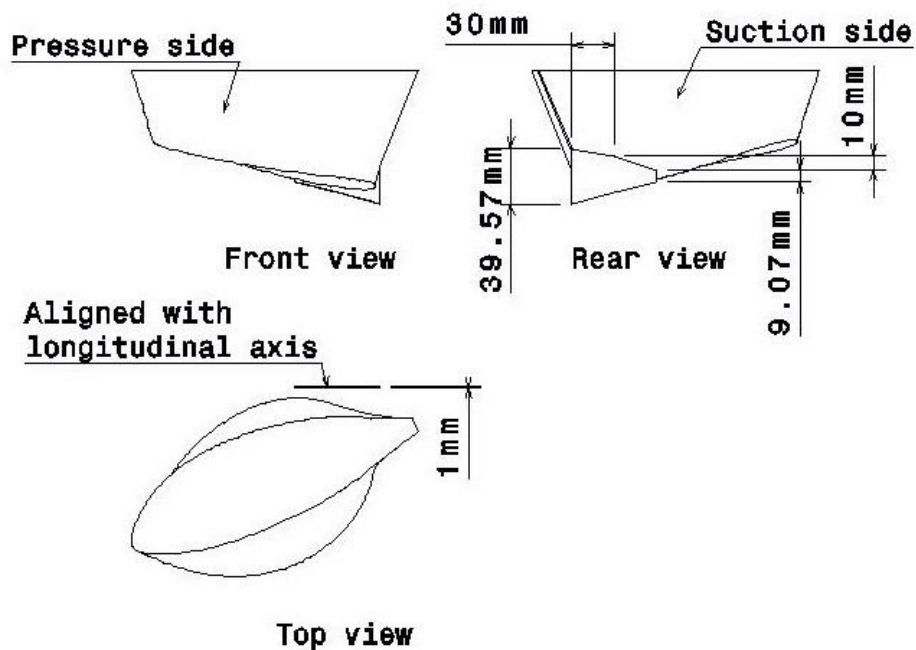


Figure 6.3: Trailing baffle sketch and dimensions.

The sketch of Figure 6.3 portrays the dimensions of the trailing baffle that was designed in order to match the separation vortex core. The trailing baffle was placed close to the trailing edge in order to prevent the transverse flow from interacting with the spinner boundary layer as a separation vortex. The baffle shape was designed to have less influence in the large shear stress area of the suction side (Upstream) which is why it became higher in axial direction.

In a similar way, the spoiler depicted in Figure 6.2 was designed to interact with the blade root pressure side boundary layer. Instead of deflecting the transverse flow coming from the pressure side, as done with the trailing baffle, the purpose of the spoiler was to induce an early detachment of the boundary layer of the pressure side, thus avoiding the formation of the separation vortex.

Figure 6.4 shows the axial force coefficient acting along the baffle-spinner configurations. Favorable values of axial force coefficient were especially observed at the configurations with baffles located at the suction side HSV, at the separation vortex and at the combination of both. The flow separation was delayed for most of the test except for the one that incorporates a spoiler.

The concept of the baffle seemed to work fine especially on the suction side, either breaking the HSV or deflecting the transverse flow coming from the pressure side in the trailing edge.

Figure 6.5 shows the influence that the different baffle configurations had on the flow expansion, being the trailing edge one the baffle design that induced the largest values of pressure coefficients. Even when the pressure distribution corresponding to the trailing baffle maintained a positive averaged C_p over most of the plot, a sudden decrement could be observed towards the lowest radial positions. The pressure drop was caused by the hub vortex that despite being formed at the ending part of the spinner ($0.025 r/R$) it was strong enough to decrease the pressure in a significant way.

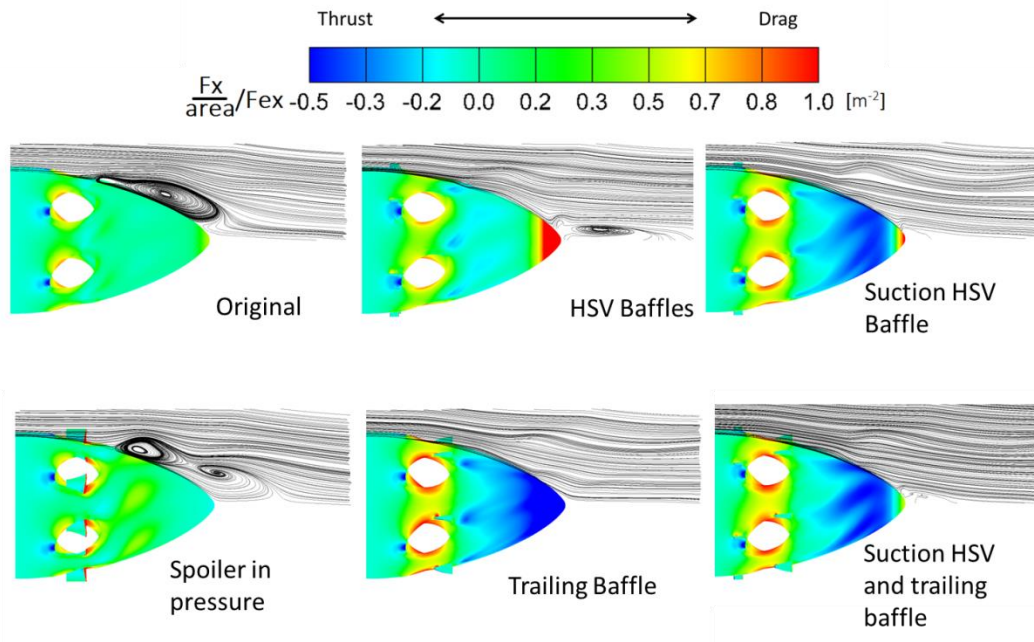


Figure 6.4: Axial force coefficient contours and flow separation streamlines at 20° plane.

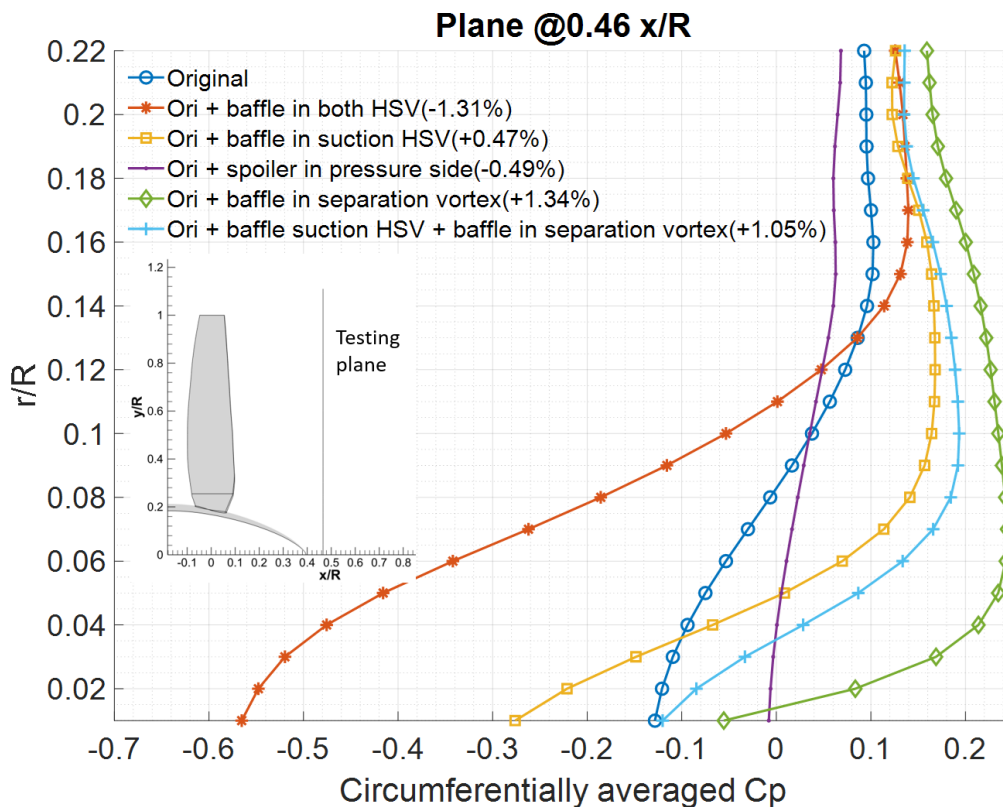


Figure 6.5: Pressure distribution of the original spinner design and the different baffle configurations (Relative propeller efficiency variations are shown in the legend).

The trailing baffle tested on the original spinner design improved the relative propeller efficiency regardless the strong hub vortex formed at the spinner end (Table 6.1). The hub vortex core had a relatively smaller size compared to the other baffle configurations, especially when compared to the one with baffles at both of the HSV.

Figure 6.6 shows the axial component of the shear stress acting on the blade root pressure and suction sides. Just as observed for the most efficient spinners of the tangent group, the spinners with the largest efficiency were the ones that presented positive values of axial shear stress further downstream in the blade root suction side. Fig. 6.6 shows negative axial shear stresses repeatedly on the pressure side of the designs with the best efficiency such as the Trailing baffle and the last one that combines a suction HSV baffle and the trailing one. Even when large areas of negative axial shear stresses acting on the pressure side were also observed at the spoiler configuration, the suction side exhibited large negative axial shear stresses as well.

Table 6.1: Baffle configuration effect on hub vortex strength and relative propeller efficiency (Sample taken at 0.72 x/R plane)

Spinner design	Baffle design and location	Hub vortex (Max. Q value) / Original tip vortex (Max. Q value)	Relative Propeller efficiency (η)
Original	No baffle	22.4%	100.00%
Original	Pressure and suction HSV	36.4%	98.69%
Original	Suction HSV	46.3%	100.47%
Original	Spoiler in pressure side	2.3%	99.51%
Original	Trailing	55.1%	101.34%
Original	Suction HSV + Trailing baffle	20.1%	101.05%

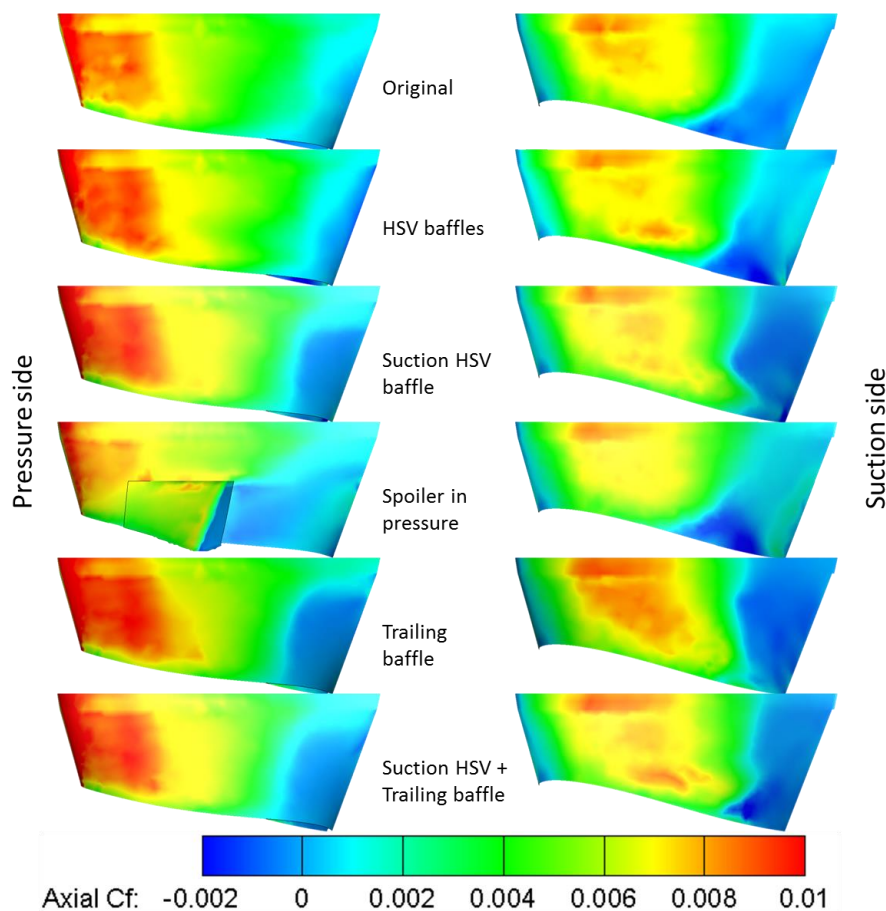


Figure 6.6: Axial friction coefficient contours on the blade root pressure and suction sides.

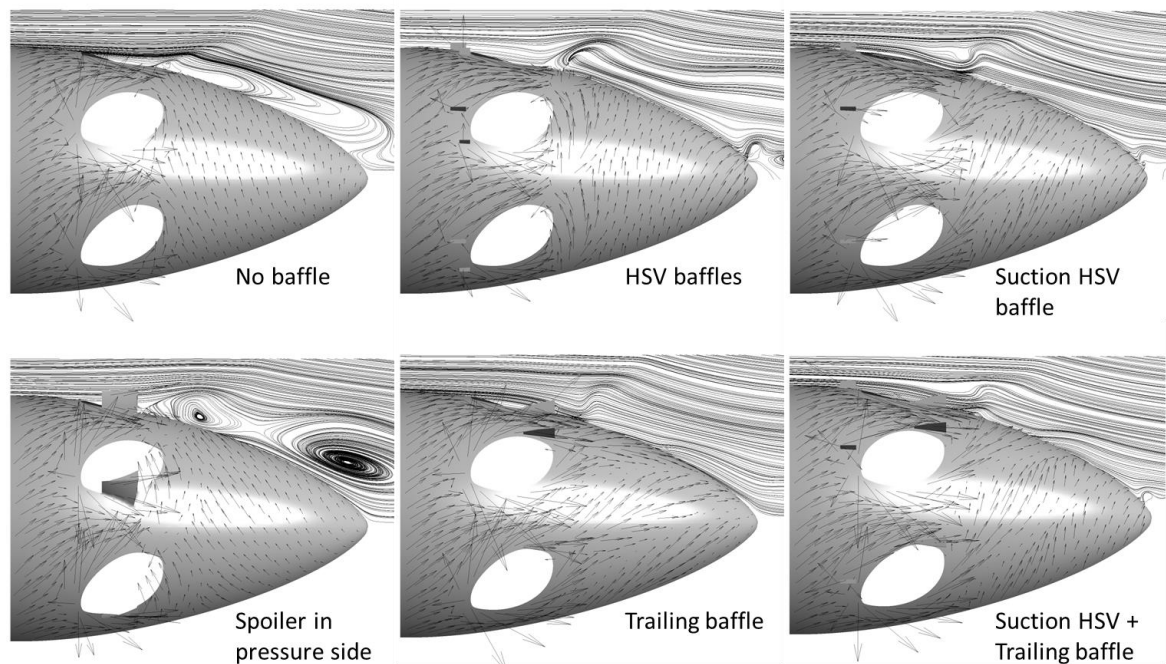


Figure 6.7: Shear stress vectors on spinner with different baffle configurations and separation streamlines at 20°.

Independently on the baffle configuration tested and whether or not it delayed the flow separation on the spinner, the direction of the shear stresses was modified. As showed in Figure 6.7, the original configuration without any type of baffle and the spoiler configuration, showed early flow separation and reverse flow which inevitably increased the spinner drag. On the other hand, the cases where only one baffle was located in the suction side, either breaking the HSV or the separation vortex, exhibited attached flow over practically all the length. The shear stress vectors of both cases followed a more axial direction compared to the rest of the cases. In addition to the different direction of shear stresses, the magnitude of the stress vectors was clearly higher on the most efficient designs. However, when both suction HSV baffle and the baffle located at the separation vortex were placed in the same spinner, the efficiency decreased compared to the one obtained with only the separation baffle.

With the exception of the tests where a device was placed in the pressure side, spinner early flow separation was delayed by means of the baffle configurations and two of them managed to exceed 1% of improvement in the propeller efficiency. However, the baffle configurations were tested on the original spinner design that encountered separated flow over most of the spinner wall, so the concept of the boundary layer control was tested on the spinner designs that caused the relative propeller efficiency to increase.

6.1.2 Effect of the baffle concept on efficient spinner designs.

The relative propeller efficiency was improved by delaying flow separation at the spinner. The use of one or two baffles located at the spinner, demonstrated that flow separation could be delayed as much or even more than by solely modifying the spinner geometry. This is why the more baffle tests were performed in combination with some of the spinners that previously increased the propeller performance. Different designs and locations of the baffles were evaluated.

Given that the baffle located close to the trailing edge (Inside the separation vortex) induced the largest improvement in propeller efficiency, more designs of trailing baffles were tested on tangent designs such as T2, T4c and test 16. The location of each of the baffle was determined accordingly to the location of the separation vortex formed at the spinner geometry. The height was set to barely exceed

the size of the vortex core, in the same manner as for the original configuration, and the thickness was kept as 1mm. Besides the spinners from the tangent group (T2 and T4c), the test 16 was also tested in combination with a trailing baffle since it had a larger blade exposure than the one shown by the tangent spinner group and the original spinner design.

Table 6.2: Baffle configuration effect on hub vortex strength and relative propeller efficiency (Sample taken at 0.72 x/R plane)

Spinner design	Baffle type	Hub vortex (Max. Q value) / Original tip vortex (Max. Q value)	Relative Propeller efficiency (η)
T2	No baffle	25.7%	100.88%
T2	Matching separation vortex	24.3%	100.54%
T4c	No baffle	36.4%	100.74%
T4c	Matching separation vortex	50.5%	100.57%
Test 16	No baffle	11.7%	100.56%
Test 16	Matching separation vortex	18.2%	100.48%

As depicted in the Table 6.2, despite that the relative propeller efficiency was kept larger than the one observed at the control group (Original design), all the baffle cases decreased the efficiency of their spinner alone.

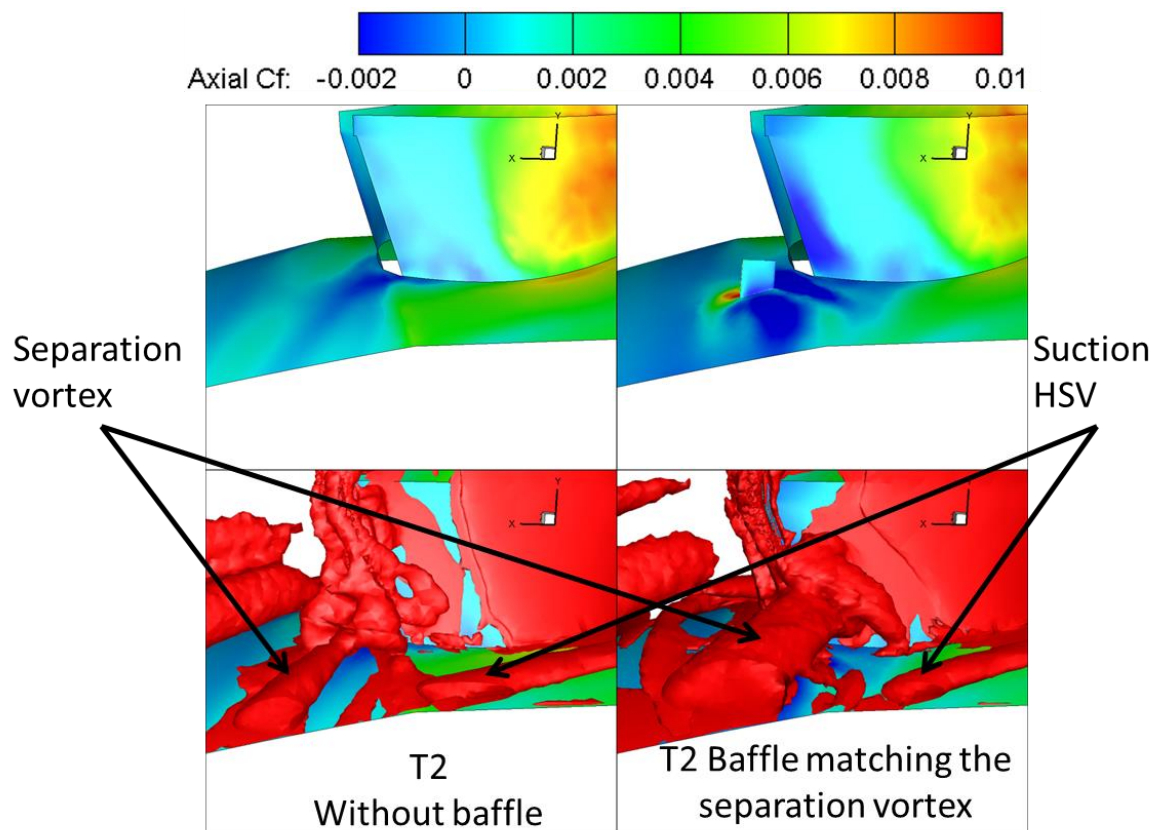


Figure 6.8: Trailing baffle placement and Q-criterion isosurface (470000s⁻²) for T2 spinner.

Figure 6.8 depicts the blade root suction side axial shear stress distribution of spinner T2 before and after the placement of a trailing baffle. Unlike the original design, T2 showed detrimental consequences when the baffle was located. Not only negative axial shear stresses were observed over a larger area, but also the separation vortex was increased triggering early flow separation.

The location of the trailing baffle was based on the same concept than the one used for HSV baffles of interrupting the vortex core, thus dissipating the energy of the vortex that induced separation when it was interacting with the boundary layer coming from the nacelle. The same approach was followed in order to find a location of the trailing baffle; however, the flow separation occurring close to the blade root trailing edge of most of the spinner designs, was not produced by the separation vortex but the other way around. The separation vortex was the swirling motion that was produced by the transverse flow jet coming from the pressure side that was particularly pronounced when the suction side presented early flow separation. Nevertheless, the trailing baffle brought an efficiency improvement as large as 1.34% suggesting that the success of the trailing baffle on the original designed spinner was due to the flow deflection more than the separation vortex interruption.

Based on the assumption that the trailing baffle should not be designed as a vortex breaker but more as flow deflector, the baffle was located where the flow separation occurring at the blade root suction side has its maximum.

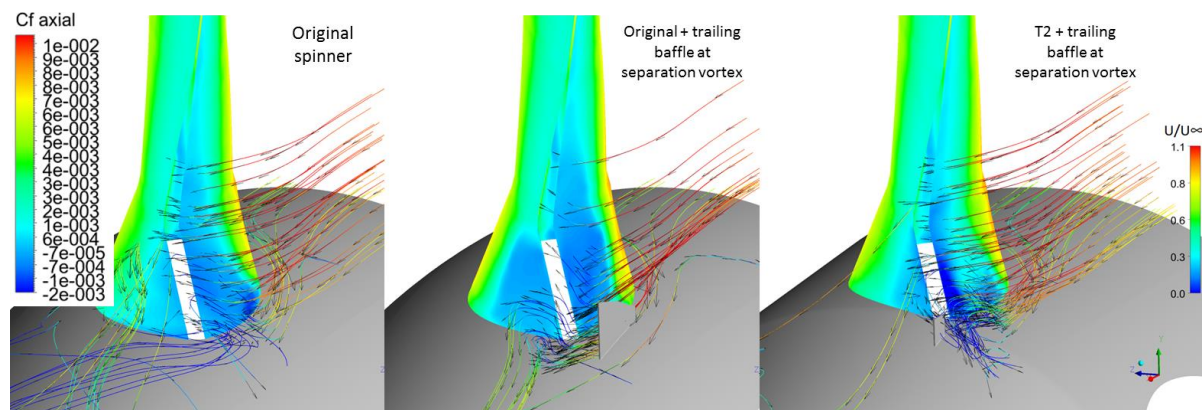


Figure 6.9: Trailing baffle flow deflection acting on original spinner and T2. Axial shear stress contours and streamlines velocity are shown.

Picture 6.9 depicts the flow deflection as a result of the trailing baffle placed at the T2 and the original spinner design. It can be observed that in the case of the middle, the velocity streamlines increased their magnitude at both the entrance and at the exit of the baffle location. The baffle changed the outflow angle close to the trailing edge. This reduced the tangential component (Z direction) of velocity and increased the axial one (X). On the other hand, the velocity streamlines depicted for the tangent case T2 showed a decrement in velocity magnitude, especially towards the trailing edge. Despite the high efficiency of the T2, the trailing baffle did not prevent flow from detaching in the blade root suction side. The baffle location that matches the position and height of the separation vortex core, proved to be ineffective in terms of avoidance of the separation vortex formation, thus decreasing the spinner drag.

By changing the geometrical parameters of the original spinner used as a control variable, 36 spinner designs have been put to test. During the experiments, 23 out of those spinner designs managed to improve the relative propeller efficiency without the usage of any baffle; however, the trailing baffle located on the control spinner increased the efficiency of the propeller more than any of the 23 spinner designs alone, which emphasized the importance of delaying the flow separation in the suction side in

order to delay it in the spinner as well. Figure 6.9 showed that the trailing baffle of the T2 not only did not deflect the flow in the same way than for the original spinner but increased the velocity of the transverse jet flow coming from the pressure side, which also increased the strength of the separation vortex and decreased the relative propeller efficiency compared to the same configuration with no baffles.

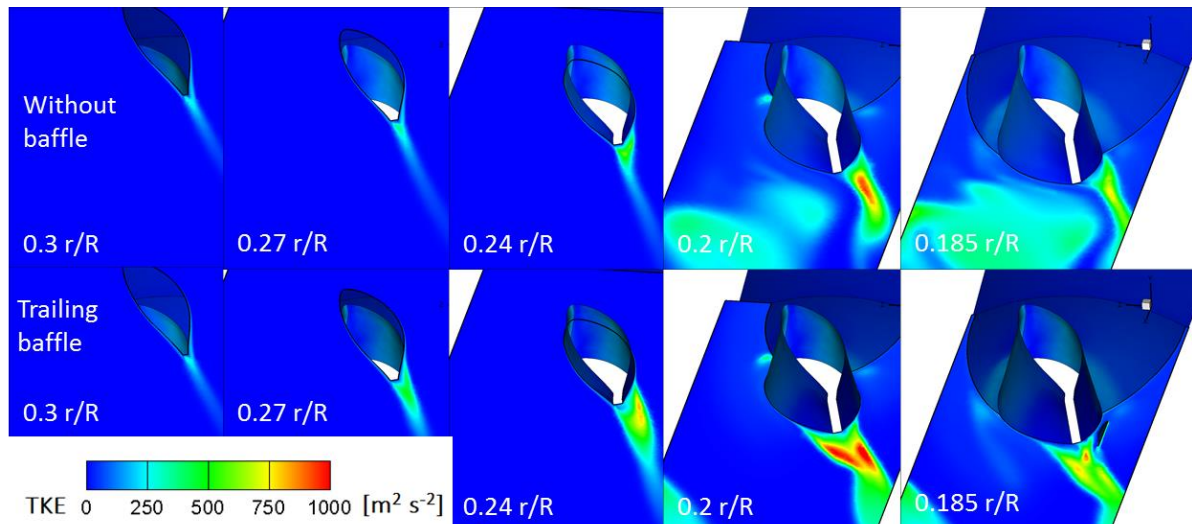


Figure 6.10: Turbulent kinetic energy contours for the original spinner alone and with the trailing baffle.

As it can be seen in Figure 6.10, the turbulent kinetic energy (TKE) was plotted on planes that cut the blade in the lowest radial locations, showing the contours for the original spinner design with and without the trailing baffle. As the boundary layer thickened or separated, the production of eddies increases and so did the TKE. This turbulence production allowed the highlight of boundary layer interaction between the blade root and the spinner. The larger values of TKE observed in the suction side worked as an indicator of flow separation which was more evident after 0.24 R. The TKE contours were initially very similar to each other, especially at the highest radial positions shown in the picture; however, as the plane intersected the blade in lower positions, the TKE contours showed larger values that were less scattered in the image due to the more axial direction of the outflow that regardless of being fully turbulent showed no evidence of early flow separation.

Around 0.2 R the TKE values close to the blade wall were higher for the baffle configuration than for the spinner alone, especially the ones located nearby the pressure side. The increased TKE observed at the pressure side was an indication of separated flow that decreased the interaction between the blade root boundary layer and the spinner one by changing the outflow angle of the transverse jet flow that was coming from the pressure side. For lower radial locations, the values of TKE became larger but less scattered because of the still attached boundary layer that followed an outflow path more aligned with the axial direction.

The trailing baffle used in combination with the original spinner, induced an increment of the axial shear stresses especially observed at the lowest part of the blade root (Fig. 6.11). The increment of the axial shear stress was caused by the attached flow induced by the trailing baffle, especially at the upstream edge located at 10 mm from the blade suction side.

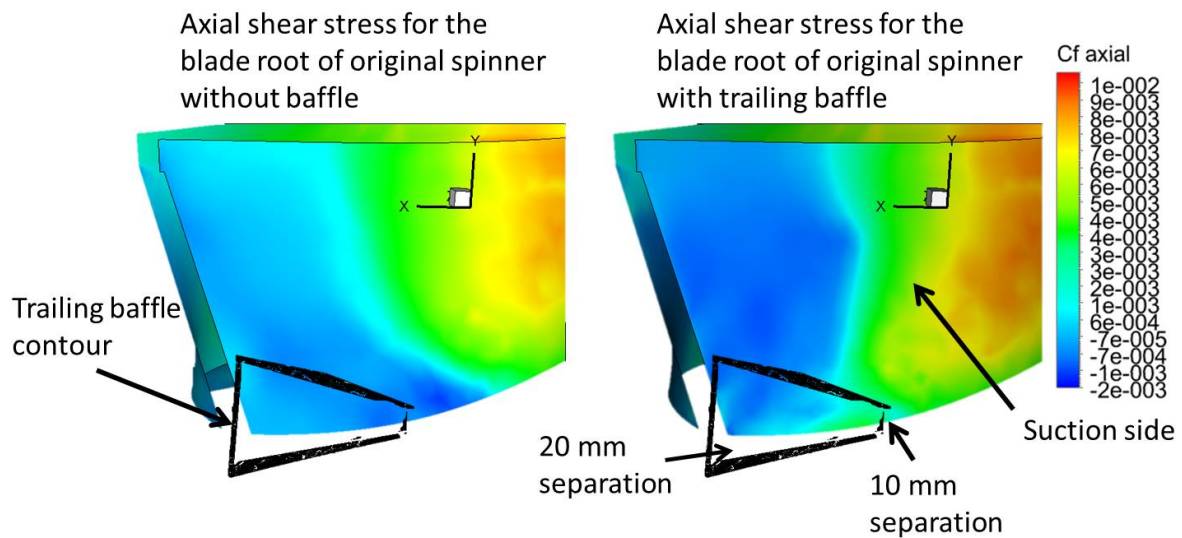


Figure 6.11: Effect of trailing edge baffle on the blade root shear stress of the suction side (Original spinner).

The trailing baffle showed performance benefits mostly because of the delay in flow separation observed on the spinner. This decreased its pressure drag; however, despite the flow separation delay, the pressure drag reduction depended directly on the pressure recovery achieved by the flow expansion. Test 16 can be taken as an example of spinner drag reduction for attached flow. When flow separation took place at the very end of the blade-off spinner tests, or was not observed at all, the flow expansion at the end of the spinner was increased, always favored by a narrow section at the expansion section of the spinner.

Considering that similar designs of the trailing baffle might have beneficial effects on the propeller performance such as flow separation delay and the change in the trajectory that was followed by the attached flow, the design of the trailing baffle was tested with the most efficient spinner designs. This is why a new experimental set up was conducted in order to assess the effects of a baffle as flow deflector in combination with relatively highly efficient spinner design.

The set of simulations combined two types of baffles. The baffle type (a) was tested on tangent designs. Due to the relatively higher radial position that tangent spinners had compared to the original one, the design of the baffle used with tangent spinners was similar to the one used with the original spinner but with an increment in height. The second type (b) comprehended the trailing baffles that were designed so they could be used with the test 16 spinner. Given that test 16 exposed the blade root the most, the trailing baffles of this type were designed to match the area of the suction side that showed separated flow (Based on the shear stresses). Each of the baffle types added a tilted version of the design. The positive angle of baffle rotation was measured respect to the free stream axial direction around the radial axis that positioned the rear edge of the baffle closer to the suction wall. The baffle designs are shown in Table 6.3.

Table 6.3: Description of the baffle designs.

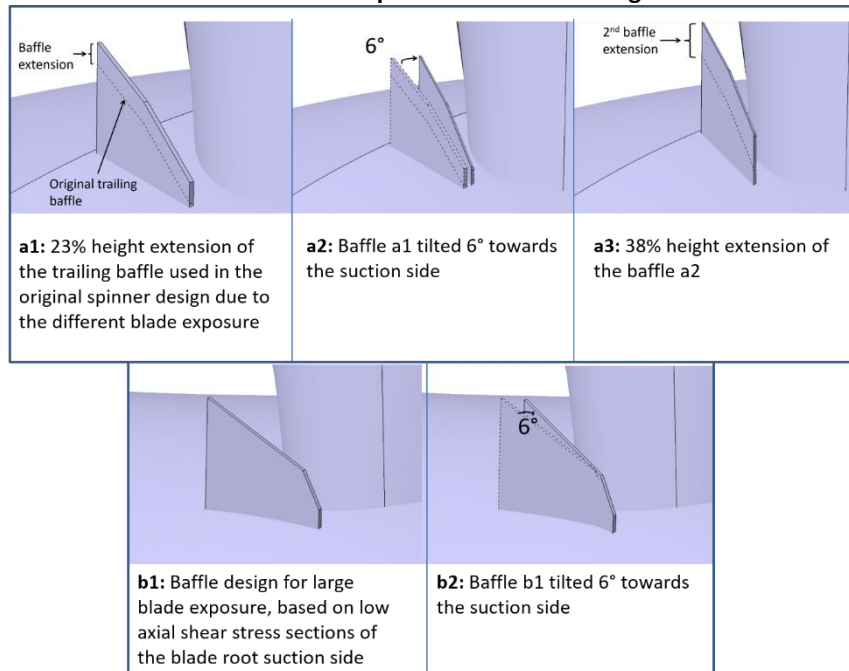


Table 6.4: Relative propeller efficiency variation (Efficiency values below the one of the spinner without a baffle are shown in red).

Spinner type \ Baffle type	a1	a2	a3	b1	b2
test 16 (+0.56% η)		-1.36% η		+0.81% η	+0.46% η
T2 (+0.88% η)	+1.71% η	+1.88% η	+1.40% η		
T4c (+0.74% η)	+1.47% η	+1.55% η	+1.20% η		
T4d (+0.60% η)		+1.76% η			
T5 (+0.59% η)		+1.89% η			

As expected, the combination of a baffle acting as flow deflector and an efficient tangent spinner resulted in even larger efficiency improvements. Table 6.4 depicts the efficiency variations throughout the set of simulations that combined a trailing baffle and a spinner design with high efficiency. The first baffle design (a1) was tested in combination with T2 and T4c spinners where the relative propeller efficiency was increased up to 1.71% and 1.47% more than the control efficiency respectively. After tilting the baffle 6° an even larger increment on the relative propeller efficiency was produced on the T2 and T4c spinners where the a2 baffle increased their efficiencies in 1.88% and 1.55% respectively, compared to the original designs used as control.

Given the results obtained with the a2, the same baffle was tested on the other tangent spinner designs that exhibited large efficiencies as well. The a2 baffle produced the largest increment in efficiency (1.89%) when combined with the spinner T5. Even when T5 had an efficiency of 0.59% without the baffle, it seemed that not only the separation was delayed but also the negative effect of the low pressure region caused by the hub vortex.

The baffle type a3 showed that the height extension of the tilted baffle decreased the efficiency for both T2 and T4c compared to the a2 type; however, the use of the baffle maintained efficiency values larger than the ones without any baffle.

Despite being tested with spinner cases that presented already large values of efficiency without any device for boundary layer control, baffle a2 consistently increased the relative propeller efficiency when tested with tangent designs. However, when tested in combination with a spinner design of large blade exposure such as the test 16, the propeller performance was affected instead of being improved (-1.36%). The objective of using a baffle was to prevent the boundary layer from separating in the blade root suction side; nevertheless, a different blade exposure required a specific baffle design. When the test 16 was simulated in combination of baffles designed for its specific blade root loading, both baffles b1 and b2 induced efficiency values of +0.81% and +0.46% respectively. It was evident that the baffles that were designed to match the areas of low axial shear stresses of test 16 performed significantly better than the ones designed for tangent spinners.

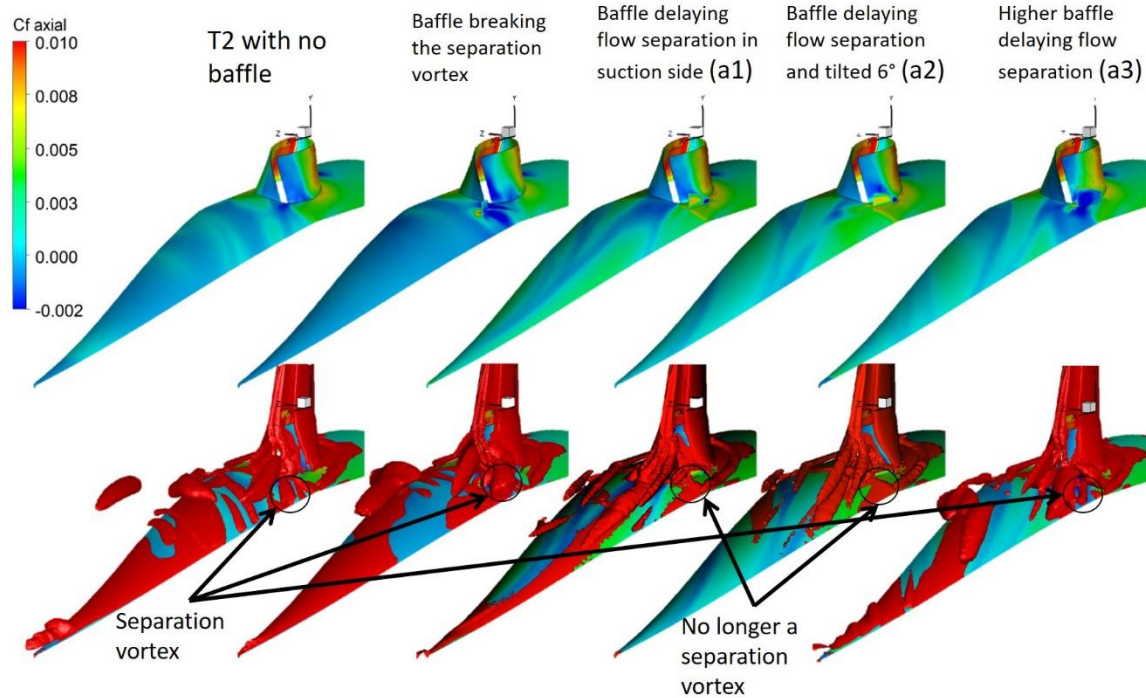


Figure 6.12: T2 spinner isosurface of Q criterion 470000 s^{-2} with different baffle designs.

Although the axial shear stresses were increased on the last three spinners of Figure 6.12, a2 baffle was the only case that showed relatively large values of axial shear stresses close to the trailing edge on the suction side. The Q criterion isosurface of 470000 s^{-2} was another indication of the flow separation delay that caused the increment of axial shear stress especially around the region of the spinner close to the baffle. The absence of the separation vortex suggested a weaker interaction among the transverse flow coming from the blade root pressure side and the spinner boundary layer.

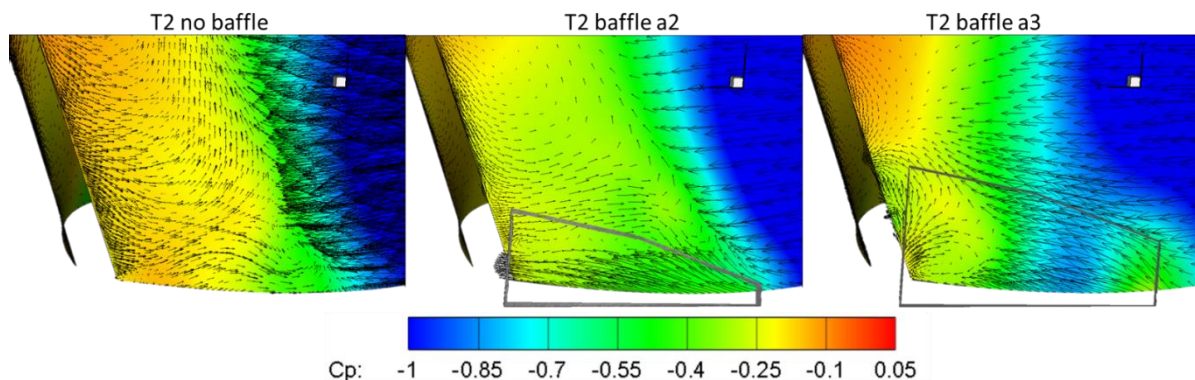


Figure 6.13: Blade root suction side axial shear vectors and pressure distribution due to a trailing baffle.

As observed in Figure 6.13, both a2 and a3 trailing baffles increased the viscous shear forces of the lowest part of the suction side. However, as soon as the baffle got increased in height (a3), the beneficial contribution decayed in a significant way despite that it kept the flow attached further downstream over a larger area compared to the a2; in fact, baffle a2 seemed to keep attached flow longer than the a3 only at the junction of the root suction side and the spinner. In part, the baffle a3 decreased the relative propeller efficiency because independently of the separation delay, the lowest part of the blade still faced separated flow most likely due to the accelerated flow that passed throughout the channel between the blade and the baffle. In addition, the negative C_p values that resulted from the attached flow did not produce effective thrust but more an increment in torque.

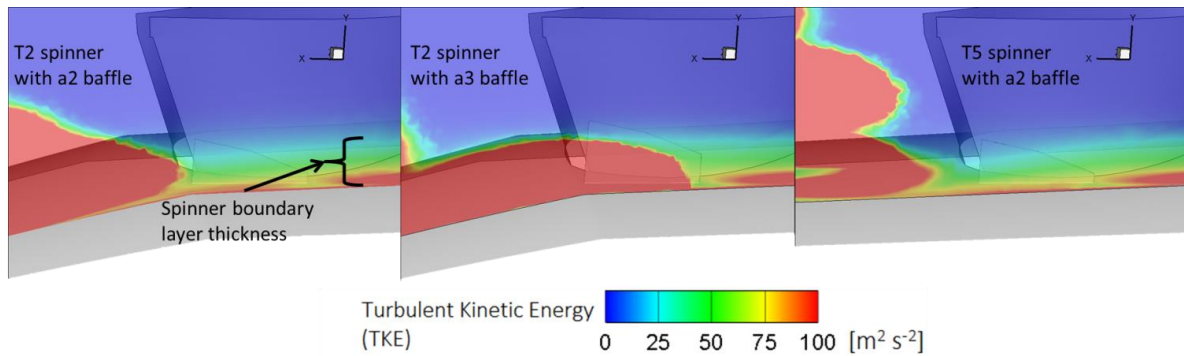


Figure 6.14: Baffle height (a2 and a3) compared to the spinner boundary layer thickness of an axial plane tilted 20° around the rotational axis. Very low values of TKE are shown in order to depict the boundary layer.

The relatively low values of turbulent kinetic energy shown in Figure 6.14 helped to depict the boundary layer thickness and its displacement thickness. Both baffles seemed to be acting within a radial location that matched the size of the boundary layer thickness observed at the spinner, especially on the suction side of the blade. While the height of the baffle a3 might have surpassed the boundary layer thickness, a more significant indication of its poorer performance was the increment of turbulent kinetic energy observed in the shear layer of the external part of the baffle a3.

Similar to the efficiency improvement found in T2, baffle a2 in combination with the spinner T5 resulted in the largest relative propeller efficiency found throughout the research and the performance upturn was also related to the delay in flow separation occurring at the lowest radial position of the suction side and hence also occurring over the entire spinner wall (Fig. 6.15).

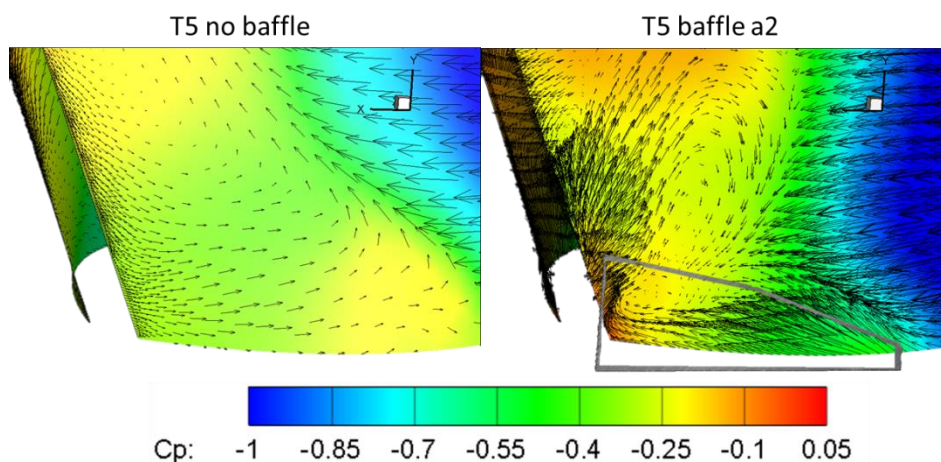


Figure 6.15: Blade root suction side axial shear vectors and pressure distribution due to a2 trailing baffle.

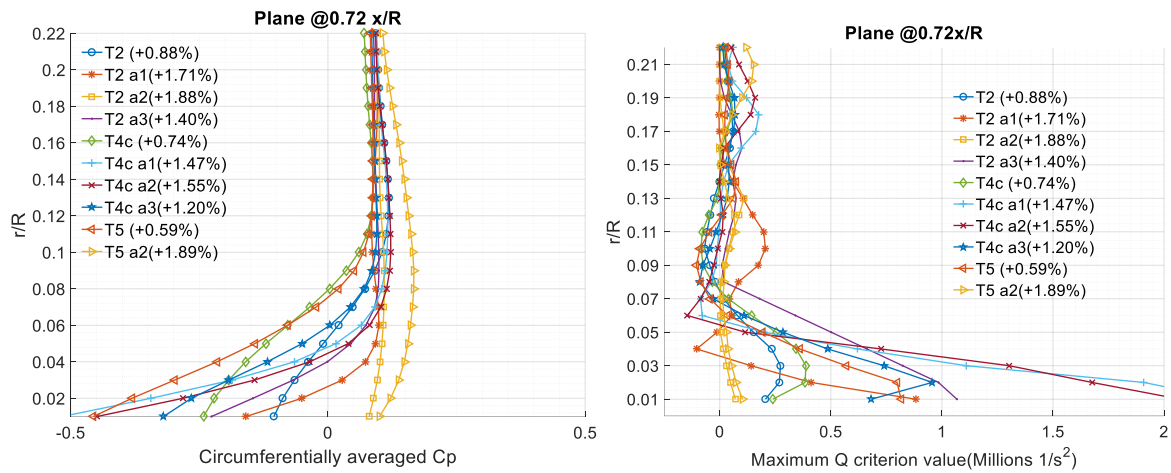


Figure 6.16: Effect of the trailing baffles on pressure and Q criterion of the most efficient spinner designs.

The positive effect that the baffle had on the propeller performance was observed in Figure 6.16. This was especially noticeable on the pressure depicted by both T5 a2 and T2 a2 (Spinners with baffles) where only positive values of C_p were encountered behind the spinner. Independently of the maximum increment in efficiency achieved at the end, T5 showed the largest improvement when comparing the spinner alone and the spinner with the baffle (T5 a2). The reason is that despite the large efficiency showed in a no-baffle configuration, T5 started to have negative pressure coefficients at a relatively early radial position which gave more room for improving the efficiency once that the pressure recovery was enhanced by one of the baffles.

The low values of pressure were caused by both the early flow separation and the vortices formed by it. As the flow encountered a straighter path induced by the baffle a2, the pressure recovery improved showing only positive values of C_p at all radial positions of the plane for both T2 and T5. As a result, the maximum Q criterion values for low radial positions got decreased, indicating that the vortex strength and formation was also diminished.

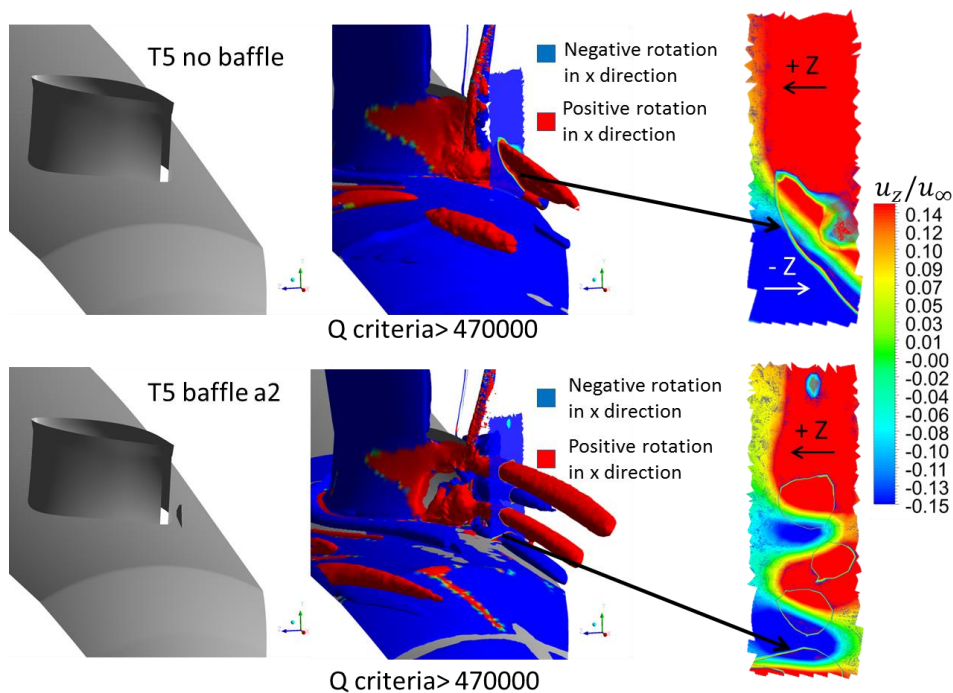


Figure 6.17: Vortical structures sign of rotation behind the T5 blade root with and without the a2 baffle.

Figure 6.17 shows the vortical structures and their rotational sign observed when the a2 baffle was tested on the spinner T5. It was clear that the crossed flow formed mostly due the flow separation on either pressure or suction side of the blade root was the reason of the vortical structures observed with an isosurface of Q criteria of $470\,000\text{ s}^{-1}$. Even when 4 relatively strong vortices were formed due to the different signs and magnitude of tangential velocities, the positive values that was observed close to the spinner wall seemed to be the main cause of the performance improvement because it indicated an evident change in direction of the shear layer.

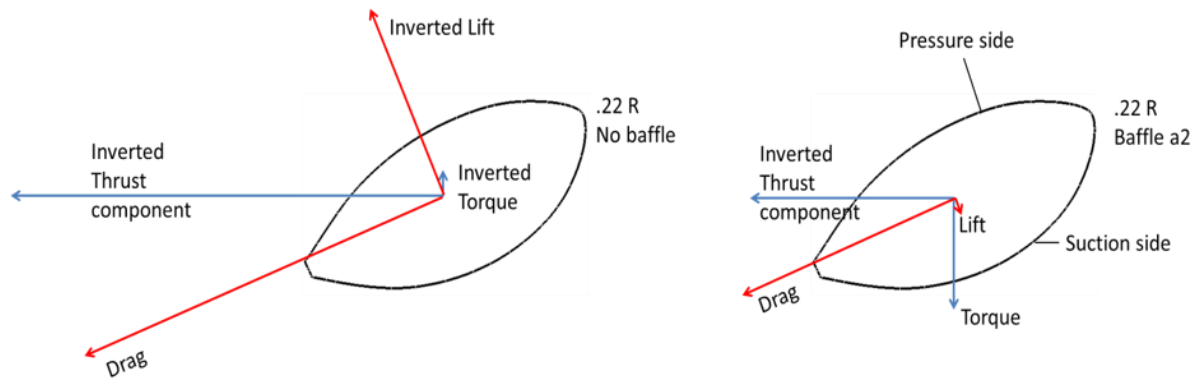


Figure 6.18: Schematic blade force representation of the T5 spinner with and without a2 baffle at 0.22 R.

Despite the propeller improvements in terms of efficiency after combining the tangent spinner T5 with the baffle a2, the lower part of the blade still showed a negative thrust component as shown in Figure 6.18; however, the negative thrust component was decreased after placing the baffle. The large negative thrust or the reversed lift were repeatedly observed among the tests without a baffle indicating their relatively poorer performance. The large pressure side loading altogether with the flow separation occurring at the suction side explained inverted lift direction.

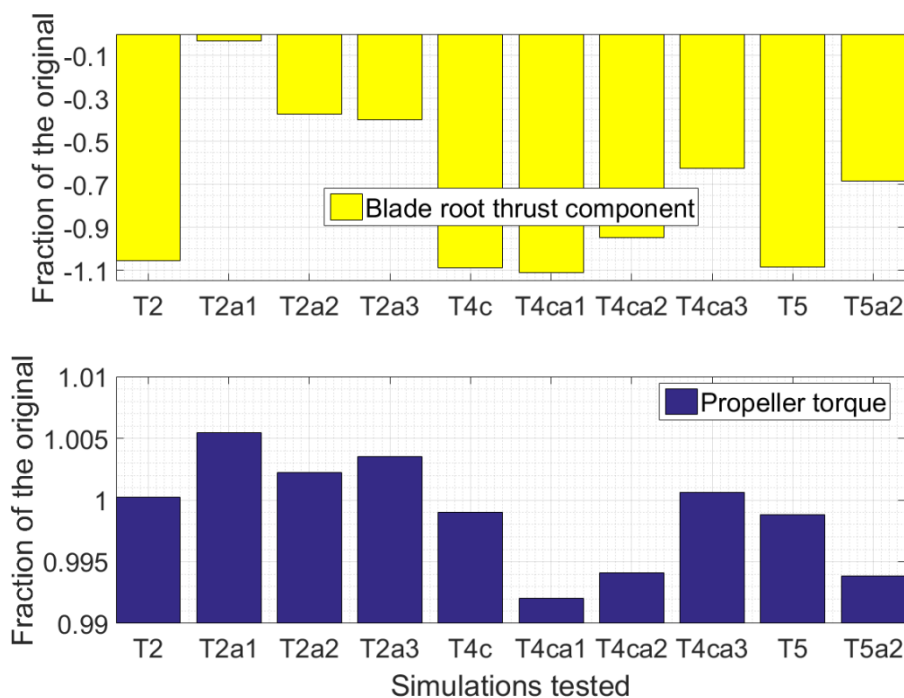


Figure 6.19: Baffle effect on the blade root negative thrust component and the propeller torque (Most efficient cases).

The most efficient cases of baffle-spinner combinations decreased significantly the negative thrust component induced by the blade root (Below 0.254 R). Figure 6.19 depicts the magnitude of the thrust component integrated over the blade root surface in both pressure and suction sides. The direction of the thrust was not changed, but the baffles reduced the negative thrust component when combined with T2, T4c and T5 tangent spinner designs. Just as observed among the spinners that were modified in length and height, the larger propeller efficiencies were found among the spinner-baffle configurations that decreased the spinner drag regardless the increment of torque that typically came after delaying flow separation in the spinner. This was clearly related to the almost negligible amount of torque increased by the blade root, compared to the torque contribution of the rest of the blade.

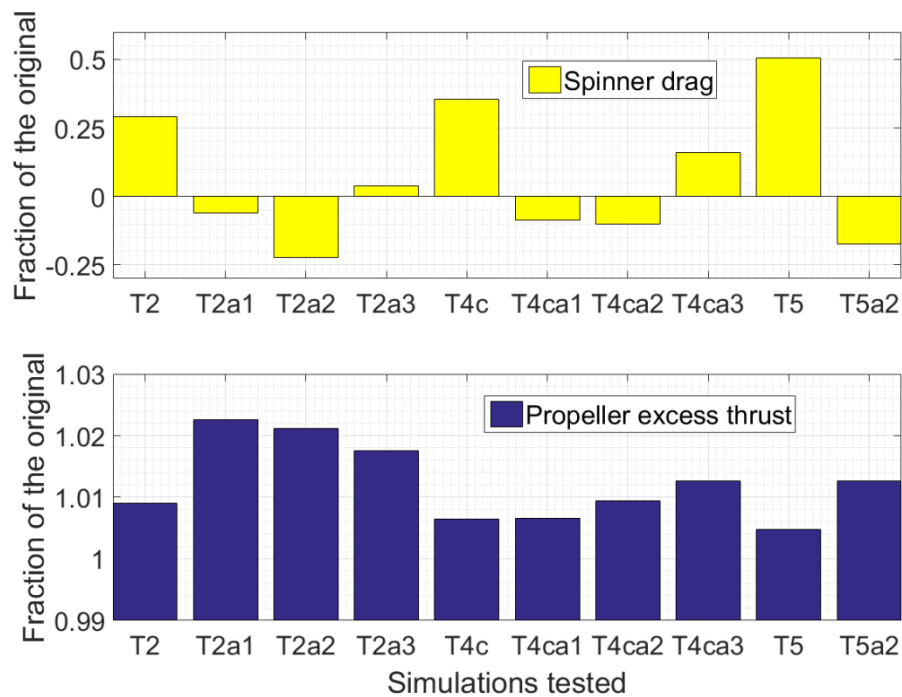


Figure 6.20: Baffle effect on spinner drag and propeller excess thrust (Most efficient cases).

As observed with shorter and longer spinner tests (Fig. 6.20), the spinner drag reduction was directly reflected on the propeller excess thrust; however, the largest efficiencies were observed on spinner designs that not necessarily presented the largest excess thrust. If the T2a1 is taken as an example, it is possible to see that even when the negative component of the thrust was reduced to a value close to zero, the spinner induced an increment of the total propeller torque of barely 0.5%. On the other hand, the relative spinner drag reduction of 105% increased the propeller excess thrust around 2.3%. In other words, the performance improvement of the spinner T2 with the baffle a1 was based on the larger relative increment of excess thrust that outweighs the gain in propeller torque.

T5 in combination with baffle a2 presented the largest relative propeller efficiency not only by decreasing the spinner drag nearly as much as the T2, but also because it kept lower values of propeller torque.

6.2 Spinner grooves and their effect on the propeller performance

The utilization of passive boundary layer control methods such as the baffles represented a relatively large improvement in the relative propeller efficiency when compared to the one obtained by re-designing only the spinner geometry. This emphasized the relevance of studying mechanisms that can prevent the boundary layer separation not only by straightening the flow as the baffles did, but also

maintaining larger velocities close to the spinner wall due to the increased momentum of the boundary layer.

Commonly, features such as longitudinal vortices are repeatedly chosen among passive boundary layer control methods due its relative simplicity to energize the low momentum wall flow since 1950 [45]. Passive methods tent to use the energy of the rotating flow such as vortical structures to exchange momentum with the boundary layer as shown by G. Godard [46] or earlier by Lin [47]. However, the vortical structures that were formed at the blade root of the pusher propeller used for this research were reducing the momentum of the boundary layer instead of increasing it. This induced early flow separation on the spinner until the baffles were used as flow deflectors. New vortical structures were formed because the direction of the blade root outflow jet changed direction, especially close to the wall.

The most efficient cases found in this research exhibited attached flow over most of the path followed by the boundary layer; however, given that the flow has to be inevitably detached, the longer that the flow separation delay is, the largest pressure recovery that could be encountered. Besides the longitudinal vortices, the cavity method has been used before as a mechanism to decrease pressure drag, using the same boundary-layer-energizing concept that delays separation or increase the momentum of the attached flow [45].

The cavity concept in the form of a contoured transversal groove has also proved to work as a boundary layer control tool according to A. Mariotti [48]. Due to the axisymmetric boat-tailed body setup of Mariotti's experiment, the concept was adapted to the pusher propeller configuration of the present research. The grooves worked under the concept of 'Trapped vortex', where a steady structure with a constant vorticity creates a recirculation region separated from the outer flow that might increase the downstream boundary layer momentum. Although the transverse groove technique uses the concept of rotating flow, there is no momentum exchange among the boundary layer and longitudinal vortices, instead, the benefit should come from the relaxation of the no-slip condition in the region close to the wall that would reduce momentum losses around the edge of the recirculation region [48].

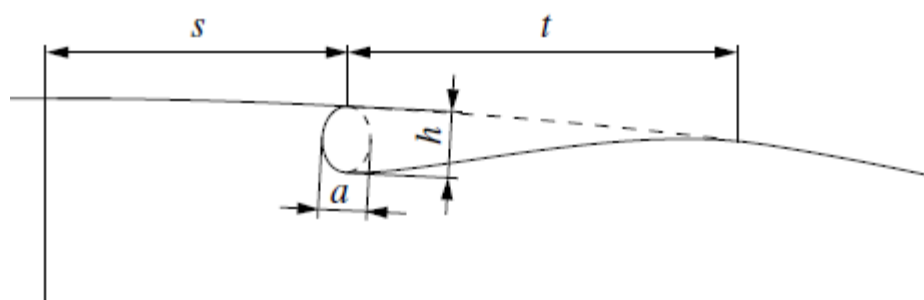


Figure 6.21: Groove dimensions nomenclature, Mariotti [48].

Four parameters were taken into account in order to designate the position and size of the contoured grooves. Figure 6.21 shows Mariotti's experiment designation of the geometry where the main cavity was an ellipse with a minor axis a and a major axis h . The major axis or cavity depth equals one third of the boundary layer thickness; while the minor one represents $2/3$ of h . The letters s and t , indicated the distances prior and after the cavity respectively, where s/D and t/D had values of 0.107 and 0.129 respectively for Mariotti's configuration. The maximum thickness of the axisymmetric body was represented with the letter D .

The groove location was suggested to be slightly upstream the boat-tailed geometry. In order to use the groove concept in the propeller configuration, the groove was located in the spinner since it was the region where the thickness decreased rapidly (Boat-tail). Both configurations, before the blade and

after the blade, were simulated in order to obtain a broader perspective of the cavity effect on the boundary layer (Figure 6.22).

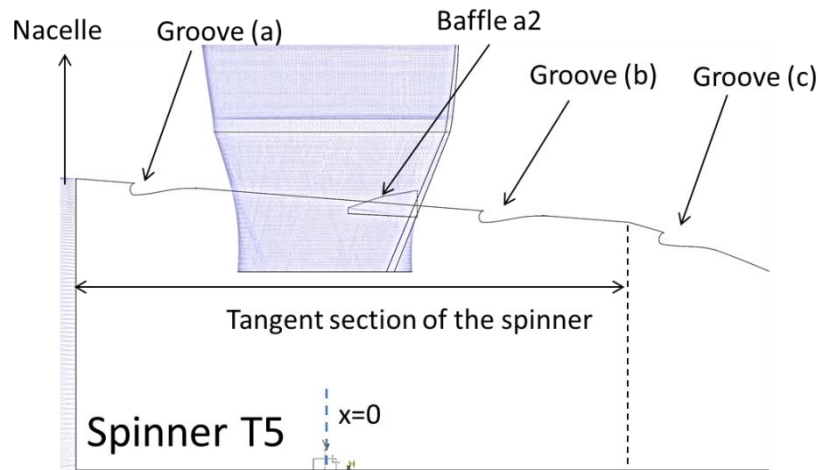


Figure 6.22: Groove positioning in tangent spinner T5.

Table 6.5: Effect of grooves on relative propeller efficiency

Groove type in T5 with baffle a2	Axial position respect to blade origin x/D	Groove depth h/D	Depth/Boundary layer thickness	Relative efficiency variations (η)
a1	-0.287	0.0087	0.28	+1.92%
a2	-0.287	0.0131	0.41	+1.81%
a3	-0.287	0.0175	0.55	+1.82%
b1	0.238	0.0087	0.20	+1.90%
b2	0.238	0.0131	0.30	+1.72%
b3	0.238	0.0175	0.40	+1.74%
c1	0.508	0.0087	0.10	+1.79%
c2	0.508	0.0131	0.15	+1.76%
c3	0.508	0.0175	0.20	+1.82%

Table 6.5 shows the effect of grooves on the relative propeller efficiency when tested on spinner T5a2 where the propeller performance was mainly improved when the cavities were located before the expansion section of the spinner (Grooves a, b). Taking into account that the relative propeller efficiency with the spinner T5 and baffle a2 was already 1.89% higher than the original one, only the addition of Grooves a1 and b1 managed to improve the performance beyond the no-groove value.

Just as observed for the baffles, the efficiency increment induced by the grooves was related to the increased pressure coefficients reached at the spinner tip. Figure 6.23 shows the axial velocity contours of the T5 spinner at the three different locations of the grooves with minimum depth. Groove a1 showed larger axial velocities close to the spinner end than the spinner without groove or than any of the other groove positions tested. Despite the flow separation encountered in the spinner end of all of the cases, the increased velocities allowed a larger pressure recovery as the flow expanded.

The cavities that induced greater efficiencies at the shortest depth represented around 0.28 times the thickness of the boundary layer formed at the nacelle-spinner junction. As their depth increased, the cavities induced lower overall efficiency than the least deep cases that represented 0.41 and 0.55 times the boundary layer thickness; however, the groove at position c showed larger improvement at the deepest cavity, contrary to the results observed for the other groove locations. It has to be emphasized that the boundary layer thickness at the expansion section of the spinner had gotten around 2.6 times

thicker than the boundary layer encountered at the other groove positions. This changed the depth to boundary-layer-thickness ratio to 0.1, 0.15 and 0.2 respectively, being the last of them the one corresponding to the deepest cavity of groove c and the closest to the ratio suggested by Mariotti.

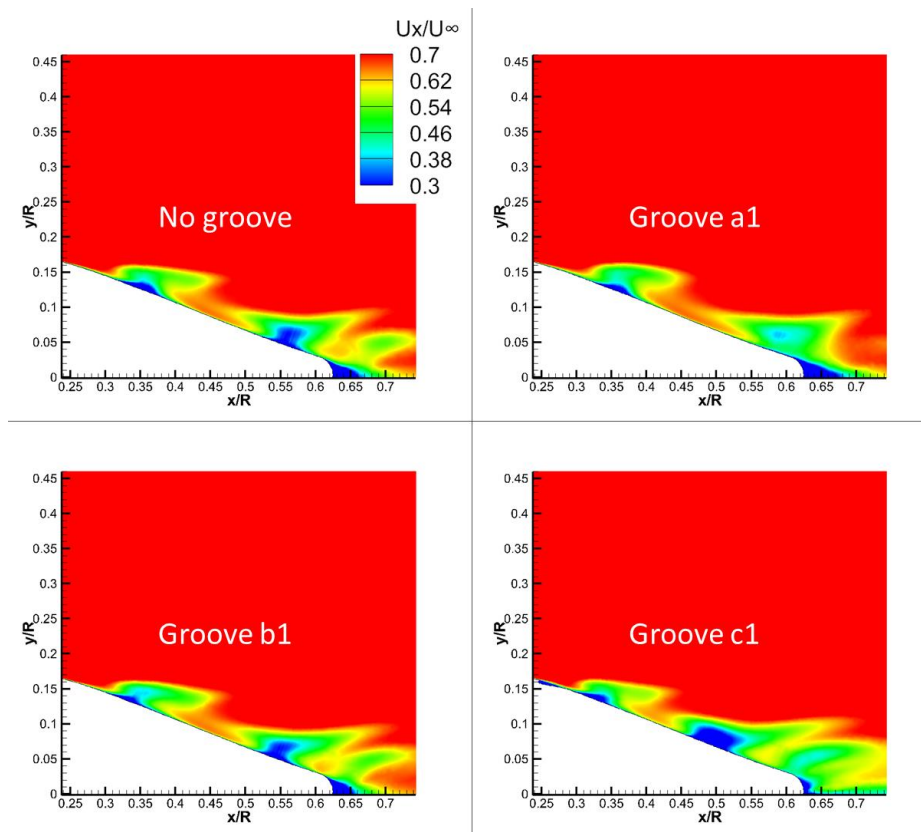


Figure 6.23: Groove effect on the axial velocity of the T5 spinner end.

From a stability perspective, the shear layer perturbations are unwanted since those typically affect the stability of the vortex formed in the cavity, as suggested by Zannetti [49]; however, the simulations carried out showed a recirculation region for all the grooves even when secondary separation was present, especially at the deeper cavities (Fig. 6.24).

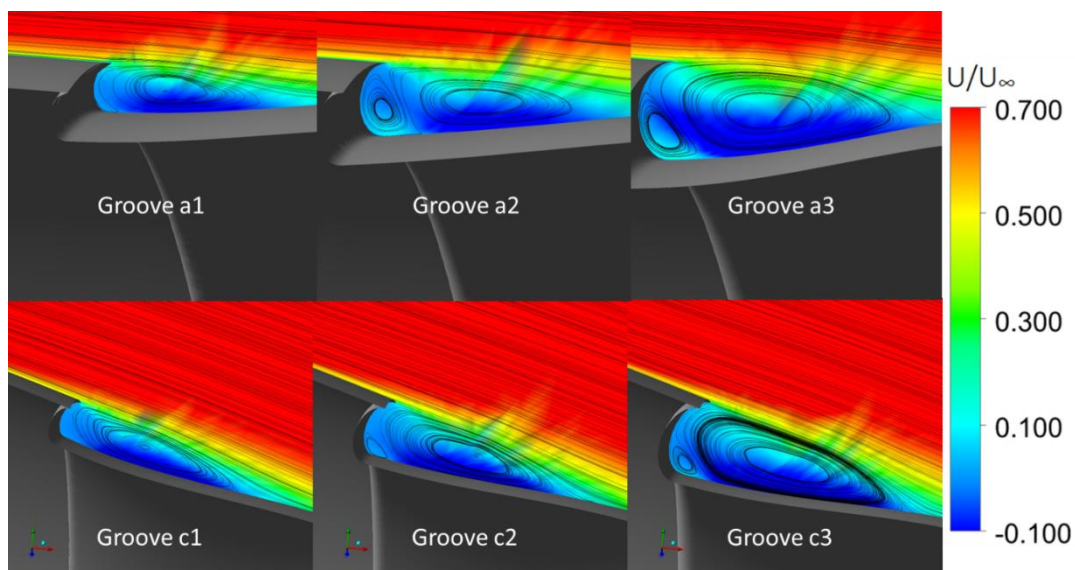


Figure 6.24: Recirculation regions for Groove types *a* and *c*.

A region of secondary separation was observed in both *a* and *c* types of grooves (Fig. 6.24) but it was certainly larger in deepest cavities of type *a*. Even when both types presented the same depth for the three variations, their different depth to boundary-layer ratio seemed to prevent secondary separation from happening inside the groove cavity. The cavity method effectiveness relied on the concept of relaxing the no-slip condition of the shear stress layer; hence, the secondary separation would represent unwanted effects not only from a stability perspective but also from an energetic one since the momentum that could potentially be transferred to the boundary layer would be decreased as the region of secondary recirculation grows.

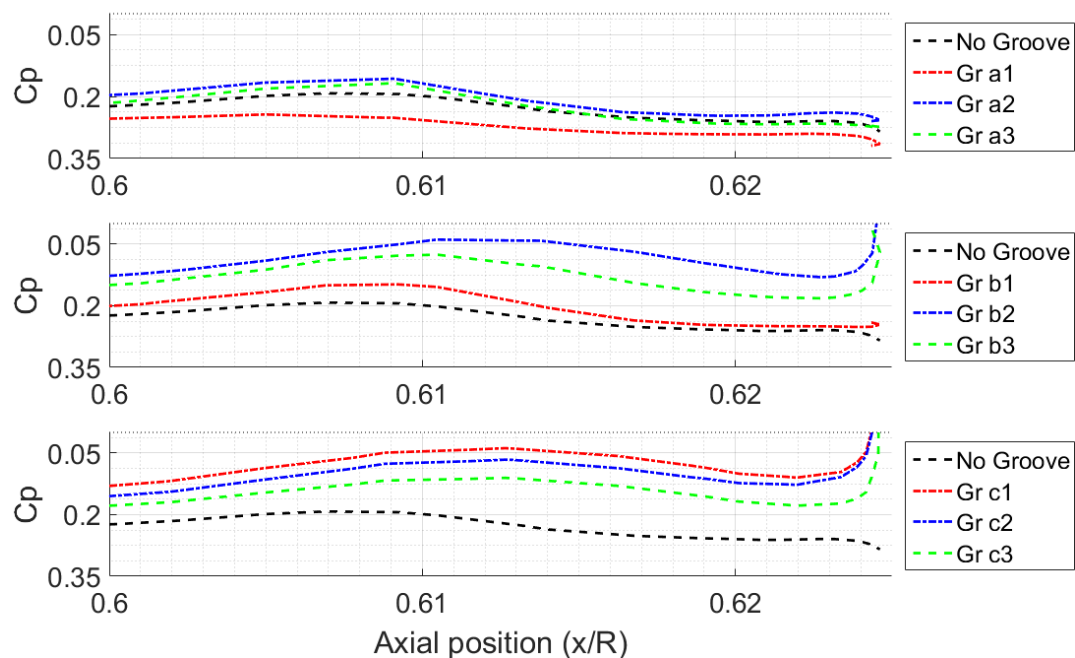


Figure 6.25: Effect of the groove depth on the pressure coefficient of T5 spinner end (After 97% of its length).

The pressure distribution along the spinner T5 and the baffle a2 was improved only at the very last part of the spinner when combined with the groove design placed at the most upstream position. Figure 6.25 shows the pressure coefficients distribution for each one of the groove designs where only case *a1* exhibited larger C_p values along the last 5% of the spinner which decreased the spinner drag at the same time that extended the gain in propeller efficiency; however, the gain in efficiency was as much as 0.03% since most of the attached flow was already expanded. Larger pressure coefficients have been repeatedly observed on spinner designs that performed relatively better than others accompanied of a negative tangential direction of the shear stresses (Opposite to the spinner direction of rotation); however, the apparent negative tangential direction was observed in the spinner rotational frame of reference. This is important because in order to extrapolate the beneficial effects caused by the grooves to other pusher propeller designs with more flow separation, not only the pressure distribution have to be assessed but also the change in direction that was induced on the shear layer.

Figure 6.26 depicts the shear stress contours that maintained a diagonal-like path in a negative tangential direction and that got straightened towards the spinner tip downstream ahead, especially for the spinner with the largest efficiency. This apparent change in direction was observed because the shear stress vectors were the result of the interaction between the rotating spinner and the straight velocity streamlines of the flow that was relatively unaffected by the blade downwash and by the positive tangential velocity induced by the spinner rotation. In other words, the direction of the blade root outflow would seem to be relatively aligned with the free stream direction for a stationary observer when compared to the rest of the flow coming from other parts of the blade. Nonetheless, at

the spinner tip the tangential velocity due to the spinner rotation was negligible and the direction followed by both the shear stresses and the velocity streamlines was similar independently of the reference frame used to look at them. Hence, given that the effect of the groove was mainly observed at the spinner end, a shear stress contour that is aligned with the free stream direction would inevitably mean larger pressure coefficients produced by the steeper curvature encountered by the attached flow.

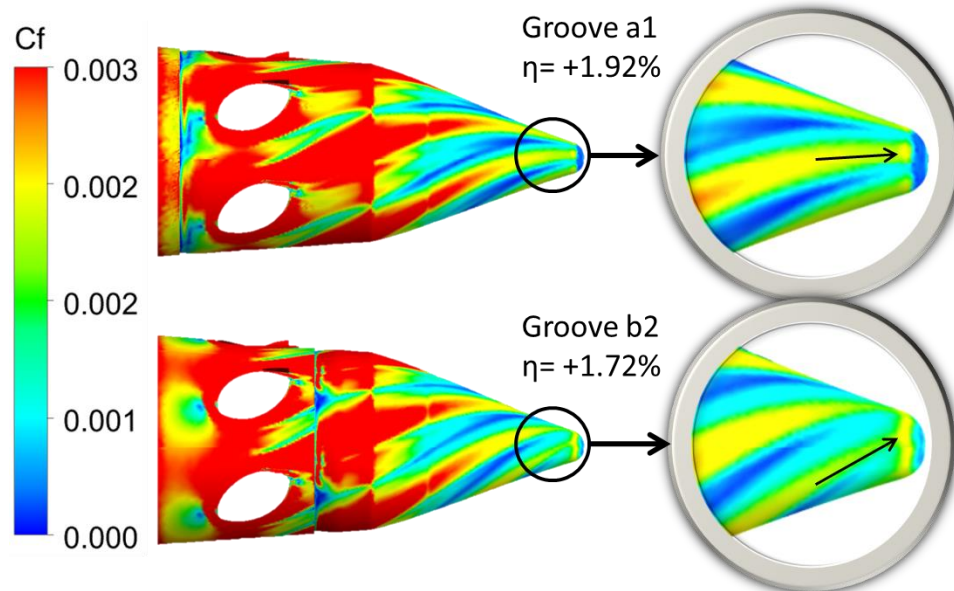


Figure 6.26: Comparison of best and worst groove-induced relative propeller efficiency and their respective shear stress coefficient contours (Spinner T5 with baffle a2 shown in both images).

Since the spinner T5 in combination with baffle a2 showed attached flow over almost the entire spinner, the transversal grooves based their effectiveness on the pressure recovery that was especially achieved at the end of the spinner due to the redirection of the boundary layer. However, the method of cavities found in literature was mostly focused on the delay of flow separation. This can be observed better in less efficient cases in Figure 6.27.

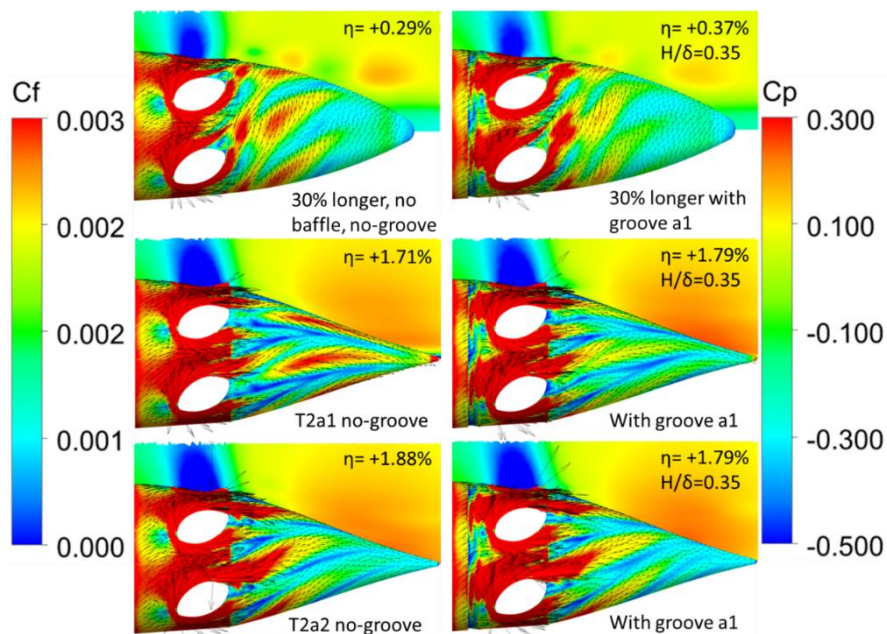


Figure 6.27: Groove a1 effect on friction and pressure coefficient contours of 30% longer and T2 spinners (Relative propeller efficiency induced by each of the spinner is shown at the upper right corner).

The results obtained when the groove a1 was tested on spinner designs that were not as efficient as the T5 were mostly positive and the pressure coefficients observed in the vicinities of the spinner surfaces were either larger or spread more evenly along the spinner. However; the second most efficient spinner (T2 with the baffle a2) decreased the efficiency regardless the larger values of pressure coefficients observed in Figure 6.27. The decrement in efficiency was related to the location at which the flow expansion took place. For the case without a groove, the maximum values of C_p were shifted further downstream in the spinner compared to the maximum values observed in the spinner with the groove (Fig. 6.28). The addition of the groove to an already efficient design such as the T2 did not induce significant changes in the way the flow separated; nevertheless, the direction of the velocity streamlines looked from a stationary perspective were aligned with the rotational axis due to the small blade root loading changes. This alignment increased the adverse pressure gradient encountered by the boundary layer increasing the C_p values locally at the expense of decreased values at the spinner tip.

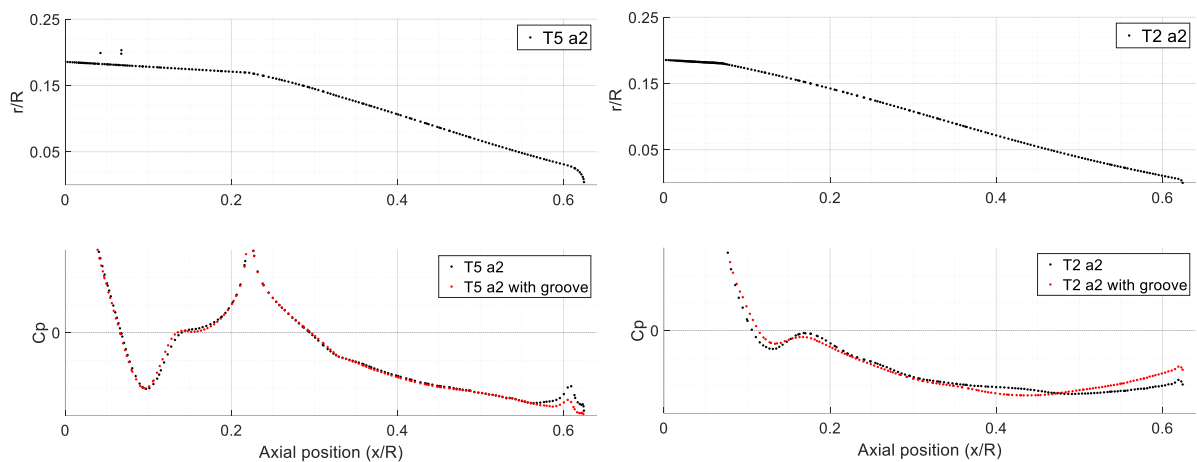


Figure 6.28: T5a2 and T2a2 pressure distributions with and without groove a1 (Sample taken at 20°).

Part of the blade root loading modification caused by the groove started in the root leading edge with a different pressure distribution at the stagnation point (Figure 6.29). For most of the cases, the cavities decreased the blade root loading especially at the suction side. However, the reduction of the blade loading seemed to be produced by a large pressure region that pushed part of the flow away from the blade root. The large pressure region shown in Figure 6.29 extends from the stagnation point as the result of the expansion encountered by the flow after passing over a well formed trapped vortex.

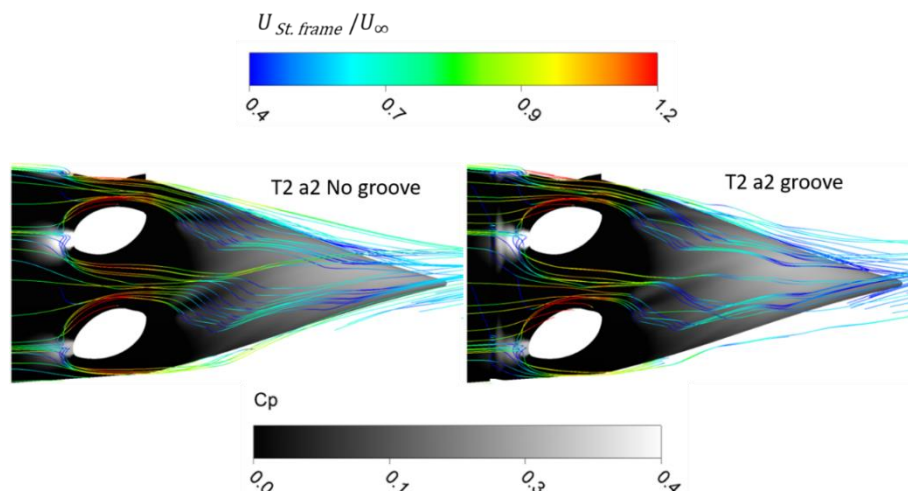


Figure 6.29: Groove effect on pressure contours of T2 a2 spinner design and stationary frame velocity streamlines.

The concept of the grooved cavities enhanced the spinner efficiency due to a beneficial redirect of the flow passing between the blades at the lowest radial positions. In fact, the change in direction was the same concept used by the baffle addition in order to improve the spinner efficiency. Although a small increment in the relative propeller efficiency was observed, such small amounts would very likely be within the uncertainty range. This is why further analysis need be made in order to find a better design for the cavities and maximize the pressure recovery increment achieved by them, especially because the transversal groove was placed in the 360° of the spinner as encountered in literature.

7 Conclusions and recommendations

The present work has placed particular importance on the spinner aerodynamic design in order to enhance the performance of a pusher propeller configuration. The research has been focused on the aerodynamic shaping of the spinner in order to provide a better understanding of the nacelle-blade-spinner interaction in cruise conditions. The set of experiments were carried out by performing a series of steady-state Reynolds-averaged Navier-Stokes (RANS) CFD simulations.

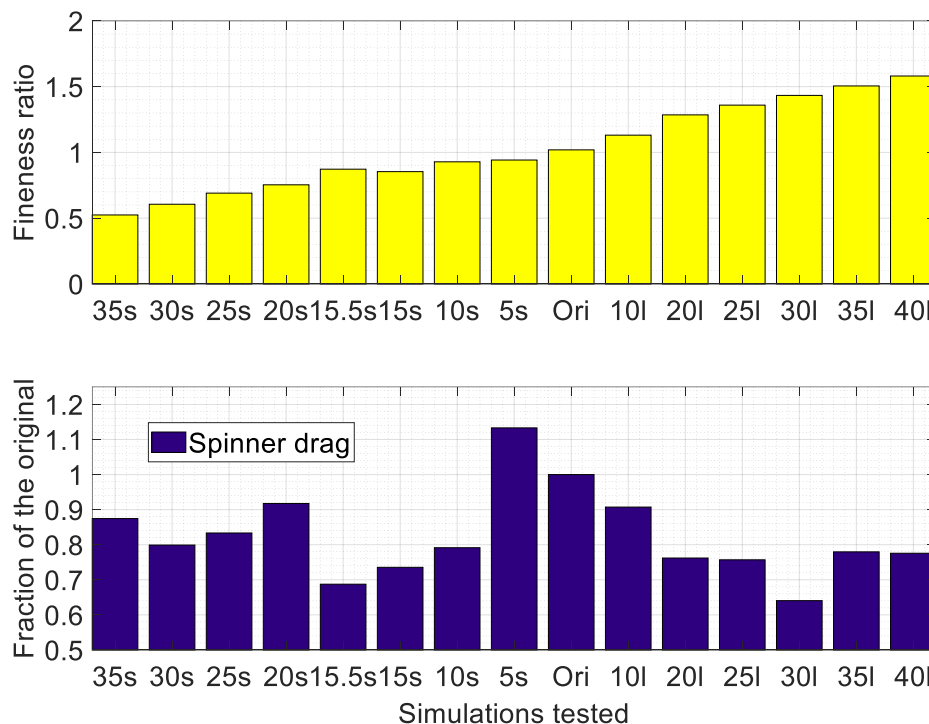
The model tested was composed of nacelle and spinner that hosted 6 blades. Due to the axisymmetric nature of the model, the simulations were performed using periodic boundary conditions that replicated the results obtained for one blade saving significant computational power. The mesh was selected by means of a grid dependence study that followed both, classic and least squares approaches to the grid convergence index methodology (GCI). The order of convergence exhibited far more realistic values with the least squares approach in comparison with the classic fit that suggested super convergent orders, pointing out the greater accuracy of comparing four or more grids using the least squares approach when moderate refinement/coarsening ratios are available. The volumetric and wall refinement did not show a significant effect on the excess thrust of the entire propeller; however, the hub region certainly presented the variations that induced most of the changes in propeller performance. In order to accurately capture the information around the rotor hub, the mesh was especially refined close to the spinner and blade root. Comparing the zero grid-spacing values obtained with the GCI, the local hub refinement reduced the spinner drag relative error of the finest grid by one order of magnitude, going from 7%-8% to 0.5% without major changes in thrust prediction. The hub refinement allowed a reliable assessment of the spinner-induced propeller performance variations using 3.3 times less number of elements in the mesh with negligible information loss in the slipstream wake.

The setup was simulated for different spinner designs in order to assess their effect on the propeller performance. In order to isolate the spinner effect, neither the blades nor the nacelle were modified whatsoever. The first of the series of simulations was focused on the effect of spinner shortening where the flow separation observed originally on the control design was mostly aggravated as the spinner length was shortened and the fineness ratio was decreased. Given that the percentage of reduction in length exceeded the reduction in spinner diameter, shorter spinner induced steeper adverse pressure gradients; however, out of 7 cases that reduced the spinner length from 5% to 35%, 5 increased the propeller thrust, 6 decreased the spinner drag of the original design and 3 cases increased the overall relative propeller efficiency by a maximum of +0.27%. Spinner length reduction had an overall relative efficiency improvement on the propeller performance mostly due to the reduction of the spinner drag. Considering that flow separation was encountered for all the spinners with reduced length and even in the original one, it can be concluded that the performance enhancement of shorter spinner was mostly related to the reduction of pressure drag that was very sensitive to the formation of a hub vortex at the rear part of the spinner. As the spinner length was decreased, the low C_p region caused by the hub vortex started to be further away since the part of the hub vortex that showed similar Q criterion values was formed at approximately the same axial position independently of the spinner tested. The detrimental performance effects, especially among shorter spinners, emphasized the hub vortex effect on the last portion of the spinner. It was observed that the last 10% of the spinner length went from representing only 5.2% of the original spinner drag to 9.5% in the worst cases that exhibited the largest Q criterion values for the hub vortex. This meant that for designs with noticeable hub vortex influence

such as the 5% shorter spinner case, even when the flow was mostly separated, the increment in spinner drag was 80% due to the last tenth of the length, leading to an overall relative propeller efficiency reduction (-0.33%).

The propeller efficiency variation observed for shorter spinners not only depended on the spinner itself, but also on the blade portion that was hosted by the spinner. As the spinner diameter decreased for a fixed length, so its fineness ratio; however, despite the benefits showed in terms of pressure recovery, a lower spinner diameter also meant larger blade root exposure. This was not an optimal aerodynamic condition since the blade was not being redesigned together with the spinner. The torque variation was assessed among 4 spinners with fineness ratios between 0.7 and 0.78 and a constant length of 20% shorter than the original. Despite the negative thrust generated at the blade root, lower diameter spinners showed the largest propeller efficiency. This emphasized the importance of low spinner drag in the propeller performance. Larger blade root exposure seemed to affect more the suction side of the blade than the pressure one in terms of flow separation thus increasing wetted surface and the aerodynamic loading of the root pressure side. Larger blade root exposure resulted in increased torque values, since both the magnitude and the lever arm of the positive tangential force component were reduced at low radial positions of the blade. Torque variations assessment was limited to the blade root since the spinner contribution showed to be almost negligible (One order of magnitude lower).

Longer spinners improved the propeller performance in a more significant way compared to the short ones, mostly because the flow separation over the spinner was notably delayed. In 6 out of 6 cases where the propeller was tested with longer spinners (10% to 40% longer) the spinner drag was reduced compared to the one of the original design and in 5 out of 6 cases it showed larger relative propeller efficiency than the original design with a maximum efficiency improvement of +0.29%. The blade exposure was lower than the one of the original spinner; nevertheless, it was very similar among longer spinners. This is why the torque variations were considered negligible. The spinners with larger fineness ratios allowed maintaining less steep curvature thus decreasing the adverse pressure gradients induced by the attached flow. This was independently of the few reverse flow that was observed at the very last portion of the spinner or not observed at all.



Relation between spinner fineness ratio and spinner drag.

Generally speaking, the pressure drag reduction was related to large values of C_p nearby the spinner wall; however, the pressure drag of shorter spinners depended mostly on the formation of the hub vortex, while the pressure drag improvement on the longer ones depended on the pressure recovery at the spinner. Both shorter and longer spinners exhibited early flow separation on the suction side of the blade root portion, which was consistently observed regardless the efficiency variations of the propeller. This early separation caused the blade root to induce a negative component of thrust and a positive moment (In direction of the rotation). Given that the relative propeller efficiency was improved in many of the test cases, it is important to emphasize that the largest contributions to the propeller performance came from spinner drag reductions rather than from propeller torque ones. This became more evident after looking to the standard deviation of the thrust and torque differences respect to the control values throughout the design cases tested. While the excess thrust values deviated 0.25% from the control value, the torque varied only 0.12% after the simulation of shorter and longer spinners.

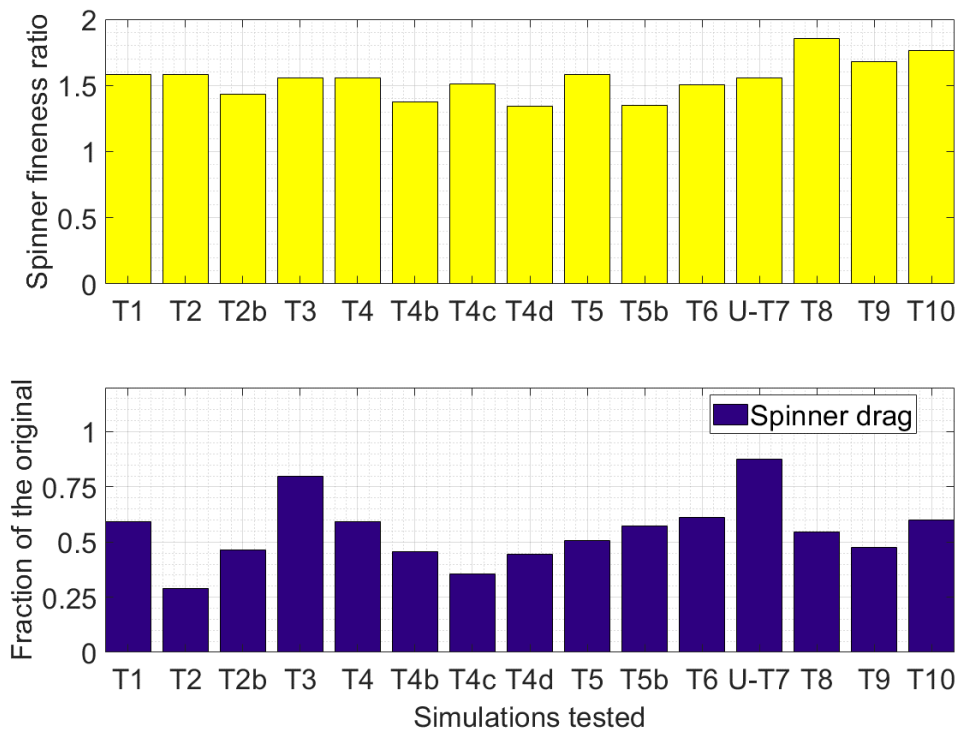
A series of 2D simulations were performed in order to assess the aerodynamic loads and pressure distribution of multiple spinner designs when the effect of the blades was not taken into account. As the spinner design was modified in order to improve the observed pressure recovery, the spinner geometry and the pressure distribution quickly resembled the one of the low drag optimal axisymmetric bodies found in literature. As the blade-off cases were tested, the total drag of the body was reduced by a maximum of 18% from the original nacelle-spinner configuration.

By isolating the nacelle-spinner configuration from the blade, the relation between a high spinner fineness ratio and a decrement in drag became much more evident. After several blade-off simulations where more than 35 design cases were tested under a trial and error approach, the point of flow separation was considerably shifted for most of the cases, including some that previously showed early flow separation under blade-on conditions.

As an example the design *test 16* represented 48% of the original blade-on spinner drag whilst in the blade-off simulation the same design accounted for only 9% of the spinner drag. Based on the observations made by the author, it needs to be emphasized that even if the axisymmetric body is optimized for blade-off conditions, the influence of the blade will definitely affect the pressure recovery in the sense that if an optimal spinner design is wanted, special attention should be payed to the interaction of the spinner and the blade root. Independently of the relatively imprecise prediction offered by the blade-off simulations, the *test 16* increased the relative propeller efficiency up to 0.56%. This increment suggested that blade-off simulations, although less representative, might be used as an initial guess of low computational cost in order to design an efficient spinner in a pusher propeller configuration, especially due to the relatively lower complexity of a nacelle-spinner axisymmetric construction.

A *tangent* spinner design was introduced to reduce the peaks of the pressure distribution observed at the nacelle-spinner transition, at the same time that moved the expansion section of the spinner downstream ahead the blade root thus improving the pressure recovery. The *tangent* cases induced an average increment in the nacelle drag of 5.77% compared to the original value, while the torque was reduced by only 0.05%. The spinner drag was reduced by 47.82% on average and the relative propeller efficiency was improved at a maximum value of 0.88%. Longer tangent portions of the spinner constantly reduced the nacelle drag due to the larger values of C_p that were observed at the nacelle-spinner transition and helped delaying flow separation on the cases with the largest extensions. Given that the expansion section of the spinner was moved further downstream relatively to the blade location, a certain part of the flow that was separated in the suction side of the blade root ended up reattaching to the spinner which contributed to the spinner overall delay in separation. Relatively strong hub vortices were formed mostly due to the difference in tangential velocities between the separated flow and the larger velocity magnitude observed close to the spinner wall, but also because

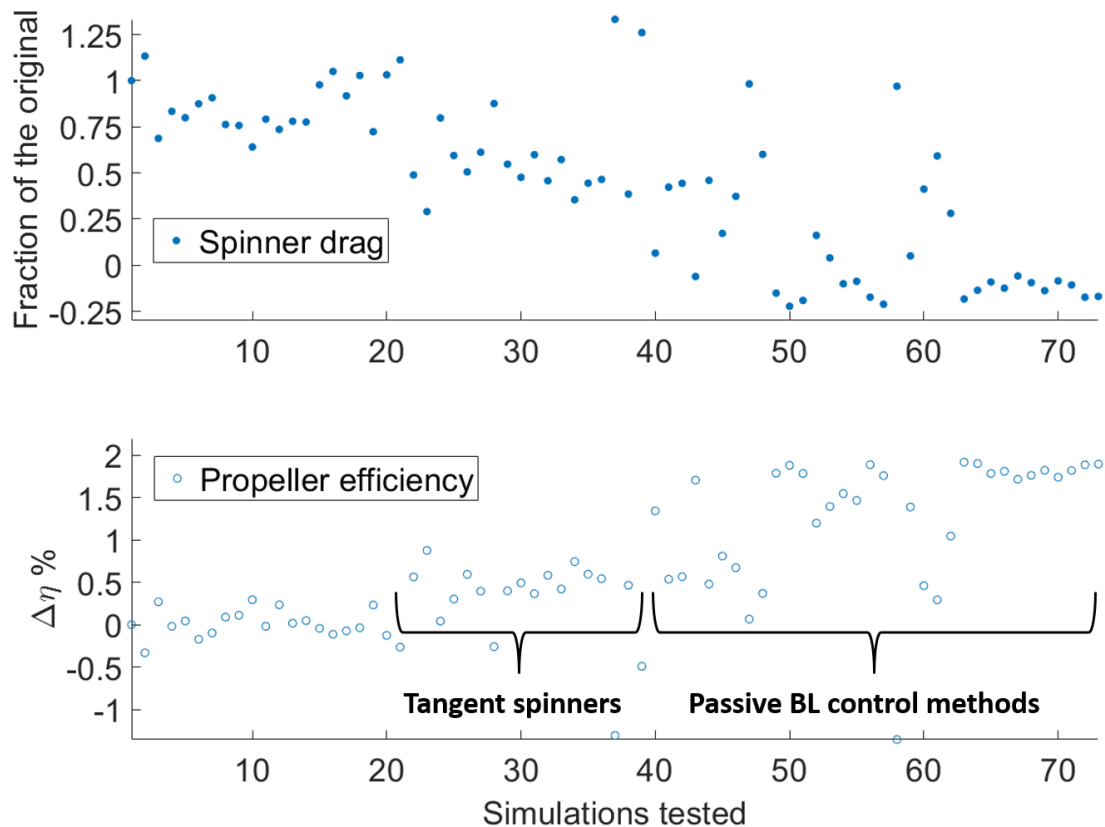
of the boundary layer swirls coming from each one of the rotor blades; nonetheless, hub vortex induced drag did not represent a major concern among the tangent spinner designs.



Tangent designs certainly induced the largest propulsive efficiencies related to the spinner geometry; however, two passive boundary layer control methods were tested based on the observation that some factors such as flow separation, vortex formation and a greater pressure recovery depended greatly on the blade root loading. The first of the methods was the use of baffles that deflected the flow at very low radial positions nearby the blade root. In an attempt to induce a more uniform velocity profile on the rotor wake, the horse shoe vortices (HSV) were interrupted at the core. The test was performed initially on the original spinner used as control variable and the best baffle location was found to be the interruption of the HSV of the root suction side. The relative propeller efficiency was improved 0.47% with no modifications whatsoever to the original spinner geometry. Nevertheless, the largest performance efficiency was induced by a deflection baffle that avoided the formation of the separation vortex. The efficiency of the original configuration was improved 1.34% while the spinner drag was reduced 93.5%. The following baffle designs were located close to the trailing edge of the blade root suction side with the intention of delaying separation in the suction side among tangent spinners. The results were similar: The relative propeller efficiency was improved at a maximum of 1.89% and the spinner drag reduced 122.3% turning the spinner drag into a thrust component. The spinner-baffle configurations with the largest efficiencies often showed similitude among the outflow angle of the streamlines that came from the blade root. The direction of the flow was significantly more aligned with the rotational axis (From a stationary perspective), especially close to the spinner wall. While the gain in excess thrust provided by the reduction of spinner drag was the main reason of the propeller performance enhancement, the relatively low torque variation caused by tangent spinner altogether with a negligible nacelle drag increment were key factors in the propeller enhancement.

The second passive boundary layer control method consisted of a series of ellipse-shaped transversal cavities placed around the spinner with the intention to increase the momentum of the boundary layer due to the local relaxation of the no-slip condition provided by the trapped vortex formed inside the cavities. Out of the multiple locations and depths tested, only 4 cases out of 13 tests improved the relative propeller efficiency by a very small percentage; however, the efficiency enhancement was

achieved on spinners that were relatively efficient already. As an example, the cavity design located upstream ahead the blade root of the tangent spinner *T5* with a depth equal to one third of the incoming boundary layer thickness, induced an additional efficiency increment of 0.03% (Possibly within the uncertainty error) so the propeller maximum efficiency went from 1.89% to 1.92% compared to the original design. The additional performance improvement was especially observed in the cavities with a depth value equal or lower than one third of the boundary layer thickness that were located upstream the expansion section of the tangent spinner *T5*.

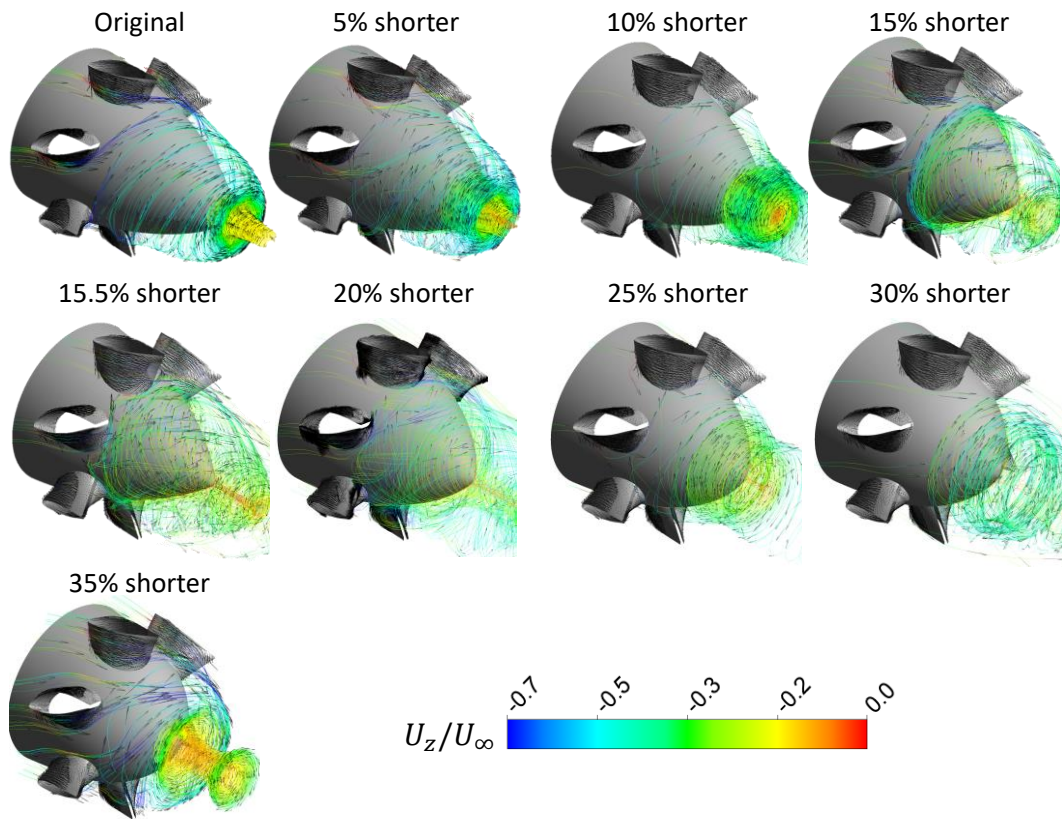


The use of passive BL control methods to avoid flow separation, especially the use of baffles, increased in a significant way the maximum values of relative propeller efficiency obtained from the spinner modifications. While the overall propulsive efficiency was improved due to the delay in separation encountered in most of the spinners after the 20th simulation, the maximum values of efficiency were attained when the combination of the spinner design and the passive BL control methods caused the straightening of the flow that was coming from the blade root. From a stationary perspective, the straightening of the velocity streamlines meant that as the flow reached the expansion section of the spinner, larger adverse pressure gradients were encountered by the attached flow. This increased the positive pressure coefficients close to the spinner wall.

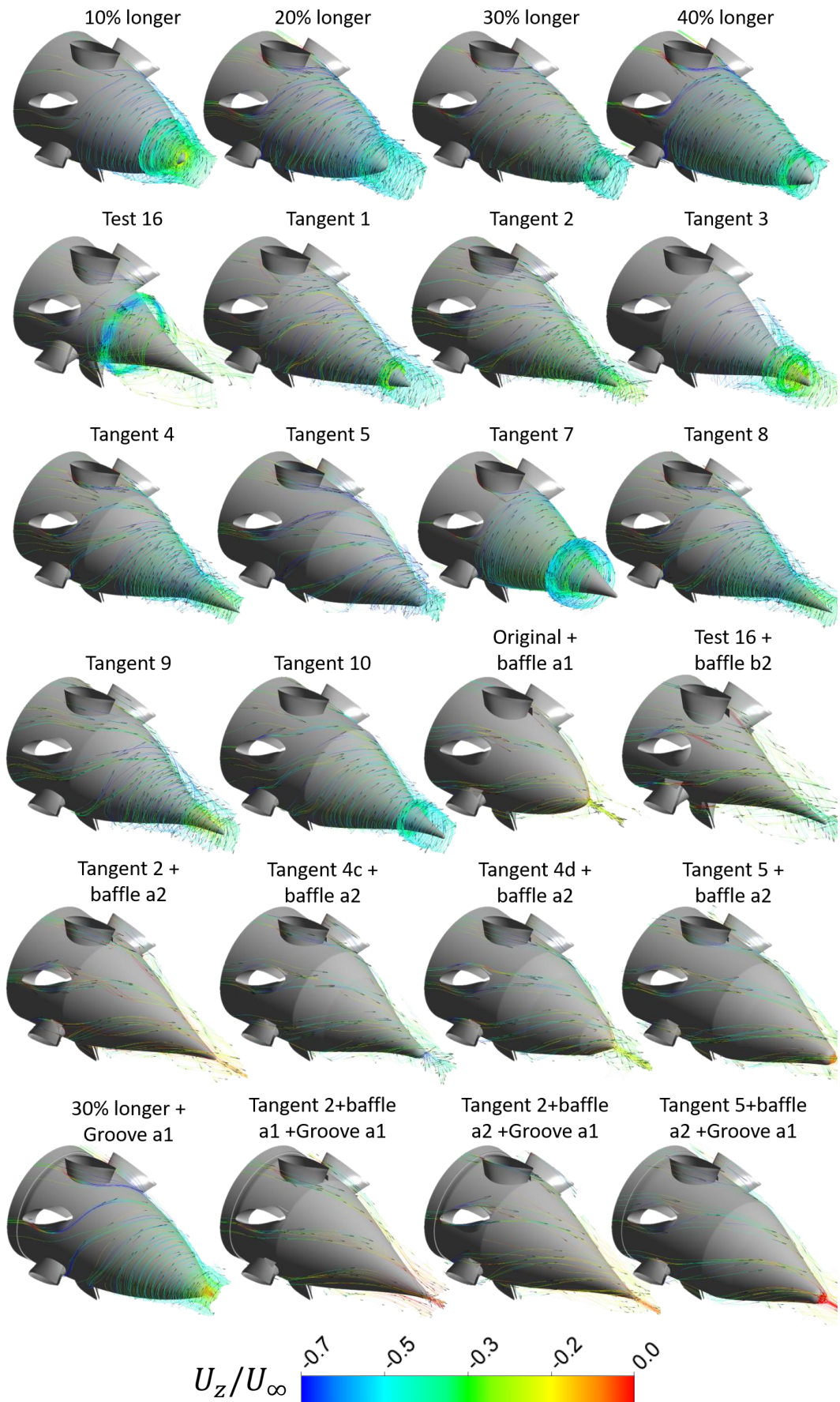
It is the belief of the author that independently of the inverted blade root loading encountered in the original configuration used for this research, the blade loading has to be taken into consideration for the optimal aerodynamic design of a pusher propeller spinner, even more than commonly used parametric variables such as fineness ratio. In particular, the specific blade root loading observed along the research not only decreased the maximum thrust that could possibly be obtained when the spinner was re-designed, but also induced a strong hub vortex with an opposite sign of rotation than the one of the rotor. Future recommendations for pusher propeller spinner designs would definitely include a synergic approach that tackles the spinner design as the interaction between blade loading and the flow separation induced by its geometry.

The spinner designs were drawn in CAD software using splines. In order to offer a simple way to approximate the spinner geometries tested in this thesis, the appendix contains a table that describes the spinner geometry as a combination of two sections. Each of the section is depicted as a polynomial function that extends as long as indicated by the table. The order of the polynomial and the coefficients are also contained in the appendix table.

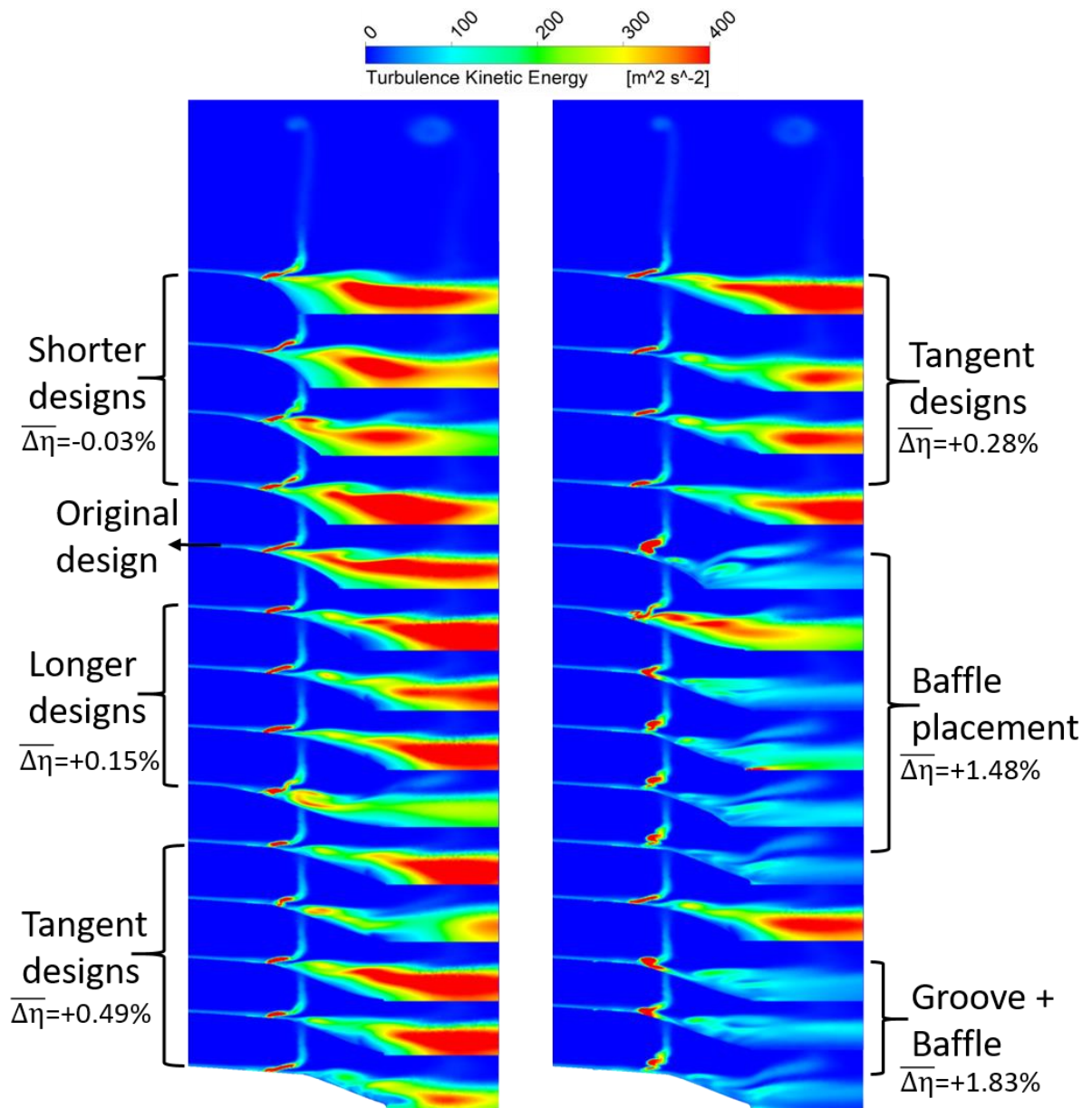
Appendix



Streamlines in shorter spinners with tangential velocity contours.



Streamlines in long and tangent spinners with tangential velocity contours.



Turbulent kinetic energy contours and efficiency increments.

Spinner design	Spinner length portion of the 2 sections	Polynomial order of the geometry equation	Spinner geometry coefficients @ 20 degrees sample line						FR	Relative length
Original	50%	3	0.172	-0.404	-0.191	0.214				
	50%	4	-43.181	51.826	-23.564	4.351	-0.113		1.02	100.00%
5% shorter	50%	3	0.054	-0.430	-0.187	0.215				
	50%	4	-74.415	82.646	-34.929	6.174	-0.220		0.94	95.00%
10% shorter	50%	3	-0.446	-0.366	-0.217	0.201				
	50%	4	-48.680	51.452	-20.968	3.340	-0.024		0.93	90.00%
15% shorter	50%	3	-0.520	-0.432	-0.233	0.200				
	50%	4	-50.996	47.245	-17.205	2.319	0.059		0.85	85.00%
20% shorter	50%	3	-0.589	-0.498	-0.251	0.199				
	50%	4	-93.296	78.488	-25.738	3.257	0.020		0.78	80.00%
20% shorter	50%	3	-0.372	-0.648	-0.261	0.205				
	50%	4	-111.830	97.986	-33.094	4.417	-0.042		0.75	80.00%
20% shorter	50%	3	-0.911	-0.627	-0.186	0.215				
	50%	4	-130.080	113.200	-38.868	5.470	-0.094		0.72	80.00%
20% shorter	50%	3	-1.021	-0.645	-0.162	0.220				
	50%	4	-146.200	126.690	-43.470	6.207	-0.131		0.70	80.00%
25% shorter	50%	3	-0.910	-0.598	-0.246	0.201				
	50%	4	-236.040	185.120	-55.901	6.965	-0.145		0.69	75.00%
30% shorter	50%	3	-1.603	-0.864	-0.264	0.203				
	50%	4	-255.300	173.480	-46.223	4.856	-0.009		0.61	70.00%
35% shorter	50%	3	-2.288	-1.054	-0.269	0.204				
	50%	4	-574.830	333.510	-75.609	6.970	-0.054		0.52	65.00%
10% longer	50%	3	-0.254	-0.288	-0.114	0.221				
	50%	4	-6.844	8.615	-4.866	0.945	0.131		1.13	110.00%
20% longer	50%	3	-0.423	-0.163	-0.088	0.220				
	50%	4	-14.539	23.504	-14.602	3.692	-0.143		1.29	120.00%
25% shorter	50%	3	-0.338	-0.148	-0.089	0.219				
	50%	4	-17.929	32.262	-21.971	6.287	-0.467		1.36	125.00%
30% longer	50%	3	-0.266	-0.136	-0.091	0.219				
	50%	4	-15.174	28.445	-20.090	5.950	-0.453		1.43	130.00%
35% longer	50%	3	-0.244	-0.123	-0.089	0.219				
	50%	4	-6.299	12.274	-9.241	2.799	-0.117		1.51	135.00%
40% longer	50%	3	-0.186	-0.124	-0.093	0.219				
	50%	4	-4.102	8.357	-6.634	2.063	-0.043		1.58	140.00%
Test 16	50%	3	0.160	-0.300	-0.256	0.193				
	50%	4	-1.958	3.874	-2.459	0.313	0.133		1.71	135.00%
Tangent 1	78%	4	-0.096	0.218	-0.307	-0.157	0.228		1.58	140.00%
	22%	1	-0.074	0.219						
Tangent 2	78%	4	-0.212	0.748	-0.665	-0.132	0.227		1.58	140.00%
	21%	1	-0.074	0.219						
Tangent 3	79%	4	-0.477	1.467	-1.116	-0.079	0.225		1.55	138.00%
	31%	1	-0.074	0.219						
Tangent 4	69%	4	-0.752	1.960	-1.626	0.151	0.218		1.55	138.00%
	42%	1	-0.074	0.219						
Tangent 5	58%	4	-5.633	11.337	-8.360	2.287	-0.005		1.58	140.00%
	24%	1	-0.074	0.219						
Tangent 6	76%	4	-0.244	0.490	-0.267	-0.303	0.239		1.51	135.00%
	24%	1	-0.115	0.210						
Tangent 7	76%	4	-0.587	1.610	-1.319	0.051	0.204		1.56	134.00%
	27%	1	-0.074	0.219						
Tangent 8	73%	5	-3.605	7.285	-4.580	0.835	-0.281	0.247	1.85	159.00%
	25%	1	-0.074	0.219						
Tangent 9	75%	4	-0.604	1.928	-1.694	0.176	0.209		1.68	147.00%
	34%	1	-0.074	0.219						
Tangent 10	66%	4	-0.444	1.622	-1.612	0.218	0.218		1.76	153.00%

Spinner geometries described by two curves with polynomial fit. The geometry sample was taken at 20 degrees tilted plane.

Bibliography

- [1] D. P. Witkowski, A. K. H. Lee and J. P. Sullivan, "Aerodynamic Interaction Between Propellers and Wings," *Journal of Aircraft*, pp. 829-836, 1989.
- [2] A. Pagano, M. Barbarino, D. Casalino and L. Federico, "Tonal and Broadband Noise Calculations for Aeroacoustic Optimization of a Pusher Propeller," *Journal of Aircraft*, vol. 47, no. 3, pp. 835-848, 2010.
- [3] L.-Z. Wang, C.-Y. Guo, Y.-M. Su and T.-C. Wu, "A numerical study on the correlation between the evolution of propeller trailing vortex wake and skew of propellers," *International Journal of Naval Architecture and Ocean Engineering*, vol. 10, pp. 212-224, 2018.
- [4] C.-M. Jang, M. Furukawa and M. Inoue, "Analysis of Vortical Flow Field in a Propeller Fan by LDV Measurements and LES—Part I: Three-Dimensional Vortical Flow Structures," *Journal of Fluids Engineering, Transactions of the ASME*, vol. 123, no. 4, pp. 748-754, 2001.
- [5] M. F. Islam, B. Veitch and P. Liu, "EXPERIMENTAL RESEARCH ON MARINE PODDED PROPULSORS," *Journal of Naval Architecture and Marine Engineering*, vol. 4, no. 2, pp. 57-71, 2007.
- [6] K. Mizzi, Y. K. Demirel, C. Banks, O. Turan, P. Kaklis and M. Atlar, "Design optimisation of Propeller Boss Cap Fins for enhanced propeller performance," *Applied Ocean Research*, vol. 62, pp. 210-222, 2017.
- [7] T. Kawamura, K. Ouchi and T. Nojiri, "Model and full scale CFD analysis of propeller boss cap fins (PBCF)," *Journal of Marine Science and Technology*, vol. 17, no. 4, pp. 469-480, 2012.
- [8] A. Javadi and H. Nilsson, "Unsteady numerical simulation of the flow in the U9 Kaplan turbine model," *IOP Conference Series Earth and Environmental Science*, vol. 22, no. 2, 2014.
- [9] R. Shamsi and H. Ghassemi, "Hydrodynamic analysis of puller and pusher of azimuthing podded drive at various yaw angles," *Journal of Engineering for the Maritime Environment*, vol. 228, no. 1, pp. 55-69, 2014.
- [10] S. Choi and J. Ahn, "A Computational Study on the Aerodynamic Influence of a Pusher Propeller on a MAV," in *40th Fluid Dynamics Conference and Exhibit*, Chicago Illinois, 2010.
- [11] Z. M. Hall, "CFD Modeling of US Army UAVs using NASA's Overflow CFD Code," in *55th AIAA Aerospace Sciences Meeting*, Grapevine, Texas, 2017.
- [12] A. Leslie, K. C. Wong and D. Auld, "Broadband noise reduction on a mini-UAV Propeller," in *29th AIAA Aeroacoustics Conference*, Vancouver, British Columbia, 2008.
- [13] J. Yin, A. Stuermer and M. Aversano, "Aerodynamic and Aeroacoustic Analysis of Installed Pusher-Propeller Aircraft Configurations," *Journal of Aircraft*, vol. 49, no. 5, pp. 1423-1433, 2012.
- [14] W. Khan and M. Nahon, "A propeller model for general forward flight conditions," *International Journal of Intelligent Unmanned Systems*, vol. 3, no. 2-3, pp. 72-92, 2015.
- [15] B. Ortun, R. Boisard and I. Gonzalez-Martino, "In-plane airloads of a propeller with inflow angle: prediction vs experiment," in *30th AIAA Applied Aerodynamics Conference*, New Orleans, Louisiana, 2012.
- [16] H. Ghassemi, M. A. and A. Ardeshir, "Numerical Analysis of Hub Effect on Hydrodynamic Performance of Propellers with Inclusion of PBCF to Equalize the Induced velocity," *Polish Maritime Research*, vol. 19, no. 2, pp. 17-24, 2012.
- [17] W. Stalewski and J. Zoltak, "The preliminary design of the air-intake system and the nacelle in the small aircraft-engine integration process," *Aircraft Engineering and Aerospace Technology*, vol. 86, no. 3, pp. 250-258, 2014.
- [18] J. Liu, H. Lin and S. Purimtla, "Wake field studies of tidal current turbines with different numerical methods," *Ocean Engineering*, pp. 383-397, 2016.
- [19] M. Keating; ANSYS, "Accelerating CFD Solutions," ANSYS Advantage, 2011.

- [20] Z. Jiang, Y. Chen, Y. An and Q. Wang, "New actuator disk model for propeller-aircraft computation," *Science China Technological Sciences*, vol. 59, no. 8, pp. 1201-1207, 2016.
- [21] T. C. A. Stokkermans, "Design and Analysis of Swirl Recovery Vanes for an Isolated and a Wing Mounted Tractor Propeller," TU Delft, Delft, 2015.
- [22] F. Menter and T. Esch, "ELEMENTS OF INDUSTRIAL HEAT TRANSFER PREDICTIONS," in *XVI CONGRESSO BRASILEIRO DE ENGENHARIA MECÂNICA 16th BRAZILIAN CONGRESS OF MECHANICAL ENGINEERING*, Goiania, 2011.
- [23] K. Dhinsa, C. Bailey and K. Pericleous, "Investigation into the performance of turbulence models for fluid flow and heat transfer phenomena in electronic applications," *IEEE Transactions on Components and Packaging Technologies*, vol. 28, no. 4, pp. 686-699, 2005.
- [24] F. Menter, M. Kuntz and R. Langtry, "Ten Years of Industrial Experience with the SST Turbulence Model," *Turbulence Heat and Mass Transfer*, vol. 4, pp. 625-632, 2003.
- [25] L. E. Schwer, "Is your meshed refined enough?, Estimating Discretization error using GCI," DYNAMORE GmbH, Bamberg, 2008.
- [26] P. Roache, "Perspective: A Method for Uniform Reporting of Grid Refinement Studies," *Journal of Fluids Engineering, Transactions of the ASME*, vol. 116, no. 3, pp. 405-413, 1994.
- [27] L. Eca and M. Hoekstra, "Discretization Uncertainty Estimation based on a Least Squares version of the Grid Convergence Index," in *2nd workshop on CFD Uncertainty Analysis*, Lisbon, 2006.
- [28] M. S. M. ALI, J. DOOLAN and V. WHEATLEY, "GRID CONVERGENCE STUDY FOR A TWO-DIMENSIONAL SIMULATION OF FLOW AROUND A SQUARE CYLINDER AT A LOW REYNOLDS NUMBER," in *Seventh International Conference on CFD in the Minerals and Process Industries*, CSIRO, Melbourne, Australia, 2009.
- [29] A. C. Aranake, V. K. Lakshminarayan and K. Duraisamy, "Assessment of transition model and CFD methodology for wind turbine flows," in *42nd AIAA Fluid Dynamics Conference and Exhibit*, New Orleans, Louisiana, 2012.
- [30] S. Ivanell, J. Sørensen, R. Mikkelsen and D. Henningson, "Numerical analysis of the tip and root vortex position in the wake of a wind turbine," *Journal of Physics: Conference Series*, vol. 75, no. 1, pp. 1-8, 2007.
- [31] C. E. Thomson and J. H. Rowse, "Pusher propeller installation for turboprop engines". USA Patent 4930725, 5 June 1990.
- [32] Y.-Y. Tsui and C.-K. Wang, "Calculation of laminar separated flow in symmetric two-dimensional diffusers," *Journal of Fluids Engineering, Transactions of the ASME*, vol. 117, no. 4, pp. 612-616, 1995.
- [33] C. B. Da Silva and J. C. F. Pereira, "Invariants of the velocity-gradient, rate-of-strain, and rate-of-rotation tensors across the turbulent/nonturbulent interface in jets," *PHYSICS OF FLUIDS*, vol. 20, no. 5, pp. 55101-1 to 55101-8, 2008.
- [34] G. HALLER, "An objective definition of a vortex," *Journal of Fluid Mechanics*, vol. 525, pp. 1-26, 2005.
- [35] Y. Zhang, K. Liu, Y. L. K. X. H. Zhang and X. Du, "A review of methods for vortex identification in hydroturbines," *Renewable and Sustainable Energy Reviews*, vol. 81, pp. 1269-1285, 21 November 2018.
- [36] D. Reubush, "Effect of Reynolds Number on Boattail Drag," *Journal of Aircraft*, vol. 13, pp. 334-337, 1976.
- [37] T. Lutz and S. Wagner, "Drag Reduction and Shape Optimization of Airship Bodies," *American Institute of Aeronautics and Astronautics*, vol. 35, no. 3, pp. 345-351, 1997.
- [38] S. Dodbele and C. v. Dam, "Design of Fuselage Shapes for Natural Laminar Flow," NASA, Hampton, Virginia., 1986.

- [39] PURDUE UNIV LAFAYETTE IN AUTOMATIC CONTROL CENTER, "The Optimum Shaping of Axisymmetric Bodies for Minimum Drag in Incompressible Flow," Purdue University, Office of Naval Research, Lafayette, Indiana, 1972.
- [40] G. Buresti., G. Iungo and G. Lombardi, "Methods for the Drag Reduction of Bluff Bodies and Their Application to Heavy Road-Vehicles," University of Pisa, Pisa, Italy., 2007.
- [41] P. Bearman, "Bluff body flow research with application to road vehicles," *Lecture Notes in Applied and Computational Mechanics*, vol. 41, pp. 3-13, 2009.
- [42] T. Gustavsson and T. Melin, "Application of Vortex Generators to a blunt body," KTH, Department of Aeronautical and Vehicle Engineering Royal Institute of Technology, Stockholm, 2006.
- [43] R. M. Kelso and A. J. Smits, "Horseshoe vortex systems resulting from the interaction between a laminar boundary layer and a transverse jet," *Physics of Fluids*, vol. 7, pp. 153-158, 1995.
- [44] L. Zhi-hua and X. Ying, "The method to control the submarine horseshoe vortex by breaking the vortex core," *Journal of Hydrodynamics*, vol. 26, no. 4, pp. 637-645, 2014.
- [45] D. McCormick, "Shock/Boundary-Layer interaction control with vortex generators and Passive cavity," *AIAA*, vol. 31, pp. 91-96, 1993.
- [46] G. Godard and M. Stanislas, "Control of a decelerating boundary layer. Part 1: Optimization of passive vortex generators," *Aerospace Science and Technology*, vol. 10, pp. 181-191, 2006.
- [47] J. Lin, F. Howard and D. Bushnell, "Investigation of several pasive and active methods for turbulent flow separation control.," in *AIAA 21st Fluid Dynamics, Plasma Dynamics and Lasers Conference*, Seattle, 1990.
- [48] A. Mariotti, G. Buresti, G. Gaggini and M. V. Salvetti, "Separation control and drag reduction for boat-tailed axisymmetric bodies through contoured transverse grooves," *Fluid Mechanics*, vol. 832, pp. 514-549, 2017.
- [49] A. Iollo and L. Zannetti, "Trapped vortex optimal control by suction and blowing at the wall," *European Journal of Mechanics - B/Fluids*, vol. 20, pp. 7-24, 2001.
- [50] I. B. Celik, U. Ghia, P. J. Roache, C. J. Freitas, H. Coleman and P. E. Raad, "Procedure for estimation and reporting of uncertainty due to discretization in CFD applications," *Journal of Fluids Engineering, Transactions of the ASME*, vol. 130, no. 7, pp. 78001-780014, 2008.